UNIVERSITY OF OKLAHOMA

GRADUATE COLLEGE

PROPPANT FLOW AND TRANSPORT MODELING IN DEFORMABLE HYDRAULIC FRACTURE NETWORKS

A THESIS

SUBMITTED TO THE GRADUATE FACULTY

in partial fulfillment of the requirements for the

Degree of

MASTER OF SCIENCE

By

RUBEN ALBERTO GONZALEZ LOPEZ
Norman, Oklahoma
2018

PROPPANT FLOW AND TRANSPORT MODELING IN DEFORMABLE HYDRAULIC FRACTURE NETWORKS

A THESIS APPROVED FOR THE
MEWBOURNE SCHOOL OF PETROLEUM AND GEOLOGICAL ENGINEERING

BY

Dr. Ahmad Ghassemi, Chair

Dr. Mashhad Fahes

Dr. Siddharth Misra

This thesis is dedicated to my parents, Gloria and Ruben, my sisters Judy and Stephanie, for showing me the path and always believe in my journey. To Laura, my beloved wife, for supporting me in the toughest moments and for sharing this rewarding adventure with me. Also to my friends Saurabh, Yuliana, Michael, Andrea and Felipe, for being that supporting family always helping us and relieving our loads.

Acknowledgements

I would like to express my deepest gratitude and appreciation to my advisor Dr. Ahmad Ghassemi, for his patience, continuous support and encouragement. His advice was vital to find the correct direction throughout this work.

To the members of my thesis committee, Dr. Mashhad Fahes and Dr. Siddharth Misra, I am extremely grateful for your suggestions and help, especially during the last stages of my studies.

To Dr. Dharmendra Kumar, I am grateful for all the constructive discussion and for the invaluable guide to materialize this project. To the members of my research group Amirhossein Kamali, Behzad Hemami, Yawei Li, Qian Gao and Kai Huang, Thank you for the inspiration and disinterested interchange of ideas.

To Laura Hernandez for encourage me to brainstorm in those moments when I felt stuck and her unconditional support.

To Dr. Jean-Claude Roegiers for his disinterested advice aiming to make this work better.

Additionally, I would like to thank the Mewbourne School of Petroleum and Geological Engineering staff for their valuable assistance and support.

Table of Contents

List of Tables

List of Figures

Abstract

The objective of the hydraulic fracturing stimulation is to create a large volume of fractured rock with enhanced permeability. The effectiveness of a hydraulic fracturing stimulation depends on maintaining the created fractures permeable so that proppant are used. The proppant placement process and the properties of the proppant bed strongly affects the productivity of the wells; hence, proppant transport and deposition is an essential component of the hydraulic fracture modeling. In hydraulic fracturing of low permeability unconventional reservoir, proppant transport and deposition are even more important because of the low viscosity of the fracturing fluid (usually slick water used in these treatments). The early proppant settling in low viscosity fluid may significantly reduce the effective propped length, fracture length, and therefore reduce the expected productivity of the stimulated well. Also, proppants might not be able to go through the very small natural fracture apertures which are intersected by the main hydraulic fracture. This study presents the development and verification of proppant flow and transport model for the deformable hydraulic fracture and natural networks. A proppant transport module is developed and is implemented in a 3D hydraulic fracture model "GeoFrac-3D". The main considerations in this study is given to numerical modeling of proppant transport and deposition. The proppant flow and transport within the fracture is modeled by assuming incompressible and Newtonian fluid and representing the slurry as a mixture of fluid and proppant particles. The flow inside the fracture (s) is simulated using the finite element method. The proppant flow and transport equation is a convection dominated problem; which shows numerical instability or oscillations when using the standard Galerkin's approach. To overcome this numerical instability of the proppant transport governing equation, the Streamline Upwinding Petrov Galerkin (SUPG) scheme is used in this

work. Thedeposition of the proppant particles is modeled using the concept of the terminal velocity of a single particle which is calculated based on empirical relationships and later applying correction factors to account for the effect of the walls of the fracture and concentration of particles. The verifications of the numerical models against known analytical solutions are presented first, followed by detailed numerical examples. The numerical simulations of proppant flow and deposition in a single and multiple fractures from a horizontal well, and in networks of hydraulic and natural fractures are carried-out. A sensitivity analysis is performed to investigate the impact of parameters such as proppant size, fluid viscosity, and the discretized fracture grid sizes. The simulation results show that proppant transport and settling velocities are impacted by fluid velocity, proppant size, fluid rheology, fracture aperture, and hydraulic and natural fracture interaction angle. In case of the multiple interacting fractures, the proppant distribution is strongly impacted by the stress shadowing effect or mechanical interactions among the fractures.

Chapter 1. Introduction

The most prominent technique for unconventional reservoir development is hydraulic fracturing. The main objective of hydraulic fracturing is to increase the permeability of reservoirs by injecting pressurized fluid until the rock is fractured, creating new channels of flow for the fluid that was trapped. When the fluid injection is stopped, the fracture tends to close. To avoid closure of fractures and to maintain its conductivity, solid particles known as proppant are pumped along with the fracturing fluid. It is safe to assume that the geometry of the fracture after closure is defined by the final proppant distribution; hence, it is important to assess proppant transport and distribution in fractures. The effectiveness of reservoir stimulation by hydraulic fracturing depends on flow area and proppant pack permeability. The proppant placement process and properties of the proppant beds strongly affects the productivity of the wells; hence, proppant transport and deposition are an essential component of the hydraulic fracture modeling. In hydraulic fracturing of the low permeability unconventional reservoir, proppant transport and deposition are even more important because of the low viscosity of the carrying fluid (usually slick water used in these treatments). The early proppant settling in the low viscosity fluid may significantly reduce the effective propped length, fracture length, and therefore reduce the expected productivity of the stimulated well.

The existence of natural fractures in shale reservoirs is evident from the analysis of data gathered with techniques like micro-seismicity interpretation, core interpretation, tilt measurements interpretation and outcrops interpretation (Fisher et al., 2002; Gale et al., 2007). With these methods, they could determine that the hydraulic fracture generally intercept the natural fracture,

this complicated geometry adds complexity to the problem of estimating the rock deformation, the fluid flow and the proppant flow and transport.

1.1.Problem Statement

The objective of this work is to study proppant transport in a single hydraulic fracture as well as in fracture networks formed by hydraulic and natural fractures during reservoir stimulation. This is an important issue in hydraulic fracturing design and the need to optimize proppant placement through manipulation of injection rate, proppant concentration, size and fluid viscosity. To reach the project objectives, a proppant transport model is to be developed and implemented in "GeoFrac-3D", the hydraulic fracturing platform of the Reservoir Geomechanics and Seismicity Research Group. Using the model, the conditions for optimum proppant placement are studied.

1.2. Methodology

The proppant transport in a hydraulic fracture it is not an isolated phenomenon, hence it needs to be studied as a complex system considering, the deformation of the rock mass and the flow of slurry. The slurry is a mixture of fracturing fluid and proppant particles. The flow of slurry is estimated as a mixture, instead of each individual component and the proppant distribution is calculated using the concept of concentration, defined as the ratio of the volume of proppant and the total slurry volume, $c = v_p / v_T$. The proppant transport is treated using a loosely coupled approach i.e., the fluid properties are calculated at each time step using the concentration of proppant with velocity and pressure data from the previous time step.

The fracture deformation and fluid flow form a coupled system and are solved together using the Boundary Elements Method (BEM), and the Finite Element Method (FEM), respectively. The resultant fracture aperture and pressure distributions are then used to calculate the velocity field for calculating the proppant concentration distribution. The proppant transport equation in a hydraulic fracture governing equation is discretized with FEM, furthermore. To overcome the numerical instability characteristic of the advective type of equations, the Streamline Upwind Petrov Galerkin (SUPG) is applied. After the proppant concentration distribution is solved, the fluid properties are updated and used as input for the next time step. For numerical verification, eachequation (i.e., fracture deformation, fracture fluid flow, and proppant flow and transport) is solved separately and the numerical results are compared with analytical solution to verify the correct implementation of the numerical scheme.

The assumptions considered in this work to estimate fracture aperture, pressure distribution and proppant distribution are:

- Static fracture networks with no propagation
- All the fractures are completely open before the proppant is injected
- Homogeneous and isotropic rock mass
- The fracturing fluid is Newtonian
- Fluid velocity in laminar regime (lubrication theory holds)
- Proppant particles and fracturing fluid are incompressible
- Proppant particles are spherical with equal sizes
- The diameter of proppant particles is much smaller than the width of the fracture

1.3. Thesis Organization

A literature review presenting previous experimental and numerical studies aiming to explain the behavior of proppant flow and transport in a single fracture and in fracture networks is presented in Chapter 2. The governing equations and their numerical implementation methodologies for the fracture deformation, the fracturing fluid flow and the proppant flow and transport are presented in Chapter 3. Additionally, the verifications of each component against known analytical solutions are also provided in Chapter 3. A detailed study of the proppant distribution in a single hydraulic fracture and a sensitivity analysis of the main parameters which impact the proppant distributions is presented in Chapter 4. The solution of the proppant transport model coupled with the Geo-Frac 3D to solve the cases of multiple fracture networks is presented in Chapter 5. Finally, conclusions and recommendations are presented in the Chapter 6.

Chapter 2. Literature Review

This chapter presents a brief view of the experimental and numerical studies on the proppant flow and transport. Proppants are natural or synthetic granular materials that are injected into a hydraulic fracture after the fracture has been initiated with a clean fluid. Most commonly used proppants in the conventional hydraulic fracturing are shown in Fig. 2-1. Microppproppant also exist and are increasingly used in unconventional reservoir stimulation. The selection of the proppant type for a particular reservoir depends on its characteristics such as formation depth, in-situ stress state, temperature, and rock type, and natural fractures. A slurry which is a mixture of proppant particles and fracturing fluid is transported through the wellbore to the hydraulically induced fracture in the formation. The proppant placement process can be mainly divided in two phases; firstly, a low viscosity fluid is injected from the wellbore to the rock formation to initiate and propagate the fracture to create a pathway for the proppant flow, and secondly a higher viscosity fluid that carries proppant is injected to the fracture. As a result, a propped hydraulic fracture or a system of fractures is formed in the rock formation.

Figure 2-1. Commonly used proppant types in hydraulic fracturing stimulations. (Kullman, 2011).

In several black shale as well as in grey shale units which are gas reservoirs, there is evidence of the pre-existing joints. An example is the Marcellus shale whose joints are cataloged as J1 and J2 sets as shown in Fig 2-2 (Engelder et al., 2009; Evans, 1994).

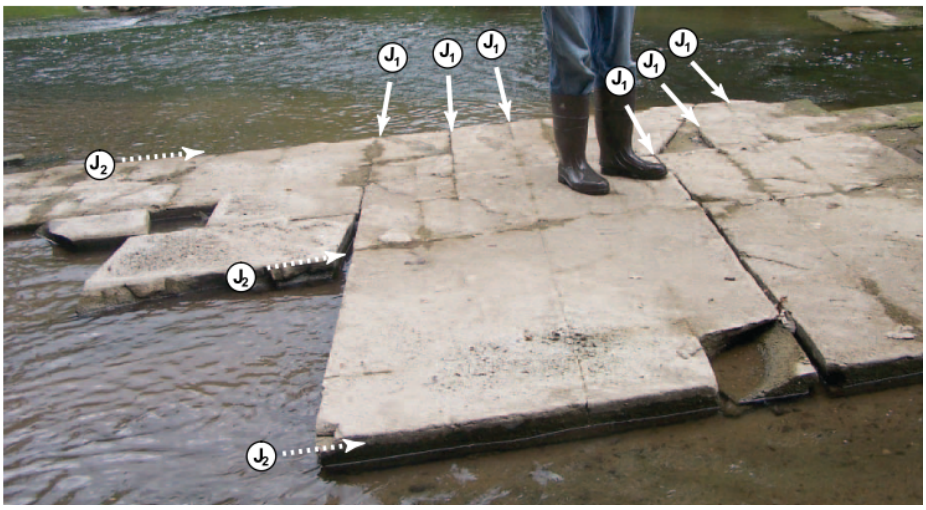

Figure 2-2. J1 and J2 joints intersecting in the Marcellus black shale (Engelder et al., 2009).

Hydraulic fractures often intersect these natural fractures and create a network of fractures with potential for the flow of fracturing fluid and proppant. The fracture network formation has been affirmed using microseismic mapping (see, Figure 2.3) and interpretation of data from tiltmeters, core, etc. Prior to the execution of the hydraulic fracturing job, seismic receivers and tiltmeters are installed in wells adjacent to the zone to be stimulated, tiltmeters are also installed in the surface. The microseismic events and the deformation of the rock while the hydraulic fracture is being created are recorded by the sensor and the resultant data is later interpreted to produce maps not only of the hydraulic fracture just created but also of the preexisting natural fractures which were affected by the fracking job as shown in Fig. 2-3 (Fisher et al., 2002).

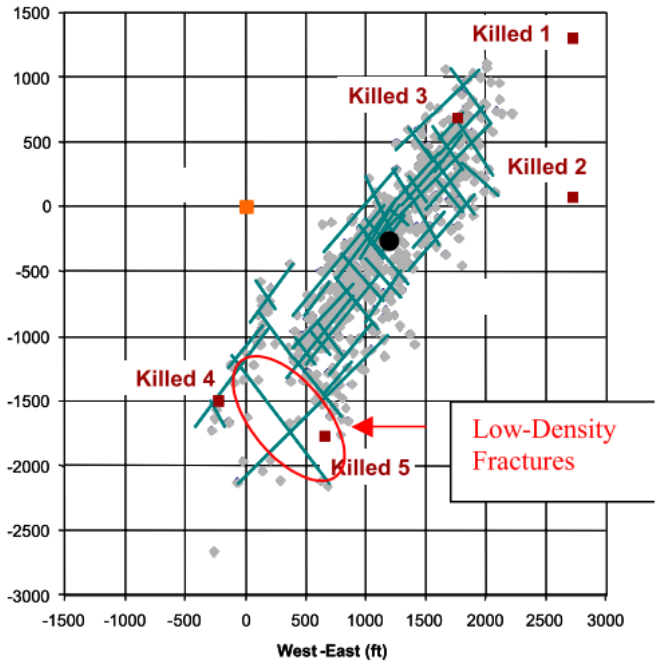

Figure 2-3. Fracture structure plot interpretation from microseismicity and tiltmeters data. Hydraulic fractures are shown in the direction NE-SW and natural fractures are shown in the direction NW-SE (Fisher et al., 2002).

Several experimental and numerical studies on the proppant flow and transport have been presented. A general understanding of the proppant flow and transport in hydraulic fractures begins with the analysis of this phenomena in a single fracture to understand flow mechanism and constitutive relationships. With the findings of complex geometries in reservoirs where hydraulic fractures intersect natural fractures, the principles found for single fractures, needed to be extended to match such complicated cases.

2.1. Experimental Studies on Proppant Flow and Transport

2.1.1. Experimental Studies for a Single Hydraulic Fracture

One of the first proppant materials which is still in use is sand. The earliest experiments trying to explain the behavior of sand movement in a hydraulic fracture was reported by (Kern et al., 1959) in their setup the fracture was simulated with two parallel plexiglas plates, the slurry (i.e., mixture of fluid and sand) was injected from one end while restricting the flow in the upper and lower edges to ensure an horizontal flow. The slurry was recovered from the other end, and separated to form a closed system as shown in Fig. 2-4. They observed a limited growth in the sand bed height due to the poor transport properties of the water. Kern et al. (1959) defined the critical velocity as an equilibrium value that the system will automatically seek, if possible. Once the equilibrium velocity is reached, the injected sand, denoted as 'sand injected later' is deposited preferably in front of the previously formed sand bed denoted as 'sand injected earlier' as shown in Fig. 2-5.

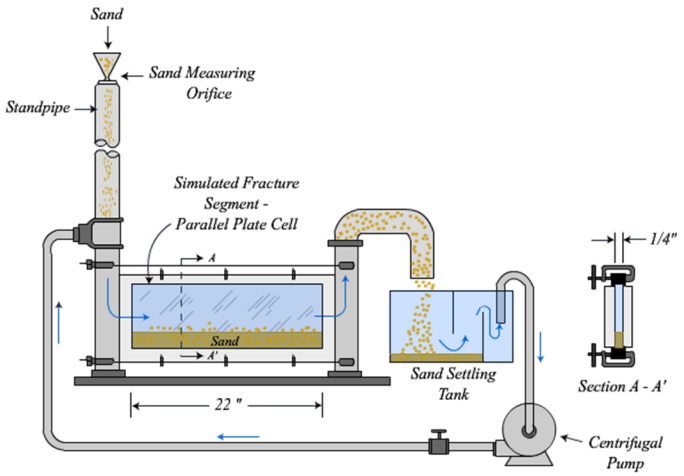

Figure 2-4. Equipment to study sand movement proposed by (Kern et al., 1959).

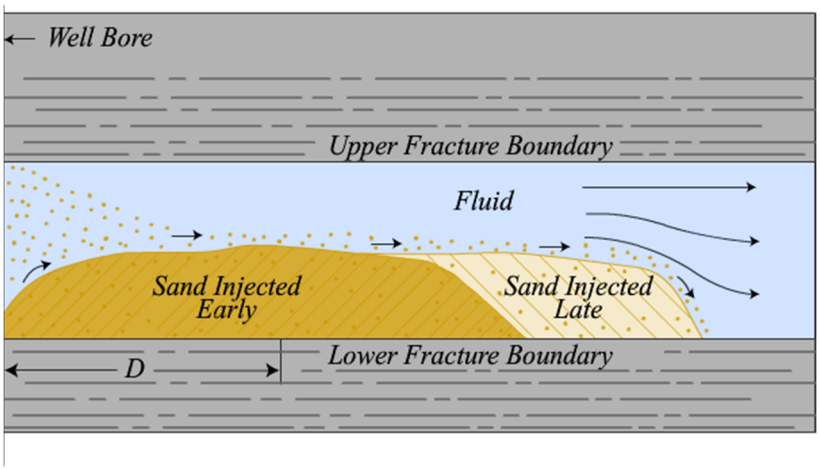

Figure 2-5. Result from the study of sand movement. The sand bed instead of been growing in height, it was growing in length (Kern et al., 1959).

To help with a quantitative analysis of the sand transport injected through two parallel plates Wahl & Campbell (1963) filmed the process for further analysis. From the many parameters that could affect this phenomenon, they centered their attention on the sand concentration, fluid viscosity, and flow rate. The effect of fluid viscosity was controlled in the experiments using three kind of oils, 6.06, 57.8 and 487.9cp. They proposed the concept of two flow regimes; the first where the proppant is transported by direct action of the fluid movement and is dominated by suspended flow, and the second where the proppants settle to form a layer in the bottom of the fracture. These flow regimes are divided in regions considering the ratio oil viscosity – bulk velocity of the slurry $(\mu_o v_B)$ vs sand concentration as shown in Fig. 2-6. Region I, represents the mentioned suspended flow, Region II is divided in 3 sub regions, IIa, IIb and IIc. In Region IIa the solids are transported over a moving deposit. In Region IIb the particles are transported over a deposit which is experiencing sliding, and finally, in Region IIc, the solids are not transported or show small erratic movement.

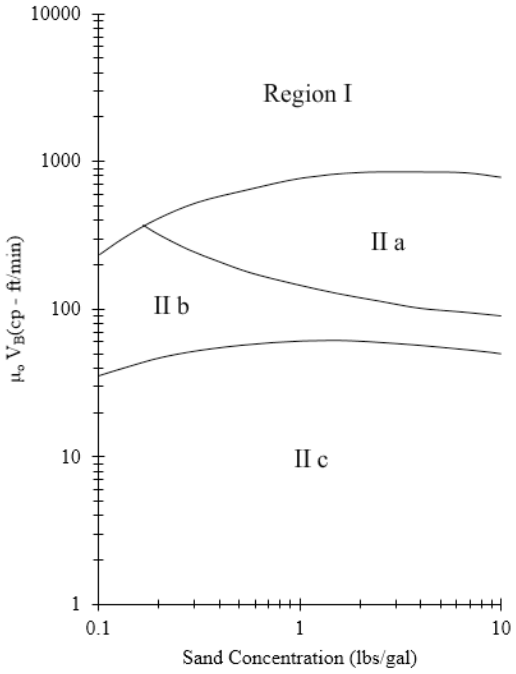

Figure 2-6. Flow regimes regions considering the ratio oil viscosity - bulk velocity of the slurry vs sand concentration (Wahl & Campbell, 1963)**.**

The deposition of proppant in a hydraulic fracture was studied by Novotny (1977) using the concept of settling velocity of a single sphere in a Newtonian fluid in an unconstrained fluid, this parameter denoted with v_∞ was divided according to the flow regime which was classified considering the Reynold's number. As an analytical relation was not always possible, it was necessary to run several experiments using a plexiglass parallel plates apparatus to simulate the movement of the sand as well as experiments using rheometers to measure shear rates (Novotny, 1977). More details about the results of this study are discussed in section 3.1.4.

A settling velocity correlation validated with experimental data was proposed by Acharya (1984). They proposed a correlation for settling velocity of a single particle that best fit the experimental results considering an intermediate flow regime (i.e. Reynolds number ($2<N_{Re}<500$)) in non-Newtonian fluids expressed as (Acharya, 1984):

$$v_\infty = \left\{ \frac{3\rho_f}{4(\rho_p - \rho_f) g d_p} \left[\frac{24F(n)}{R_e} + \frac{F_2(n)}{R_e^{F_3(n)}} \right] \right\} \tag{2.1}$$

where n is the pseudo plastic index of a power law fluid, ρ_f is the fluid density, ρ_p is the proppant density, g is the gravitational force, d_p is de proppant diameter, R_e is the particle Reynolds number and $F(n)$, $F_2(n)$, $F_3(n)$ are functions defined as:

$$F(n) = 3^{\frac{3n-3}{2}} \left[\frac{33n^5 - 63n^4 - 11n^3 + 97n^2 + 16n}{4n^2(n+1)(n+2)(2n+1)} \right] \tag{2.2}$$

$$F_2(n) = 10.5n - 3.5 \tag{2.3}$$

$$F_3(n) = 0.32n - 0.13 \tag{2.4}$$

Proppant flow experiments in a parallel plate chamber were also performed by (Gadde et al., 2004), the results were recorded with a video camera allowing the study of proppant mechanisms variation with time. Additionally, to verify the results from other authors, they presented empirical factors aimed to correct the settling velocity modeled initially with Stokes' law as proposed by (Novotny, 1977). The factors proposed accounts for proppant concentration and the effect of the fracture walls. The correction factor which accounts for the effect of proppant concentration is given as (Gadde et al., 2004):

$$v_\phi = v_s(2.37\phi^2 - 3.08\phi + 1) \tag{2.5}$$

where v_s is the settling velocity and ϕ is concentration. The correction factor relating the effect of the fracture walls is:

$$v_w = v_s \left[1 - \frac{9}{16} \left(\frac{m}{1-m} \right) ln \frac{9}{16} \left(\frac{m}{1-m} \right) \right] \tag{2.6}$$

where $m = a/l$, a is radius of a particle of proppant and l is the distance of the particle form the walls. This equation is used in this thesis.

The importance of convection as a mechanism of flow movement in a hydraulic fracture was studied by (Clark, 1996). The results of experimental observations in a parallel plate apparatus which simulates a static hydraulic fracture, were analyzed with two non-dimensional parameters; one for Newtonian fluids and one for non-Newtonian fluids. The non-dimensional parameter for Newtonian fluids is given as (Clark, 1996):

$$N_C = \frac{12\mu q}{\Delta\rho g w^3} \tag{2.7}$$

where μ is the fluid viscosity, q is the fluid injection rate, $\Delta\rho$ is the difference between the densities of the fluid and the proppant material, g is the gravitational force and w is the fracture width. This non-dimensional number combines the horizontal and vertical forces, the values reported from the experiments showed that $N_C < 1$, meaning that convective flow was predominant. In the case of the non-Newtonian fluid the non-dimensional parameter is:

$$N_C = 2\left(4 + \frac{2}{n}\right)^n \frac{Kq^n}{\Delta\rho g w^{(1+2n)}} \tag{2.8}$$

where K and n are the power law coefficients. In this case the results suggested that convection was also a predominant mechanism in the proppant transport phenomenon.

The rheology of fluids with suspended particles was studied by Boyer et al. (2011). In their work, they proposed a friction law for the shear stress τ, and a volume-fraction law ϕ of the slurry. In the experimental setup to determine these laws, the slurry (i.e., a mixture of fracturing fluid and proppant particles) is placed in a rheometer with a conic shaped chamber, covered by a plate connected to a rheometer which apply simultaneously confining force, F, torque, M, and the rotational speed, ω , as shown in Fig. 2-7a. The plate is free to compress or expands as needed.

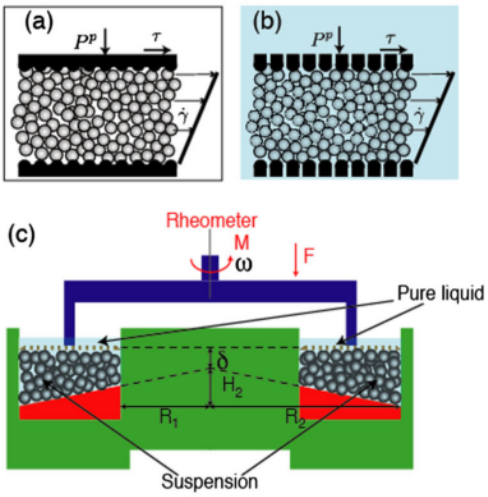

Figure 2-7. Experiment setup proposed by (Boyer et al., 2011) to study the rheology of a mixture of Newtonian fluid and proppant particles.

They found one dimensionless parameter describing the phenomenon called inertial number I defined as:

$$I = d\sqrt{\frac{\rho_p}{P^p}}\dot{\gamma} \tag{2.9}$$

where ρ_p is the density of suspended particles, P^p is granular pressure, d is proppant diameter and $\dot{\gamma}$ is shear rate of the slurry. From their measurements they propose relationships between the friction coefficient and the inertial number μ vs I and the particles concentration with the inertial number ϕ vs I. The behaviors describing the dimensionless shear stress can be mathematically described without the addition of any correction factor as:

$$\eta_s(\phi) = 1 + \frac{5}{2}\phi\left(1 - \frac{\phi}{\phi_m}\right)^{-1} + \mu^c(\phi)\left(\frac{\phi}{\phi_m} - \phi\right)^2 \tag{2.10}$$

with $\mu^c(\phi)$ defined as:

$$\mu^c(\phi) = \mu_1 + \frac{\mu_2 - \mu_1}{1 + I_0\phi^2(\phi_m - \phi)^{-2}} \tag{2.11}$$

where $\mu_1 = 0.32$, $\mu_2 = 0.7$, $\phi_m = 0.585$ and $I_0 = 0.005$ taken from experimental observations. And the dimensionless effective normal viscosity is described by:

$$\eta_n(\phi) = \left(\frac{\phi}{\phi_m} - \phi\right)^2 \tag{2.12}$$

2.1.2. Experimental Studies for Multiple Fractures and Fracture Networks

The behavior of proppant flow in fracture networks has been studied by setting up experiments with a low pressure system in the laboratory. Many scenarios have been simulated by pumping sand slimy through a series of complex slot configurations while varying the slot complexity, pump rate, proppant concentration, and proppant size. A total of 27 test cases were run in four types of slot configurations as shown in Fig. 2-8 (Sahai et al., 2014). The major conclusions of this study are: the effect of pump rate was found to be different in the case of primary and secondary slot configuration, the proppant transport in the primary vertical slot was observed to occur via sedimentation and fluidization in the form of a thin layer of high concentration of proppant, in sedimentology is referred as traction carpet, after the creation of a proppant dune. However, in the case of secondary vertical slots, the proppant transport was observed to be dependent on the pump rate, confirming that there is a minimum value of pump rate required to transport proppant inside the secondary slots, denominated threshold pump rate. Two mechanisms were observed to be transporting the proppant into the secondary vertical slots: I) when the fluid velocity inside the primary fracture was higher than the threshold velocity, the fluid could drag proppant into the secondary slot, and II) independently of the pump rate proppant was falling from the primary slot to the secondary slot due to the gravitational force effects. The fluid velocity inside the primary slot can be expected to dictate the proppant buildup in the secondary slot. It was also observed that the rate of proppant settling is highly affected by the proppant concentration, with a direct relationship with the sediment height as shown in Fig. 2-9.

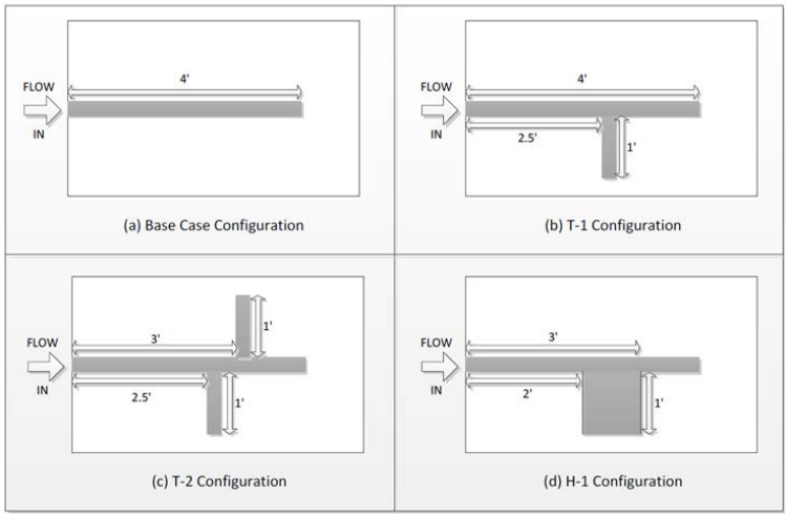

Figure 2-8. Schematic diagrams of the four different slot configurations. Top view (Sahai et al., 2014).

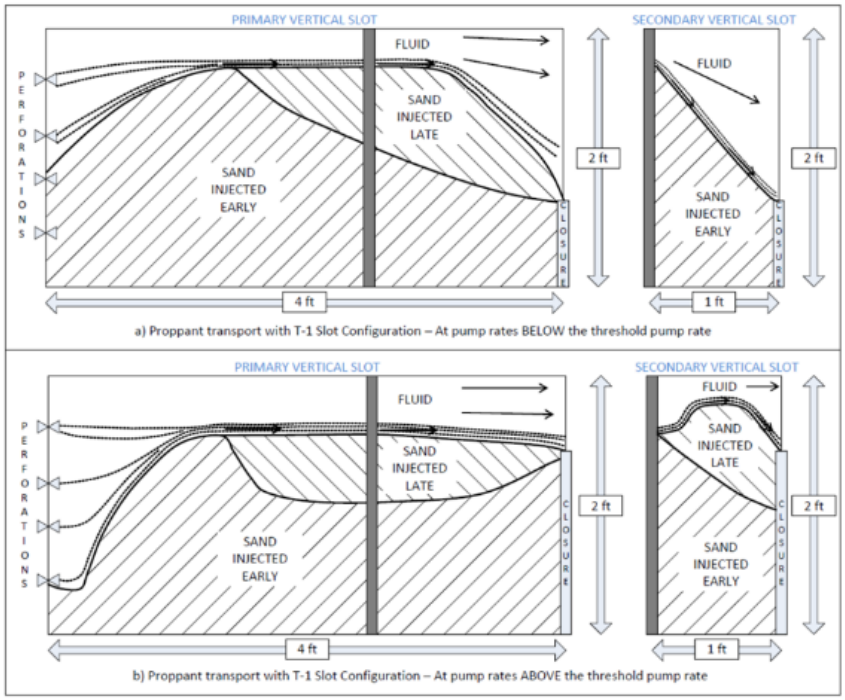

Figure 2-9. Schematic diagrams summarizing the results from the proppant flow and transport analysis- side view (Sahai et al., 2014).

A set of experiments where transparent fracture slots, with bypass angles 45, 90 and 135, as shown in Fig. 2-10, were constructed to mimic intersections of natural fractures with hydraulic fractures by (Tong & Mohanty, 2016). The inlet is on the right, and the outlet is on the left. The length,

height and width of the main slot were 15”, 3” and 0.08”, respectively. The bypass slot was 7.5 in length, and had the same height and width as that of the main one. Typical hydraulic fracture width ranges from 1 mm to 5 mm. A typical proppant flow pattern in the main slot and the bypass slot is shown in Fig. 2-11. From the study, it was determine (as one would expect) that there is a direct relationship between the quantity of proppant entering the bypass slot and the angle of inclination of the bypass slot, it was also concluded that the shear rate of the fluid used to transport the proppant influences directly in the quantity of proppant allocated into the bypass slot (Tong & Mohanty, 2016).

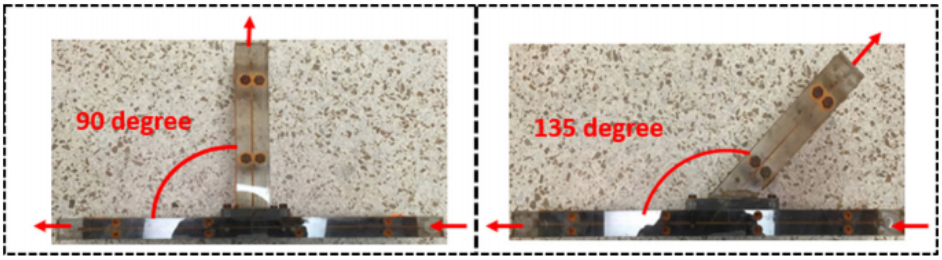

Figure 2-10. Top view of slot configurations to simulate hydraulic fracture networks, red arrows indicate the fluid flow pattern. (Tong & Mohanty, 2016).

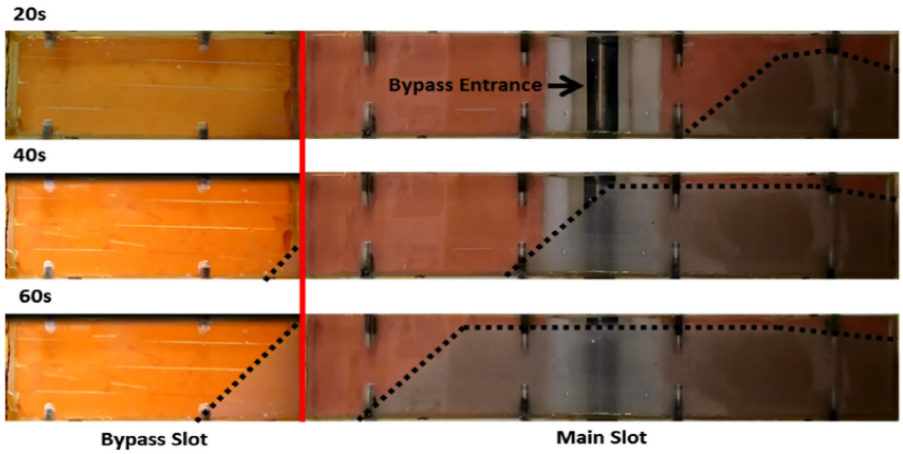

Figure 2-11. Results at different times of the experiment where the bypass slot inclination is 90° (Tong & Mohanty, 2016).

To get more insight of this phenomenon the variables measured in addition to the fracture orientation were: proppant size, proppant concentration and pump rate, the behavior was reported at 20 s, 40 s and 60 s to compare the cases of study. Three zones were observed in the sand bed that have a direct relationship with the water injection rate: the bottom immobile sand bed zone, the middle flowing slurry zone, and the top clear fluid zone. The bottom of the sand bed was mainly composed by the sand injected in earlier stages; the sand pumped after, forms the top part of the bed and continues the movement downstream.

The sand bed length has a direct relationship with the shear rate, at higher injection rates the length was found to be substantially longer. Proppant placement in the bypass has a direct relationship with the injection rate and the shear rate and it is inversely affected with the angle.

All these experimental studies are an effort to understand the proppant transport in a hydraulic fracture and the impact in the system of variables like, geometry of the system, fluid properties, fluid velocities, as well as geometry and properties of the proppant. The proppant transport is described qualitatively and relationships like settling velocity as well as other factors like wall effect and concentration factors are developed to mathematically describe the observed phenomena which can then be used in modeling.

2.2.Numerical Studies on Proppant Flow and Transport

2.2.1. Numerical Studies for a Single Hydraulic Fracture

One of the first numerical attempts to solve the problem of proppant distribution in a hydraulic fractures, divided the domain representing the fracture in small element to calculate progressively

parameters like fluid volume loss, increase in sand concentration, sand settling velocity, the height of the deposited bed and volume of deposited sand as a function of fracture aperture, fracture length and injection rate (Daneshy, 1978). Among his results he showed a concept which aggress with the work exposed by (Kern et al., 1959), where after the equilibrium velocity was reached, the height of the sand bed tends to keep constant h_{eq} and the proppant is deposited in front of the sand bed previously formed as shown in Fig. 2-12.

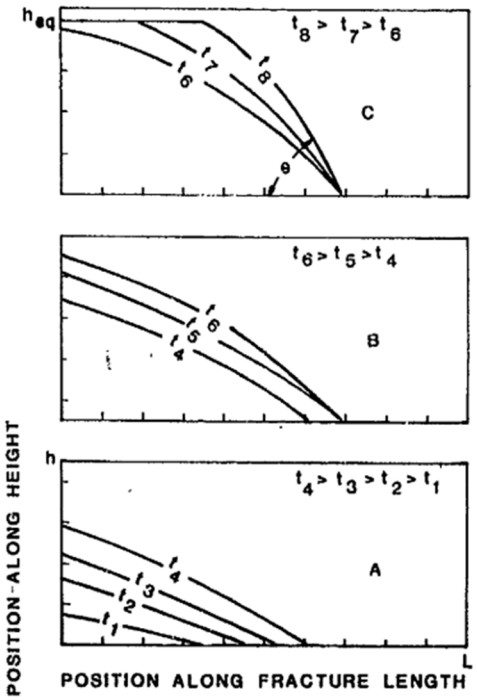

Figure 2-12. Proppant accumulation pattern at different times (Daneshy, 1978).

Several mathematical models have been proposed to simulate proppant flow and transport in a hydraulic fracture (Biot & Medlin, 1985; Clifton et al., 1988; Ouyang, 1994; Pearson, 1994). They are similar in that the governing equations are obtained using single phase flow of a slurry and applying the principle of mass balance, and the main parameters that appear are fracture width denoted by w, pressure distribution denoted by p, proppant concentration denoted by c, proppant velocity denoted by v_p, fluid velocity denoted by v_f and mixture velocity denoted by v. A detailed

description of the methodology proposed to describe the proppant transport in hydraulic fractures is presented in Chapter 3. The resultant expression for the transport of proppant is (Pearson, 1994):

$$\frac{\partial(cw)}{\partial t} + \frac{\partial\left(cv_{px}w\right)}{\partial x} + \frac{\partial\left(cv_{pz}w\right)}{\partial z} = 0 \tag{2.13}$$

This equation is derived in a later chapter. They also use the lubrication equation to approximate the velocity of the fluid in the fracture envisioned as smooth parallel plates:

$$v_x = -\frac{w^2}{12\mu}\frac{\partial p}{\partial x} \tag{2.14}$$

$$v_z = -\frac{w^2}{12\mu}\frac{\partial p}{\partial z} \tag{2.15}$$

Finally they used the expression proposed by (Novotny, 1977) to include the effect of the settling velocity.

An equation that governs the proppant transport in a hydraulic fracture which directly account for the fluid lost in the formation due to the Carter's leak-off phenomenon was proposed by (Ouyang et al., 1997). Based on the principle of mass conservation they combine the equations of proppant transport and fluid flow in a hydraulic fracture to produce the following expression:

$$w\frac{\partial c}{\partial t} - (1-c)\frac{\partial w}{\partial t} - \frac{\partial[(1-c)wv_x]}{\partial x} - \frac{\partial\left[(1-c)wv_y\right]}{\partial y} - q_l \tag{2.16}$$

where w is the fracture width, c is the proppant concentration, v_x and v_y are proppant velocities in the x and y directions respectively. They also proposed a framework to discretize this type of differential equations using a Finite Element Method.

Until this point, the proposed models to simulate the proppant transport in hydraulic fractures suggested to weakly couple the proppant concentration with the fracture aperture and fluid pressure phenomenon via the calculation of fluid properties. But the procedure and the constitutive equations were not clearly defined, furthermore the models did not address the phenomenon

proppant accumulation inside the fracture which resembles a porous medium with variable (in space and time) permeability which affects the flow of the slurry. Recently, a methodology to describe the proppant transport in a hydraulic fracture is presented by (Dontsov & Peirce, 2014a) whereby two phases (fluid and particles) are considered. Using the constitutive equation derived by (Boyer et al., 2011) which estimates particle pressure and the shear stresses in the slurry (mixture of fracturing fluid and proppant), they formulated the fluid velocity and the proppant velocity equations and obtained governing equation of fluid flow and proppant transport in a hydraulic fracture:

$$\frac{\partial w}{\partial t} + \nabla \cdot \boldsymbol{q}^s + g_L = 0 \tag{2.17}$$

$$\frac{\partial w\bar{\phi}}{\partial t} + \nabla \cdot \boldsymbol{q}^p = 0 \tag{2.18}$$

where w is the fracture width, $\bar{\phi} = \langle \phi \rangle / \phi_m$ is the normalized proppant concentration (the ratio between proppant concentration averaged over the fracture width and the maximum concentration of proppant, the maximum concentration of proppant was measured in experiments with a customized rheometer by (Boyer et al., 2011), $\phi_m = 0.585$, g_L is the Carter's leak-off, $\boldsymbol{q}^s$ and $\boldsymbol{q}^p$ are the slurry and the proppant fluxes vectors:

$$\boldsymbol{q}^s = -\frac{w^3}{12\mu} \hat{Q}^s \left(\bar{\phi}, \frac{w}{a}\right) \nabla \hat{\boldsymbol{p}} \tag{2.19}$$

$$\boldsymbol{q}^p = B\left(\frac{w}{a}\right) \hat{Q}^p \left(\bar{\phi}, \frac{w}{a}\right) \boldsymbol{q}^s - B\left(\frac{w}{a}\right) \frac{a^2 w}{12\mu} (\rho^p - \rho^f) g \hat{G}^p \left(\bar{\phi}, \frac{w}{a}\right) \tag{2.20}$$

where μ is the viscosity of the fracturing fluid, $\hat{p}$ is the fluid pressure, ρ^p is the density of the proppant, ρ^f is the density of the fracturing fluid, g is the gravitational force, a is the redius of a particle of proppant, B is a blocking function which considers the process of flow restriction due to proppant trapped in areas where the facture width is not large enough (greater than 3 times the

proppant diameter), i.e., proppant bridging. The blocking function is defined as (e.g., Dontsov & Peirce, 2014b):

$$B\left(\frac{w}{a}\right) = \frac{1}{2}H\left(\frac{w}{2a} - N\right)H\left(\frac{w_B - w}{2a}\right)\left[1 + \cos\left(\pi\,\frac{w_B - w}{2a}\right)\right] + H\left(\frac{w - w_B}{2a}\right) \tag{2.21}$$

where $N = 3$ is suggested by Dontsov & Peirce (2014b), H is the Heaviside function and $w_b = 2a(N + 1)$. The functions $\hat{Q}^s$, $\hat{Q}^p$ and $\hat{G}^p$ are calculated from the slurry flow solution (Dontsov & Peirce, 2014a) and represented graphically for convenience as shown in Fig. 2-13. This model is suitable to describe proppant transport including the settling effect using the numerically calculated functions $\hat{Q}^p$ and $\hat{G}^p$. The function $\hat{Q}^p$ modifies the result of slurry flux implying that the proppant particles have different velocity than the fluid. The numerically calculated function $\hat{G}^p$ dictates the gravitational settling effect. Flow of slurry in the fracture can change as the as the concentration of proppant increases and forms a compact pack of particles. In this situation, the fluid is not flowing in an empty space (as in Poiseuille flow rather it occurs in a porous space (i.e., Darcy flow). The change from Poiseuille to Darcy flow is captured with the function $\hat{Q}^s$; it takes on a value of 1 when the proppant concentration is zero, causing equation (2.19) to simplify as:

$$\boldsymbol{q}^s = -\frac{w^3}{12\mu}\nabla\hat{\boldsymbol{p}} \tag{2.22}$$

when the concentration of proppant increases, the values of slurry flow will decrease as the values $\hat{Q}^s$ are smaller than 1, simulating the decrease in velocity as the fluid is now flowing through a porous media, and when the proppant concentration reaches maximum values, this function takes on values tending to zero, therefor the movement of the slurry will tend to small values. The behavior of the function $\hat{Q}^s$ is also shown in Fig. 2-13. They also proposed a blocking function to

account for proppant bridging so the proppant is not transported beyond some imposed limit, 3 proppant diameters as suggested in (Dontsov & Peirce, 2014a).

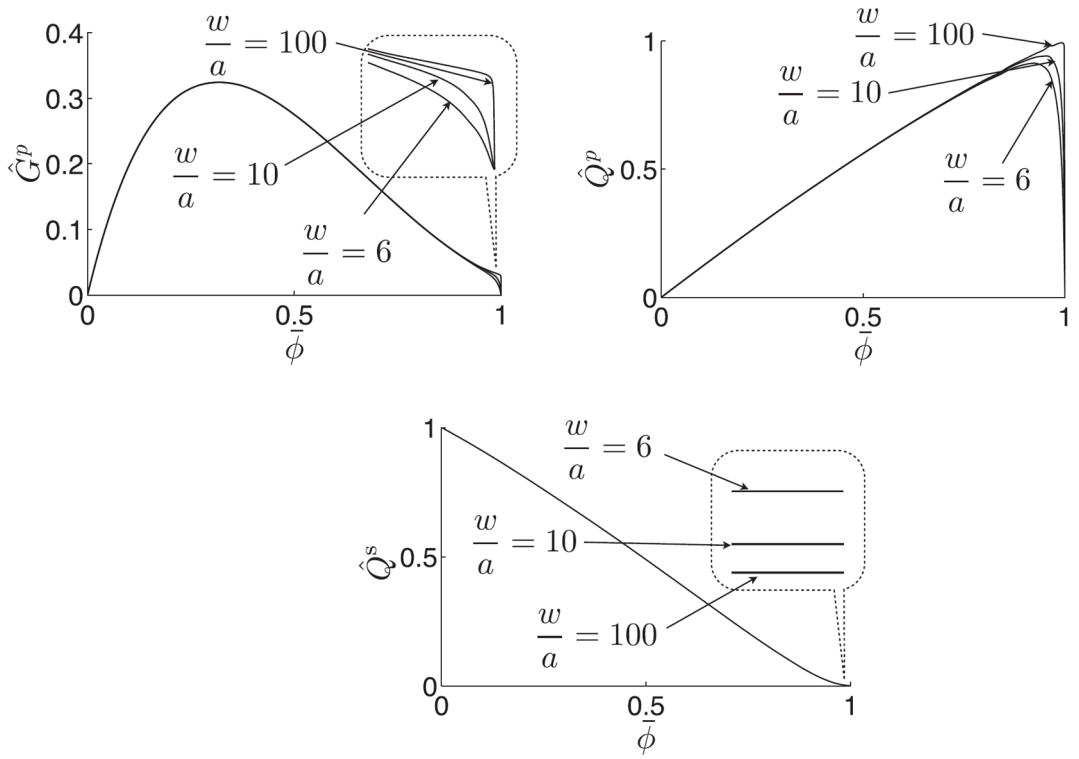

Figure 2-13. Graphical representation of functions $\widehat{Q}^s$, $\widehat{Q}^p$ and $\widehat{G}^p$ calculated from the slurry flow solution (Dontsov & Peirce, 2014a).

Chapter 3. Model Development

Hydraulic fractures are created by pumping fluid at high pressure into target reservoirs, as the fluid is being injected in the formation the rock deforms to the point that is fractured. These fractures are thin gaps (in the order of millimeters) that could extend meters until mechanical barriers, i.e. stronger rocks, are found. After some volume of fluid has been injected, a particulate material known as proppant is injected with the fracturing fluid, this material will ensure that the fracture remains open even after the injection of the fluid is stopped.

The rock mass is subjected to a stress field as shown in Fig. 3-1 the vertical stress is denoted with σ_v and the horizontal minimum and maximum stresses are denoted with σ_h and σ_H, respectively.This stress field is caused by the weight of the rock layers above the interest zone, tectonic regime, pressure of the fluids in the reservoir, properties of the rock and other phenomena (Goodman, 1989). The orientation of the stress field greatly dictates the geometry and direction of the fracture, as they open in the direction of the minimum stress σ_h and propagate in the other 2 directions as shown if Fig. 3-2.

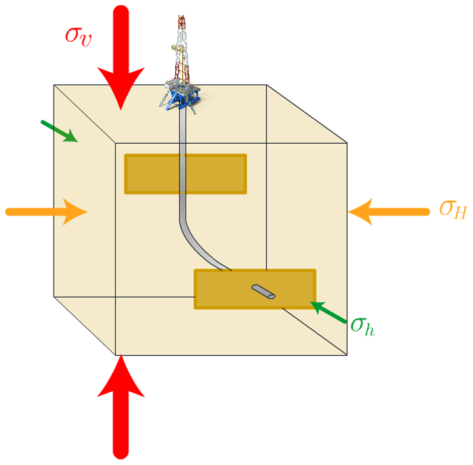

Figure 3-1. Schematic of hydraulic fractures with stress field.

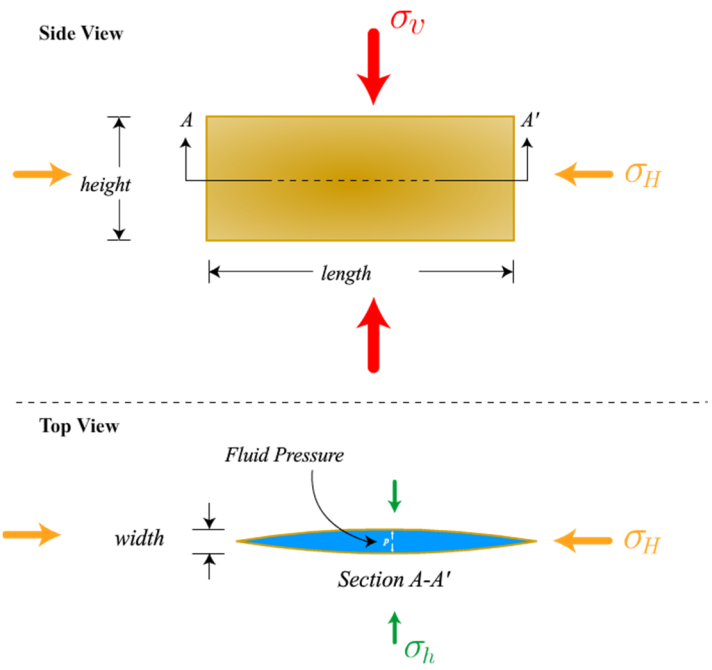

Figure 3-2. Hydraulic fracture showing the main geometrical dimensions with respect to the stress field, the fracture opens in the direction of the minimum stress σ_h and propagates in the other two directions σ_v and σ_H.

The proppant transport in a hydraulic fracture is not an isolated phenomenon, instead a coupled relationship between the rock deformation and the fracturing fluid pressure and proppant transport needs to be considered, since, the proppant concentration change alters the fluid rheology (i.e., its viscosity and density). A mixture of solid mechanics to estimate the fracture deformation and fluid mechanics to describe the fluid flow and proppant flow, is needed to perform a proper analysis. As the main focus of this work is to model the proppant flow and transport, a non-propagating fracture will be first analyzed which means that the fracture geometry, i.e., its length and height will remain constant thought the proppant flow simulation. Later, the module is implemented in a Boundary Elements Method (BEM) model so that the fracture aperture changes due to the impact of the fluid injection and the proppant concentration can be considered.

The fracture deformation and the fluid flow, are strongly coupled as the fracture deformation influences in the pressure distribution and the pressure distribution heavily influences in the

fracture deformation, so a system of equations combining the coefficient matrices of BEM and FEM is formed to simultaneously calculate the fracture width w, and the pressure p. After these two parameters are calculated the velocity field in the fracture can be estimated for use in determining proppant concentration distribution. The slurry is a mixture of fracturing fluid and proppant particles, the flow of slurry is estimated as a mixture (instead of treating each individual component) and later the proppant distribution is calculated using the concept of concentration, which is a factor that relates the volume of proppant and the total volume $c = \frac{V_p}{V}$. To continue with the next time step, the fluid properties (i.e. viscosity and density) are updated and used as input. The assumptions considered in the models to estimate fracture aperture, pressure distribution and proppant distribution are:

- Static fracture networks with no propagation
- All the fractures are completely open before the proppant is injected.
- Homogeneous and isotropic rock mass, Newtonian, incompressible fracture fluid
- Fluid velocity in laminar regime (lubrication theory holds).
- Proppant particles are spherical with equal sizes and are incompressible, and the diameter of proppant particles is much smaller than the width of the fracture.

. Fig. 3-3 shows the general framework of the coupled system. Details of each component of the methodology are discussed in the following sections.

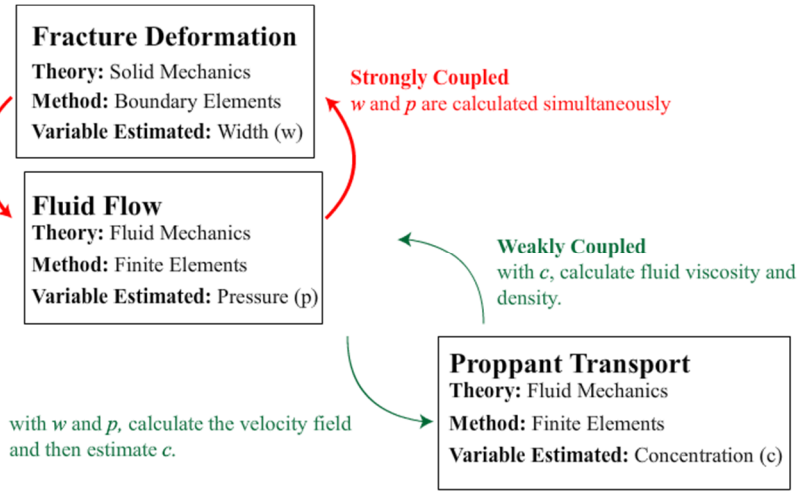

Figure 3-3. General framework to estimate the proppant concentration distribution in a hydraulic fracture.

3.1. Theory and Governing Equations for Proppant Transport and Deposition in a Hydraulic Fracture

3.1.1. Elastic Deformation of the Rock Matrix

The stress state at a point of an elastic deformable material can be described with a stress tensor defined as (Timoshenko & Goodier, 1970):

$$\begin{bmatrix} \sigma_{xx} & \sigma_{xy} & \sigma_{xz} \\ \sigma_{yx} & \sigma_{yy} & \sigma_{yz} \\ \sigma_{zx} & \sigma_{zy} & \sigma_{zz} \end{bmatrix} \tag{3.1}$$

where $\sigma_{ij}; (i,j) = (x,y,z)$ are the stress components acting on the faces of an infinitesimal elements as shown in Fig. 3-4.

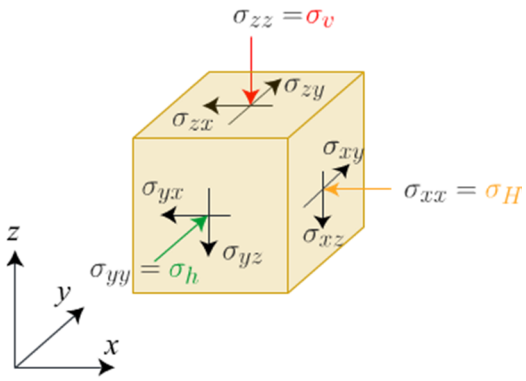

Figure 3-4. Infinitesimal volume subjected to stress state.

The equilibrium equation derived from the fundamental concept of equilibrium of forces in the x, y and z directions is expressed as:

$$\frac{\partial \sigma_{xx}}{\partial x} + \frac{\partial \sigma_{xy}}{\partial y} + \frac{\partial \sigma_{xy}}{\partial y} + f_x = 0 \tag{3.2}$$

$$\frac{\partial \sigma_{yx}}{\partial x} + \frac{\partial \sigma_{yy}}{\partial y} + \frac{\partial \sigma_{yz}}{\partial z} + f_y = 0 \tag{3.3}$$

$$\frac{\partial \sigma_{zx}}{\partial x} + \frac{\partial \sigma_{zy}}{\partial y} + \frac{\partial \sigma_{zz}}{\partial z} + f_z = 0 \tag{3.4}$$

where f_x, f_y, f_z are the body forces applied to the system in the x, y and z directions, respectively. In indicial notation the equilibrium equations are expressed as (Timoshenko & Goodier, 1970):

$$\sigma_{ij,j} + f_i = 0 \tag{3.5}$$

where the comma after the first index denotes partial derivate. In solid mechanics there are fundamental concept to describe the deformation of a body. The first one is displacement denoted by u and is defined as the change in position of one reference point. The second one is strain denoted by ε and is defined as the change of displacement with respect to a reference coordinates system. Normal strains are mathematically expressed as:

$$\varepsilon_{xx} = \frac{\partial u_x}{\partial x};\ \varepsilon_{yy} = \frac{\partial u_y}{\partial y};\ \varepsilon_{zz} = \frac{\partial u_z}{\partial z}; \tag{3.6}$$

And shear strains are defined as:

$$\begin{aligned} \varepsilon_{xy} &= \varepsilon_{yx} = \frac{1}{2}\left(\frac{\partial u_x}{\partial y} + \frac{\partial u_y}{\partial x}\right); \\ \varepsilon_{xz} &= \varepsilon_{zx} = \frac{1}{2}\left(\frac{\partial u_x}{\partial z} + \frac{\partial u_z}{\partial x}\right); \\ \varepsilon_{yz} &= \varepsilon_{zy} = \frac{1}{2}\left(\frac{\partial u_y}{\partial z} + \frac{\partial u_z}{\partial y}\right); \end{aligned} \tag{3.7}$$

Normal and shear strains can be expressed in a single term using indicial notation as:

$$\varepsilon_{ij} = \frac{1}{2}(u_{i,j} + u_{j,i}); \tag{3.8}$$

The constitutive relationship between stress and strain is given by:

$$\begin{Bmatrix} \sigma_{xx} \\ \sigma_{yy} \\ \sigma_{zz} \\ \sigma_{yz} \\ \sigma_{xz} \\ \sigma_{xy} \end{Bmatrix} = \frac{2G}{1-2v} \begin{bmatrix} 1-v & v & v & 0 & 0 & 0 \\ v & 1-v & v & 0 & 0 & 0 \\ v & v & 1-v & 0 & 0 & 0 \\ 0 & 0 & 0 & \frac{1-2v}{2} & 0 & 0 \\ 0 & 0 & 0 & 0 & \frac{1-2v}{2} & 0 \\ 0 & 0 & 0 & 0 & 0 & \frac{1-2v}{2} \end{bmatrix} \begin{Bmatrix} \varepsilon_{xx} \\ \varepsilon_{yy} \\ \varepsilon_{zz} \\ 2\varepsilon_{yz} \\ 2\varepsilon_{xz} \\ 2\varepsilon_{xy} \end{Bmatrix} \tag{3.9}$$

or in indicial notation

$$\sigma_{ij} = \frac{2Gv}{1-2v}\varepsilon_{kk}\delta_{ij} + 2G\varepsilon_{ij} \tag{3.10}$$

where v is the Poisson's ratio, E is the Young's modulus, δ_{ij} is the Kronecker delta operator and G is the shear modulus defined as:

$$G = \frac{E}{2(1+v)} \tag{3.11}$$

The equilibrium equation (3.5) can be rewritten in terms of displacements components using the relationship between stress equation (3.10) and the relationship between strain and displacement equation (3.8). This form is known as the Navier's equations and is expressed as:

$$\left(\frac{1}{1-2v}\right)u_{j,ji} + u_{i,jj} = -\frac{f_i}{G} \tag{3.12}$$

3.1.2. Governing Equation of Fluid Flow Inside a Fracture

A fundamental parameter to describe the movement of the fracturing fluid that is injected to create the hydraulic fracture is pressure, p. Taking advantage of the law of conservation of mass and analyzing the fluid flow in an infinitesimal control volume, an expression that governs the fluid flow in a hydraulic fracture can be derived. The mass conservation of proppant for the control volume in Fig. 3-5 is described by:

$$\begin{matrix} Mass\ accumulation \\ within\ a\ system \end{matrix} = \begin{matrix} Mass\ entering \\ the\ system \end{matrix} - \begin{matrix} Mass\ leaving \\ the\ system \end{matrix} \tag{3.13}$$

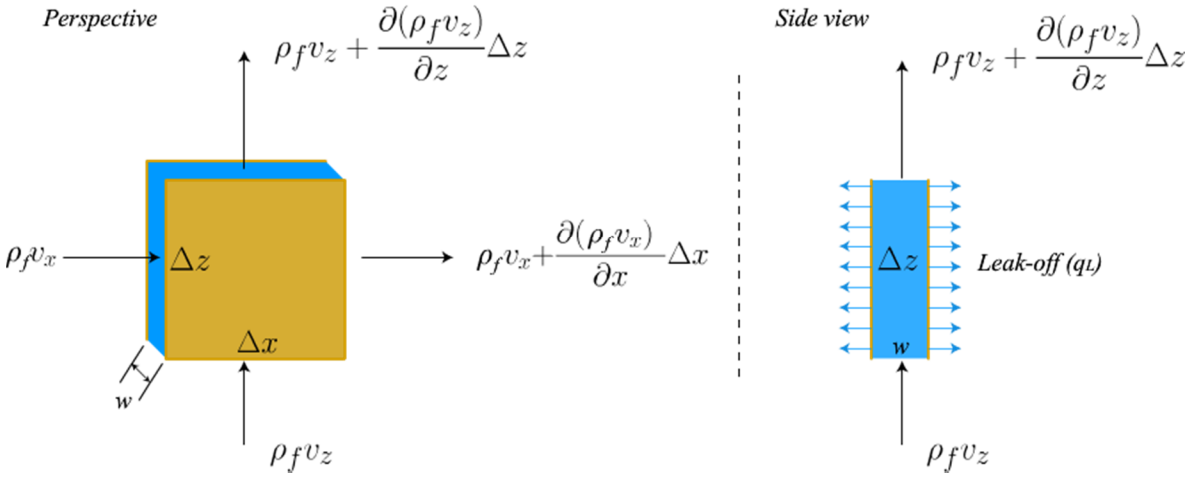

Figure 3-5. Infinitesimal control volume of fluid flowing in a hydraulic fracture.

Considering the relationships

$$mass\ flux = \frac{mass}{(area)(time)} = \frac{mass}{volume} \cdot \frac{lenght}{time} = density \cdot velocity \tag{3.14}$$

The mass flux of fluid entering the element at location x through the face $(w \cdot \Delta z)$ during a time interval Δt is:

$$(\rho v_x)(w\Delta z)\Delta t \tag{3.15}$$

The mass flux of fluid leaving the element, at location $x + \Delta x$ through the face $w \cdot \Delta z$ during a time interval Δt is:

$$\left(\rho v_x + \frac{\partial(\rho v_x)}{\partial x}\Delta x\right)(w\Delta z)\Delta t \tag{3.16}$$

The mass of fluid entering the element at location z, through the face $w \cdot \Delta x$ during a time interval Δt is:

$$(\rho v_z)(w\Delta z)\Delta t \tag{3.17}$$

The mass of fluid leaving the element, at location $z + \Delta z$ through the face $w \cdot \Delta x$ during a time interval Δt is:

$$\left(\rho v_z + \frac{\partial(\rho v_z)}{\partial x}\Delta z\right)(w\Delta x)\Delta t \tag{3.18}$$

The fluid mass accumulation or depletion is represented with the change in mass of fluid per unit volume ΔV during the period of time Δt expressed as:

$$\left[\rho\Delta V + \frac{\partial(\rho\Delta V)}{\partial t}\Delta t\right] - (\rho)\Delta V \tag{3.19}$$

Substituting equations (3.15) through (3.19) into equation (3.14) as:

$$\frac{\partial(\rho w\Delta x\Delta z)}{\partial t}\Delta t = (\rho v_x)(w\Delta z)\Delta t - \left(\rho v_x + \frac{\partial(\rho v_x)}{\partial x}\Delta x\right)(w\Delta z)\Delta t \tag{3.20}$$

$$+(\rho v_z)(w\Delta z)\Delta t - \left(\rho v_z + \frac{\partial(\rho v_z)}{\partial x}\Delta z\right)(w\Delta x)\Delta t$$

Dividing the equation by $(\Delta x \Delta z \Delta t)$ we obtain:

$$\frac{\partial}{\partial t}(\rho w) + \frac{\partial(\rho v_x w)}{\partial x} + \frac{\partial(\rho v_z w)}{\partial z} = 0 \tag{3.21}$$

If the rock mass is permeable, it is expected that some fluid mass without proppant is injected into the formation as shown in Fig. 3-5 in the perspective view, this phenomena is called leak-off and commonly denoted with q_l. Considering, this leak-off coefficient the governing equation of the fluid flow in a hydraulic fracture is:

$$\frac{\partial}{\partial t}(\rho w) + \frac{\partial(\rho v_x w)}{\partial x} + \frac{\partial(\rho v_z w)}{\partial z} + q_l \rho_f = 0 \tag{3.22}$$

The leak-off coefficient can be modeled with the Carter's model of leak-off (Howard & Fast, 1970) expressed as:

$$q_l = \frac{2C_l}{\sqrt{t-\tau}} \tag{3.23}$$

where C_l is the leak off coefficient which is found from experimental results and t is the current time and τ is the time when the element gets in contact with the fracturing fluid.

Additionally, if there is a well adding or subtracting mass from the system, it can be represented with an extra parameter as follows:

$$\frac{\partial}{\partial t}(\rho w) + \frac{\partial(\rho v_x w)}{\partial x} + \frac{\partial(\rho v_z w)}{\partial z} + q_l \rho_f + \rho Q = 0 \tag{3.24}$$

where Q is the source term. The pressure distribution in the hydraulic fracture can be calculated combining the governing equation (3.22), and the relationship between fluidities and pressure found with the parallel plates flow model, equations (A.27) and (A.28) are rewritten here for convenience as:

$$\overline{v_x} = -\frac{w^2}{12\mu}\frac{\partial p}{\partial x} \tag{3.25}$$

$$\overline{v_z} = -\frac{w^2}{12\mu}\frac{\partial p}{\partial z} \tag{3.26}$$

Substituting equations (3.25) and (3.26) into equation (3.22) yields to (Gu, 1987):

$$\frac{\partial}{\partial t}(\rho w) - \frac{\partial}{\partial x}\left(\rho\frac{w^3}{12\mu}\frac{\partial p}{\partial x}\right) + \frac{\partial}{\partial z}\left(\rho\frac{w^3}{12\mu}\frac{\partial p}{\partial z}\right) + q_l\rho_f + \rho Q = 0 \tag{3.27}$$

To classify the derived expression, the most general form of a second order partial differential equation for a stationary process is considered:

$$A\frac{\partial^2 u}{\partial x^2} + B\frac{\partial^2 u}{\partial x \partial y} + C\frac{\partial^2 u}{\partial y^2} + D\frac{\partial u}{\partial x} + E\frac{\partial u}{\partial y} + Fu + G = 0 \tag{3.28}$$

where $A, B, \dots, G$ are constants and u is the dependent variable. In the resultant governing equation (3.27) the dependent variable contains only spatial partial derivatives of order two, making the coefficients of equation A = C = G = 1 and B = D = E = F = 0. As the determinant $B^2 - 4AC < 0$ then this governing equation is a elliptic type differential equation (Fritz, 1982). The two boundary conditions are the fluid flux (injection rate) Q. An additional boundary condition required relates to the fracture front which is usually assumed as a no-flow boundary condition or zero fluid flux condition. The zero fluid flux condition at the fracture front is valid only for the cases where there is no lag between the fracture and fluid fronts, which is a prevalent condition in most of the hydraulic fracturing problems (Dontsov & Peirce, 2014a). If we consider a domain describing a hydraulic fracture surface (Ω) as shown in Fig. 3-6 and recognize that at the tip of the fracture is

close, a no flow boundary condition at the tip is appropriate to describe the phenomenon, which is mathematically expressed as (Gu, 1987):

$$\rho \frac{w^3}{12\mu} \frac{\partial p}{\partial n} = 0 \; on \; \Gamma \tag{3.29}$$

where Γ represents the boundary enclosing the domain Ω and n represents the normal vector to the fracture boundary as shown in Fig. 3-6.

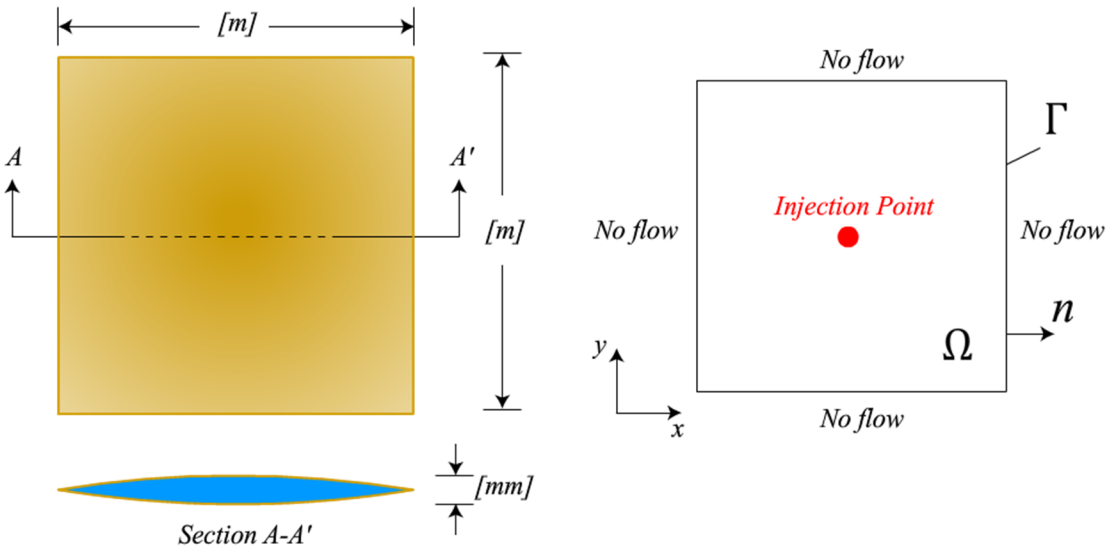

Figure 3-6. Idealized square shaped fracture. Length and height are in meters while the fracture aperture represented by section A-A' is in millimeters. Ω represents the domain of the fracture, Γ represent the boundary of the fracture which are set to no flow boundaries and n represents the outward normal vector to the fracture.

3.1.3. Proppant Transport Governing Equation

To derive a governing equation for the proppant flow and transport inside a hydraulic fracture, the flow of slurry (i.e., mixture of fracturing fluid and proppant particles) through an infinitesimal volume as shown in Fig. 3-7 is analyzed following an approach similar to (Ouyang et al., 1997). Applying the law of conservation of mass, a differential equation is obtained. Instead of solving

the problem for each component of the mixture, only one expression is used to solve the proppant distribution which relates the volume of the mixture and the volumetric concentration of proppant (Adachi et al., 2007; Gadde & Sharma, 2005; Ouyang et al., 1997; Pearson, 1994).

The following assumption are made: (a) The proppant particles are spherical with equal sizes (b) The diameter of proppant particles is much smaller than the fracture width (c) proppant particles and fracturing fluid are incompressible.

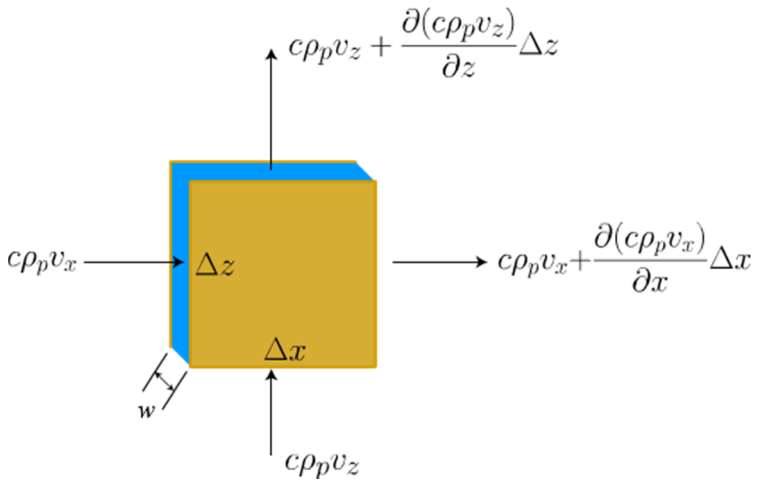

Figure 3-7. Infinitesimal control volume for conservation of mass to studry the proppant transport in a hydraulic fracture.

The volume concentration of proppant can be defined as the volume of proppant per unit volume of slurry as (Ouyang et al., 1997):

$$c = \frac{V_p}{V} \tag{3.30}$$

where V_p is the volume of proppant and V is the volume of slurry. The mass density of proppant consisting of particles of uniform size can be defined as:

$$\rho_p = \frac{M_p}{V_p} \tag{3.31}$$

where M_p is the proppant mass. The density of proppant in fracturing fluid, defined as the mass of proppant per unit volume of slurry (V) is:

$$\rho_{ps} = \frac{M_p}{V} \tag{3.32}$$

a correlation among c, ρ_{ps} and ρ_p is then

$$\rho_{ps} = \frac{M_p}{V} = \frac{V_p}{V}\frac{M_p}{V_p} = c\rho_p \tag{3.33}$$

Recalling that $mass\ flux = density \cdot velocity$ as shown in equation (3.14), the mass flux of proppant then relates density of the proppant in as follows:

$$mass\ flux\ of\ proppant = c\rho_p v \tag{3.34}$$

The mass flux of proppant entering the element at location x through the face $(w \cdot \Delta z)$ during a time interval Δt is:

$$(c\rho_p v_x)(w\Delta z)\Delta t \tag{3.35}$$

The mass flux of proppant leaving the element, at location $x + \Delta x$ through the face $w \cdot \Delta z$ during a time interval Δt is given as:

$$\left(c\rho_p v_x + \frac{\partial(c\rho_p v_x)}{\partial x}\Delta x\right)(w\Delta z)\Delta t \tag{3.36}$$

The mass of proppant entering the element at location z, through the face $w \cdot \Delta x$ during a time interval Δt is given as:

$$(c\rho_p v_z)(w\Delta x)\Delta t \tag{3.37}$$

The mass of proppant leaving the element, at location $z + \Delta z$ through the face $w \cdot \Delta x$ during a time interval Δt is given as:

$$\left(c\rho_p v_z + \frac{\partial\left(c\rho_p v_z\right)}{\partial z}\Delta z\right)(w\Delta x)\Delta t \tag{3.38}$$

The proppant mass accumulation is represented with the change in mass of proppant per unit volume ΔV during the period of time Δt expressed as

$$\left[c\rho_p \Delta V + \frac{\partial\left(c\rho_p \Delta V\right)}{\partial t}\Delta t\right] - \left(c\rho_p\right)\Delta V \tag{3.39}$$

Substituting equation (3.35) through (3.39) into equation (3.13) results as:

$$\begin{aligned}\frac{\partial\left(c\rho_p w\Delta x\Delta z\right)}{\partial t}\Delta t = {} & \left(c\rho_p v_x\right)(w\Delta z)\Delta t - \left(c\rho_p v_x + \frac{\partial\left(c\rho_p v_x\right)}{\partial x}\Delta x\right)(w\Delta z)\Delta t \\ & + \left(c\rho_p v_z\right)(w\Delta z)\Delta t - \left(c\rho_p v_z + \frac{\partial\left(c\rho_p v_z\right)}{\partial x}\Delta z\right)(w\Delta x)\Delta t\end{aligned} \tag{3.40}$$

Dividing the equation by $(\Delta x\Delta z\Delta t)$ we obtain,

$$\frac{\partial}{\partial t}\left(c\rho_p w\right) + \frac{\partial\left(c\rho_p v_x w\right)}{\partial x} + \frac{\partial\left(c\rho_p v_z w\right)}{\partial z} = 0 \tag{3.41}$$

If we assume that the proppant density is constant, the above equation can be further simplified. The final form on the governing equation is given as (Adachi et al., 2007; Gadde & Sharma, 2005; Pearson, 1994):

$$\frac{\partial(cw)}{\partial t} + \frac{\partial(cv_x w)}{\partial x} + \frac{\partial(cv_z w)}{\partial z} = 0 \tag{3.42}$$

The dependent variable in the resulting governing equation (3.42) contains only partial derivatives of order one, if we consider the general form of a second order partial differential equation, the coefficients of the equation (3.28), are D = E = 1 and A = B = C = F = G = 0. As the determinant $B^2 - 4AC = 0$, then this governing equation is a parabolic type differential equation (Fritz, 1982), also known as the pure advection equation, The first term in Eq. (3.42) is referred to as the accumulation term and the second and third terms are referred to as the advective terms (Donea & Huerta, 2004).

The boundary conditions can be described by considering that there is no flow of proppant (and fluid) beyond the boundary (i.e., the fracture surface and edge or tips) so that a Newman type boundary condition is set:

$$\frac{\partial c}{\partial n} = 0 \; on \; \Gamma \tag{3.43}$$

where n represents the normal direction to the boundary and Γ represents the boundary of the domain Ω as shown in Fig. 3-8. Considering zero proppant concentration as initial condition which is mathematically represented as:

$$c(x, y, 0) = 0 \; on \; \Omega \tag{3.44}$$

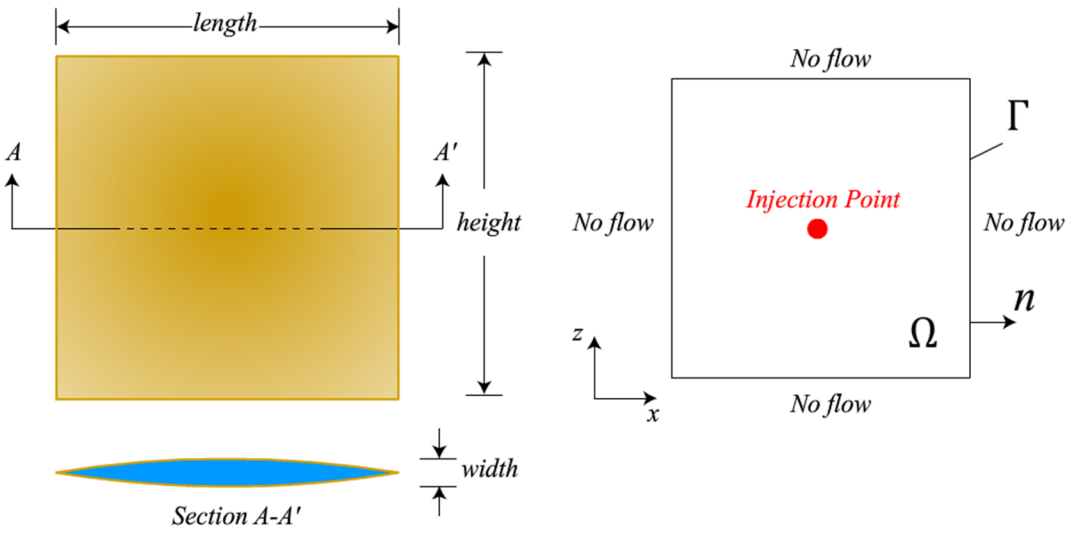

Figure 3-8. Idealized square shaped fracture. Length and height are in meters while the fracture aperture represented by section A-A' is in millimeters. Ω represents the domain of the fracture, Γ represent the boundary of the fracture which are set to no flow boundaries and n represents the outward normal vector to the fracture.

3.1.4. Proppant Settling in a Hydraulic Fracture

In equation (3.42), the proppant concentration would vary with fluid velocity and fracture aperture; hence, to be able to solve for the proppant concentration, the pressure and fracture aperture distributions need to be determined. This is usually done by solving a fracture deformation and fluid flow model where the pressure and fracture aperture are calculated using a coupled scheme. Then, assuming that the change in aperture and in pressure is not affected within each time step, i.e. a quasi-steady state, implies that the concentration of the proppant does not affect the velocity field in a small time increment (compared with the total injection time) the proppant concentration is determined. The proppant concentration is considered to only affect the fluid properties and not the pressure and width directly. As a result, these relationships are considered as weakly coupled whereby the proppant concentration is calculated at the end of each time step. A similar approach

is adopted by other investigators (Adachi et al., 2007; Dontsov & Peirce, 2015; Lavrov, 2011; Ouyang et al., 1997; Tang et al., 2016).

Considering, the parallel plates flow model, the average velocities in a fracture with respect to the aperture w and pressure p are expressed by equations (A.27) and (A.28) shown in Appendix A, these equations are rewritten here for convenience:

$$v_x = -\frac{w^2}{12\mu}\frac{\partial p}{\partial x} \tag{3.45}$$

$$v_z = -\frac{w^2}{12\mu}\frac{\partial p}{\partial z} \tag{3.46}$$

Substituting the fluid velocities in the governing equation (3.42) results as:

$$\frac{\partial (cw)}{\partial t} - \frac{\partial}{\partial x}\left(c\frac{w^3}{12\mu}\frac{\partial p}{\partial x}\right) - \frac{\partial}{\partial z}\left(c\frac{w^3}{12\mu}\frac{\partial p}{\partial z}\right) = 0 \tag{3.47}$$

To account for the proppant settling phenomenon in the model, the velocity field is modified by adding the settling velocity to the vertical (i.e., z-component) of the fluid velocity (Novotny, 1977):

$$v_z = v_z + v_{settle} \tag{3.48}$$

The settling velocity v_{settle} is determined based on the calculations of the terminal velocity and additional empirical correction factors that account for the effect of the fracture width, and proppant concentration (Adachi et al., 2007; Gadde et al., 2004; Novotny, 1977). When the gravitational force (F_g), the drag force (F_D) and the buoyancy force (F_B) acting in a particle moving in a fluid as shown in Fig. 3-9 are in equilibrium, an expression to calculate the terminal velocity can be estimated. The gravitational force is defines as (Batchelor, 1967; Stokes, 1905):

$$F_D = \frac{1}{2}\rho v^2 C_D A \tag{3.49}$$

where ρ is the density of the fluid, v is the flow velocity relative to the object, A is the cross sectional area of the object and C_D is the drag coefficient. The reference area of a sphere is:

$$A = \frac{\pi d^2}{4} \tag{3.50}$$

Replacing equation (3.50) into equation (3.49), the result is:

$$F_D = \frac{\pi \rho v^2 C_D d^2}{8} \tag{3.51}$$

The gravitational force is defined as:

$$F_g = mg = \rho_p V_p g = \rho_p \left(\frac{1}{6}\pi d^3\right) g \tag{3.52}$$

where m is the mass of the particle, g is the gravity, ρ_p is the density of the particle and V_p is the volume of the particle. The buoyancy force is the weight of the displaced fluid expressed as:

$$F_B = \rho_f V_f g = \rho_f \left(\frac{1}{6}\pi d^3\right) g \tag{3.53}$$

where ρ_f is the density of the fluid and V_f is the volume of the displaced fluid. The force equilibrium is expressed as:

$$F_B + F_D = F_g \tag{3.54}$$

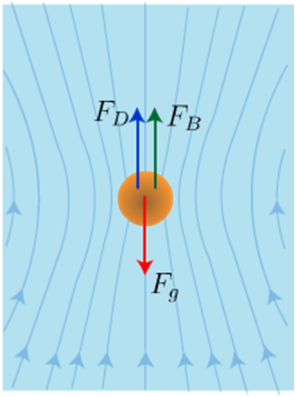

Figure 3-9. Forces and Streamlines for flow due to a moving spherical particle (Batchelor, 1967).

Substituting equations (3.51), (3.52) and (3.53) into equation (3.54), the result is:

$$\frac{\pi\rho v^2 C_D d^2}{8} = \frac{1}{6}\pi d^3(\rho_p - \rho_f)g \tag{3.55}$$

The Reynolds number is define as (Stokes, 1905):

$$Re = \frac{\rho_f * v_y * d_p}{\mu} \tag{3.56}$$

For $Re < 2$ (Stokes' law region) the inertial effects can be neglected and $C_D = 24/Re$, resulting in the terminal velocity (Stokes, 1905):

$$v_\infty = \frac{g(\rho_p - \rho_f)d_p^2}{18\mu} \tag{3.57}$$

If $2 < Re < 500$ (intermediate region) then $C_D = 18.5/Re^{0.6}$, this drag coefficient was obtained experimentally, resulting in the terminal velocity (Novotny, 1977):

$$v_\infty = \frac{20.34(\rho_p - \rho_f)^{0.71} d_p^{1.14}}{\rho_f^{0.29}\mu^{0.43}} \tag{3.58}$$

If $Re > 500$ (turbulent flow) then $C_D = 0.44$, this drag coefficient was also obtained experimentally, resulting in the terminal velocity (Novotny, 1977):

$$v_\infty = 1.74\sqrt{\frac{g(\rho_p - \rho_f)d_p}{\rho_f}} \tag{3.59}$$

The behavior of a particle transported in an infinite fluid and a particle transported between rough parallel walls is different, hence an empirical correction factor that account for this phenomenon needs to be considered. As shown in Fig. 3-10, if the particle is relatively large with respect to the fracture width, the correction factor tends to smaller values, restricting the settling velocity. This correction factor is expressed as (Gadde et al., 2004):

$$f_w = \left[0.563\left(\frac{d_p}{w}\right)^2 - 1.563\left(\frac{d_p}{w}\right) + 1\right] \tag{3.60}$$

The particle concentration also affects the behavior of the movement of the particles and an additional correction factor is needed, it was found that the higher concentrations lead to a decrease in the settling velocity, as shown in Fig. 3-11. The correction factor is expressed as (Gadde et al., 2004):

$$f_c = (2.37c^2 - 3.08c + 1) \tag{3.61}$$

Finally, combining all of the above effects, the corrected settling velocity is given as:

$$v_{settle} = v_\infty * f_w * f_c \tag{3.62}$$

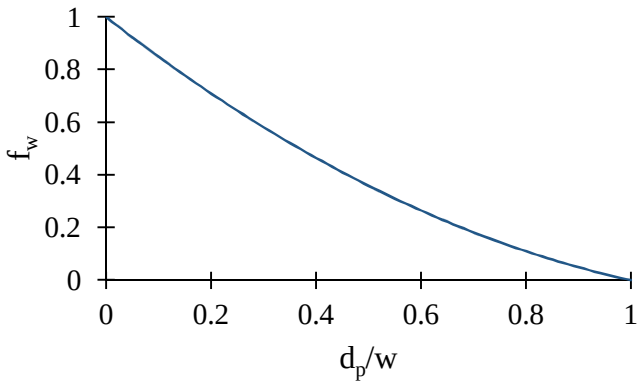

Figure 3-10. Wall effect correction factor behavior as expressed with equation (3.60) (Gadde et al., 2004).

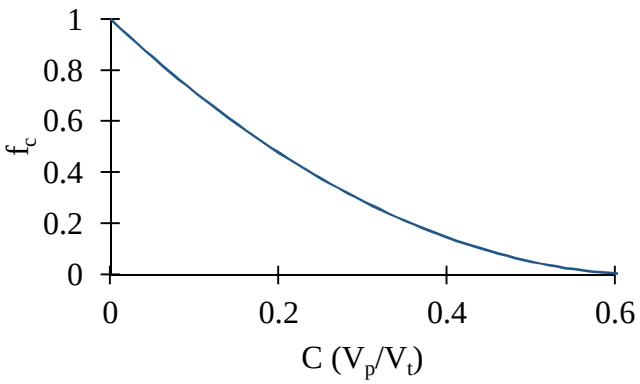

Figure 3-11. Concentration effect correction factor behavior as expressed with equation (3.61) (Gadde et al., 2004).

Figure 3-12 shows an example of an idealized hydraulic fracture where the injection point is located at the center (wellbore). The fluid velocity field is calculated in two cases, in the first case the settling velocity is neglected and in a second case the settling velocity is added to the y-component to study the effect in the velocity field. It can be noticed that in the first case the vectors follow a radial path while in the second case after some distance of the injection point the trajectory of the vectors is downwards.

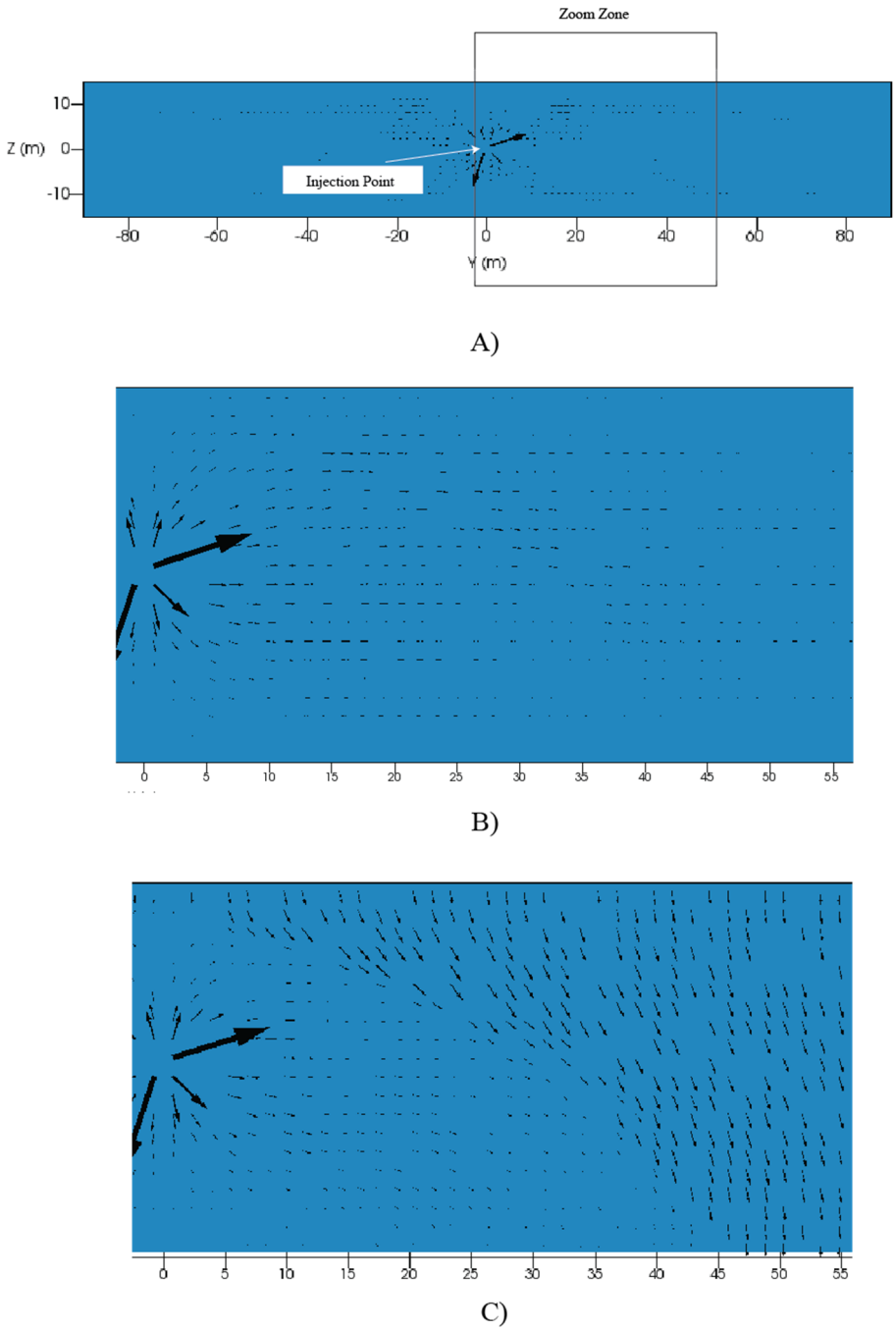

Figure 3-12. Example of velocity field calculations in an idealized rectangular hydraulic fracture. A) Injection into a hydraulic fracture showing the injection point and zoom area, B) Zoom in showing the resultant velocity field disregarding the settling velocity. B) Zoom in showing the resultant velocity field considering the settling velocity with equation (3.62).

3.1. Numerical Procedures

In this section, detailed descriptions of the numerical implementation procedures for the model are presented. A coupled scheme is applied to simultaneously solve the solid rock and fracture deformation described by equation (3.12).The fluid flow equation inside the hydraulic fracture is described by equation (3.27) so the coupling of fracture width (w) and fluid pressure (p) is strong. The fracture deformation is solve for by using the Displacement Discontinuity Method, and the fluid flow equation is discretized using the Finite Element Method (FEM), the resultant matrices from the discretization are solved simultaneously using a coupled scheme (Kumar & Ghassemi, 2016). With the solutions of fracture width and fluid pressure as input, the proppant flow and transport equation, equation (3.42) is discretized using the Finite Element Method with Streamline Upwinding Petrov Galerkin (SUPG) (Brooks & Hughes, 1982).

The finite difference method (FDM) and the finite volume method (FVM) are the other commonly used techniques for the numerical solution of the proppant flow and transport in a hydraulic fracture equation, equation (3.42) (Anderson, 1995). In the Finite Difference Method (FDM) each derivative in the differential equation is approximated with difference formulas derived based on the Taylor series expansions (Anderson, 1995). The FDM has flexibility to choose the flow direction, and allows explicit discretization in time. Usually domain is discretized using either square or rectangular elements, a downside when it comes to model problems with complex geometries. Although an iso-parametric formulation could be implemented, the formulation becomes complicated and in many cases impractical (Anderson, 1995). For the complex fracture geometries, the finite element and finite volume offers more flexibility; since, a wide variety of elements (i.e., triangular or quadrilateral elements) can be used to fit a given complex fracture

geometry. The Finite Element Method (FEM) being the most generalized method, brings a systematic framework to discretize and solve any type of differential equation. The FEM is based on variational method where the differential equation is written in an integral form called weak form. The solution is approximated by the addition of piecewise functions and minimizing the residual error. The objective is to reduce the demands of continuity of the functions, called shape functions, which are used to approximate the solution.

The fluid flow and proppant transport governing equation are first solved for simple and fixed geometries that could be discretized with squares. However, the proppant transport solution is then used in a more robust simulator (Kumar and Ghassemi,2016) to treat more complex problems. With these objectives in mind, the FEM seems to be the most reasonable choice to develop the complementary module to solve the proppant flow and transport equation.

3.1.1. Weak Form of the Fluid Flow Inside a Fracture Equation

In the Finite Element Method (FEM), the governing equation in differential form, in this case equation (3.27), is commonly referred as the strong form of the problem. The first step of the FEM is to derive an integral equation equivalent to the strong form, known as weak form. To obtain the weak form, the strong form of the governing equation is multiplied by an arbitrary weight function $\varepsilon(x, y)$, and integrated over the domain in which they hold, the result is expressed as (Gu, 1987):

$$\int_{\Omega} \varepsilon \left[\frac{\partial}{\partial t}(\rho w) - \frac{\partial}{\partial x}\left(\rho \frac{w^3}{12\mu} \frac{\partial p}{\partial x} \right) + \frac{\partial}{\partial z}\left(\rho \frac{w^3}{12\mu} \frac{\partial p}{\partial z} \right) + q_l \rho_f + \rho Q \right] dx dz = 0 \tag{3.63}$$

To apply Neumann or flux boundary conditions, further manipulation is required, second derivatives of the primary unknown, in this case pressure (p), are integrated by parts using Green's lemma (Donea & Huerta, 2004).

$$\int_{\Omega} \varepsilon \frac{\partial}{\partial x}\left(\rho \frac{w^3}{12\mu}\frac{\partial p}{\partial x}\right) dxdz = -\int_{\Omega} \frac{\partial \varepsilon}{\partial x}\rho \frac{w^3}{12\mu}\frac{\partial p}{\partial x} dxdz + \int_{\Gamma} \varepsilon\rho \frac{w^3}{12\mu}\frac{\partial p}{\partial x} n_x \, d\Gamma \tag{3.64}$$

$$\begin{aligned}\int_{\Omega} \varepsilon \frac{\partial}{\partial z}\left(\rho \frac{w^3}{12\mu}\frac{\partial p}{\partial z}\right) dxdz \\ = -\int_{\Omega} \frac{\partial \varepsilon}{\partial z}\rho \frac{w^3}{12\mu}\frac{\partial p}{\partial z} dxdz + \int_{\Gamma} \varepsilon\rho \frac{w^3}{12\mu}\frac{\partial p}{\partial z} n_z \, d\Gamma\end{aligned} \tag{3.65}$$

where n_x and n_z are the components of the normal vectors in x and z direction respectively and Γ represents the boundary of the fracture. Substituting equations (3.64) and (3.65) in the equation (3.63) results as:

$$\begin{aligned}\int_{\Omega} \rho \left[\varepsilon \frac{\partial (w)}{\partial t} - \frac{w^3}{12\mu}\left(\frac{\partial \varepsilon}{\partial x}\frac{\partial p}{\partial x} + \frac{\partial \varepsilon}{\partial z}\frac{\partial p}{\partial z}\right) + \varepsilon q_l \rho_f + \varepsilon\rho Q\right] dxdz + \int_{\Gamma} \varepsilon\rho \frac{w^3}{12\mu}\frac{\partial p}{\partial x} n_x \, d\Gamma \\ + \int_{\Gamma} \varepsilon\rho \frac{w^3}{12\mu}\frac{\partial p}{\partial z} n_z \, d\Gamma = 0\end{aligned} \tag{3.66}$$

As mentioned earlier, a no flow boundary condition at the fracture front (Γ) needs to be imposed to appropriately simulate the behavior of a hydraulic fracture, which can be mathematically rewritten as:

$$\rho \frac{w^3}{12\mu}\frac{\partial p}{\partial x} = 0 \tag{3.67}$$

$$\rho \frac{w^3}{12\mu} \frac{\partial p}{\partial z} = 0 \tag{3.68}$$

Using above no-flow boundary conditions, equation (3.66) reduces to

$$\int_{\Omega} \rho \left[\varepsilon \frac{\partial (w)}{\partial t} - \frac{w^3}{12\mu} \left(\frac{\partial \varepsilon}{\partial x} \frac{\partial p}{\partial x} + \frac{\partial \varepsilon}{\partial z} \frac{\partial p}{\partial z} \right) + \varepsilon q_l \rho_f + \varepsilon \rho Q \right] dx dz = 0 \tag{3.69}$$

As the continuity of the equations needed to approximate the solution are split between the weight function and the unknown, in this case pressure, this final equation is known as the weak form

3.1.2. Spatial Discretization of the Fluid Flow Inside a Fracture Equation

The continuous function representing the pressure, p, in the fluid flow governing equation (3.27), is approximated with the summation of the product of piecewise continuous functions and the nodal values of the function as follows (Zienkiewicz & Taylor, 2000):

$$p = \sum_{j=1}^{Nn} \phi_j(x, y) p_j \tag{3.70}$$

where ϕ is the shape function and Nn is the number of nodes per element. If, the weight function is chosen to be the same as the shape function, then the weak form of the fluid flow governing equation (3.69) is semi-discretized with the Galerkin finite element method as follows (Gu, 1987; Ouyang et al., 1997):

$$\int_{\Omega} \rho \left[\phi_i \frac{\partial(w)}{\partial t} - \frac{w^3}{12\mu} \left(\frac{\partial \phi_i}{\partial x} \frac{\partial \phi_j}{\partial x} p_j + \frac{\partial \phi_i}{\partial z} \frac{\partial \phi_j}{\partial z} p_j \right) + \phi_i q_l \rho_f + \phi_i \rho Q \right] dxdz = 0 \tag{3.71}$$

Equation (3.71) can be written in compact form as:

$$[B]\{p\} + \{f_w\} + \{f_l\} + \{f_q\} = 0 \tag{3.72}$$

where the coefficient matrix K_{ij} is known as the stiffness matrix and is defined as:

$$B_{ij} = \int_{\Omega} \rho \left[\frac{w^3}{12\mu} \left(\frac{\partial \phi_i}{\partial x} \frac{\partial \phi_j}{\partial x} + \frac{\partial \phi_i}{\partial z} \frac{\partial \phi_j}{\partial z} \right) p_j \right] dxdz \tag{3.73}$$

And f_i are the forcing vectors defined as:

$$f_w = \int_{\Omega} \rho \phi_i \frac{\partial(w)}{\partial t} dxdz \tag{3.74}$$

$$f_l = \int_{\Omega} \phi_i q_l \rho_f \, dxdz \tag{3.75}$$

$$f_q = \int_{\Omega} \phi_i \rho \delta(x, y) Q \, dxdz \tag{3.76}$$

Furthermore the derivative of fracture aperture (w) with respect to time is approximated with a backward finite difference as (Ouyang et al., 1997)

$$\left. \frac{\partial(w)}{\partial t} \right|_s = \frac{w^s - w^{s-1}}{\Delta t} \tag{3.77}$$

where s denotes the time step in which the derivative is being evaluated, w^s is the fracture aperture in the current time step, w^{s-1} is the fracture aperture in the previous time step, and Δt denotes the time increment.

3.1.3. Weak Form of the Proppant Flow and Transport Equation

Following a similar strategy as in section (3.1.1) the weak form of the proppant flow equation (3.42) is found multiplying by an arbitrary weight function $\varepsilon(x, z)$, and integrated over the domain in which they hold, given as (Ouyang et al., 1997):

$$\int_{\Omega} \varepsilon \left[w \frac{\partial c}{\partial t} + c \frac{\partial w}{\partial t} + \frac{\partial (c w v_x)}{\partial x} + \frac{\partial (c w v_z)}{\partial z} \right] dx dz = 0 \tag{3.78}$$

In this case to apply Neumann or flow boundary conditions, further manipulation is needed in the third and fourth terms also known as the advective terms. They are integrated by parts using Green's lemma as (Donea & Huerta, 2004):

$$\int_{\Omega} \varepsilon \frac{\partial (c w v_x)}{\partial x} dx dz = -\int_{\Omega} \frac{\partial \varepsilon}{\partial x} c w v_x dx dz + \int_{\Gamma} \varepsilon c w v_x n_x \, d\Gamma \tag{3.79}$$

$$\int_{\Omega} \varepsilon \frac{\partial (c w v_z)}{\partial y} dx dz = -\int_{\Omega} \frac{\partial \varepsilon}{\partial z} c w v_z dx dz + \int_{\Gamma} \varepsilon c w v_z n_z \, d\Gamma \tag{3.80}$$

where n_x and n_z are the components of the normal vectors in x and z direction respectively and Γ represents the boundary of the fracture. Substituting equations (3.79) and (3.80) into equation (3.78) results:

$$\int_{\Omega}\left[\varepsilon w\frac{\partial c}{\partial t}+\varepsilon c\frac{\partial w}{\partial t}-\frac{\partial \varepsilon}{\partial x}cwv_x-\frac{\partial \varepsilon}{\partial z}cwv_z\right]dxdz+\int_{\Gamma}\varepsilon cq_x n_x\,d\Gamma+\int_{\Gamma}\varepsilon wv_z n_z\,d\Gamma = 0 \tag{3.81}$$

3.1.4. Spatial Discretization of the Proppant Flow and Transport Equation

Similar to the fracture fluid pressure interpolation in an element, the continuous function representing the proppant concentration, c, is approximated with the summation of the product of piecewise continuous functions and the nodal values of the function as follows (Zienkiewicz & Taylor, 2000):

$$c=\sum_{j=1}^{Nn}\phi_j(x,y)c_j \tag{3.82}$$

where ϕ is the shape function and Nn is the number of nodes per element. If, the weight function is chosen to be the same as the shape function, then the weak form of the governing equation is semi-discretized with the Galerkin finite element method as follows:

$$\int_{\Omega}\left[w\phi_i\phi_j\frac{\partial c}{\partial t}+\frac{\partial w}{\partial t}\phi_i\phi_j c_j-wv_x\frac{\partial \phi_i}{\partial x}\phi_j c_j-wv_z\frac{\partial \phi_i}{\partial z}\phi_j c_j\right]dxdz + \int_{\Gamma}wv_x\phi_i\phi_j c_j n_x\,d\Gamma+\int_{\Gamma}wv_z\phi_i\phi_j c_j n_z\,d\Gamma = 0 \tag{3.83}$$

In the physical model the boundary integrals vanish as the velocities prescribed on the tip elements is zero, imposing naturally the boundary condition of no flow. In the verification case, these integrals need to be calculated since the velocity is being specified at the boundary. Equation (3.83) can be written in compact form as:

$$[A]\frac{\partial\{c\}}{\partial t} + [B]\{c\} = 0 \tag{3.84}$$

where the coefficient matrix A_{ij} is known as the mass matrix and is defined as:

$$A_{ij} = \int_{\Omega} w\phi_i\phi_j dxdz \tag{3.85}$$

and the coefficient matrix B_{ij} is known as the stiffness matrix and is defined as:

$$B_{ij} = \int_{\Omega}\left\{\frac{\partial w}{\partial t}\phi_i\phi_j - wv_x\frac{\partial\phi_i}{\partial x}\phi_j - wv_z\frac{\partial\phi_i}{\partial z}\phi_j\right\}dxdz + \int_{\Gamma} wv_x\phi_i\phi_j n_x\, d\Gamma + \int_{\Gamma} wv_z\phi_i\phi_j n_z\, d\Gamma \tag{3.86}$$

3.1.5. Time Discretization of the Proppant Flow and Transport Equation

The backward difference scheme or implicit scheme, is used to discretize in time the semi discretized equation (3.84). This scheme is unconditionally stable and larger Δt could be used (Ouyang et al., 1997).

$$\frac{\partial\{c\}_s}{\partial t} = \frac{\{c\}_s - \{c\}_{s-1}}{\Delta t} \tag{3.87}$$

where $\{c\}_s$ is the concentration in the current time step, $\{c\}_{s-1}$ is the concentration in the previous time step, and Δt is the increment on time. Replacing in the proppant concentration equation (3.84) results:

$$[A]\,\frac{\{c\}_s - \{c\}_{s-1}}{\Delta t} + [B]_s\{c\}_s = \{f_c\}_s \tag{3.88}$$

Rearranging the equation as:

$$[A]\,\frac{\{c\}_s}{\Delta t} + [B]_s\{c\}_s = \{f_c\}_s + \frac{[A]\,\{c\}_{s-1}}{\Delta t} \tag{3.89}$$

Factorizing and solving for $\{c\}_s$

$$\{c\}_s = ([A] + \Delta t[B]_s)^{-1}(\Delta t\{f_c\}_s + [A]\,\{c\}_{s-1}) \tag{3.90}$$

3.1.6. Coupled Solution of Rock Deformation and Fluid Flow inside a Hydraulic Fracture

While the fluid is injected in the formation to create a hydraulic fracture, the pressure exerted against the walls changes the geometry of the fracture, the change in the fracture aperture is modeled using the Displacement Discontinuity (DD) Method. In the case of a single fracture only the normal DD denoted with $D_{\bar{z}}$ is considered as the tractions affecting the system are those exerted by the fluid pressure p and by the minimum in situ stress σ_h both of these stresses are applied in a normal direction with respect to the faces of the fractures as shown in Fig 3-28. Note that this DD

normal component $D_{\bar{z}}$ is equal to the fracture aperture w. The pressure distribution in the fracture can be solved using the fluid flow in a fracture governing equation, however among the parameters needed to perform this calculation there is w, the same variable that we are aiming to solve with the DD method, such dependency is denoted as strongly coupled. A methodology for the coupled solution is presented next.

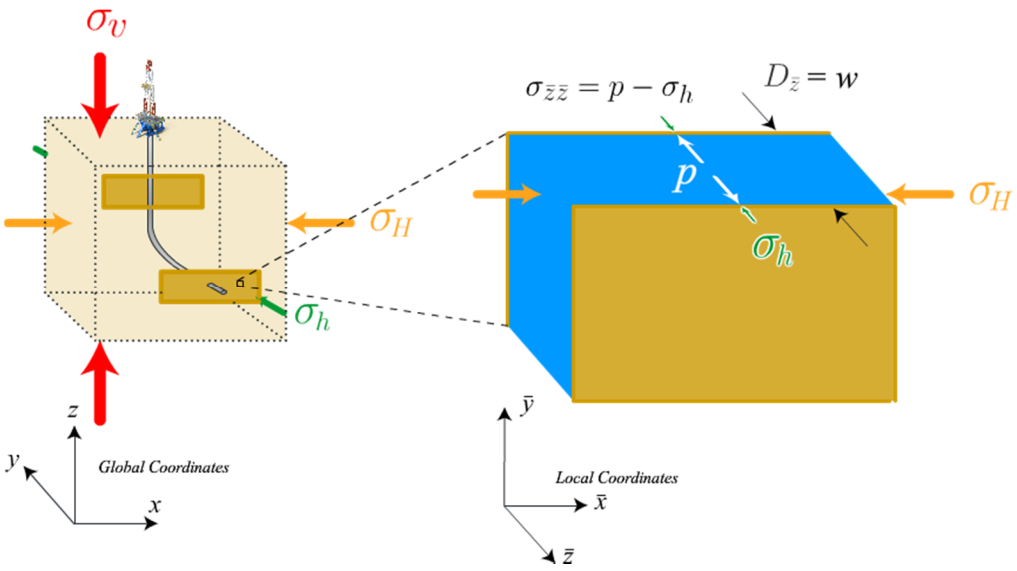

Figure 3-13. Small element of the fracture, pressure p and the minimum in situ stress are applied in the faces, the global coordinate is rotated to be consistent with the notation proposed in (Crouch & Starfield, 1983).

As discussed in Appendix B, Equation (B.17) simulates the deformation of the rock matrix and is rewritten here for convenience:

$$\overset{i,j}{\sigma'}_{\bar{z}\bar{z}} = \sum_{k=1}^{M}\sum_{l=1}^{N} \overset{i,j;k,l}{A}_{\bar{z}\bar{z}} \overset{k,l}{D}_{\bar{z}} \tag{3.91}$$

where $\overset{i,j;k,l}{A}_{\bar{j}\bar{k}}(\bar{j},\bar{k}) = (\bar{x},\bar{y},\bar{z})$ are defined as the influence coefficients, $\overset{k,l}{D}_{\bar{z}}$ is the DD normal to the surfaces of the fracture, equal to the fracture width w and $\overset{i,j}{\sigma'}_{\bar{z}\bar{z}}$ are the tractions applied in the normal direction to the faces of the fracture. A short notation for equation (3.91) is:

$$\{\sigma_{\bar{z}\bar{z}}\} = [A_{\bar{z}\bar{z}}]\{D_{\bar{z}}\} = [A_{\bar{z}\bar{z}}]\{w^s\} \tag{3.92}$$

where w^s is the fracture aperture in the current time step. As mention before, the tractions applied to the surfaces are represented by:

$$\{\sigma_{\bar{z}\bar{z}}\} = \{p^s\} - \{\sigma_n\} \tag{3.93}$$

where p^s is the injection pressure in the current time step, and σ_n is the stress normal to the fracture. Replacing equation (3.93) into equation (3.92) results:

$$[A_{\overline{zz}}]\{w\} = \{p^s\} - \{\sigma_n\} \tag{3.94}$$

Rearranging knowns in the RHS and unknowns in the LHS:

$$[A_{\overline{zz}}]\{w\} - [T_R]\{p^s\} = -\{\sigma_n\} \tag{3.95}$$

where $[T_R]$ is a transformation matrix which interpolates nodal values of the fluid pressure to centroid values in an element (Chakra, 2012). The pressure can be calculated using the fluid flow in a fracture governing equation, its discretized form, equation (3.72) is rewritten here for convenience:

$$[B]\{p^s\} = -\{f_w\} - \{f_l\} + \{f_q\} \tag{3.96}$$

where $[B]$ is the stiffness matrix. Recalling that f_w is the forcing vector which describes the fracture deformation, defined as:

$$f_w = \frac{w^s - w^{s-1}}{\Delta t} \int_{\Omega} \rho \phi_i dxdy \tag{3.97}$$

Rearranging the terms of equation (3.96) where knowns are in the RHS and unknowns in the LHS as:

$$[B]\{p\} + [B']w^s = \frac{w^{s-1}}{\Delta t} \int_{\Omega} \rho \phi_i dxdy - \{f_l\} + \{f_q\} \tag{3.98}$$

The matrix $[B']$ is defined as:

$$[B'] = [T_R]' \frac{1}{\Delta t} \int_{\Omega} \rho \phi_i \, dxdy \tag{3.99}$$

where $[T_R]'$ is the transpose of the $[T_R]$ array. Defining the vector $\{f_{fluid}\}$ as:

$$\{f_{fluid}\} = \frac{w^{s-1}}{\Delta t}\int_{\Omega} \rho\phi_i dxdy - \{f_l\} - \{f_q\} \tag{3.100}$$

The coupled system of differential equations can be solved assembling a complete system of linear equations in the form:

$$\begin{bmatrix} [B]_{Nn\times Nn} & [B']_{Nn\times Ne} \\ [T_R]_{Ne\times Nn} & [A_{\overline{zz}}]_{Ne\times Ne} \end{bmatrix} \begin{Bmatrix} p^s \\ w^s \end{Bmatrix} = \begin{Bmatrix} f_{fluid} \\ -\sigma_n \end{Bmatrix} \tag{3.101}$$

where Nn is number of nodes and Ne is number of elements. The matrix of coefficients $[A_{\overline{zz}}]$ depends only in geometrical terms and it is calculated only once, in the other hand the matrix $[B]$ is function of the unknown width, then, an initial guess is required to solve the system of equations in the first time step. The initial guess is usually a small number representing the hydraulic aperture of the fracture. The resultant width is compared with the previous value to check convergence with the following relationship:

$$\frac{\sum_{i=1}^{Ne}|w^s - w^{s-1}|}{\sum_{i=1}^{Ne}|w^s|} < \epsilon \tag{3.102}$$

where Ne is number of elements, w^s is fracture aperture in the current time step, w^{s-1} is the fracture aperture in the previous time step and ϵ is a given tolerance. If the error is greater than the tolerance then the sub-indices matrix $[B]$ is calculated again and the coupled system of linear equation is evaluated once more. The process is repeated until the method converges. A flow chart describing the process is shown in Fig. 3-14.

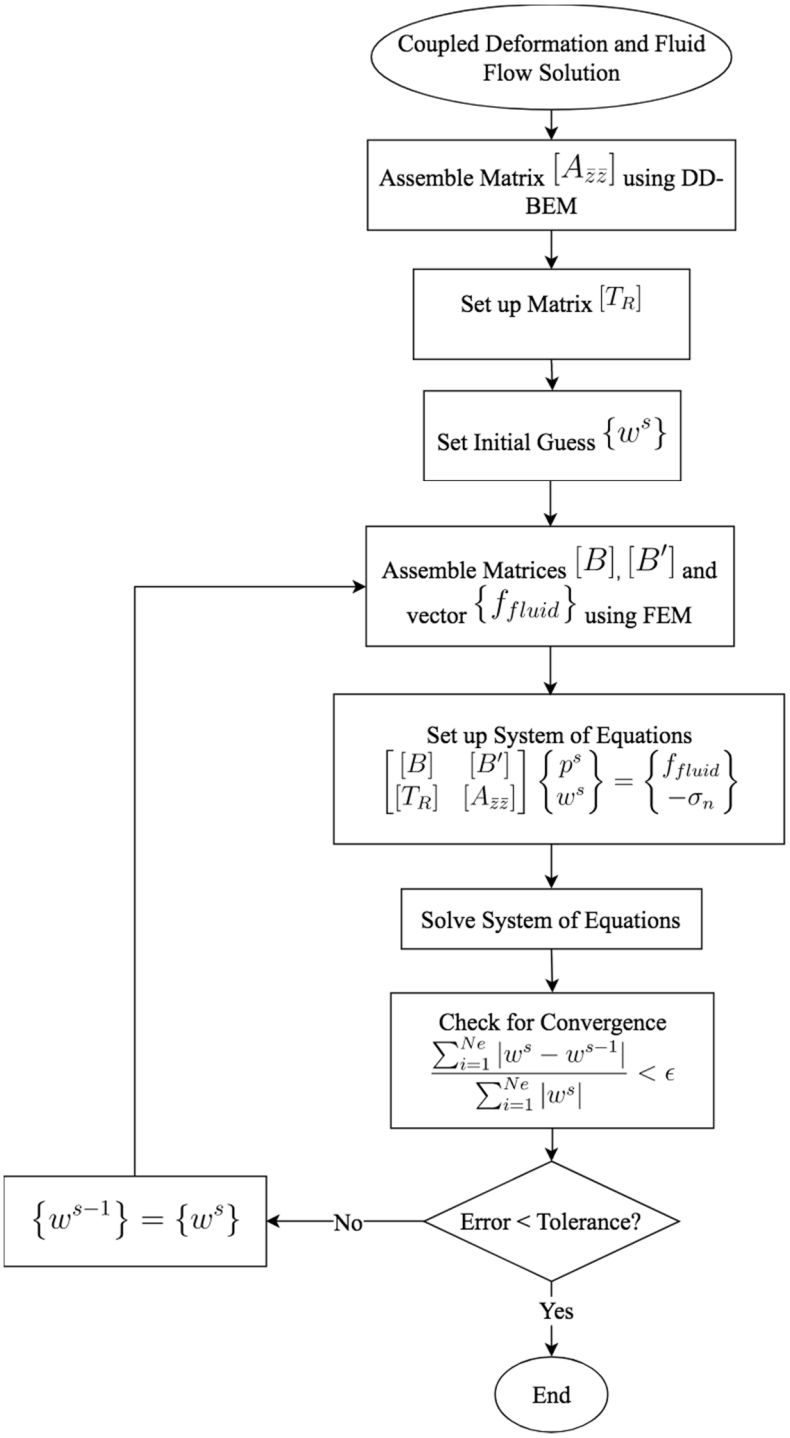

Figure 3-14. Flow chart describing the methodology to solve the coupled system of equations of deformation and fluid flow in a hydraulic fracture.

3.1.7. Coupling Proppant Flow and Transport inside a Hydraulic Fracture Model

After the pressure and fracture aperture are calculated simultaneously with the coupled scheme, a quasi-steady state within each time step is assumed implying that the concentration of the proppant does not affect the velocity field until the next time step. The proppant concentration equation is then loosely coupled and it is used to update the slurry properties of viscosity, μ, and density, ρ, that are function of proppant concentration. The dynamic viscosity μ_{SL} of the slurry can be calculated using the empirical formulation proposed by Shook (1991), in Fig. 3-15 is shown how the viscosity of the slurry will substantially increase with larger values of concentration as the solid particles require more force to flow:

$$\mu_{SL} = \mu_L[1 + 2.5c + 10c^2 + 0.00273e^{16.6c}] \tag{3.103}$$

where μ_L is the dynamic viscosity of the carrying fluid and c is the volume fraction of proppant. The density of the slurry is updated with the relationship (Ouyang, 1994):

$$\rho = c\rho_p + (1 - c)\rho_f \tag{3.104}$$

These values are calculated at the end of the time step and are input for the next time step (a flow chart describing the process is shown in Fig. 3-16).

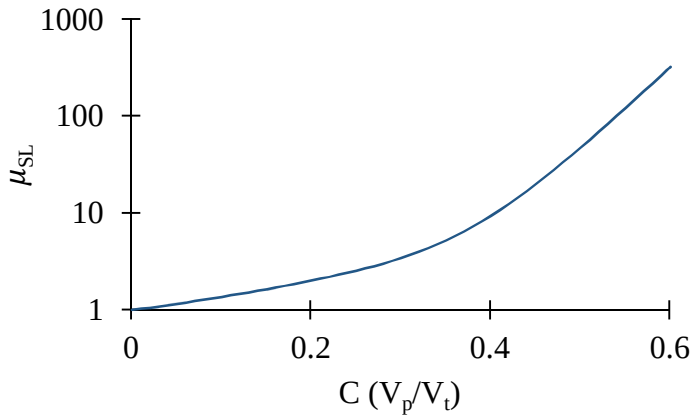

Figure 3-15. Dynamic Viscosity as expressed with equation (3.60) (Shook & Roco, 1991).

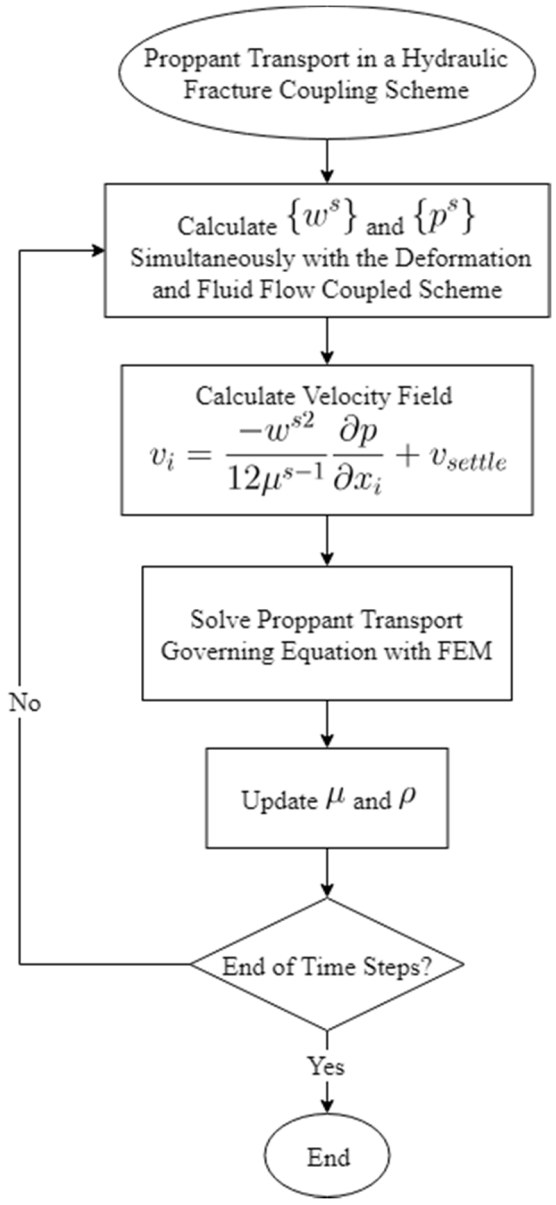

Figure 3-16. Flow chart describing the methodology to solve the coupled system of equations of proppant transport, deformation and fluid flow in a hydraulic fracture.

3.1.8. Instability of the Finite Element Solution for the Proppant Transport Governing Equation

Applying the Galerkin FEM spatial discretization to the advective terms of hyperbolic differential equations like the governing equation (3.42), leads to the product of the shape function and the derivative of the shape function expressed as (Donea & Huerta, 2004; Zienkiewicz & Taylor, 2000):

$$\int_{\Omega} w v_x \frac{\partial \phi_i}{\partial x} \phi_j dx dz \tag{3.105}$$

This product results in an unsymmetrical element matrix which contains zero values in the main diagonal, once the element matrix is assembled into the global matrix to form the final system of equations, the zero values in the diagonal cause a spurious and unstable solution (Donea & Huerta, 2004). In Fig. 3-17, an example of the proppant concentration distribution after solving the equation (3.42) is shown. Although the domain was geometrically discretized with a fine mesh containing 1600 elements, the solution is erratic and unreasonable.

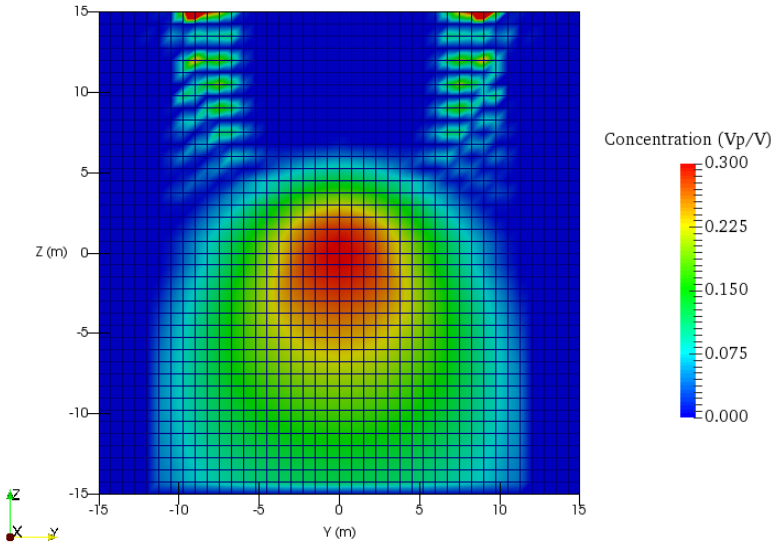

Figure 3-17. Proppant concentration distribution at t=239 s. In a 30m by 30m idealized fracture, discretized with a fine mesh consisting of 1600 square elements. The solution with Galerkin FEM shows instability and erratic behavior.

3.1.9. SUPG FEM Stabilization of the Proppant Transport Governing Equation

To overcome the solution instability of the governing equation (3.42) shown in Fig. 3-17, the Streamline Upwinding Petrov Galerkin (SUPG) was implemented. The main objective is to modify the weight function to give more weight to the upwind flux, this change in the shape function leads to more symmetric systems of equation and consequently stabilizing the approximate solution. This can be accomplish by adding an extra term to the standard shape functions, From the many options available, one term that has been implemented with success is (Brooks & Hughes, 1982):

$$N_i = \phi_i + \frac{\tilde{\alpha}}{\sqrt{v_\xi^2 + v_\eta^2}}\left(v_\xi \frac{\partial \phi_i}{\partial \xi} + v_\eta \frac{\partial \phi_i}{\partial \eta}\right) \tag{3.106}$$

where ϕ is the standard shape function, i is the i^{th} node in the element and $\tilde{\alpha}$ is defined as:

$$\tilde{\alpha} = \frac{\tilde{\xi} v_\xi h_\xi + \tilde{\eta} v_\eta h_\eta}{2} \tag{3.107}$$

where

$$\tilde{\xi} = \coth \alpha_\xi - \frac{1}{\alpha_\xi}, \quad \tilde{\eta} = \coth \alpha_\eta - \frac{1}{\alpha_\eta} \tag{3.108}$$

$$\alpha_\xi = \frac{v_\xi h_\xi}{2\kappa}, \quad \alpha_\eta = \frac{v_\eta h_\eta}{2\kappa} \tag{3.109}$$

v_ξ and v_η are the velocities in ξ and η directions, h_ξ and h_η are the characteristic lengths as shown in Fig. 3-18, κ is the slurry diffusivity coefficient. Note that when the domain is discretized with square elements, the directions ξ and η coincide with the global directions x and y.

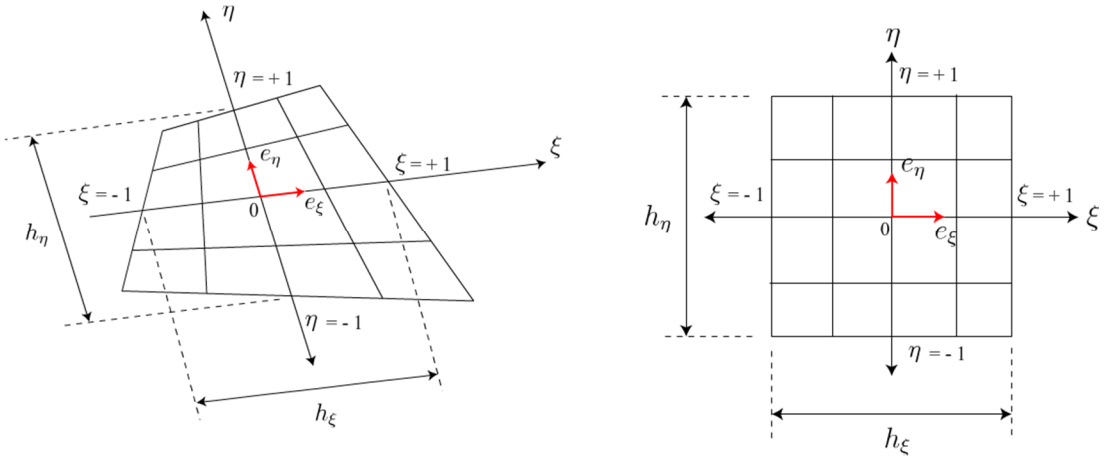

Figure 3-18. Recommended characteristic element lengths h_η and h_ξ in the ξ and η directions which are parallel to the lines $(\xi, \eta = 0)$ and $(\xi = 0, \eta)$. In case of a square elements these lengths coincide with the element side length.

The fact that the choice of the weight function is different from the shape function used to approximate the solution, and that the weigh function now accounts for the upwinding flow, gives the name to the method Streamline Upwind Petrov Galerkin (SUPG). To implement the SUPG stabilization into the formulation, the mass matrix A_{ij} from equation (3.85) is modified as follows:

$$A_{ij} = \int_{\Omega} wN_i\phi_j dxdz \tag{3.110}$$

And the stiffness matrix B_{ij} in equation (3.86) is modified as follows.

$$B_{ij} = \int_{\Omega} \left\{ \frac{\partial w}{\partial t} N_i\phi_j - wv_x \frac{\partial \phi_i}{\partial x}\phi_j - wv_z \frac{\partial \phi_i}{\partial z}\phi_j \right\} dxdz + \int_{\Gamma} wv_x N_i\phi_j n_x \, d\Gamma + \int_{\Gamma} wv_z N_i\phi_j n_z \, d\Gamma \tag{3.111}$$

To test the SUPG stabilization technique, the numerical example in Fig. 3-17 is performed again using the stabilization technique. The resultant proppant distribution is shown in Fig. 3-18, it can be observed that the proppant concentration distribution is smoothed.

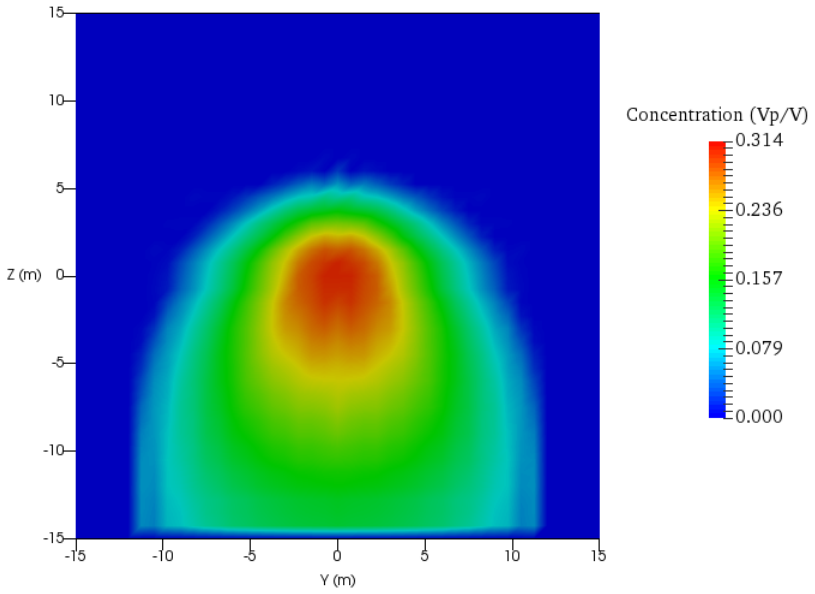

Figure 3-19. Proppant concentration distribution in at t=239 (s) In a 30m by 30m idealized fracture. The application of the SUPG FEM improves the solution as compared with Fig. 3-17.

3.2. Models Verification

In this section, verifications of each module separately are presented. In well-defined domains, the governing equations for fracture deformation, Eq. (3.12), fluid flow inside a fracture, Eq. (3.27) and proppant transport in a fracture, Eq. (3.42) are solved numerically. The results from this numerical analysis are compared against analytical solutions to verify the correctness of the implementation. The verification of the coupled scheme to calculate fracture aperture and fluid pressure can be found elsewhere (Kumar & Ghassemi, 2016, 2018) and is not repeated here.

3.2.1. Verification of the Solution of Rock Deformation

For the first verification, the width distribution in a penny-shaped fracture subjected to a constant pressure is calculated with the constant DD method. The domain is discretized with squares as shown in Fig. 3-20, the numerical result is compared with the analytical solution of a penny shaped fracture subjected to a constant pressure proposed by (Sneddon, 1945):

$$w(r) = \frac{4p_{net}(1-v)R}{\pi G}\sqrt{1-\left(\frac{r}{R}\right)^2} \tag{3.112}$$

where $w(r)$ is the fracture width, p_{net} is the net fluid pressure, R is the radius of the fracture and r is the radial distance of any point on the fracture surface. The verification simulation was performed considering the input data as listed in Table 3-1. A distribution of the fracture aperture and its comparison against the analytical solution are presented in Fig. 3-21 and 3-22, respectively. The results from the DD model and the analytical solution show a close agreement as shown in Fig. 3-22

Table 3-1. Data considered to perform the DD model verification.

Property	**Value**	**Units**
Young modulus (E)	27	GPa
Poisson's ratio (v)	0.25	
Fluid pressure (p)	3.42	MPa

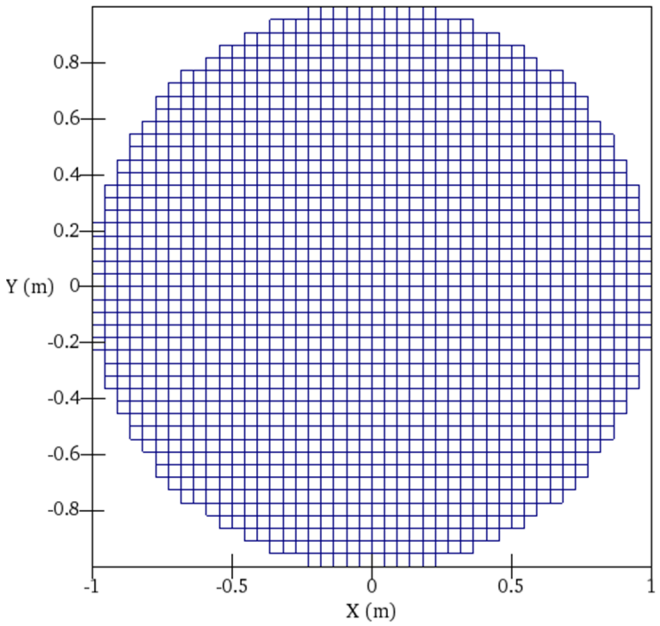

Figure 3-20. Penny shape fracture geometry discretized with squares, $\Delta x = \Delta y = 0.045\ m$, 1528 elements.

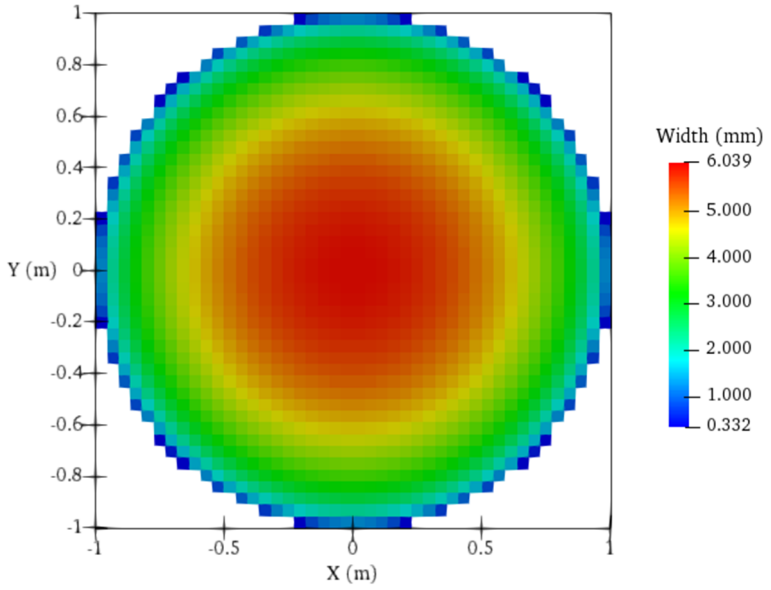

Figure 3-21. Fracture aperture distribution of a penny shaped fracture subjected to constant fluid pressure equal to 3.42 MPa.

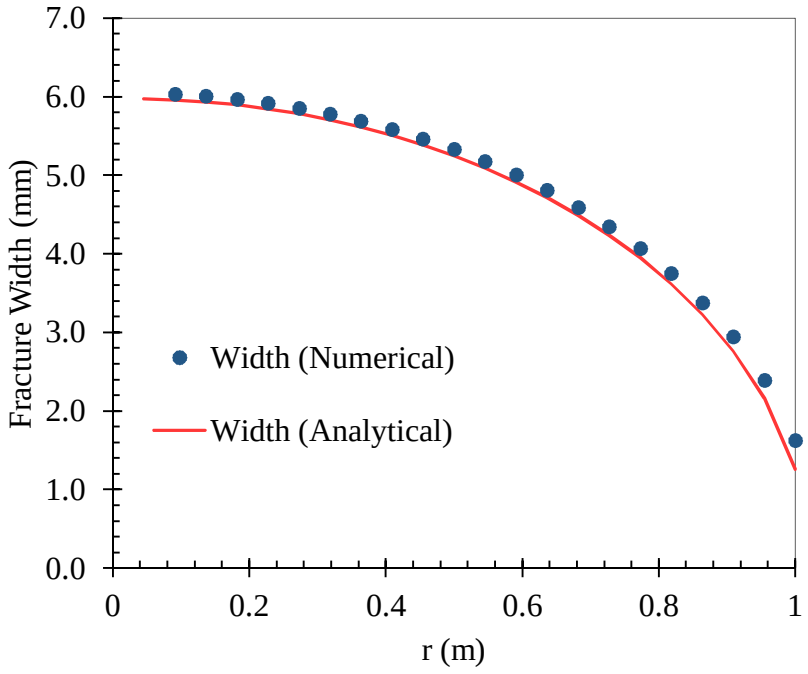

Figure 3-22. A comparison of the fracture aperture for a pressurized penny shaped fracture from the DD model and analytical solution (Sneddon, 1945). The results show a close agreement.

3.2.2. Verification of the Fluid Flow inside a Fracture Equation

For the second verification, the fluid flow inside a fracture equation (3.27) is solved in a circular fracture with an injection and a production well system as shown in Fig 3-23. A plan-view of the fracture with the injector and producer wells is shown in Fig. 3-24.

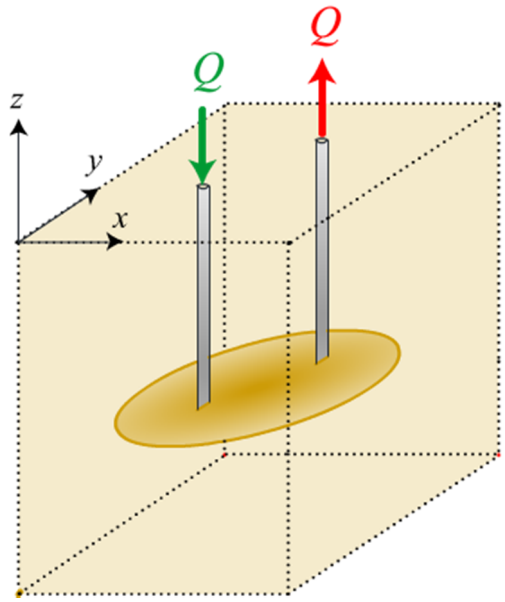

Figure 3-23. Scheme of the Penny shaped horizontal fracture intercepted by two wells, one injector and one producer.

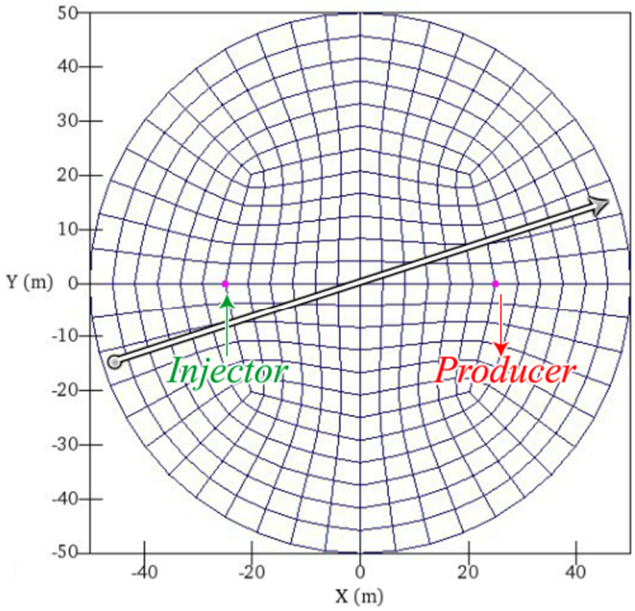

Figure 3-24. Penny shaped horizontal fracture discretized with rectangles oriented arbitrarily. The injector well is located at x=-25, y=0 and the producer is located at x=25, y=0. Additionally there is an arbitrary line where the analytical and numerical solutions are plotted for comparison.

An analytical solution for the fluid distribution for this case is given as (Ghassemi and Tarasov, 2003; Strack, 1989):

$$q_x = \frac{1}{2\pi}\sum_{i=1}^{n_w} Q_i \left[\frac{x - x_i}{(x-x_i)^2 + (y-y_i)^2} + \frac{r^2(xr_i^2 - x_iR^2)}{(xr_i^2 - x_iR^2)^2 + (yr_i^2 - y_iR^2)^2}\right] \tag{3.113}$$

$$q_y = \frac{1}{2\pi}\sum_{i=1}^{n_w} Q_i \left[\frac{y - y_i}{(x-x_i)^2 + (y-y_i)^2} + \frac{r^2(yr_i^2 - y_iR^2)}{(xr_i^2 - x_iR^2)^2 + (yr_i^2 - y_iR^2)^2}\right] \tag{3.114}$$

where q_x, q_y are the discharges per unit width in x and y directions respectively, Q_i is the fluid extraction rate of the i^{th} well, the summation of all the rates must be equal to zero since this solution doesn't account for the fluid leak-off. n_w is the number of wells, (x_i, y_i) are the

coordinates of the i^{th} well, R is the radius of the circular fracture and the radial distance r_i is defined as:

$$r_i = \sqrt{x_i^2 + y_i^2} \tag{3.115}$$

The comparison is possible considering the relationship between pressure and velocity given in Appendix A by equation (A.31) and (A.32) rewritten here for convenience as:

$$q_x = -\frac{w^3}{12\mu}\frac{\partial p}{\partial x} \tag{3.116}$$

$$q_y = -\frac{w^3}{12\mu}\frac{\partial p}{\partial y} \tag{3.117}$$

The input data used to perform the comparison is listed in Table 3-2.

Table 3-2. Input parameters for the fluid flow verification.

Property	Value	Units
Fracture radius (R)	50	m
Fluid injection rate (Q_1)	1×10^{-2}	m^3/s
(x_1, y_1) location of injection well	$(-25,0)$	m
Fluid extraction rate (Q_2)	-1×10^{-2}	m^3/s
(x_2, y_2) location of extraction well	$(25,0)$	m

In Fig. 3-25 the numerical results calculated using FEM model show a close agreement with the analytical solution, Both solutions are compared over an arbitrary line traced in the domain of the fracture as shown in Fig. 3-24.

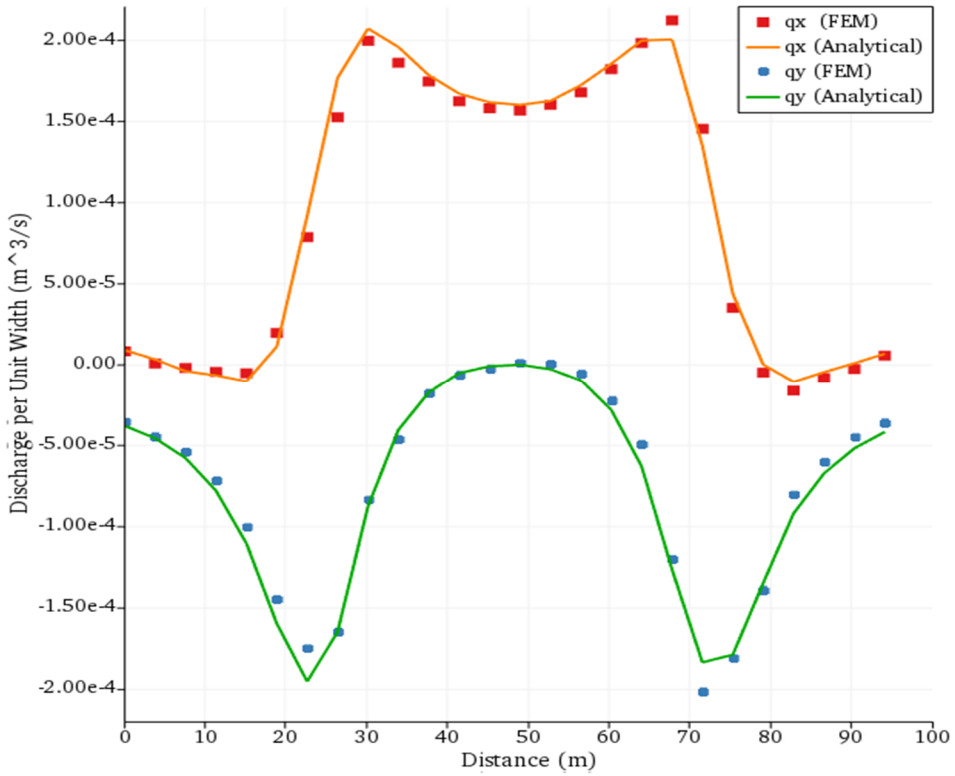

Figure 3-25. Comparison of the numerical and analytical solutions for the penny shaped fracture with two wells problem. The data is plotted over the line traced as shown in Fig. 3-24.

3.2.3. Verification of the Proppant Flow and Transport Equation

For the last verification, the governing equation of the proppant flow and transport (3.42) is rewritten here for convenience:

$$\frac{\partial(wc)}{\partial t} - \frac{\partial(cwv_x)}{\partial x} - \frac{\partial(cwv_z)}{\partial z} = 0 \tag{3.118}$$

where w is the fracture aperture, c is the concentration of proppant and v_x and v_y are the velocities in x and y directions, respectively.

To verify the FEM solution for the proppant flow and transport, in the absence of an analytical solution that could test all the terms in the governing equation, a solution is created using the method of manufactured solutions. The method, used for many time without an specific name, was finally formalized by (Roache, 1998, 2002) and (Salari & Knupp, 2000). The terms of the left hand side of the differential equation are replaced by smooth known functions (i.e. fracture width (w), proppant concentration (c), proppant velocity $(v_x \; and \; v_y)$) , after solving the differentiations in the equation, a force term is produced. To test the numerical scheme, the input would be the forcing vector; the objective is then to match as close as possible the known functions that were used as input in the first place. The selected functions do not imply a physical meaning as the main objective is to make sure that the differential equation is solved correctly with the discretization scheme selected, in this case FEM. The geometry chosen to represent the hypothetical fracture is a unit square as shown in Fig. 3-26.

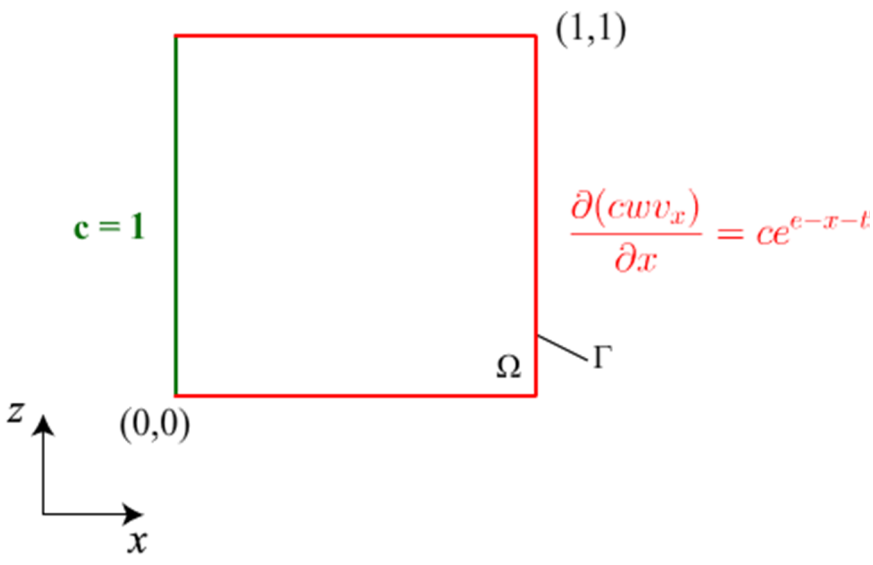

Figure 3-26. A schematic of fracture geometry with prescribed boundary conditions to verify the solution of the proppant flow and transport inside a hydraulic fracture equation.

The initial and boundary conditions, and concentration variation is (Ouyang, 1994):

$$w = e^{-x-t} \tag{3.119}$$

$$v_x = 1 \tag{3.120}$$

$$v_z = 0 \tag{3.121}$$

$$c = e^{-3x} \tag{3.122}$$

Replacing equations (3.119) through (3.122) into equation (3.118) the result is:

$$f = \frac{\partial(e^{-x-t}e^{-3x})}{\partial t} - \frac{\partial(e^{-x-t}e^{-3x})}{\partial x} \tag{3.123}$$

After solving the differentiations, the result is:

$$f = (5e^{-3x})e^{-x-t} \tag{3.124}$$

The hypothetical equation that needs to be solved for the concentration to test the numerical implementation is given as:

$$\frac{\partial(wc)}{\partial t} - \frac{\partial(cwv_x)}{\partial x} - \frac{\partial(cwv_z)}{\partial z} = (5e^{-3x})e^{-x-t} \tag{3.125}$$

With the boundary condition:

$$c = 1 \; at \; (0, z, t) \tag{3.126}$$

by setting $c = 1$ at $x = 0$, the nodes in the left edge of the fracture are considered to be injection nodes. Also the velocity is prescribed in the outer nodes with a physical meaning of flow leaving the system, to appropriately simulate this condition a Neumann boundary condition is set as:

$$\frac{\partial(cwv)}{\partial n} = ce^{-x-t} \; at \; (1, z, t) \; \cup (x, 0, t) \cup (x, 1, t) \tag{3.127}$$

When the injection of proppant begins, there is a hypothetical concentration distribution represented with the initial conditions:

$$c = e^{-3x} \; at \; (x, z, 0) \tag{3.128}$$

As the chosen function c is independent of time, expressed in equation (3.122), the result is expected not to change as in Fig. 3-27:

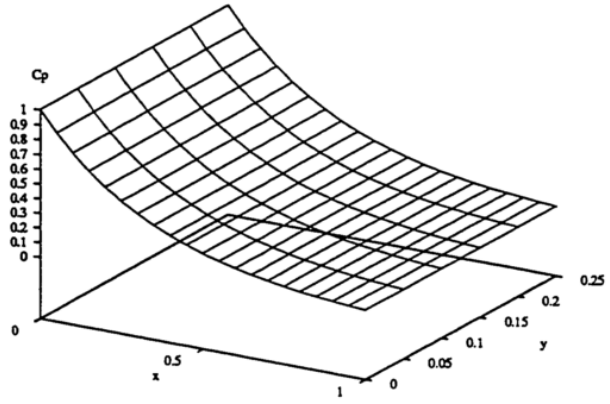

Figure 3-27. Expected numerical solution of equation (3.118) taken from (Ouyang, 1994) as a reference of a published solution. This plot represents the proppant concentration distribution after solving the hypothetical problem defined by equations (3.125) – (3.127). The simulation was run for 1s, the size of the side of the square in the geometrical discretization is $\Delta x = 0.05$ and the time discretization was perform with $\Delta t = 0.01$.

After the forcing vector from equation (3.124) was given as input in the solution scheme the concentration distribution was run for 1 s with time increments of 0.01 s. The concentration function chosen was independent of time as shown in equation (3.122) so that the solution is

expected not to change compared with the initial condition shown in equation (3.128). The solutions shown in Fig. 3-28. and 3-29. are in good agreement with the constructed analytical solution.

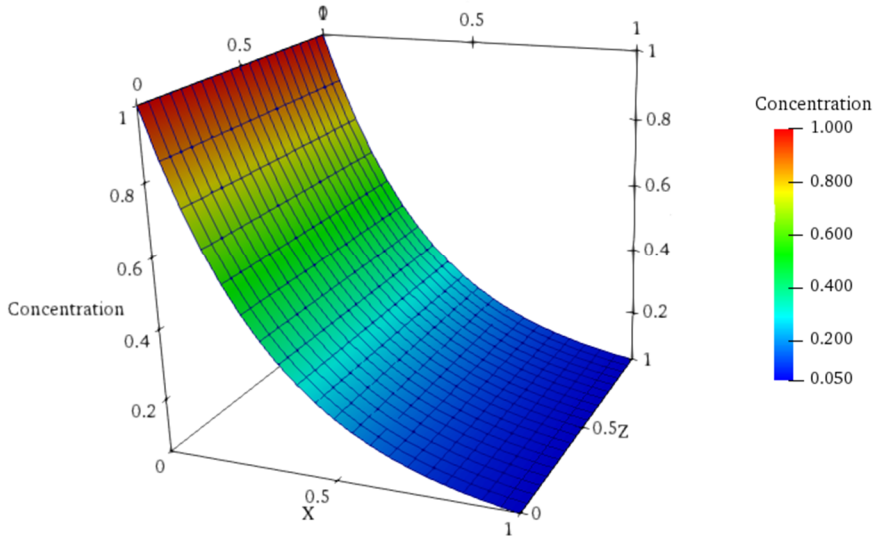

Figure 3-28. Numerical solution of equation (3.118) after 1s ($\Delta x = 0.05, \Delta t = 0.01$ s).

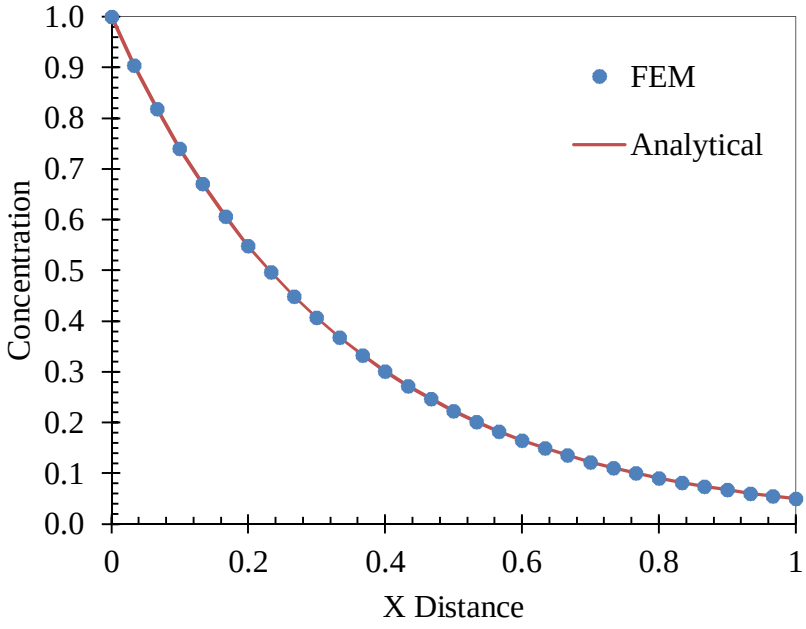

Figure 3-29. Comparison of the FEM solution at z = 0 against the analytical solution of equation (3.118).

Chapter 4. Modeling Proppant Transport and Deposition in Hydraulic Fracture (s)

This chapter presents a number of example simulations of the proppant flow and transport in a hydraulic fracture from a horizontal well. Though, the 3D fractures from a horizontal well can have a complex geometry (Kumar & Ghassemi, 2016, 2018, Sesetty & Ghassemi, 2017, 2018), to illustrate basic physics of the proppant behavior inside the hydraulic fractures, a simplified fracture geometry (i.e., rectangular shape fracture) as shown in Fig. 4-1 is considered first. The horizontal well is aligned with the minimum horizontal stress direction (i.e., along x-axis in this case). The hydraulic fracture is in the YZ-plane and has the half-length equal to 90 (m) and fracture height is equal to 30 (m). For numerical implementation, the fracture surface is discretized using 2400 constant square elements as shown in Fig. 4-2. The reservoir rock parameters and in-situ stresses are listed in Table 4-1. Two cases of the proppant concentration distributions (i.e., with and without proppant settling) are considered. A detailed sensitivity analysis of the impacts of various parameters such as the proppant size, carrying fluid viscosity, and simulation mesh size is carried-out.

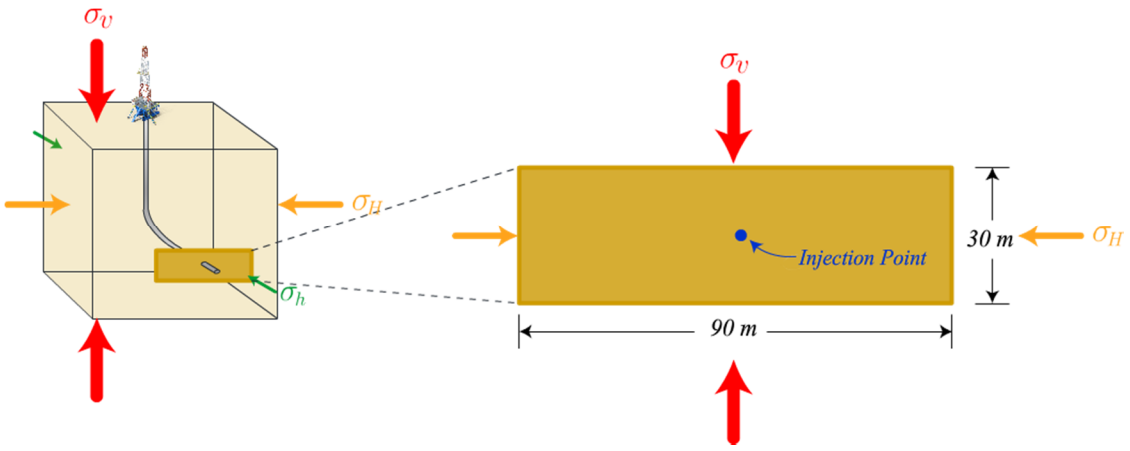

Figure 4-1. Schematic of a hydraulic fracture simulation.

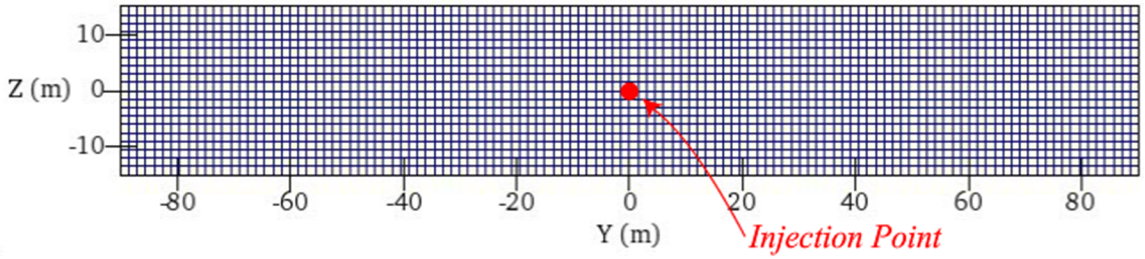

Figure 4-2. Mesh representing the domain of the fixed fracture. 180m wide, 30m high, 120 elements in the Y axis and 20 elements in Z axis. The injection point is centered in the domain at z=0, y=0.

Table 4-1. Parameters used to test the concentration distribution model

Rock Properties		
Poisson's ratio (v)	0.25	
Young's modulus (E)	27.1	GPa
Stress field		
Vertical stress (σ_v)	10	MPa
Maximum horizontal stress (σ_H)	7	MPa
Minimum horizontal stress (σ_h)	5	MPa

4.1. Proppant Concentration Distribution without Proppant Settling

In this section the proppant concentration distribution without considering the proppant settling is presented. In this first simulation, the velocity field is calculated disregarding the settling velocity to study an idealized behavior. To study the behavior of the numerical scheme used to solve the proppant transport in a hydraulic fracture governing equation, some parameters were taken from (Gadde et al., 2004). The mesh representing the domain of the fracture is shown in Fig. 4-2. The input parameters are listed in Table 4-2. The proppant flow and transport governing equation (3.42) is solved for an injection time of 1295 s. The snap-shot of the proppant concentration distribution for four different simulation times (i.e., 545 s, 795 s, 1045 s, and 1295 s) are shown in Figs. 4-4 a, b, c, and d, respectively.

The parameters necessary to calculate the thickness of the proppant pack in each element of the discretized hydraulic fracture are: element proppant concentration (c), element area (A), element volume (V), element fracture width (w), number of proppant layers (N_p) which can be estimated using the relationship in equation (4.3) , and the propped width (w_p). A schematic of a propped element of a hydraulic fracture showing these parameters is presented in Fig 4-3. To find a relationship to estimate the proppant layers distribution, first the proppant concentration definition is considered, the equation of concentration is rewritten here for convenience:

$$c = \frac{V_p}{V} = \frac{Aw_p}{Aw} \tag{4.1}$$

where V_p is volume of proppant, V is total volume, A is element area, h_p is element proppant height and w is element fracture width as shown in Fig. 4-3 Noting that the element proppant height is expressed as:

$$w_p = N_p d_p \tag{4.2}$$

Replacing equation (4.2) into equation (4.1) and solving for l_p, results in:

$$N_p = \frac{cw}{d_p} \tag{4.3}$$

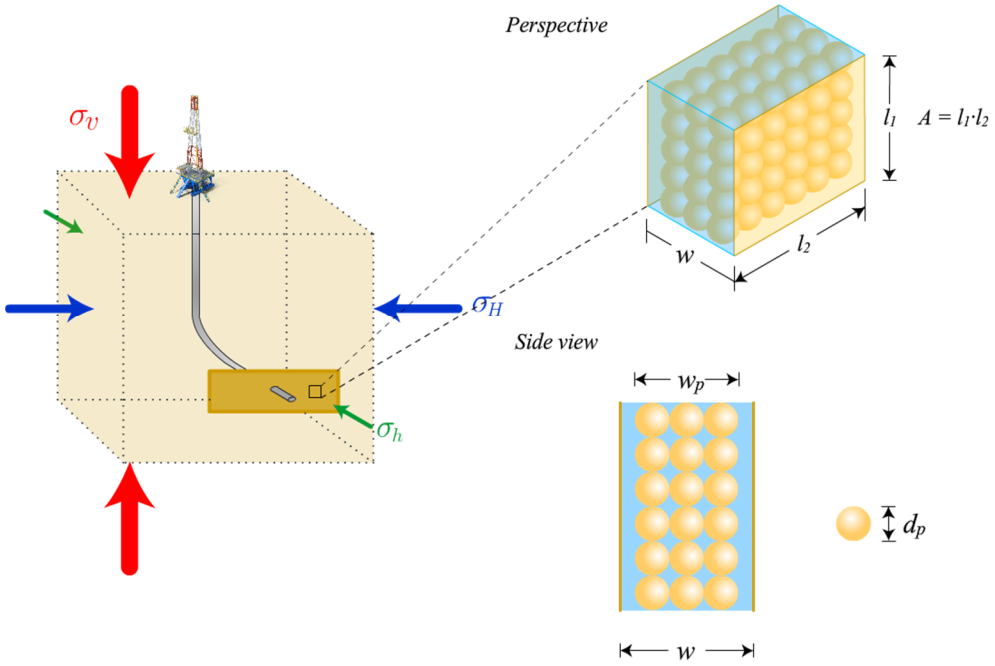

Figure 4-3. Schematic of a propped element of a hydraulic fracture.

An study that considers the proppant placement behavior and the closure of the fractures can be found in (Kumar, D., Gonzalez, R.A., and Ghassemi, 2018).

In this run the velocity field is calculated disregarding the settling velocity to study an idealized behavior. As shown in Fig. 4-4, the proppant front is symmetric and smooth as it is increasing with injection time. The maximum concentration corresponds to the injection point located at z=0, y =0 and is subjected to a radial distribution.

Table 4-2. Parameters used to test the concentration distribution model

Injection Parameters		
Injection rate (Q)	0.02	m^3/s
Injection proppant concentration (Vp/V)	0.3	
Fluid viscosity (μ)	0.001	Pa.s
Fluid density (ρ_f)	1000	kg/m^3
Proppant density (ρ_p)	2500	kg/m^3
Proppant diameter (d_p)	300	µm
Time step (Δt)	5	s

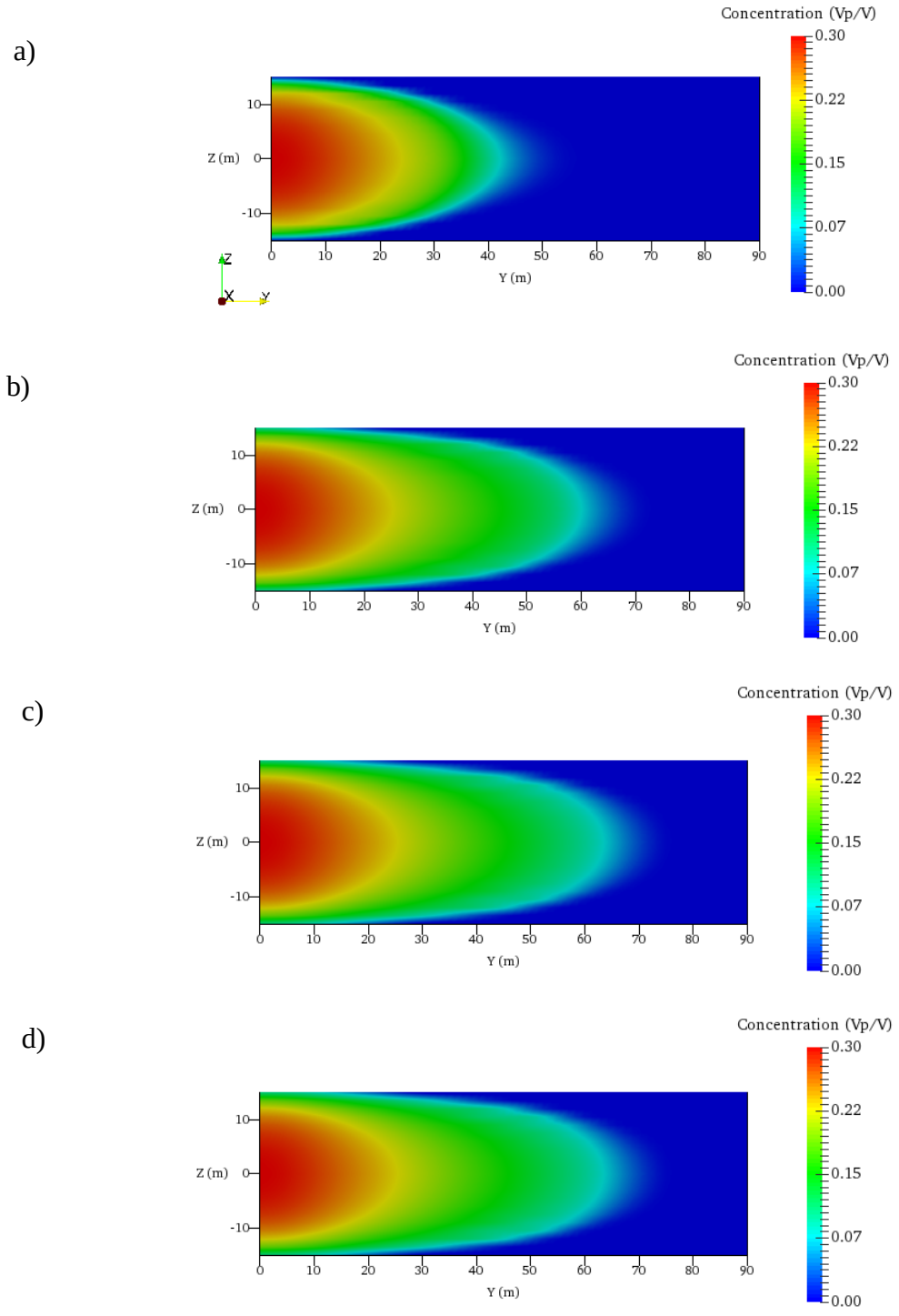

Figure 4-4. Proppant concentration distribution. Due to symmetry only half fracture is shown. The source point is located at y = 0, z = 0. Injection times are a) t=545 s b) t=795 s c) t=1045 s d) t=1295 s.

4.2.Proppant Concentration Distribution with Settling Velocity

In this section the proppant flow and transport governing equation (3.42) is solved for an injection time of 1295 s. In this run the velocity field was modified to account for the settling effect. The proppant front, as shown in Figure 4-5, is now tilted downwards and most of the concentration is being deposited in the lower part of the fracture. In the transition zone of high concentration and low concentration represented by the yellow color some fingering is noticed. It is also observed that after some time the extent of the proppant front is reduced at the top of the "layer", these phenomena are explained later in this report when the sensitivity analysis is being performed. The maximum concentration corresponds to the injection point located at z=0, y =0 and is subjected to a radial distribution:

a)

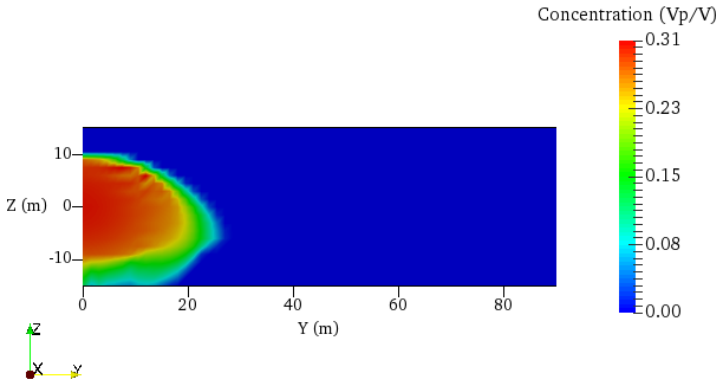

b)

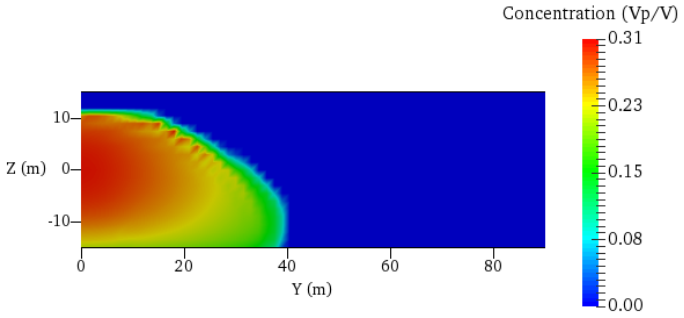

c)

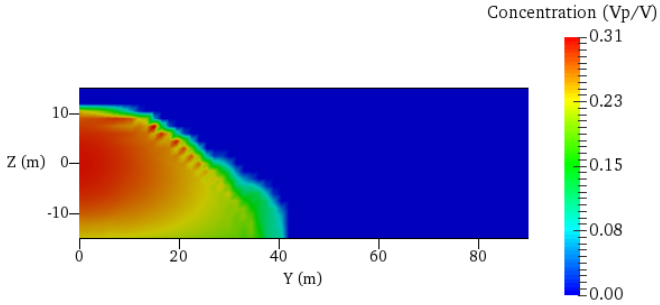

d)

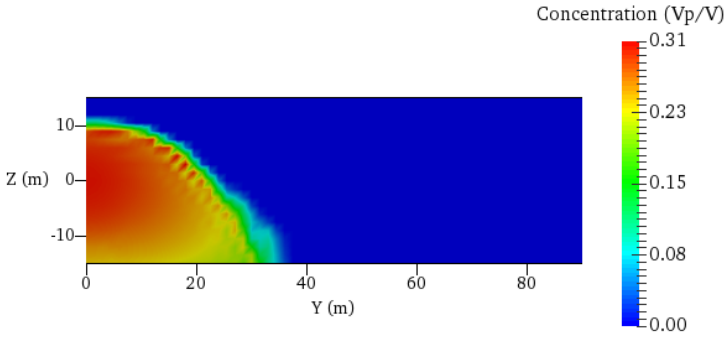

Figure 4-5. Proppant concentration distribution with settling effect. Due to symmetry half of the fracture surface is shown. The injection point is located at y = 0, z = 0 a) solution at t=545 s b) solution at t=795 s c) solution at t=1045 s d) solution at t=1295 s.

4.3. Sensitivity Analysis for the Parameters Affecting the Proppant Concentration

In this section, a detailed sensitivity analysis of the various parameters such as the proppant particle size, carrying fluid viscosity, and simulation grid size which impact the proppant flow and transport inside a hydraulic fracture is presented.

4.3.1. Effect of Proppant Size

The proppant particle size is one of the most important parameters for the proppant concentration distribution. Typically, proppants are classified based on the particle size. For example, 16/30 mesh size (i.e., the proppant diameter (d_p) ranges from 600 µm – 1180 µm), 20/40 mesh size (i.e., d_p ranges from 420 µm - 840 µm), 30/50 mesh size (i.e., d_p ranges from 300 µm – 600 µm), 40/70 mesh (i.e., d_p ranges from 212 µm - 420 µm) or 70/140 mesh size (i.e., d_p ranges from 106 µm - 212 µm). Simulations for two different type of proppant sizes 20/40 mesh ($d_p = 600\mu m$) and 40/70 mesh ($d_p = 300\mu m$) were carried out to study the effect of this parameter in the evolution of the proppant front. Recently, micro-proppants are being used, this small particles classified as 100 mesh ($d_p = 150\mu m$) had two major advantages, the first is that they can be placed in fractures with small apertures such as secondary and tertiary fractures, and the second is that less amount of viscosifier is needed to efficiently transport the micro-proppant into these fractures thereby reducing the formation damage that the viscosifier may cause. In a hydraulic fracturing job, micro proppant would be pumped first in an effort to prop open the micro fractures and then larger proppant like 20/40 mesh or 40/70 mesh is pumped to prop open the main hydraulic fracture (Dahl et al., 2015).

The results of the fluid pressure distribution, fracture aperture distribution, and proppant concentration distribution for the four simulation times (i.e., 545 s, 795 s, 1045 s, and 1295 s) are shown in Figs. 4-6, 4-7, 4-8 and 4-9, respectively. It is observed that when the proppant size is increased, there is more tendency for settling down due to the increase in the hydrodynamic drag forces.

For the proppant size 20/40 (d_p = 600μm), the proppant front reaches a maximum propped distance equal to 34.5m in y axis at t=795 s, in later times, while the horizontal distance of the proppant front is reduced, the area under the curve increases showing accumulation in the proppant concentration in a more compact front. This behavior with time can be better understood by checking Figs. 4-13 and 4-14. In the color plots, of Fig. 4-6a, Fig. 4-7a, Fig. 4-8a and Fig. 4-9a it can be noted that the pressure tends to equalize in the fracture with time, implying a reduction in the horizontal proppant velocity so that a reduction in the horizontal distance reached by the proppant is to be expected. The horizontal distance reached by the proppant is greatly affected by the change in proppant diameter. A comparison of the fluid pressure distribution at z=0 for two different proppant sizes (i.e., 40/70 and 20/40 mesh size) is shown in Figs. 4-11 a, b, c and d, respectively. In all the solution times considered, the slope of the curves for d_p = 300μm is always greater that those curves for d_p = 600μm implying a higher horizontal velocity, and as a result, a greater transport distance in the y axis.

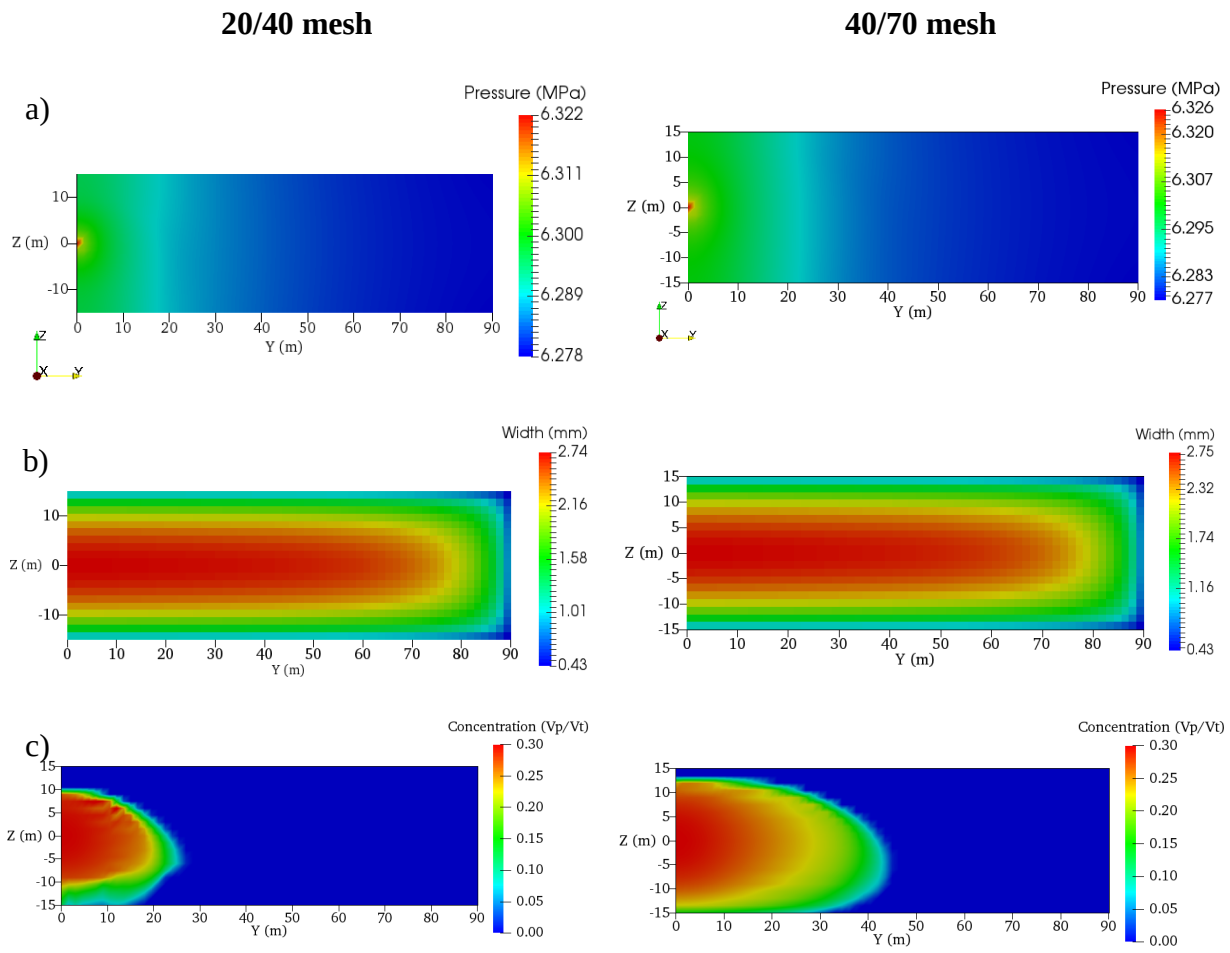

Figure 4-6. Comparison of simulation results at t = 545 s, left column with a proppant size of 600 µm and right column with a proppant size of 300 µm, only half fracture is being shown. The source point is located at y = 0, z = 0 a) pressure distribution in the fracture, b) width distribution in the fracture c) concentration distribution.

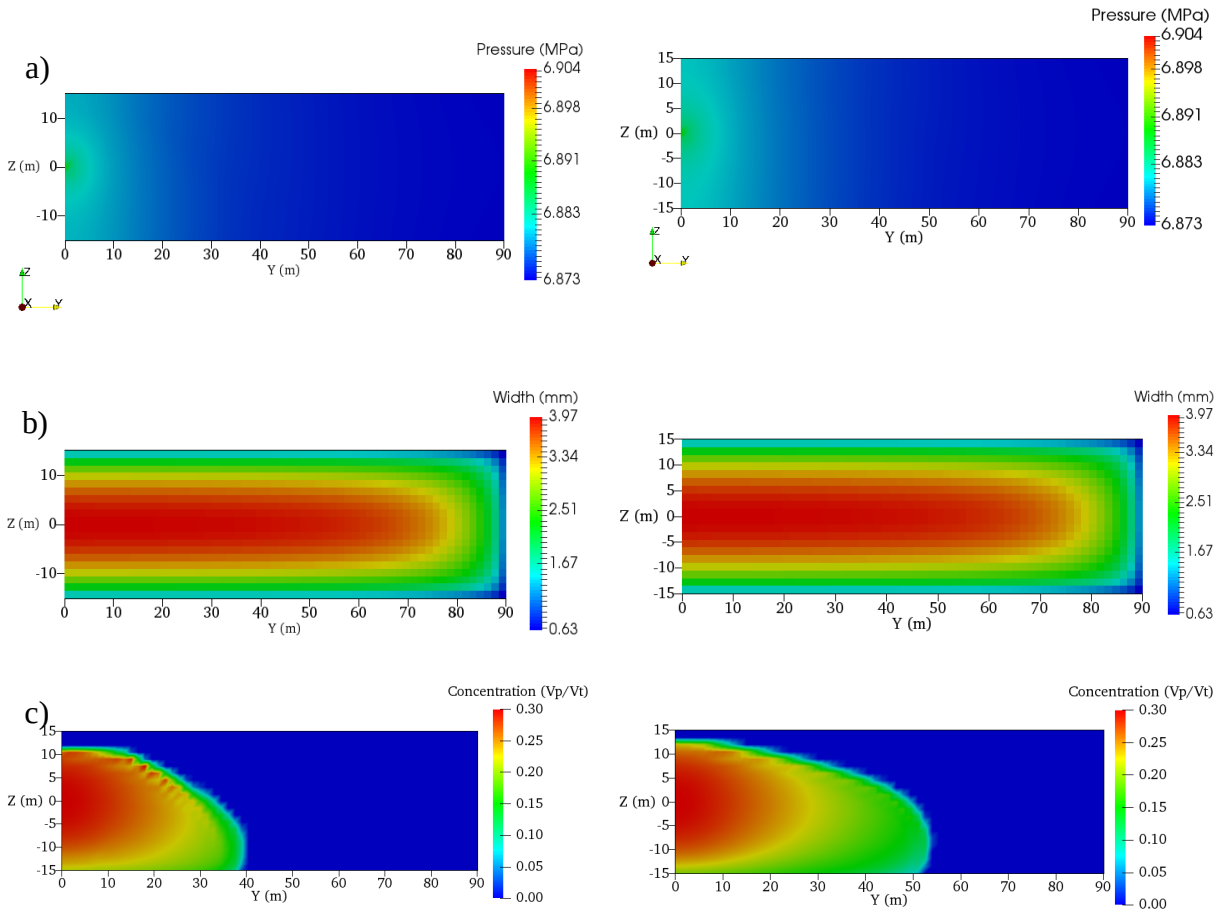

Figure 4-7.Comparison of simulation results at t = 795 s, left column with a proppant size of 600 µm and right column with a proppant size of 300 µm, only half fracture is being shown. The source point is located at y = 0, z = 0 a) pressure distribution in the fracture, b) width distribution in the fracture c) concentration distribution.

20/40 mesh **40/70 mesh**

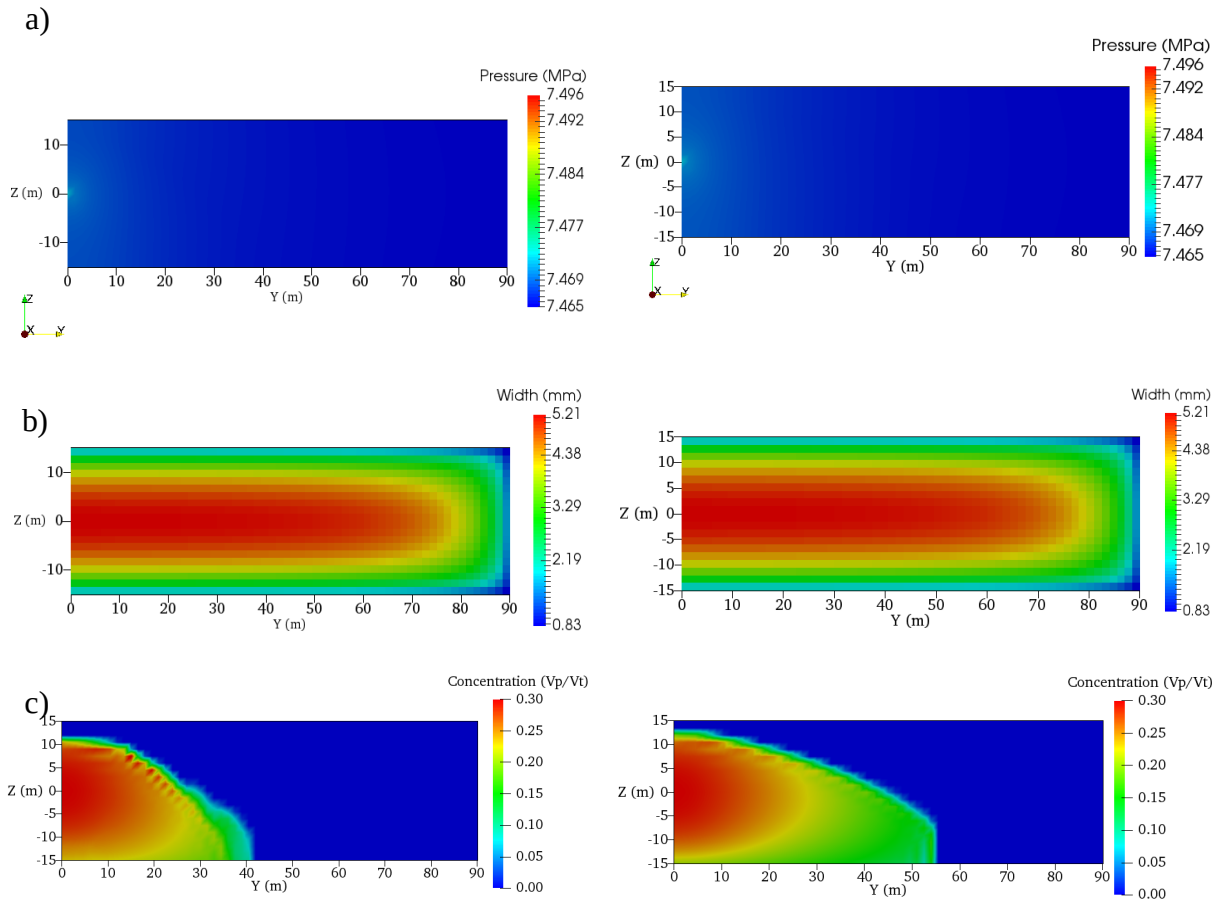

Figure 4-8. Comparison of simulation results at t = 1045 s, left column with a proppant size of 600 µm and right column with a proppant size of 300 µm, only half fracture is being shown. The source point is located at y = 0, z = 0 a) pressure distribution in the fracture, b) width distribution in the fracture c) concentration distribution.

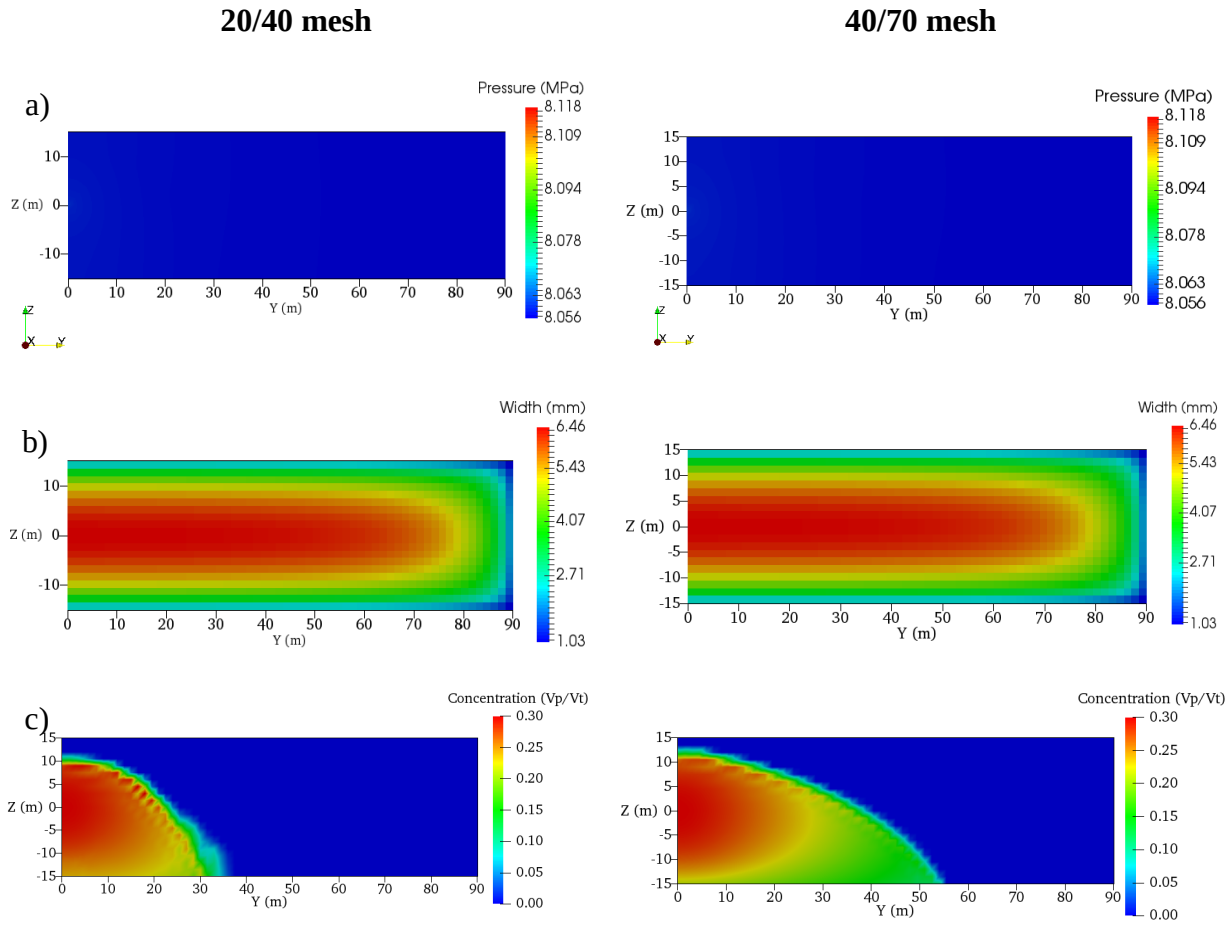

Figure 4-9. Comparison of simulation results at t = 1295 s, left column with a proppant size of 600 µm and right column with a proppant size of 300 µm, only half fracture is being shown. The source point is located at y = 0, z = 0 a) pressure distribution in the fracture, b) width distribution in the fracture c) concentration distribution.

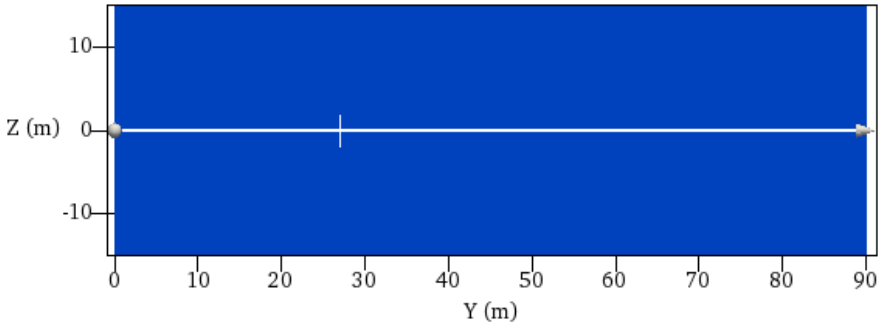

Figure 4-10. Line traced at z=0 where the data for the scatter plots is taken.

In Fig. 4-11 the difference in the pressure profile traced at $z = 0$ for four different time steps is presented, in Fig. 4-11a, the difference between the two curves is more noticeable that in the other time steps, this can be explained if we consider that at in early time steps the zones of high concentration are transported longer distances. For the case of 20/40 mesh size, the zone of concentration higher than 0.25 reaches approximately 17 m, in the y-direction, as compared with 27 m for the case of 40/70 mesh size (see Fig. 4-6c). The fluid pressure is weakly coupled with the proppant concentration via fluid properties like fluid viscosity and fluid density, so at higher concentration values the fluid viscosity is higher (equation (3.103) and a fluid with higher viscosity needs more energy to be transported leading to higher pressure values. In later time steps, although the proppant front is transported to longer distances (Figs. 4-7c, 4-8c and 4-9c), the zones of high proppant concentration are also transported to similar distances explaining the similitude in the pressure curves.

a)

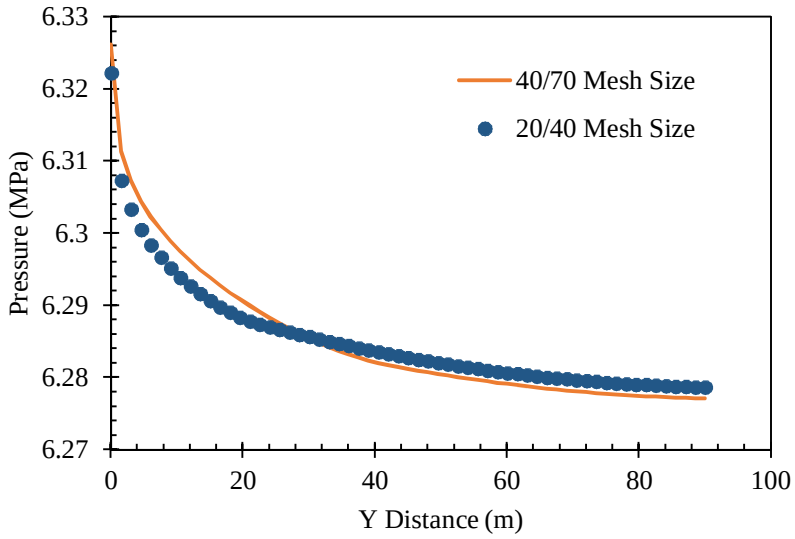

b)

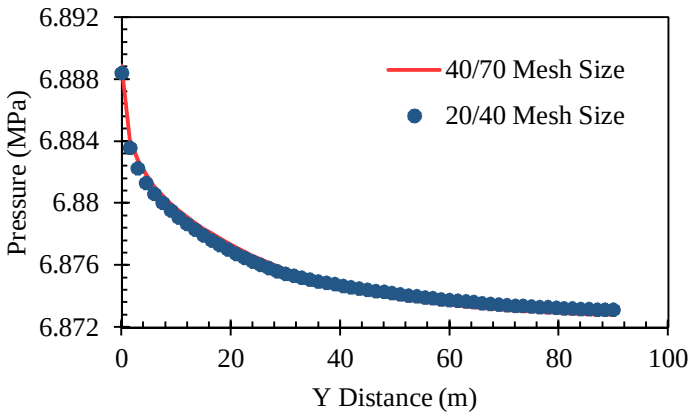

c)

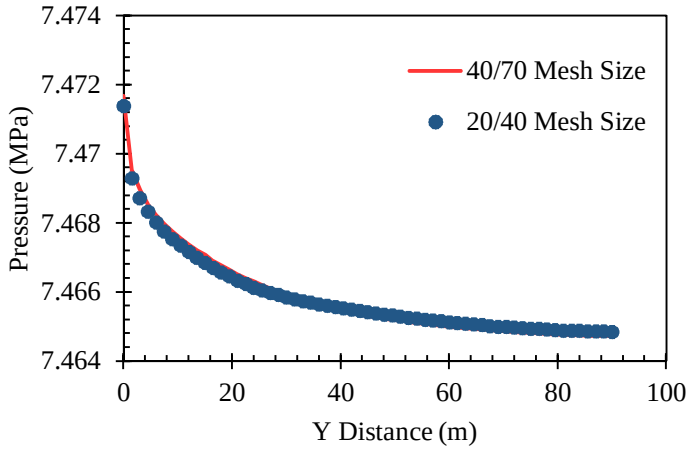

d)

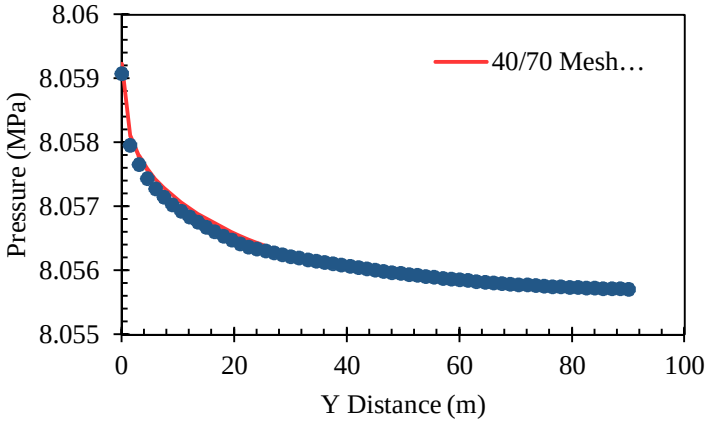

Figure 4-11. Comparison of pressure distribution in the fracture at z = 0 for two different diameters of proppant a) t = 545 s, b) t = 795 s, c) t = 1045 s, d) t = 1295 s.

Fig. 4-12 shows the fracture aperture profile, traced at $z = 0$, at four time steps, comparing two cases of 20/40 mesh size and 40/70 mesh size. In all the time steps, the difference in the width profiles between the cases is negligible. This can be explained if we analyze the difference between the pressure profiles. Take for example the pressure curves in Fig. 4-11a, the maximum difference in values in this comparison is only 0.25%, as the difference in pressure is not substantial, so similar values of fracture width are expected.

a)

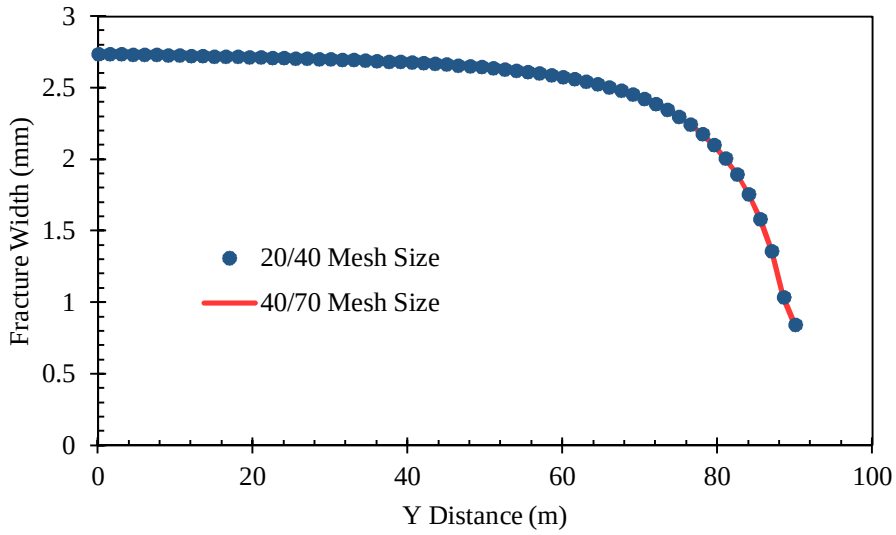

b)

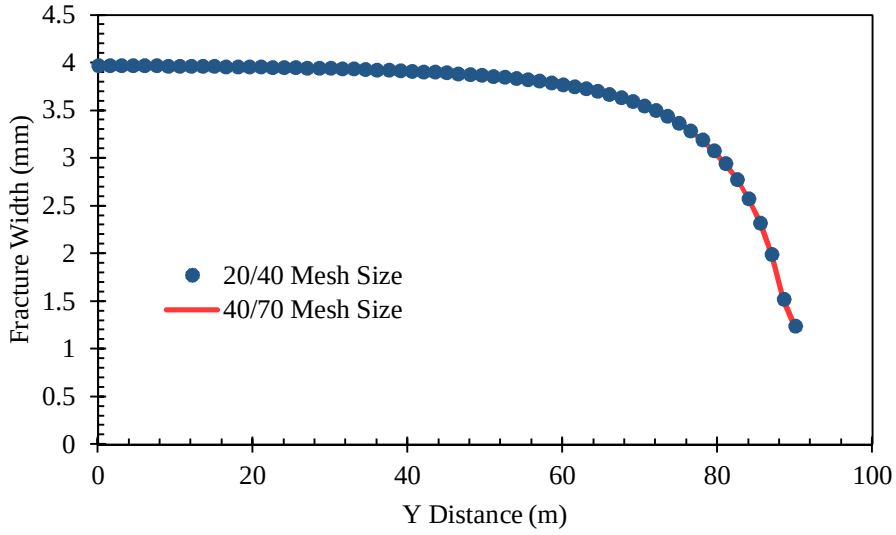

c)

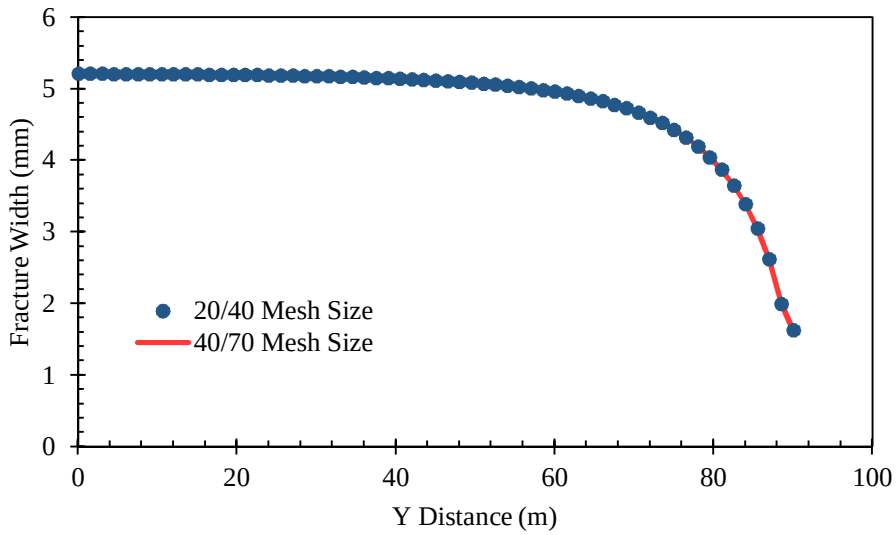

d)

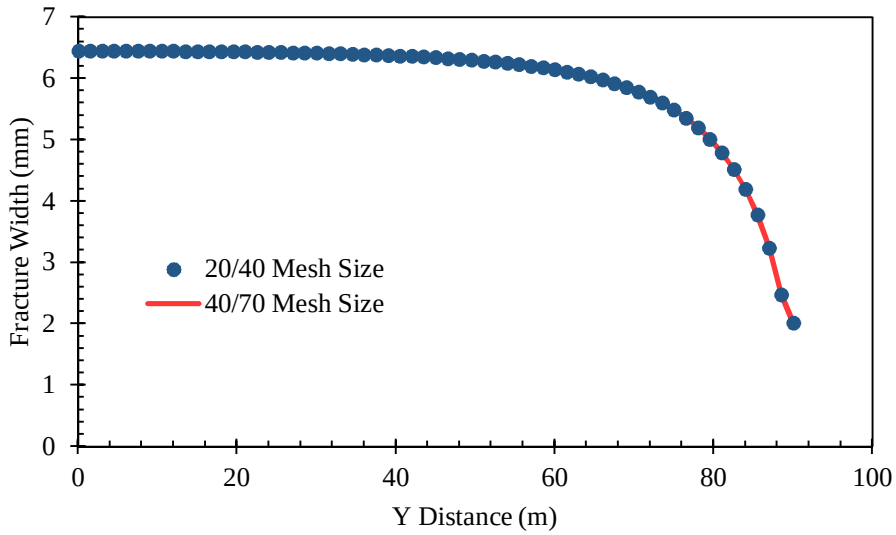

Figure 4-12. Comparison of fracture width distribution at z = 0 for two different diameters of proppant. a) t = 545 s, b) t = 795 s, c) t = 1045 s, d) t = 1295 s.

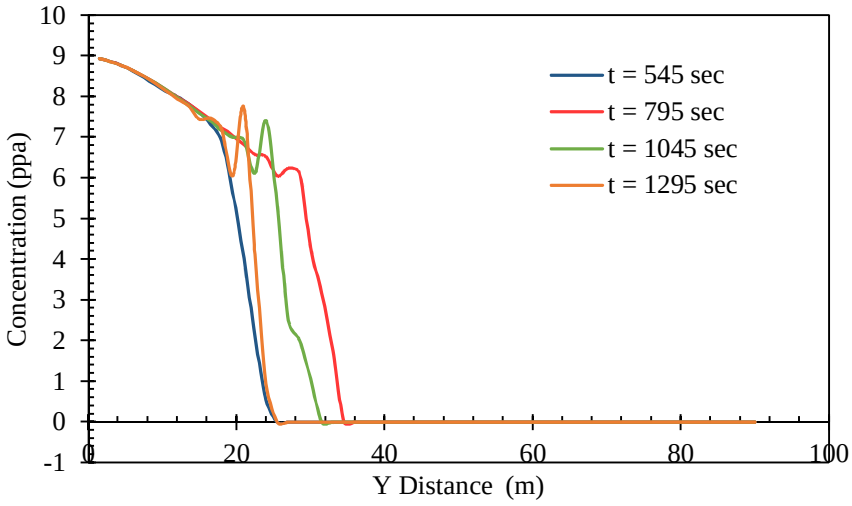

Figure 4-13. Comparison of the proppant concentration front at z=0 at various times when the proppant diameter is 600μ. At t=795 the velocity is higher than in later times, then the concentration front travels a longer distance. At t=1295 the fracture width increases and as a consequence the velocity reduces, the concentration front reaches a shorter distance however the area under the curve increases, indicating proppant accumulation.

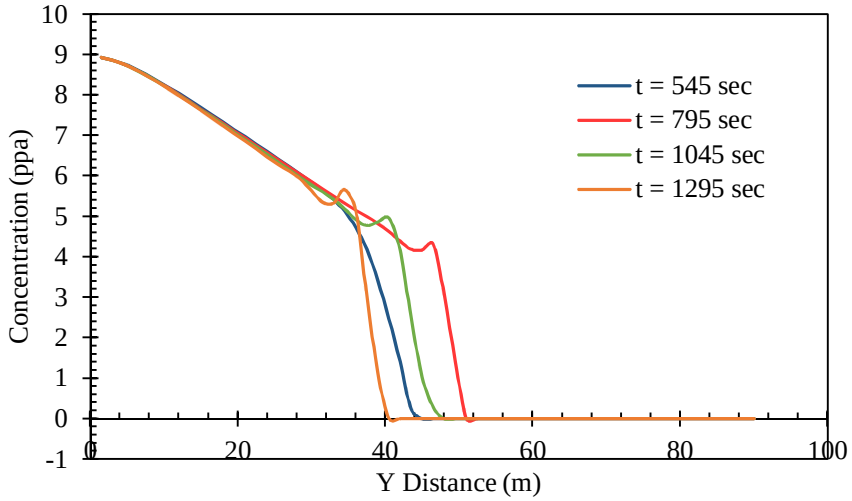

Figure 4-14. Comparison of the proppant concentration front at z=0 at various times when the proppant diameter is 300μ. At t=795 the velocity is higher than in later times, then the concentration front reaches a longer distance. At t=1295 the fracture width increases and as a consequence the velocity reduces, the concentration front reaches a shorter distance however the area under the curve increases, indicating proppant accumulation.

4.3.1. Effect of Fracturing Fluid Viscosity

To study the difference in behavior when the fracturing fluid viscosity is changed, the viscosity is varied from 1×10^{-3} Pa.s (1 cp) to 1×10^{-2} Pa.s (10 cp). Compared with Case 1 in section 4.3.1, the horizontal distance of the proppant front is greater as can be noted from the color plots from Figs. 4-15c, Fig. 4-16c, Fig. 4-17c, and Fig. 4-18c, respectively. In this case, the proppant front does not experience the same reduction in the proppant front distance as compared with the case of 1×10^{-3} Pa.s viscosity, as can be noted from Fig.4-19 and Fig. 4-20. The fluid pressure distribution in different times, show higher slope and consequently a higher proppant velocity compared with the case where the viscosity is 1×10^{-3} Pa.s (1 cp). The fracture aperture is not significantly affected with the change in proppant diameter as can be noted from Figs. 4-15b, Fig. 4-16b, Fig. 4-17b, and Fig. 4-18, respectively.

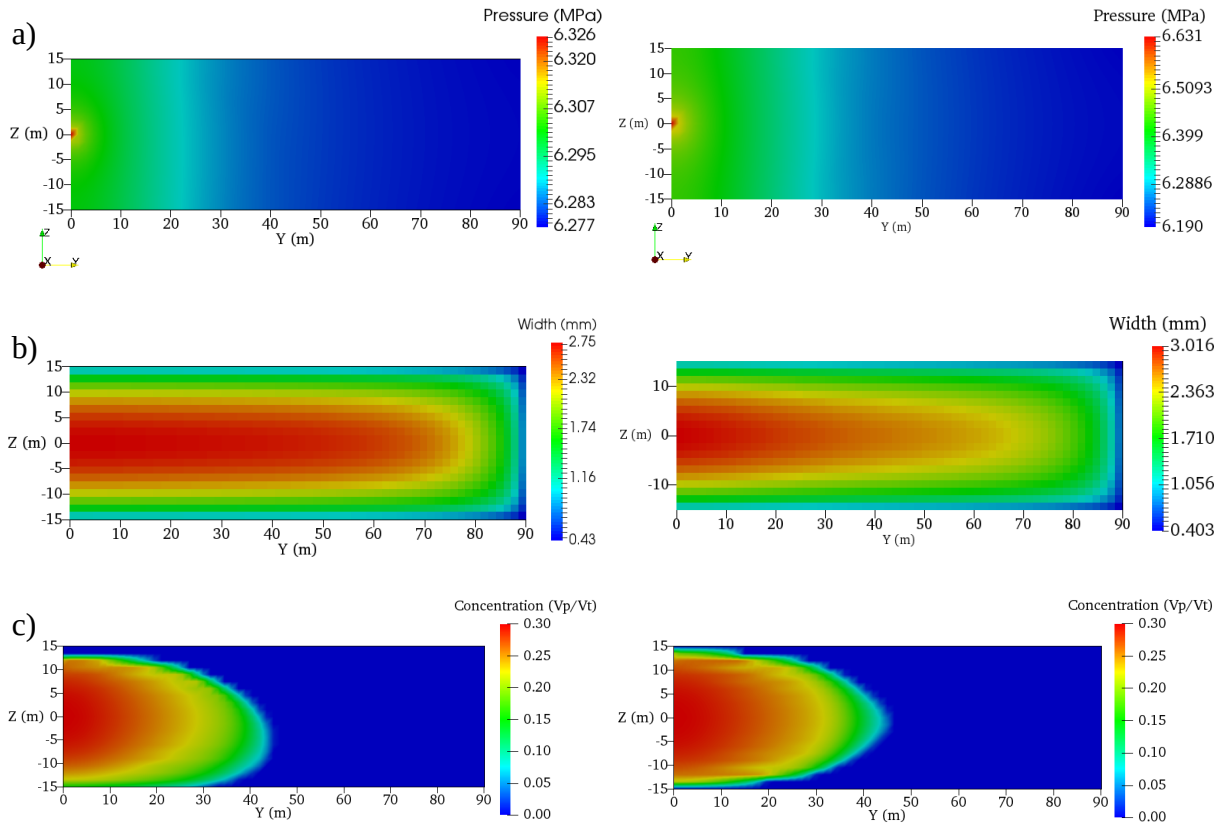

Figure 4-15. Comparison of simulation results at t = 545 sec, left column with a proppant size of 600 µm and right column with a proppant size of 300 µm, only half fracture is being shown. The source point is located at y = 0, z = 0 a) pressure distribution in the fracture, b) width distribution in the fracture c) concentration distribution.

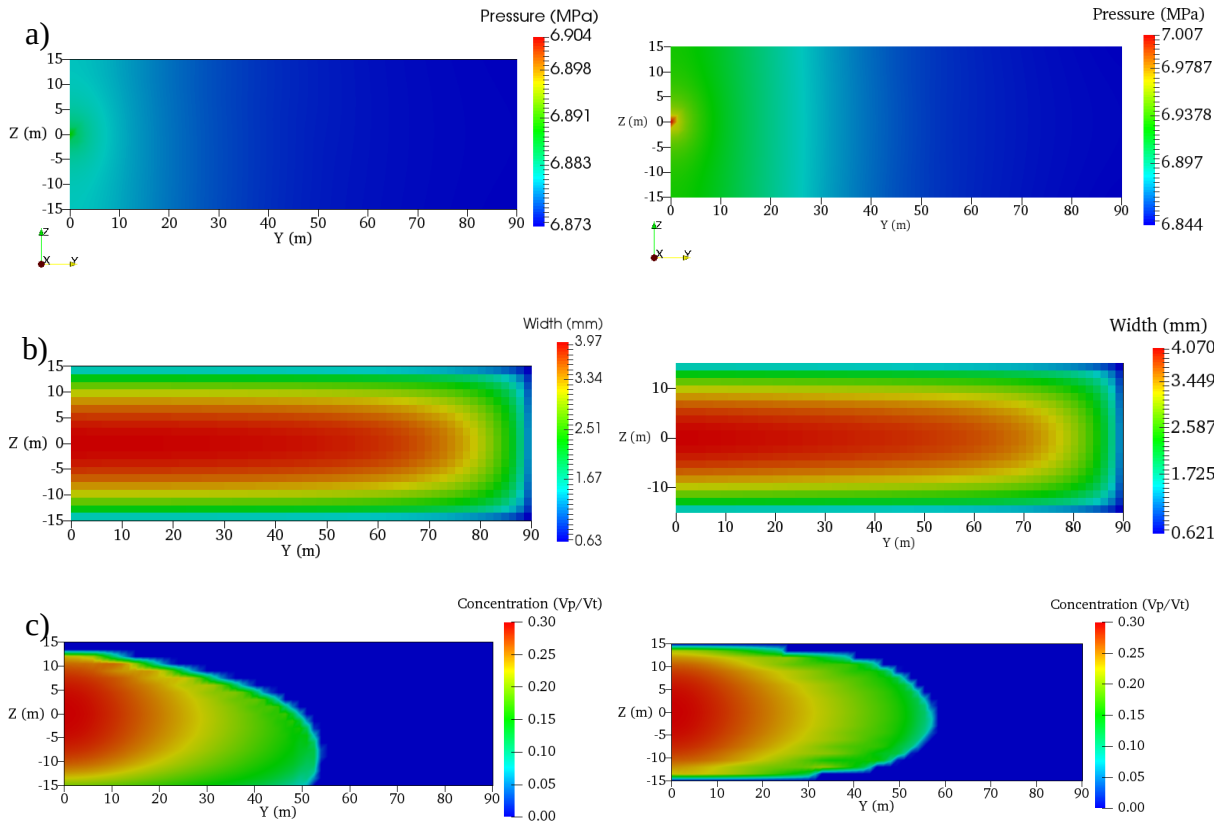

Figure 4-16. Comparison of simulation results at t = 795 sec, left column with a proppant size of 600 µm and right column with a proppant size of 300 µm, only half fracture is being shown. The source point is located at y = 0, z = 0 a) pressure distribution in the fracture, b) width distribution in the fracture c) concentration distribution.

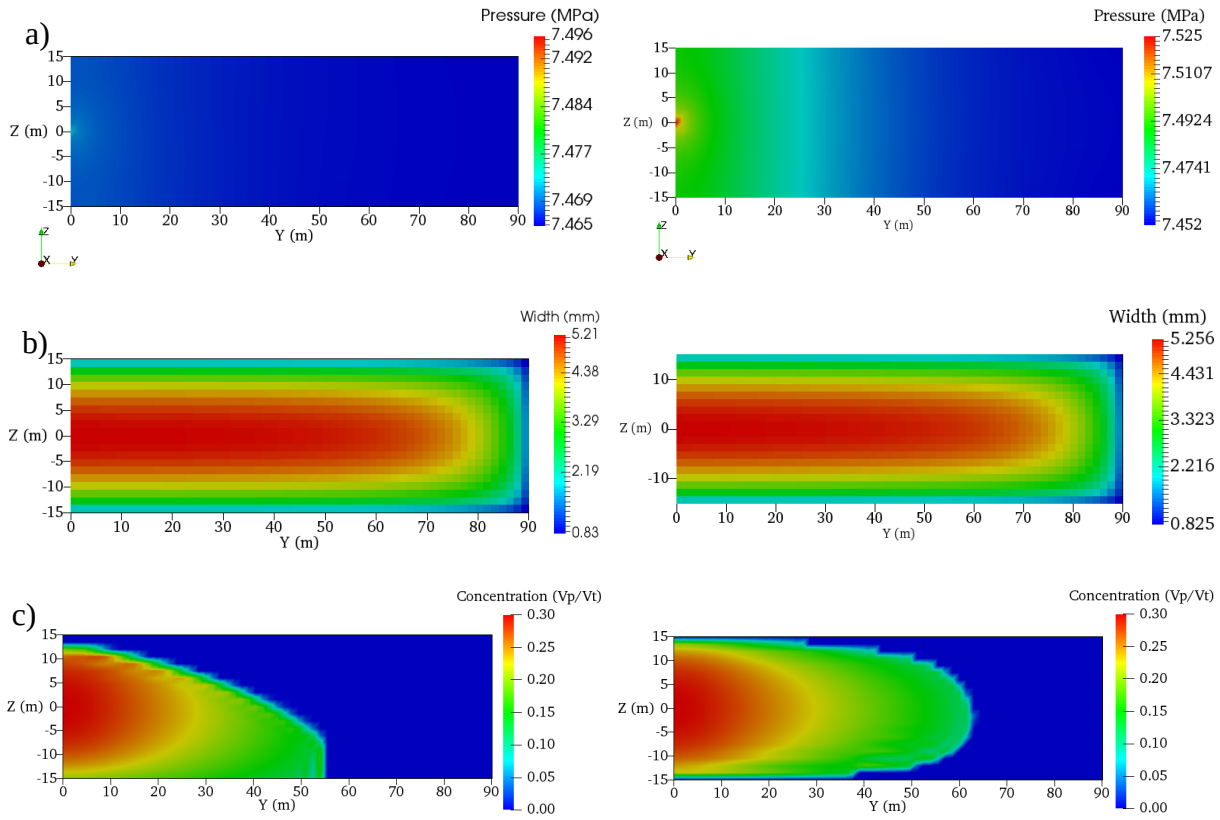

Figure 4-17. Comparison of simulation results at t = 1045 sec, left column with a proppant size of 600 µm and right column with a proppant size of 300 µm, only half fracture is being shown. The source point is located at y = 0, z = 0 a) pressure distribution in the fracture, b) width distribution in the fracture c) concentration distribution.

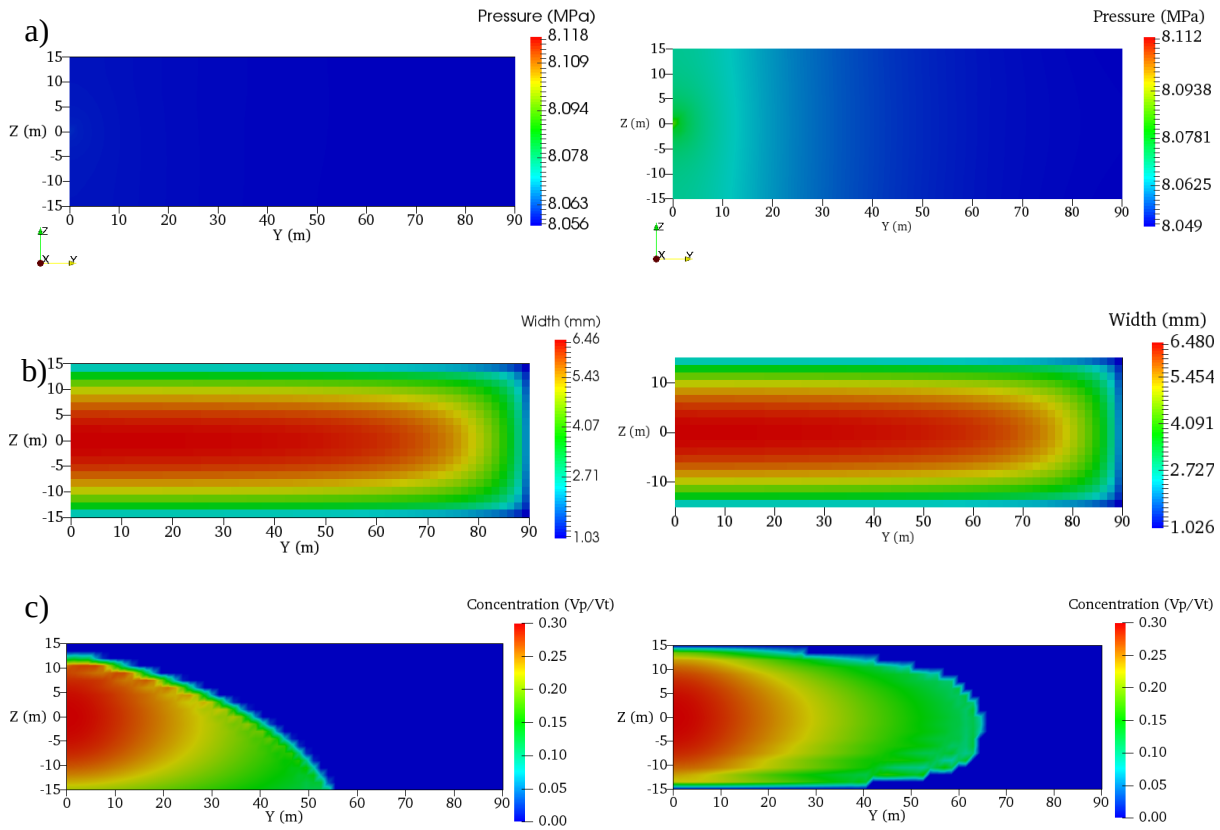

Figure 4-18. Comparison of simulation results at t = 1295 sec, left column with a proppant size of 600 µm and right column with a proppant size of 300 µm, only half fracture is being shown. The source point is located at y = 0, z = 0 a) pressure distribution in the fracture, b) width distribution in the fracture c) concentration distribution.

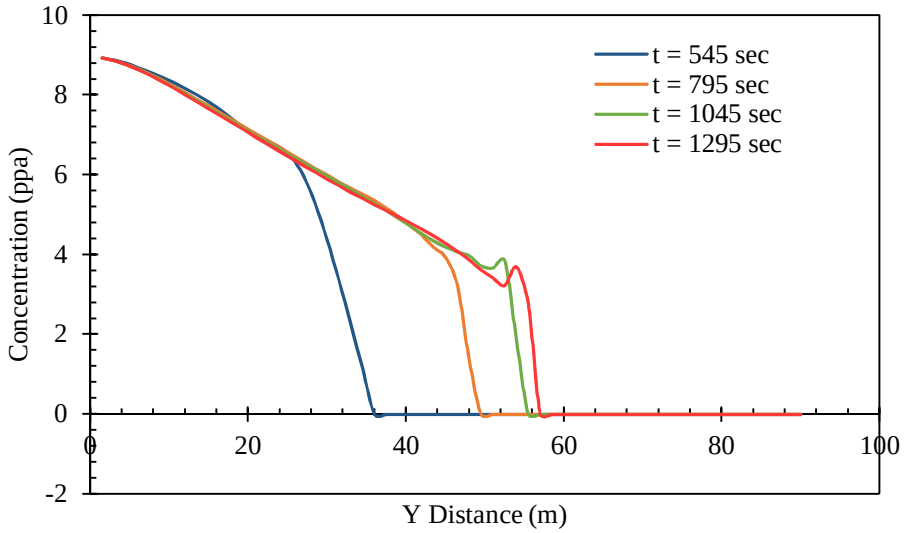

Figure 4-19. Comparison of the proppant concentration front at z=0 at various times when the fracturing fluid viscosity is $\mu = 1 \times 10^{-3}$.

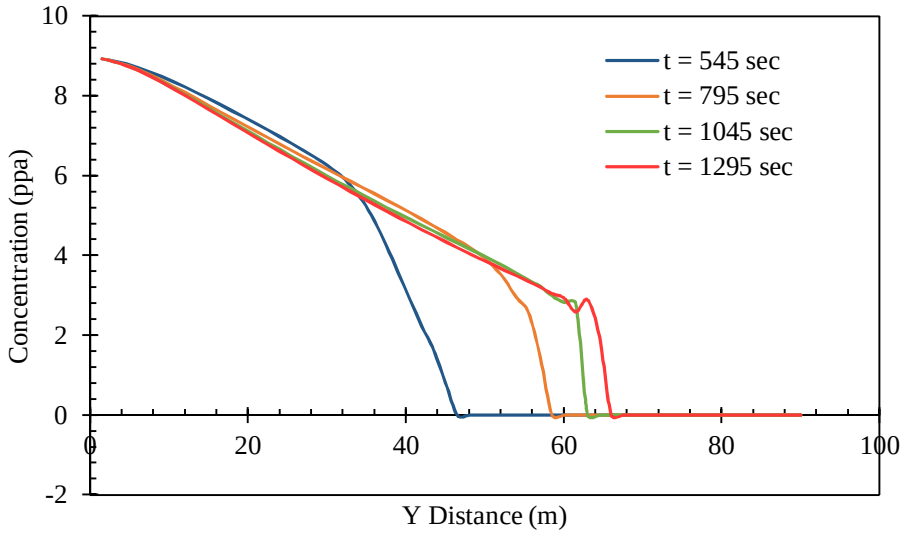

Figure 4-20. Comparison of the proppant concentration front at z=0 at various times when the fracturing fluid viscosity is $\mu = 1 \times 10^{-2}$.

4.3.1. Effect of Simulation Grid Size

To study the mesh dependency, the case of fluid viscosity = 1×10^{-3} Pa.s (1 cP) and proppant diameter = 300 μm was chosen, the meshes are defined as coarse, medium and fine as shown in Fig. 4-21. The fracture front was calculated at z = 0 and selected times, 545 s, 795 s, 1045 s, and 1295 s. From Figs. 4-22a, b, c, and d, respectively, it can be noted that the change in mesh size does not affect significantly the behavior of the solution.

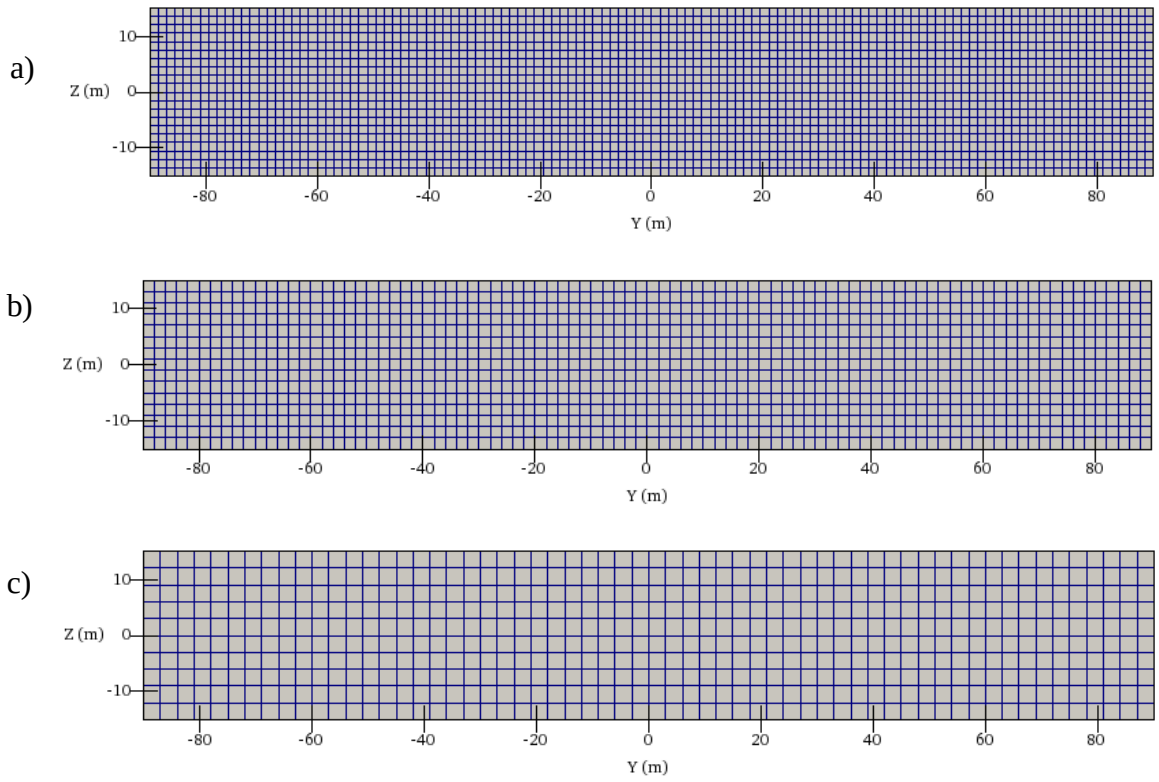

Figure 4-21. Different mesh sizes in the proppant distribution problem. a) fine mesh, the number of elements in y direction = 120 and z direction = 20. b) medium mesh, number of elements in y direction = 90 and z direction = 15 c) coarse mesh, the number of elements in y direction = 60 and z direction = 10.

a)

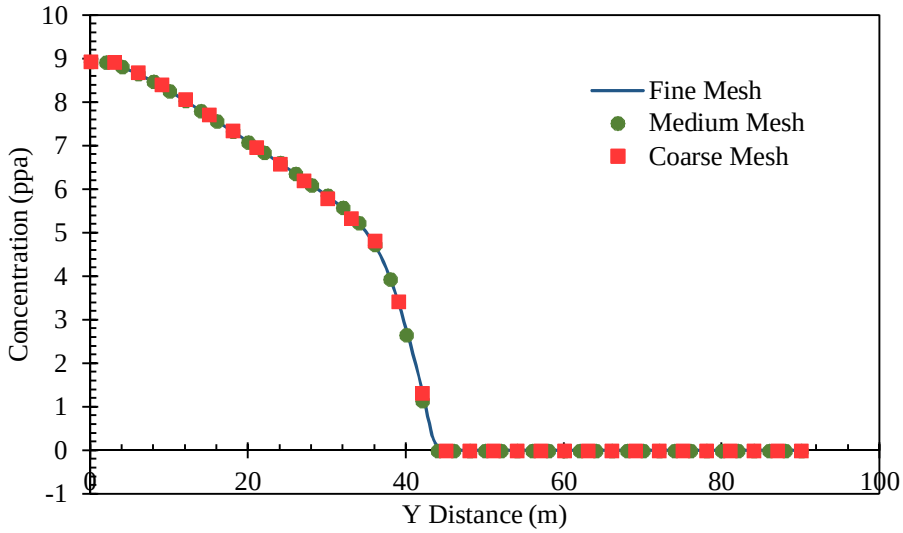
Concentration (ppa)
Y Distance (m)
Fine Mesh
Medium Mesh
Coarse Mesh
10
9
8
7
6
5
4
3
2
1
0
-1
0
20
40
60
80
100

b)

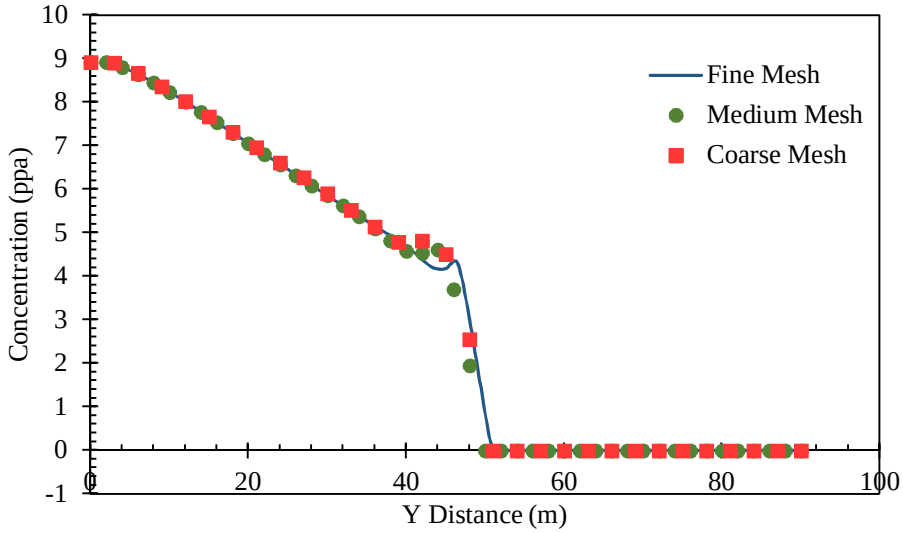
Concentration (ppa)
Y Distance (m)
Fine Mesh
Medium Mesh
Coarse Mesh
10
9
8
7
6
5
4
3
2
1
0
-1
0
20
40
60
80
100

c)

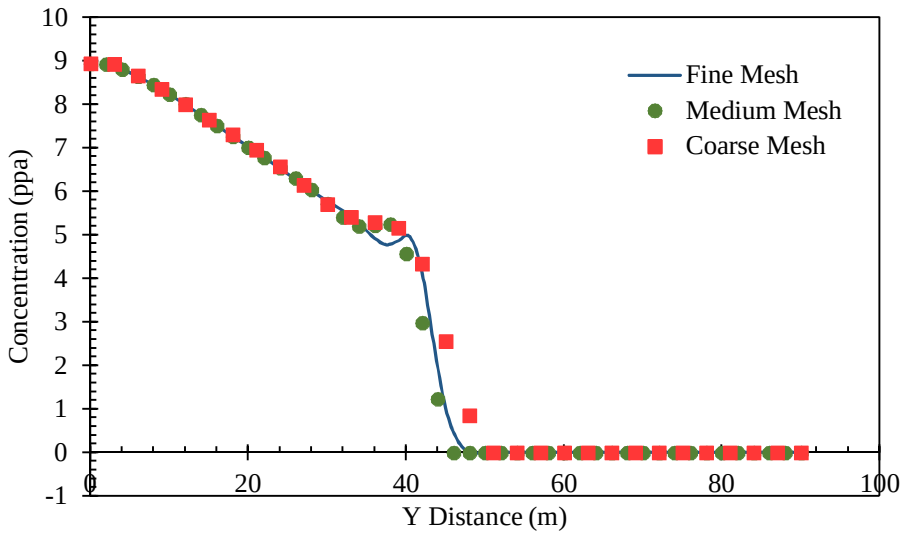

d)

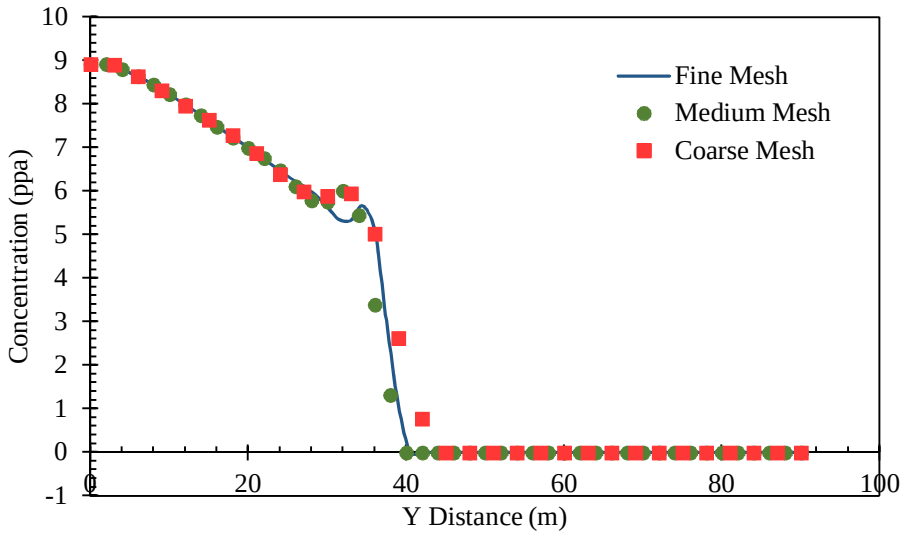

Figure 4-22. Proppant concentration distribution at z = 0 comparing different sizes of mesh. a) t = 545 s, b) t = 795 s, c) t = 1045 s, d) t = 1295 s

4.4. Proppant Concentration in Multiple Parallel Hydraulic Fractures

In this case, three parallel hydraulic fractures have extended from a horizontal well. Each fracture is assigned an injection point (Fig. 4-24). The fluid injection rate is distributed among the multiple fractures to account for the dynamic fluid flow partitioning as shown in Fig. 4-23. The boundaries of the fractures are assigned no flow conditions. The values of the parameter used in this simulation are listed in Table 4-3 and the total injection time is 110 s. The fluid pressure and aperture distributions are shown in Figures…The proppant fronts in the fractures are small and just begun to develop as shown in 4-36. Lower values of fracture aperture distribution can be observed in the central hydraulic fracture (HF2) as compared with the other outer fractures. This phenomenon is due to the fact that the development of the external hydraulic fractures will tend to restrict the opening of the inner fracture due to stress shadowing effect as shown in Fig. 4-25, Fig. 4-26, Fig 4-27 and 4-28, respectively. As the fracture aperture is restricted in the central hydraulic fracture, higher pressures are expected compared with the external hydraulic fractures as shown in the Fig. 4-29, Fig. 4-30, Fig. 4-31 and Fig. 4-32, respectively.

Table 4-3. Data considered to perform the proppant transport simulations.

Property	**Value**	**Unit**
Fluid injection rate (Q)	0.15	m^3/sec
Poisson's ratio (v)	0.29	
Fluid density (ρ_f)	1000	Kg/m^3
Fluid viscosity (μ_f)	0.1	N.s/m^2
Proppant density (ρ_p)	2400	Kg/m^3
Proppant injection volume fraction	0.2	
Carter's leak-off coefficient	1.50E-07	m/$s^{0.5}$
Vertical stress (σ_v)	48	MPa
Minimum horizontal stress (σ_h)	38	MPa
Maximum horizontal stress (σ_H)	39.5	MPa

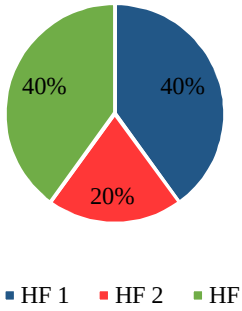

Figure 4-23. Proportions of injection rate assigned to each hydraulic fracture.

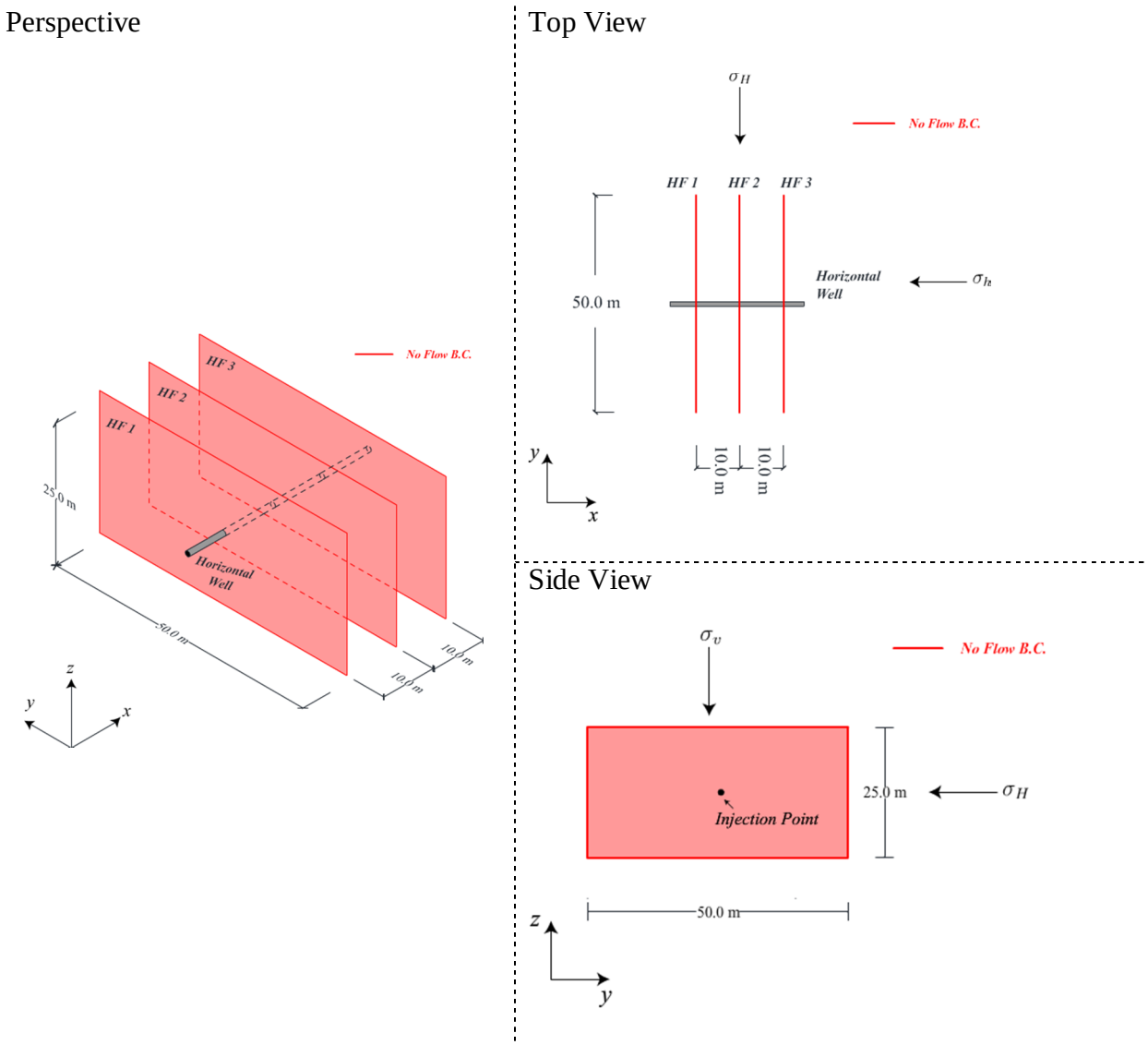

Figure 4-24. Geometry and boundary conditions for the multiple hydraulic fractures network.

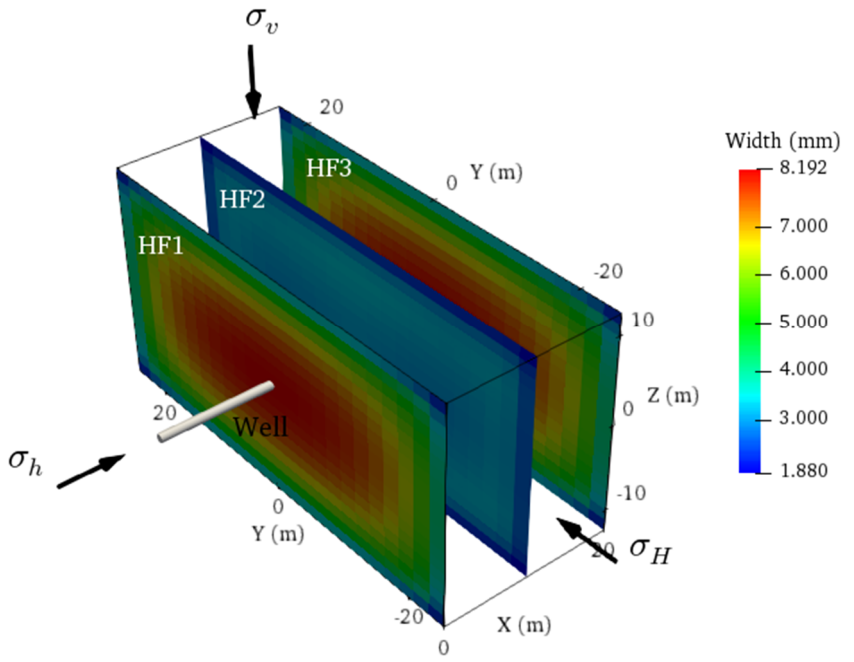

Figure 4-25. Fracture aperture distribution (perspective view) after an injection time of 110 s.

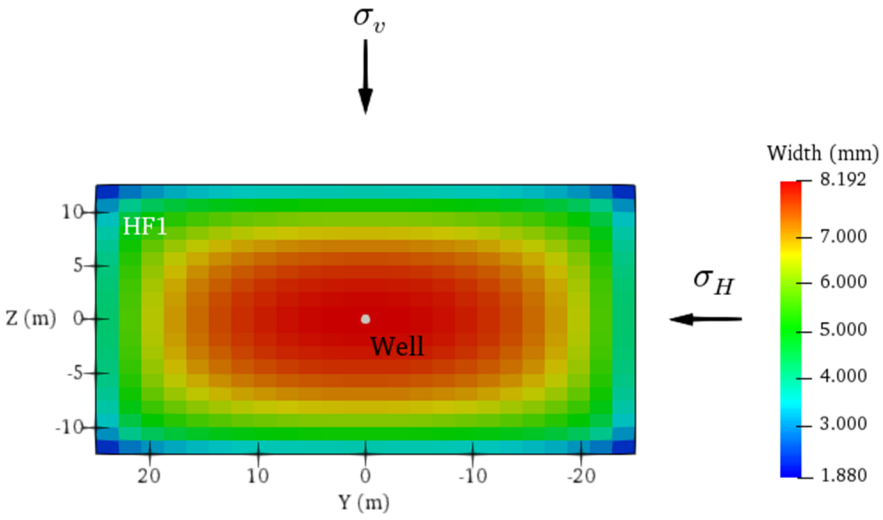

Figure 4-26. Fracture aperture distribution in the first hydraulic fracture after an injection time of 110 s.

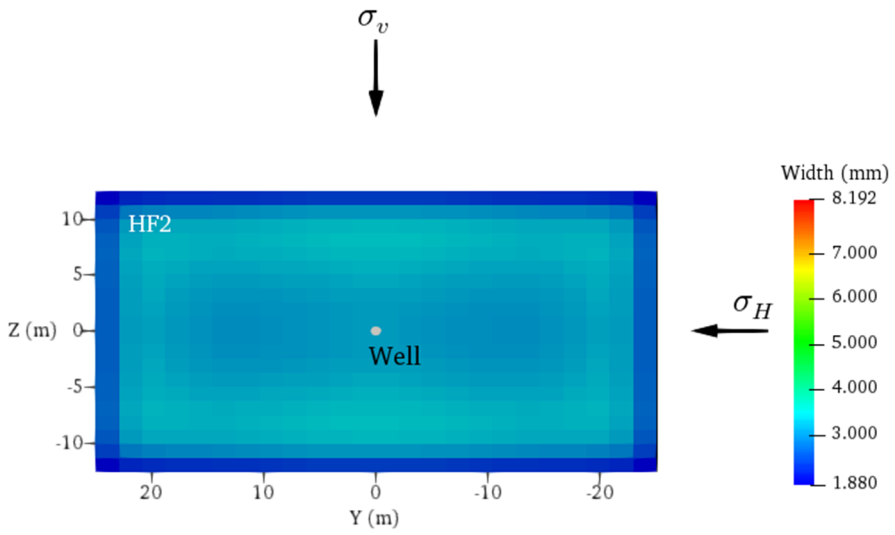

Figure 4-27. Fracture aperture distribution in the second hydraulic fracture after an injection time of 110 s.

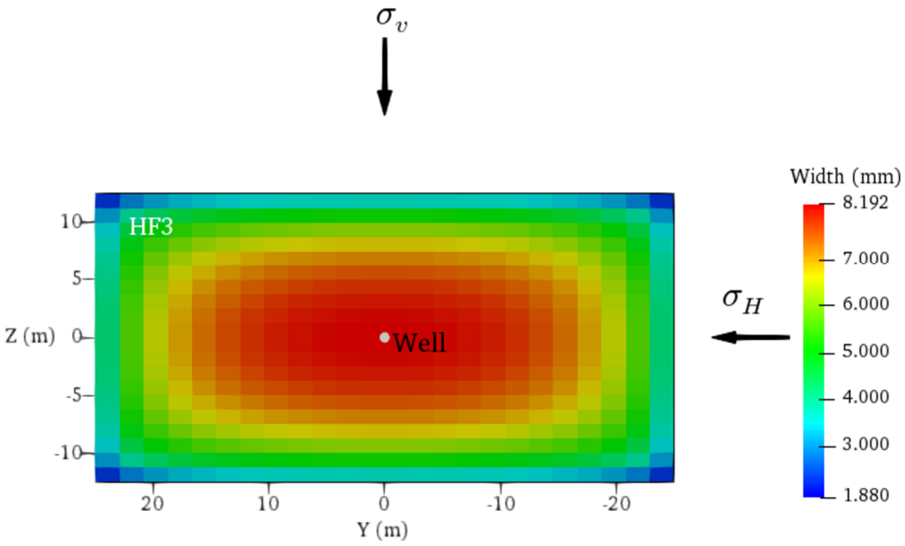

Figure 4-28. Fracture aperture distribution in the third hydraulic fracture after an injection time of 110 s.

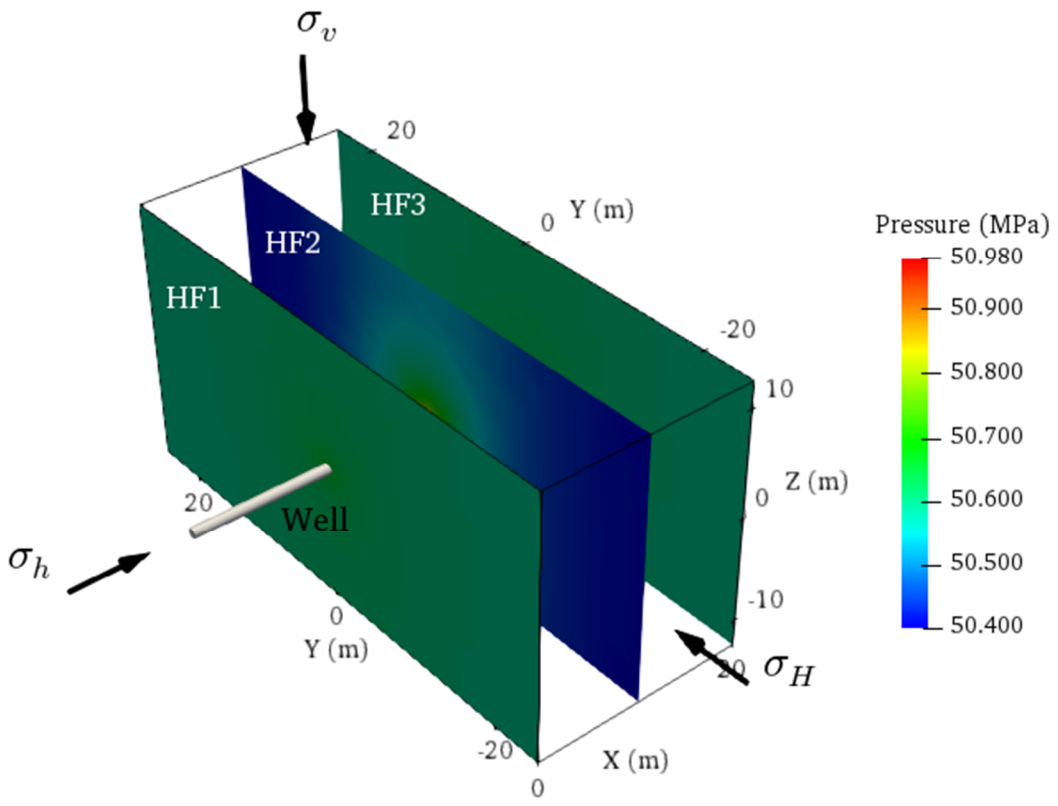

Figure 4-29. Pressure distribution (perspective view) after an injection time of 110 s.

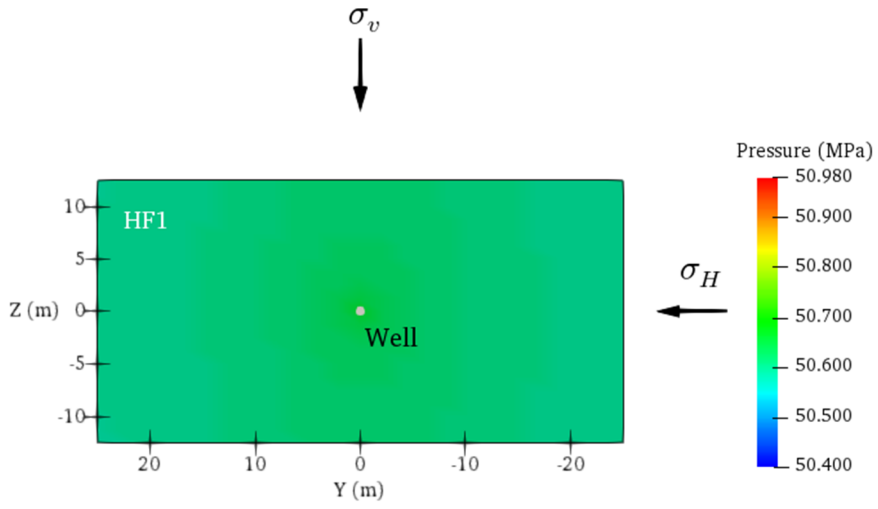

Figure 4-30. Pressure distribution in the first hydraulic fracture after an injection time of 110 s.

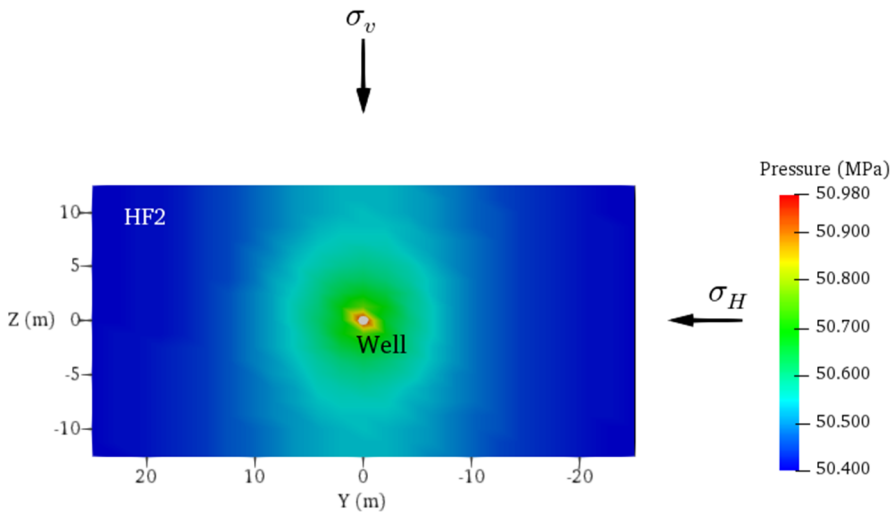

Figure 4-31. Pressure distribution in the second hydraulic fracture after an injection time of 110 s.

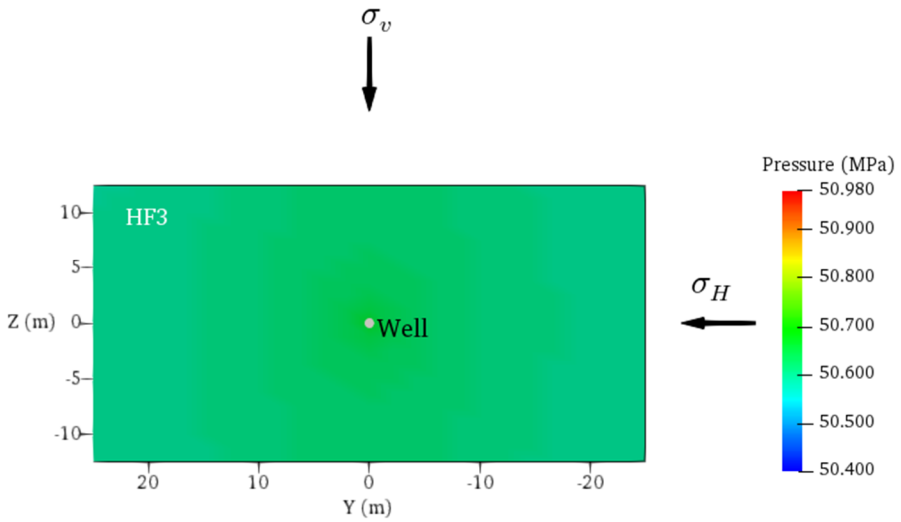

Figure 4-32. Pressure distribution in the in the third hydraulic fracture after an injection time of 110 s.

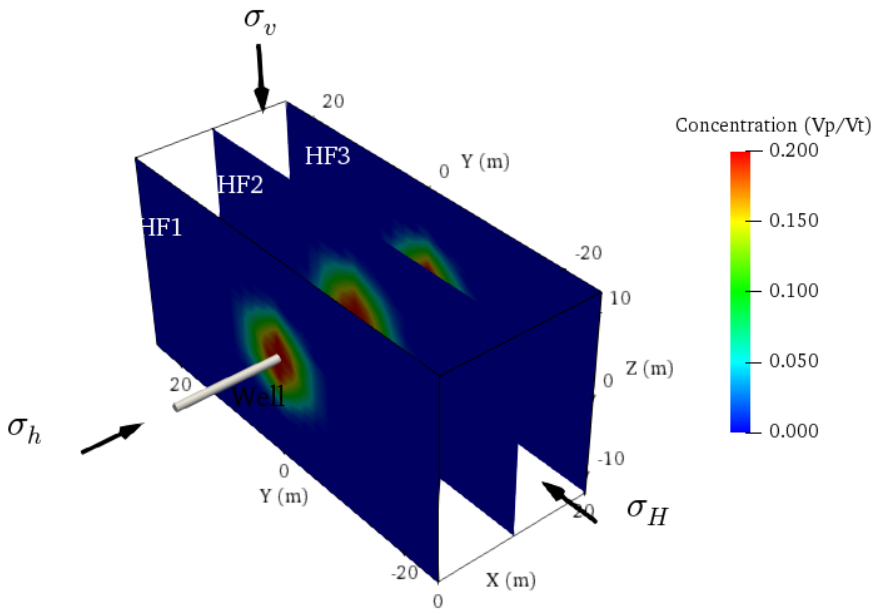

Figure 4-33. Proppant concentration distribution (perspective view) after an injection time of 110 s.

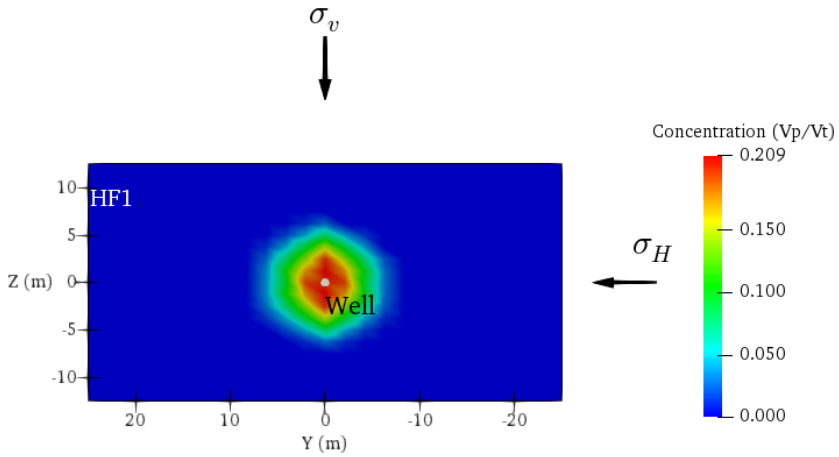

Figure 4-34. Proppant concentration distribution in the first hydraulic fracture after an injection time of 110 s.

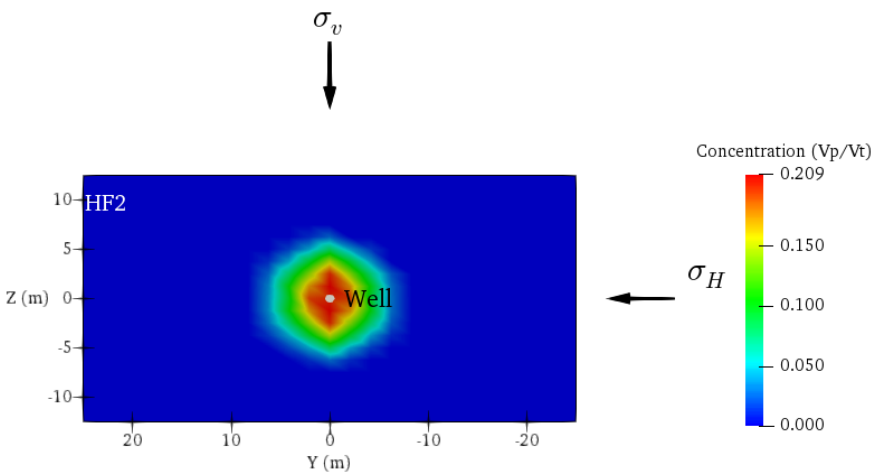

Figure 4-35. Proppant concentration distribution in the second hydraulic fracture after an injection time of 110 s.

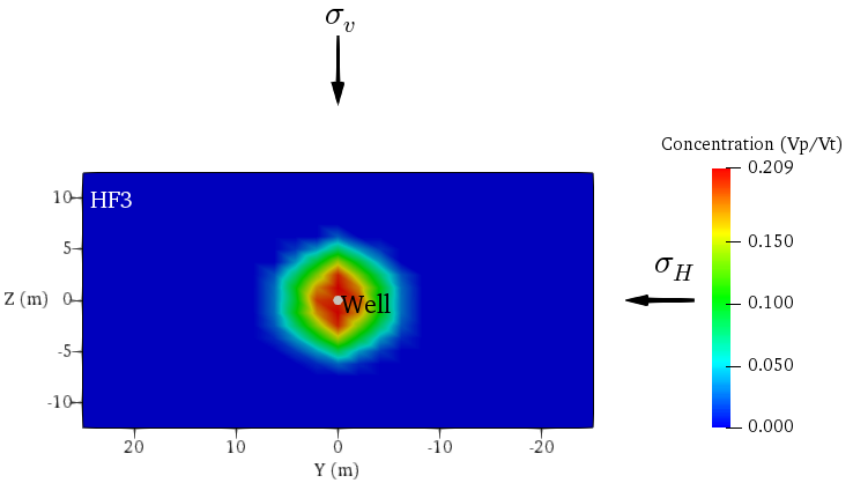

Figure 4-36. Proppant concentration distribution in the third hydraulic fracture after an injection time of 110 s.

Chapter 5. Proppant Flow and Transport Modeling in Hydraulic and Natural Fracture Networks

This chapter presents a detailed numerical study of the proppant flow and transport inside fracture networks formed by the intersection of hydraulic and natural fractures. In these cases, the deformation of the rock matrix is fully coupled with the fluid flow in the fracture, and the resultant fracture width and fluid pressure are subsequently used as input for the proppant concentration calculations. For the single fracture case, only the normal DD component, $D_{\bar{z}}$, was considered. However, for cases of multiple fractures, and hydraulic and natural fractures networks, the shear components of the DD (i.e., in-plane shear DD and out-of-plane shear DD) are also required. Hence, for all the simulations in this chapter a coupled 3D model "GeoFrac3D" was used. The mathematical details and numerical implementation procedure of the "GeoFrac3D" can be found elsewhere(Kumar & Ghassemi, 2015, 2016; Safari, 2013). Numerical examples of the proppant flow and transport in multiple fractures, and in fracture networks, where hydraulic and natural fractures interact, are discussed in the following sections. In this study it was assumed that there were pre-existing fracture networks, an study that considers the propagation of the hydraulic fractures can be found in (Kumar, D., Gonzalez, R.A., and Ghassemi, 2018)

5.1. Proppant Concentration Distribution in a Hydraulic Fracture and a Natural Fracture Intersection

In this section, numerical examples of the proppant flow and transport in the fracture networks including intersection of a hydraulic and natural fracture are presented. A 3D schematic of a

hydraulic fracture and natural fracture intersection is shown in Fig. 5-1. The model input parameters are listed in Table 5-1.

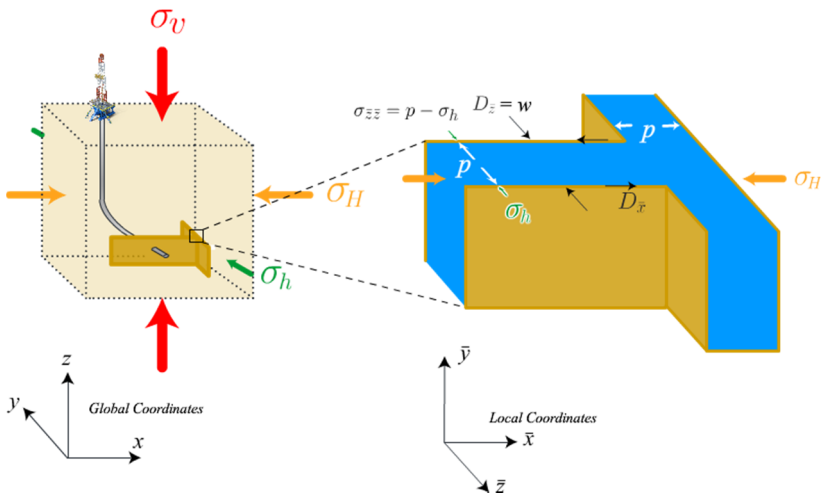

Figure 5-1. Proppant concentration distribution (perspective view) for the case 1 after an injection time of 125 s.

Table 5-1. Data considered to perform the proppant transport simulations

Property	**Value**	**Unit**
Fluid injection rate (Q)	0.05	m^3/sec
Poisson's ratio (v)	0.29	
Young's modulus (E)	27.1	GPa
Fluid density (ρ_l)	1000	Kg/m^3
Fluid viscosity (μ)	0.1	$N.s/m^2$
Proppant density (ρ_p)	2400	Kg/m^3
Proppant injection volume fraction (V_p/V)	0.2	
Carter's leak-off coefficient	1.50E-07	$m/s^{0.5}$
Vertical Stress (σ_v)	48.0	MPa
Minimum horizontal stress (σ_h)	38.0	MPa
Maximum horizontal stress (σ_H)	39.5	MPa

5.1.1. Case 1. Orthogonal Intersection of Hydraulic Fracture and Natural Fracture with no Flow Boundaries

In this case a preexisting static fracture network was assumed, the system is initially set to a fracture aperture value of 1e-5 m representing hydraulic aperture, then injection of clean fluid is simulated until the fracture aperture in the hydraulic fracture is enough to ensure proppant transport (greater than 3 times the proppant diameter). The network is composed of one hydraulic fracture that has intersected one natural fracture in a perpendicular manner, forming a T-shaped network, and the wellbore is located at the center of the hydraulic fracture as shown in Fig. 5-2. The values of the parameter used in this simulation are listed in Table 5-1 and the total injection time is 125 s. The proppant front is fully developed in the hydraulic fracture as shown in Fig. 5-9. Inside the natural fracture the proppant is poorly transported, this can be explained if we consider two factors: (a) the exposure of the natural fracture to a higher stress σ_H resulting in lower values of fracture aperture compared with the hydraulic fracture as shown in Fig. 5-4 and 5-5; and (b) the use of no flow boundaries (closed system). The latter means that the flow in the natural fracture reaches steady state faster, resulting in small differential pressure as shown in Fig.5-8 with small values of fluid velocity. In all figures, the white dashed lines show the intersection of the hydraulic and the natural fracture.

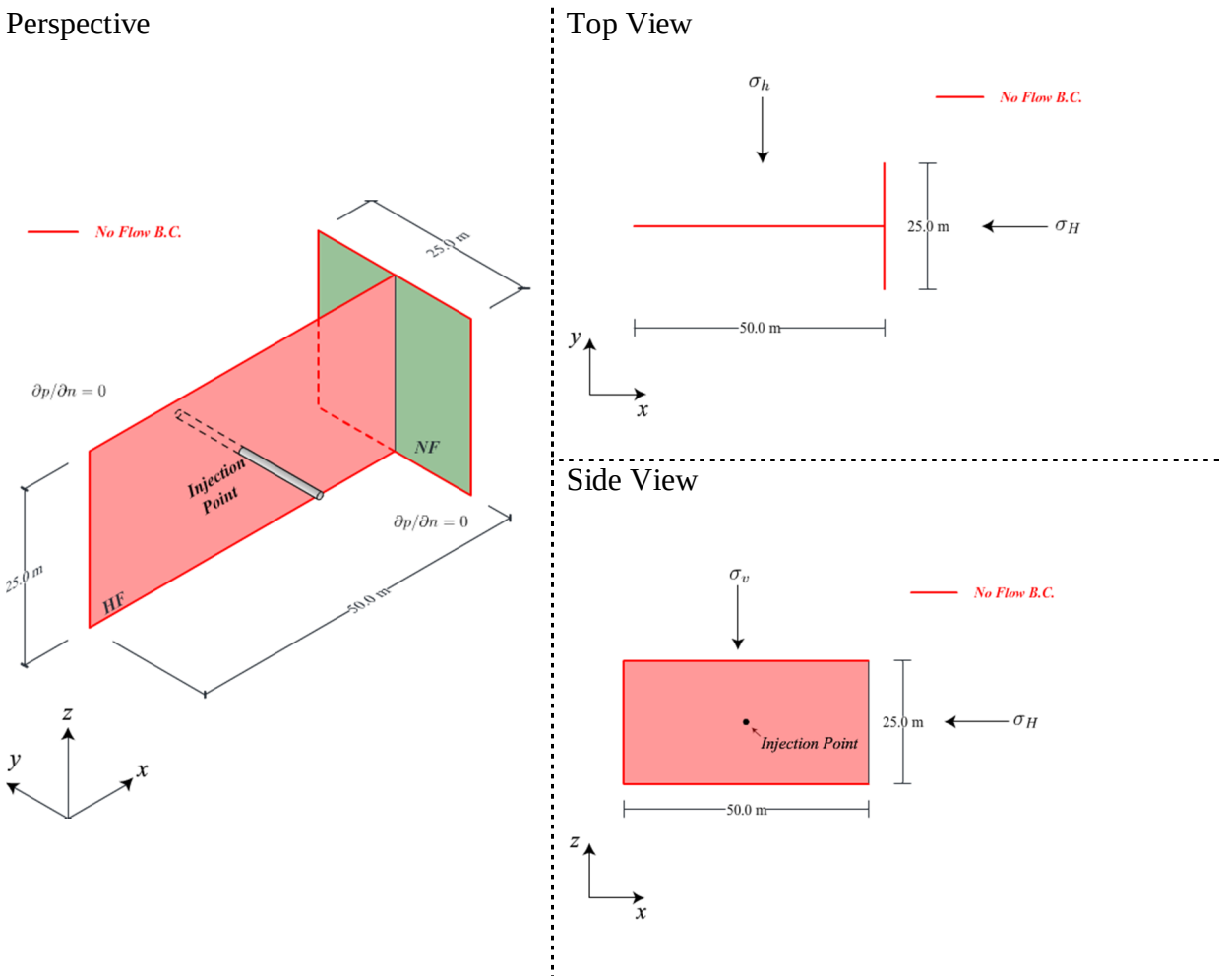

Figure 5-2. Geometry and boundary conditions of a T-shaped fracture network.

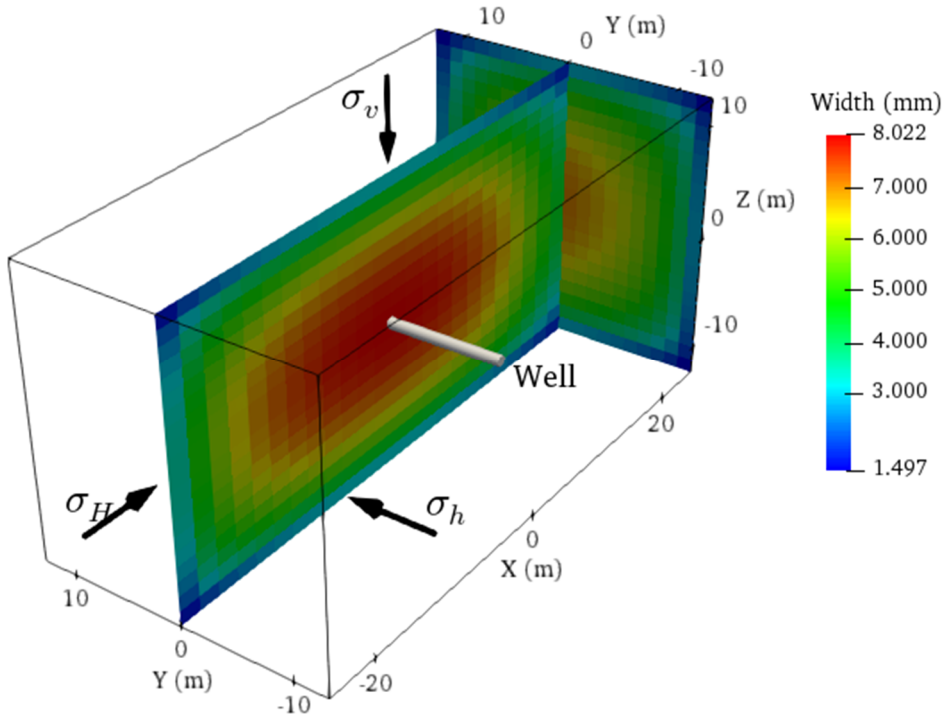

Figure 5-3. Fracture aperture distribution (perspective view) for the case 1 after an injection time of 125 s.

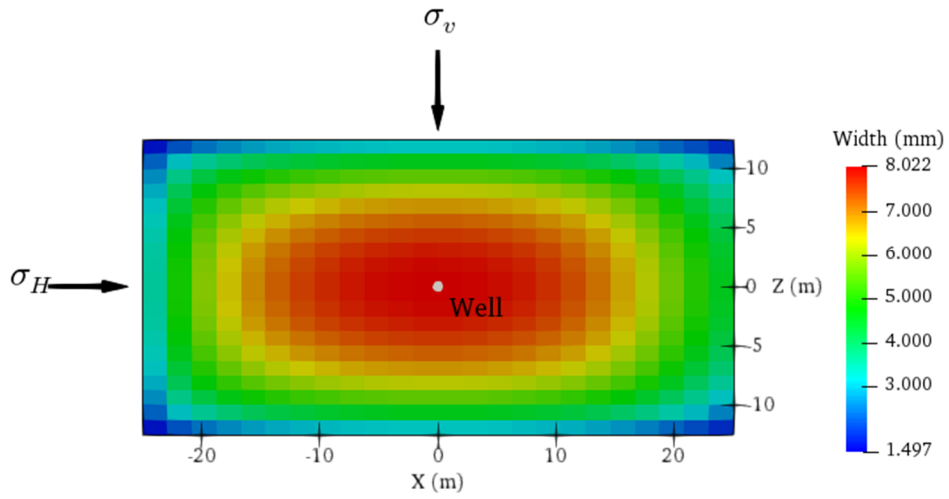

Figure 5-4. Fracture aperture distribution in the hydraulic fracture for the case 1 after an injection time of 125 s.

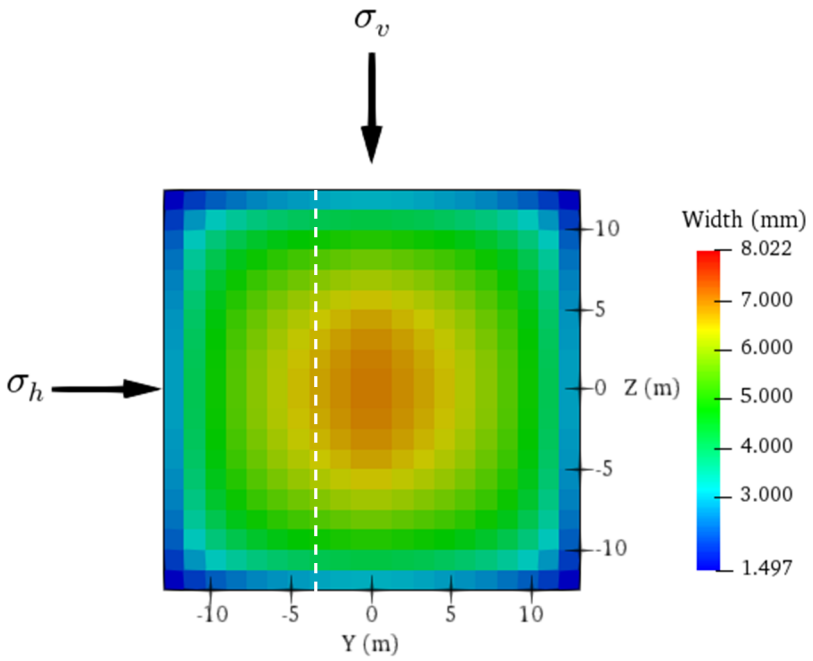

Figure 5-5. Fracture aperture distribution in the natural fracture for the case 1 after an injection time of 125 s. Dotted white line shows intersection of the hydraulic and natural fracture.

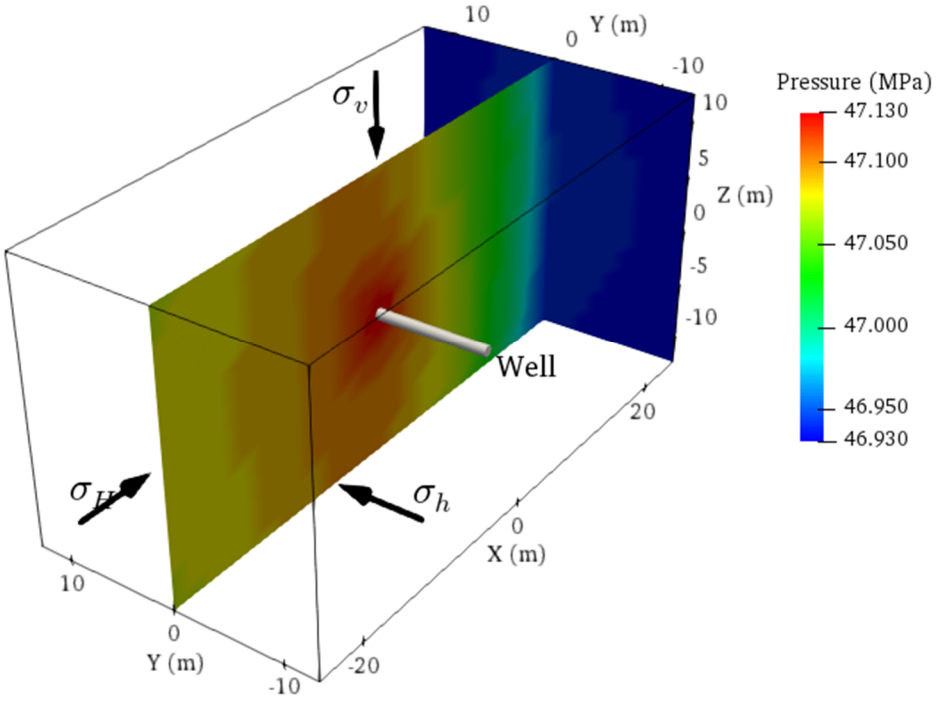

Figure 5-6. Pressure distribution (perspective view) for the case 1 after an injection time of 125 s.

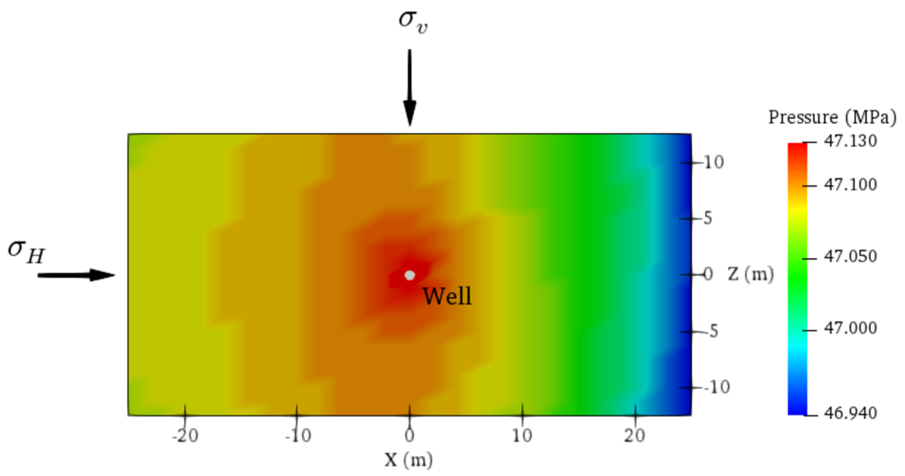

Figure 5-7. Pressure distribution in the hydraulic fracture for the case 1 after an injection time of 125 s.

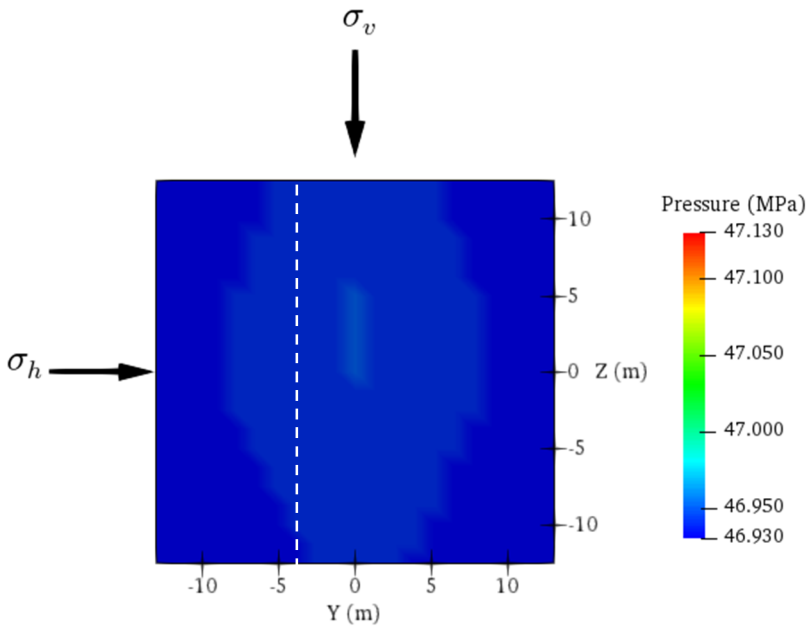

Figure 5-8. Pressure distribution in the natural fracture for the case 1 after an injection time of 125 s. Dotted white line shows intersection of the hydraulic and natural fracture.

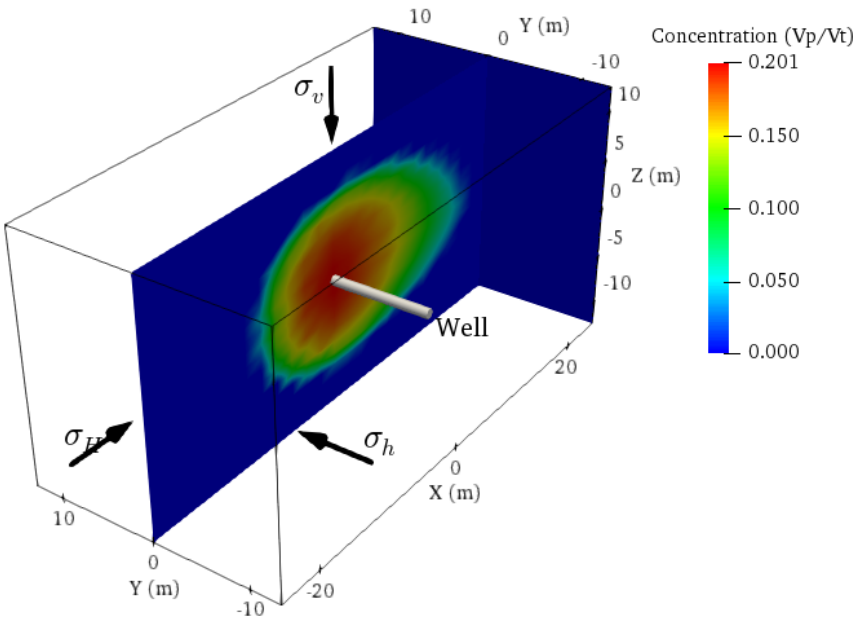

Figure 5-9. Proppant concentration distribution (perspective view) for the case 1 after an injection time of 125 s.

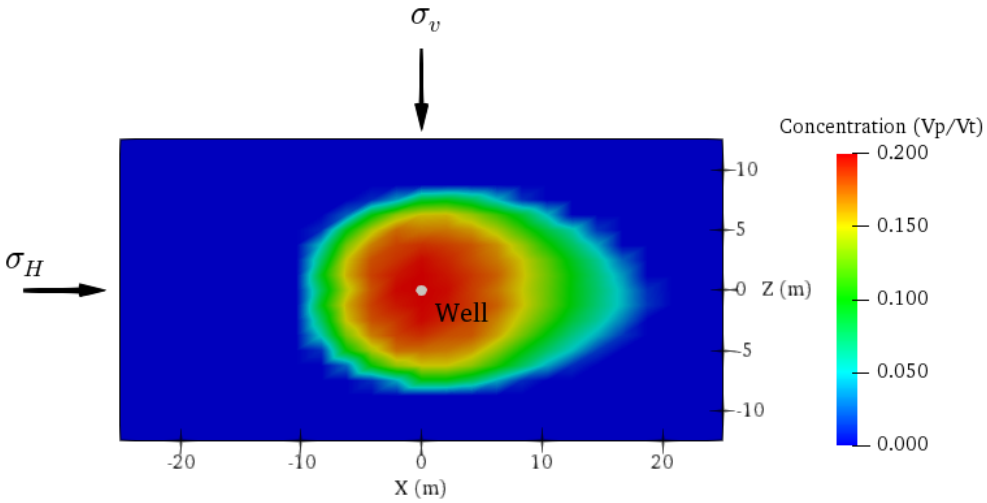

Figure 5-10. Proppant concentration distribution in the hydraulic fracture for the case 1 after an injection time of 125 s.

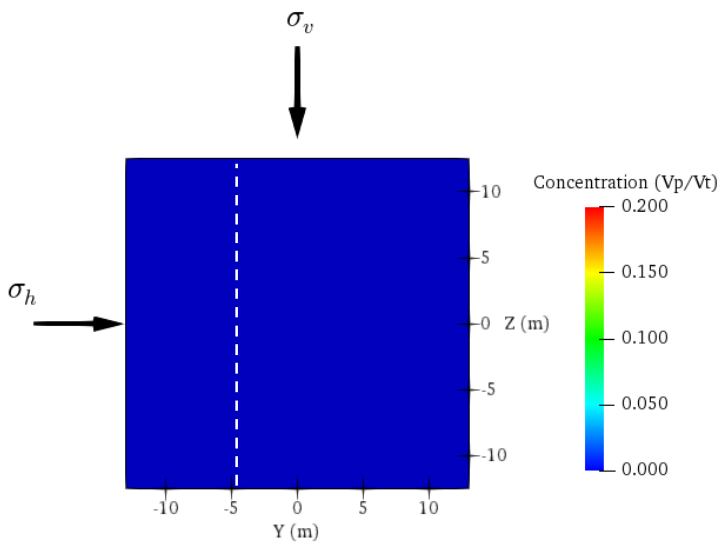

Figure 5-11. Proppant concentration distribution in the natural fracture for the case 1 after an injection time of 125 s. Dotted white line shows intersection of the hydraulic and natural fracture.

5.1.2. Case 2. Orthogonal Intersection of Hydraulic and Natural Fracture with Wellbore close to the Natural Fracture and no Flow Boundary condition

In Case 2 a preexisting static fracture network was assumed, the system is initially set to a fracture aperture value of 1e-5 m representing hydraulic aperture, then injection of clean fluid is simulated until the fracture aperture in the hydraulic fracture is enough to ensure proppant transport (greater than 3 times the proppant diameter). The network is composed of one hydraulic fracture that has intersected one natural fracture in a perpendicular manner, forming a T-shaped network. One possible argument of the small amount of proppant transported into the natural fracture in the Case 1 is that the distance between the injection point and the interception with the natural fracture is too large, then the injection point is moved closer to the natural fracture to study this condition. The geometry is identical to the Case 1 except the distance of the injection point to the natural fracture, which is 10 m instead of 25 m, as shown in Fig. 5-12. The values of the parameters used in this simulation are listed in Table 5-1 and the total injection time is 125 s. Again, the proppant front is developed in the hydraulic fracture as shown in Fig. 5-20 but inside the natural fracture the proppant is poorly transported again as shown in Fig. 5-21. This can be explained if we consider that the system is closed, i.e., no flow boundaries are used so that the fluid flowing into the natural fracture reaches steady state faster, resulting in a small differential pressure as shown in Fig.5-18, hence small values of fluid velocity are expected.

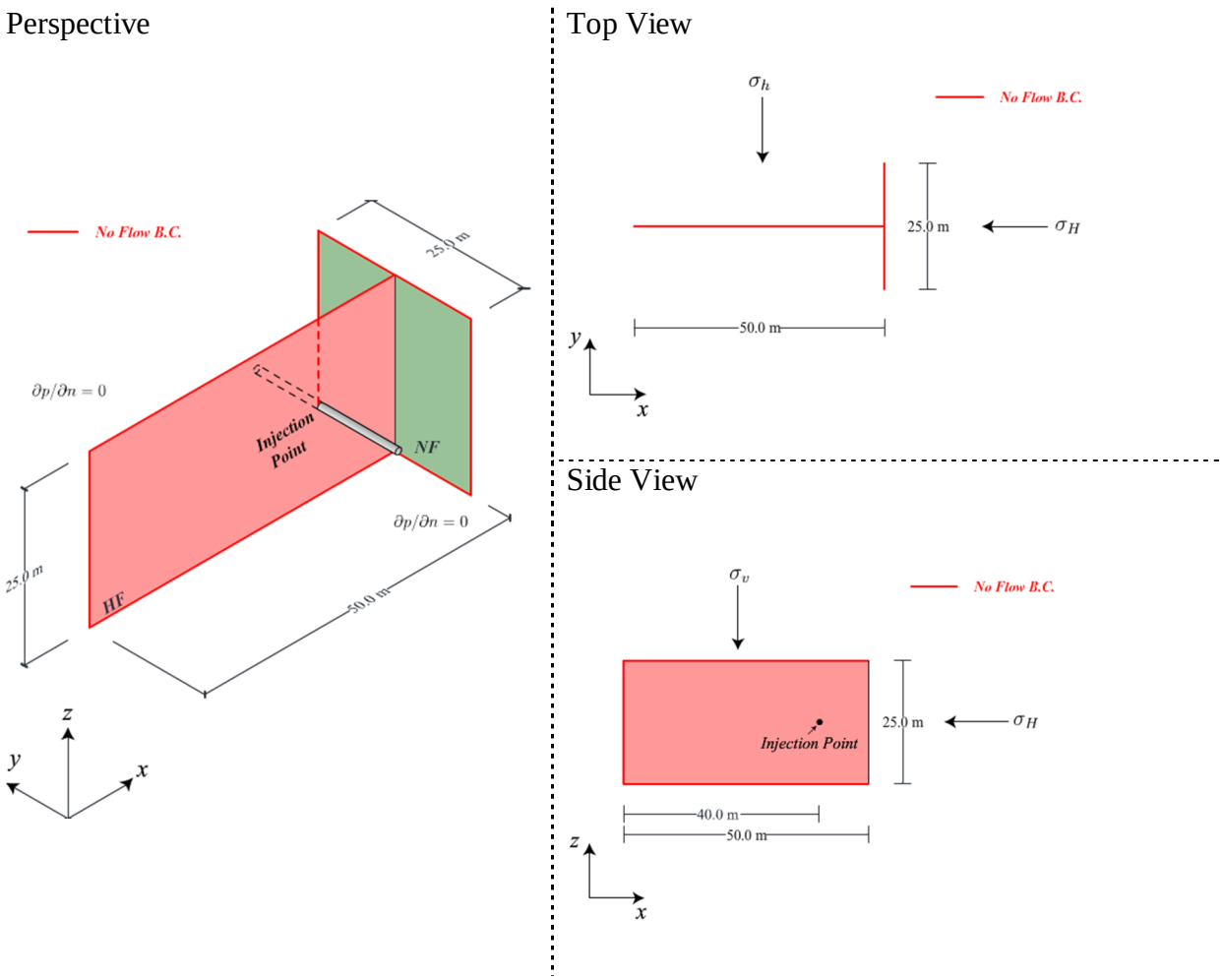

Figure 5-12. Geometry and boundary conditions for a T-shaped fracture network with wellbore close to natural fracture.

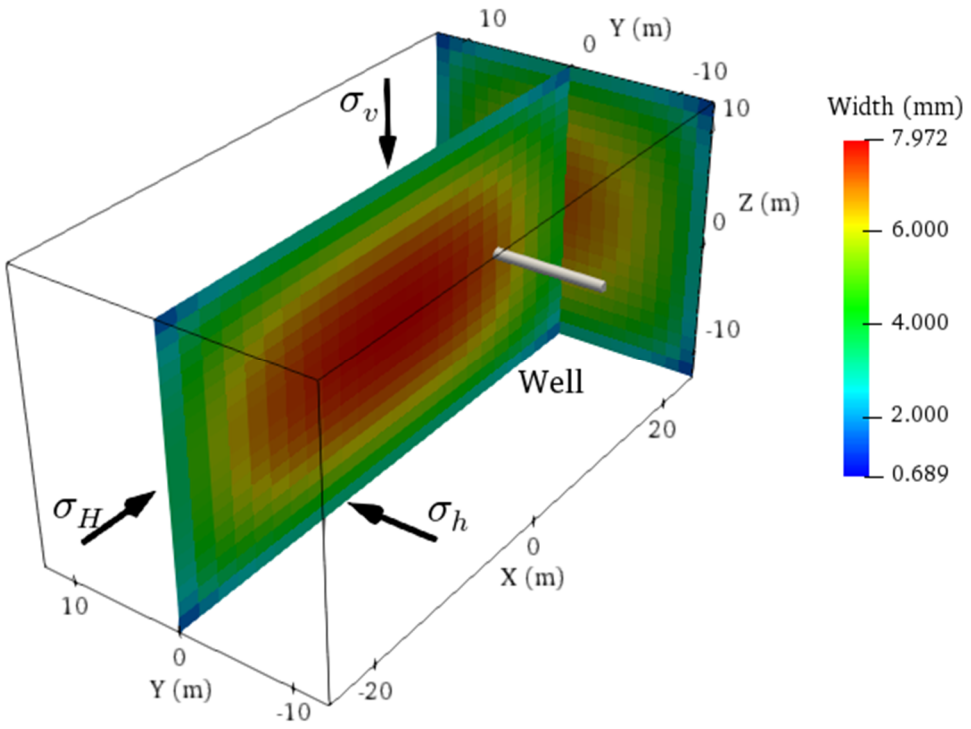

Figure 5-13. Fracture aperture distribution (perspective view) for the case 2 after an injection time of 125 s.

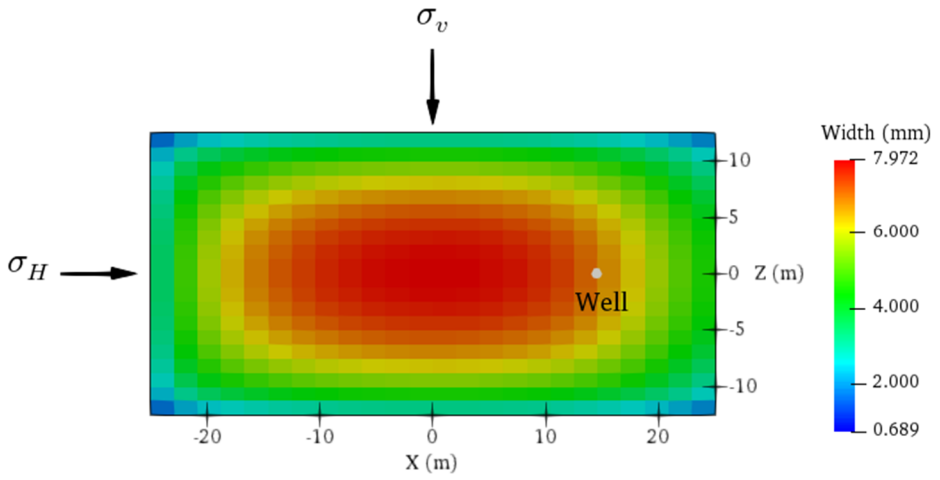

Figure 5-14. Fracture aperture distribution in the hydraulic fracture for the case 2 after an injection time of 125 s.

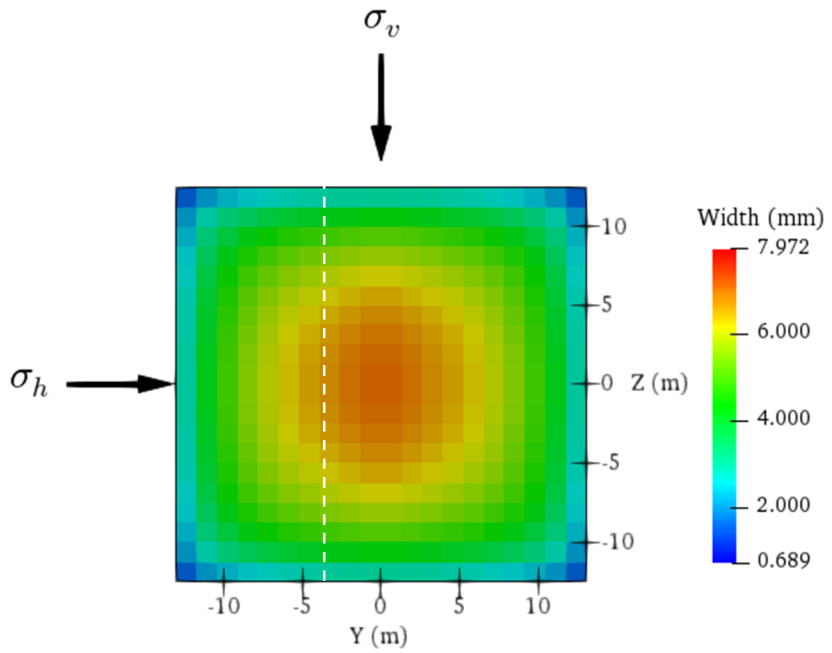

Figure 5-15. Fracture aperture distribution in the natural fracture for the case 2 after an injection time of 125 s. Dotted white line shows intersection of the hydraulic and natural fracture.

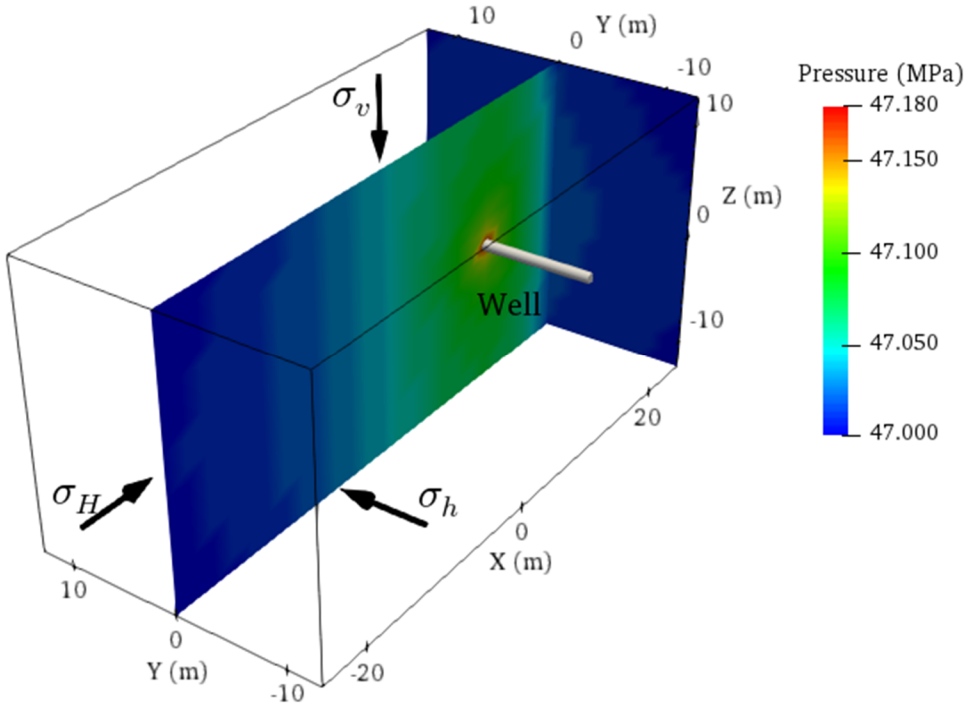

Figure 5-16. Pressure distribution (perspective view) for the case 2 after an injection time of 125 s.

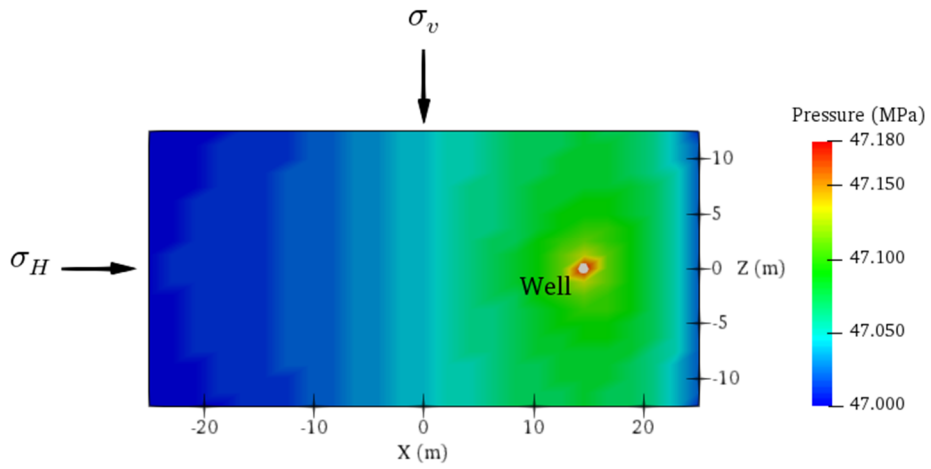

Figure 5-17. Pressure distribution in the hydraulic fracture for the case 2 after an injection time of 125 s.

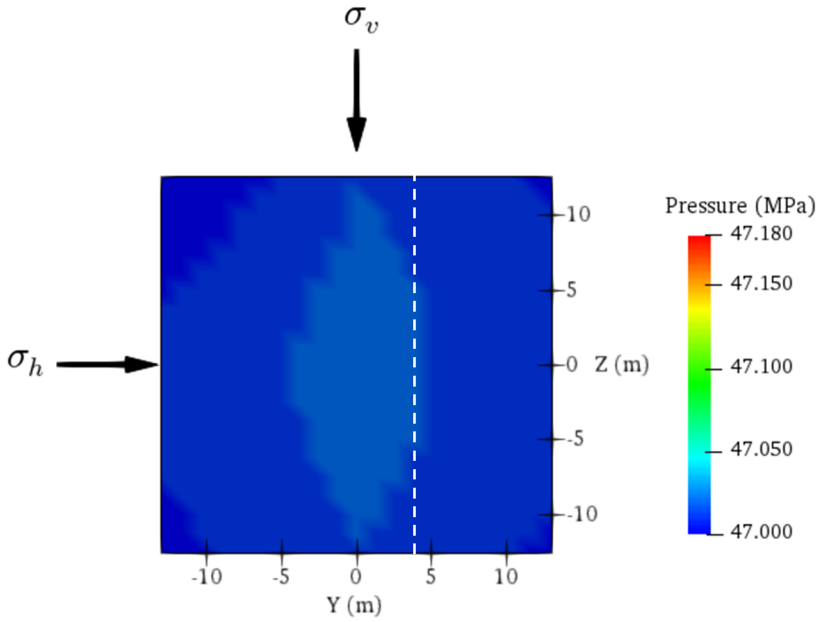

Figure 5-18. Pressure distribution in the natural fracture for the case 2 after an injection time of 125 s. Dotted white line shows intersection of the hydraulic and natural fracture.

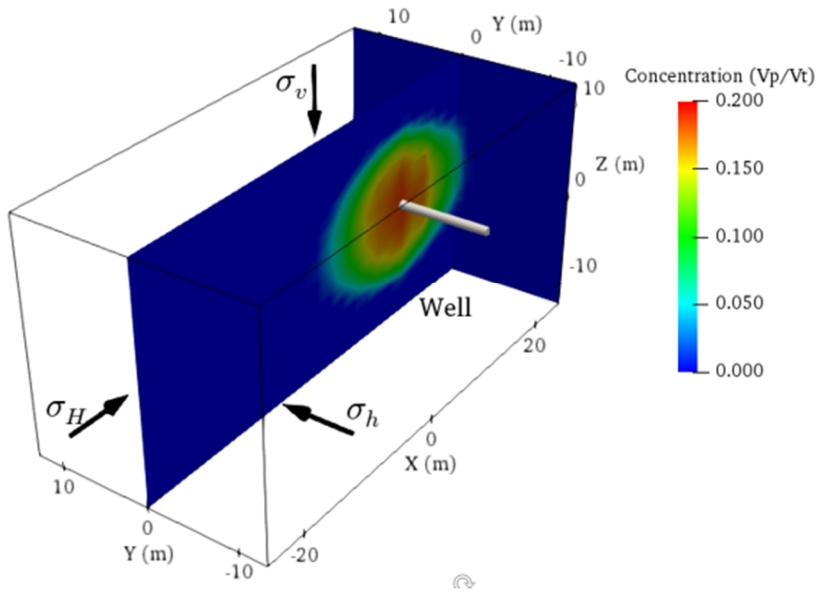

Figure 5-19. Proppant concentration distribution (perspective view) for the case 2 after an injection time of 125 s.

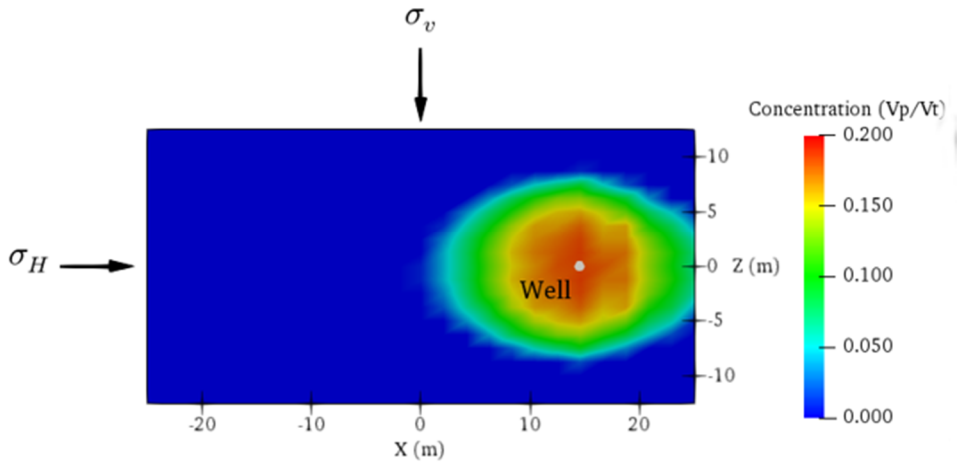

Figure 5-20. Proppant concentration distribution in the hydraulic fracture for the case 2 after an injection time of 125 s.

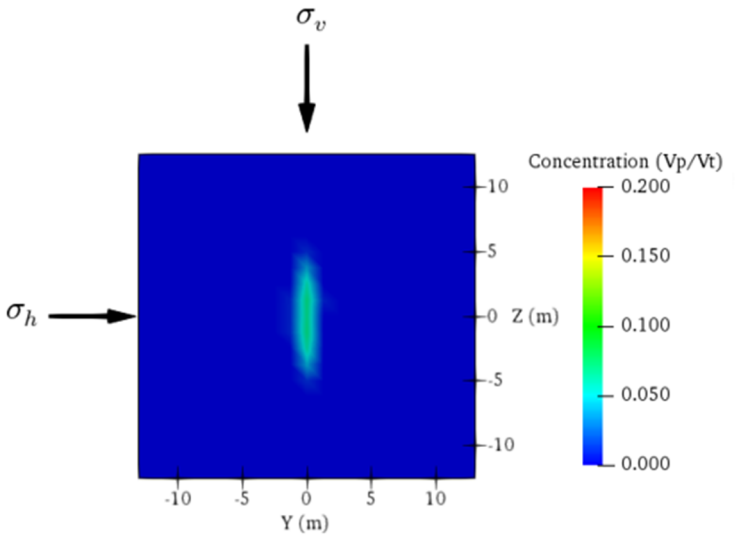

Figure 5-21. Proppant concentration distribution in the natural fracture for the case 2 after an injection time of 125 s. Dotted white line shows intersection of the hydraulic and natural fracture.

5.1.3. Case 3. Orthogonal Intersection of Hydraulic Fracture with Prescribed Fluid Pressure Boundary Condition in the NF

In this case, a preexisting static fracture network was assumed, the system is initially set to a fracture aperture value of 1e-5 m representing hydraulic aperture, then injection of clean fluid is simulated until the fracture aperture in the hydraulic fracture is enough to ensure proppant transport (greater than 3 times the proppant diameter). The network is composed of one hydraulic fracture which is intersecting the natural fracture perpendicularly and the injection point is located at the center of the hydraulic fracture. In Case 1 and Case 2, the proppant was poorly transported into the natural fracture, mainly due to the low pressure gradient in this portion of the network. To ensure a steeper pressure gradient, a fixed value of pressure is prescribed at the boundary of the natural fracture as shown in Fig. 5-22. The value was chosen to be $p_{tip} = 1.09\sigma_c$, where σ_c is the closure stress and it is calculated by the simulator "GeoFrac-3D" based on the stress field. The

values of the parameters used in this simulation are listed in Table 5-1 and the total injection time is 150 s. In this case the proppant front in the hydraulic fracture is fully developed as well as in the natural fracture in despite the fact that the values of fracture aperture are smaller compared with Case 1 or Case 2 as shown in Fig. 5-24 and 5-25. This can be explained if we analyze the pressure distribution in the network as shown in Fig. 5-27 and 5-28, the pressure gradient is steeper as the contrast in values is high.

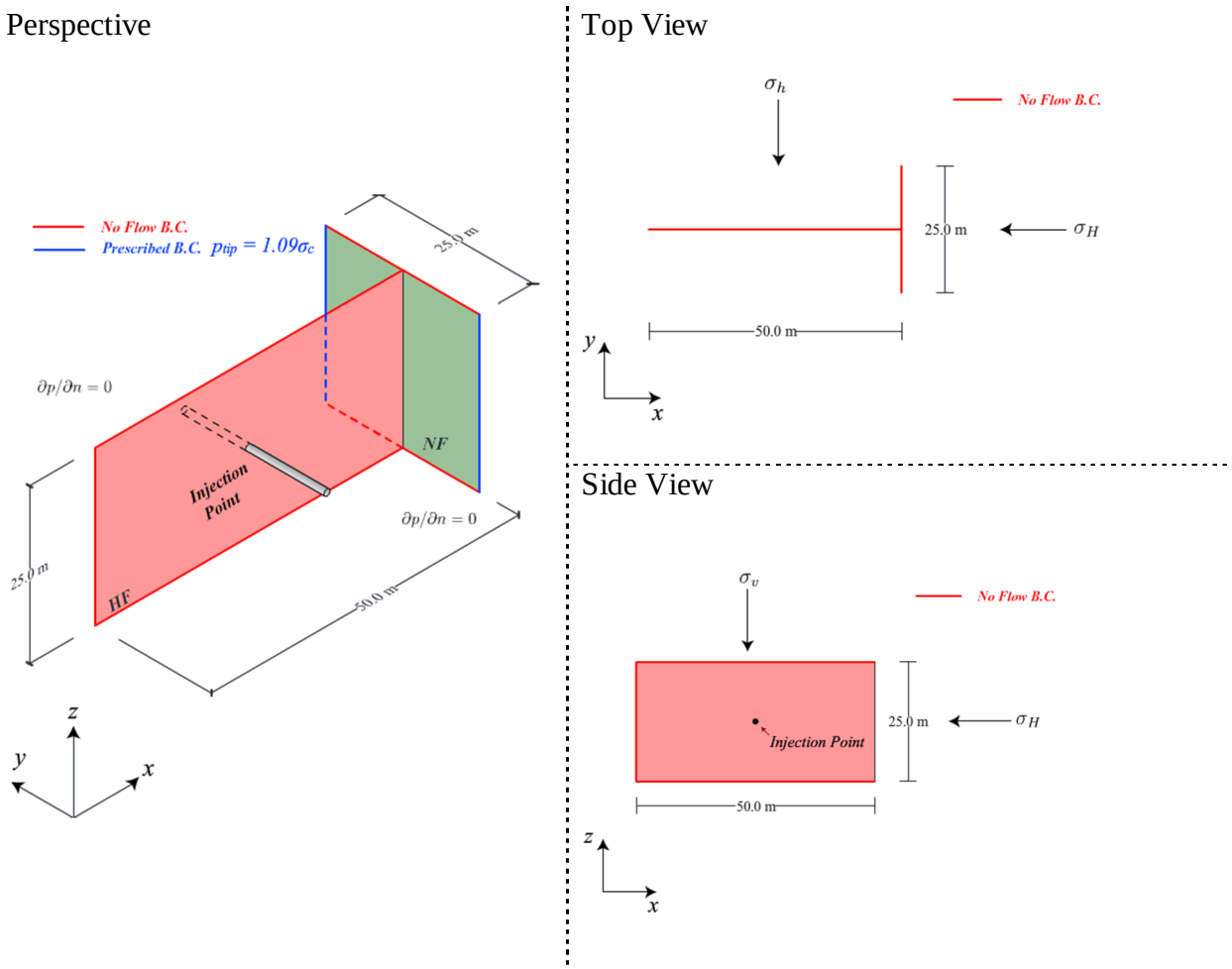

Figure 5-22. Geometry and boundary conditions for a T-shaped fracture network.

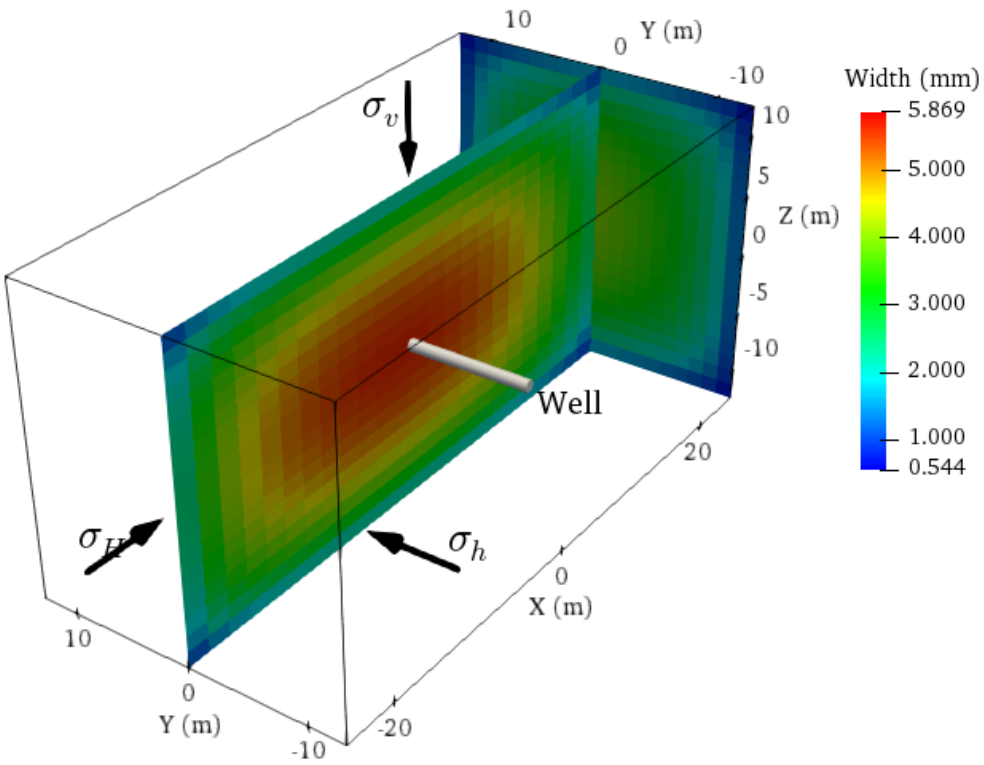

Figure 5-23. Fracture aperture distribution (perspective view) for the case 3 after an injection time of 150 s.

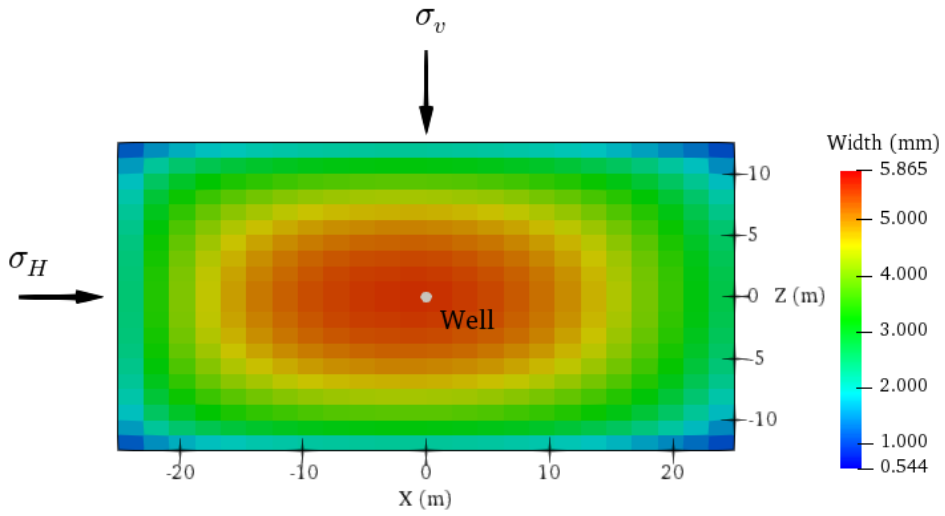

Figure 5-24. Fracture aperture distribution in the hydraulic fracture for the case 3 after an injection time of 150 s.

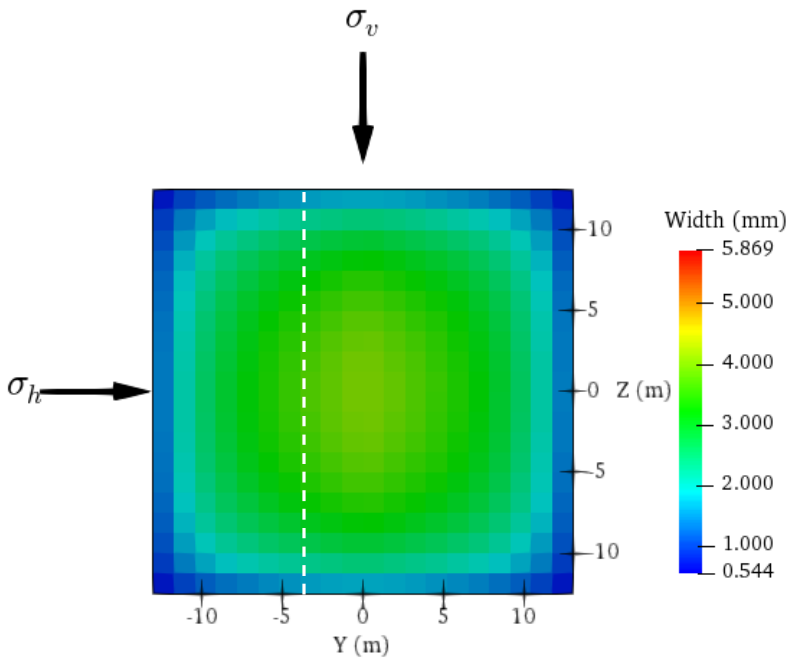

Figure 5-25. Fracture aperture distribution in the natural fracture for the case 3 after an injection time of 150 s. Dotted white line shows intersection of the hydraulic and natural fracture.

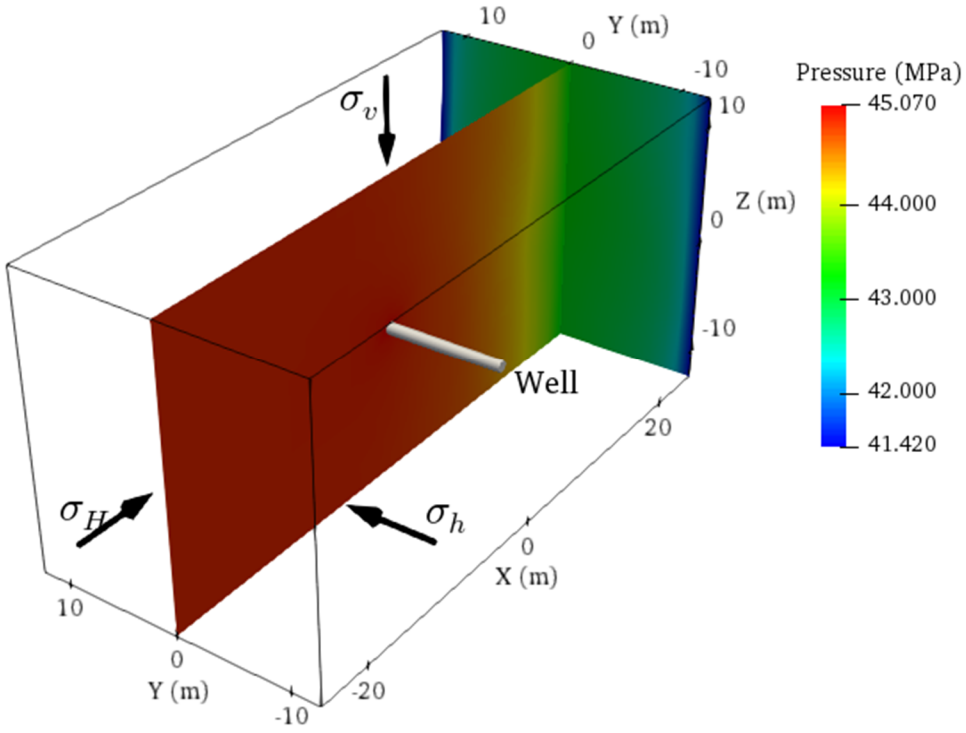

Figure 5-26. Pressure distribution (perspective view) for the case 3 after an injection time of 150 s.

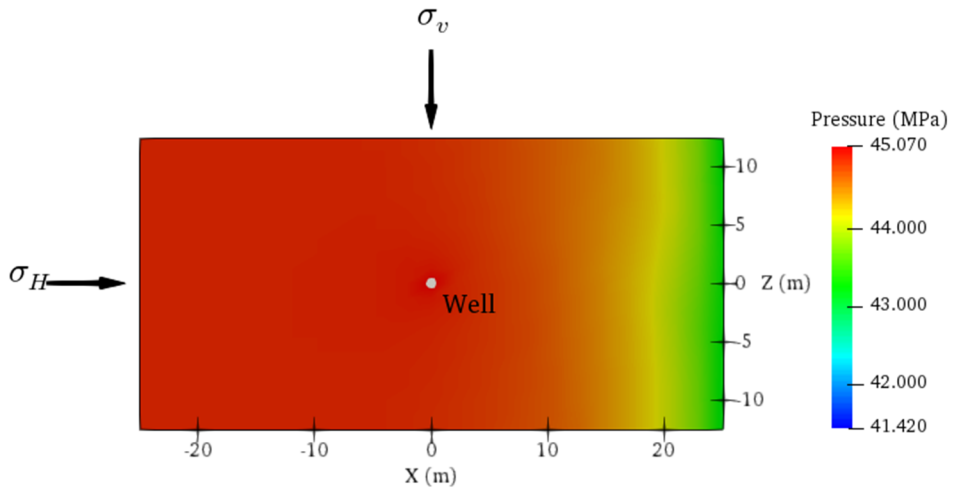

Figure 5-27. Pressure distribution in the hydraulic fracture for the case 3 after an injection time of 150 s.

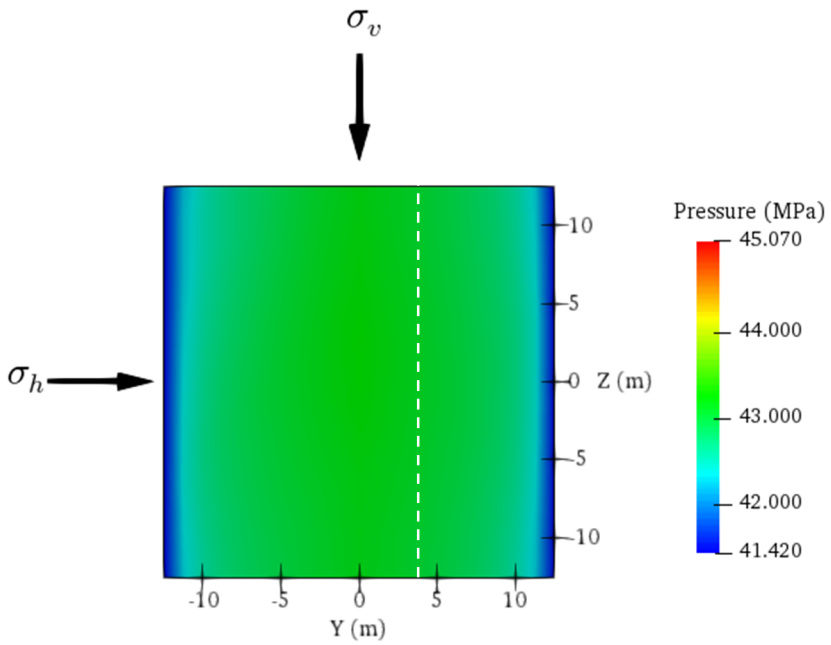

Figure 5-28. Pressure distribution in the natural fracture for the case 3 after an injection time of 150 s. Dotted white line shows intersection of the hydraulic and natural fracture.

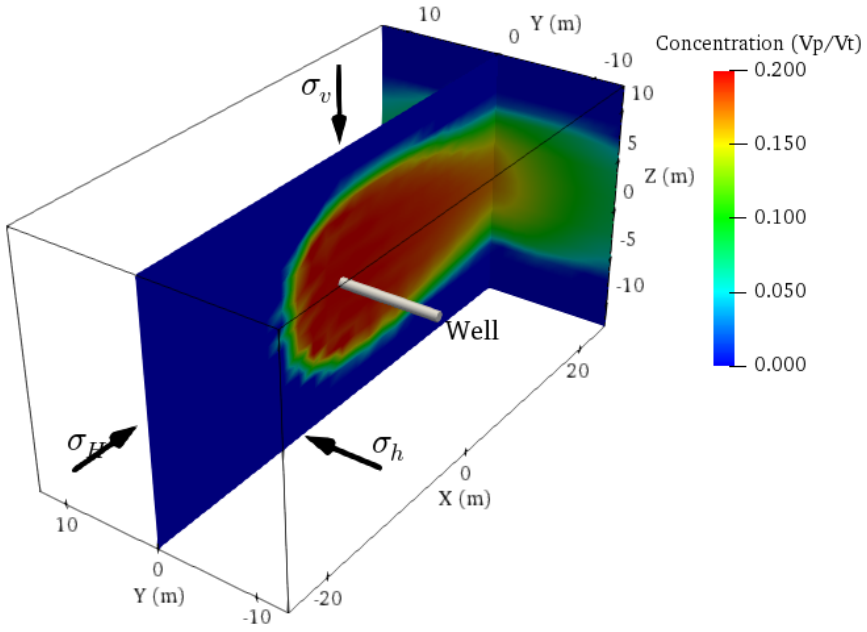

Figure 5-29. Proppant concentration distribution (perspective view) for the case 3 after an injection time of 150 s.

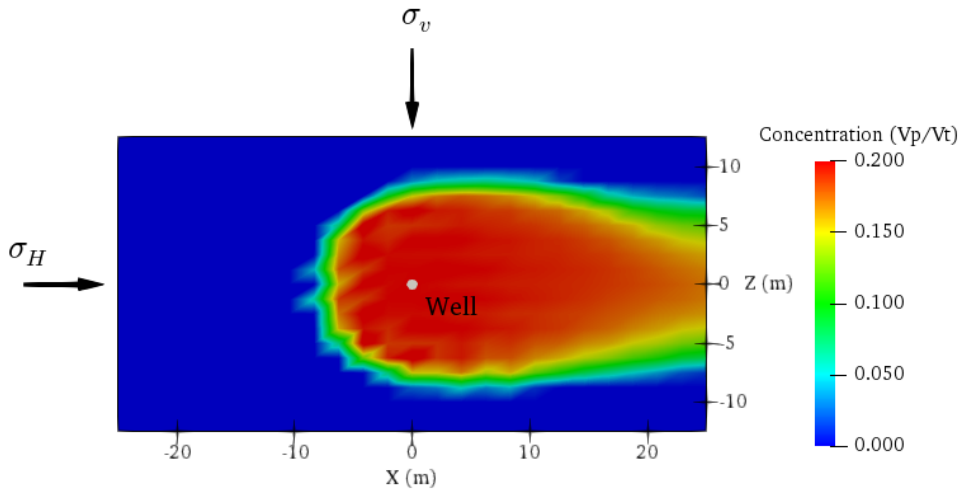

Figure 5-30. Proppant concentration distribution in the hydraulic fracture for the case 3 after an injection time of 150 s.

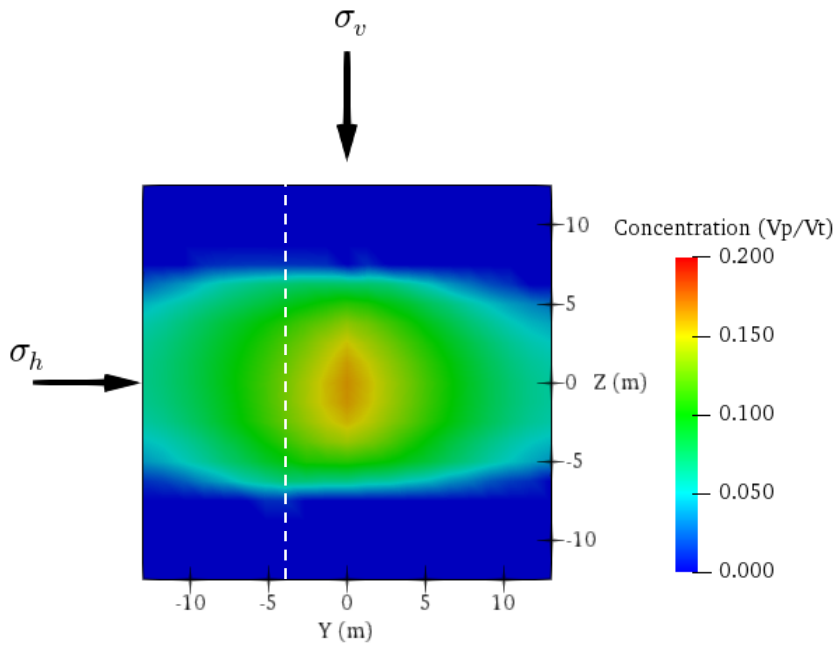

Figure 5-31. Proppant concentration distribution in the natural fracture for the case 3 after an injection time of 150 s. Dotted white line shows intersection of the hydraulic and natural fracture.

5.1.4. Case 4. Non-orthogonal Intersection of Hydraulic and Natural Fracture with Prescribed Fluid Pressure Boundary Condition in the NF (Intersection Angle = 30°)

This case is set up to study the behavior of the system when the natural fracture is not perpendicular to the hydraulic fracture. In this case, a preexisting static fracture network was assumed, the system is initially set to a fracture aperture value of 1e-5 m representing hydraulic aperture, then injection of clean fluid is simulated until the fracture aperture in the hydraulic fracture is enough to ensure proppant transport (greater than 3 times the proppant diameter). The hydraulic fracture is placed in the $x - z$ plane and the natural fracture is not perpendicular but instead it is inclined 30° to the y axis, the injection point is located at the center of the hydraulic fracture. To ensure a steeper

pressure gradient, a fixed value of pressure is prescribed at the boundary of the natural fracture as shown in Fig. 5-32. The value was chosen to be $p_{tip} = \sigma_c$, where σ_c is the closure pressure and is calculated by the simulator GeoFrac-3D based on the stress field. The values of the parameters used in this simulation are listed in Table 5-1 and the total injection time is 135 s. The proppant front is fully developed in the hydraulic fracture and in the natural fracture the accumulation pattern is not symmetric as shown in Fig. 5-40 and Fig. 5-41, this can be explained if we consider asymmetric fracture aperture distribution as shown in Fig. 5-35. When the natural fracture is inclined, the proximity with the hydraulic fracture restricts the opening more on the low angle side, affecting the symmetry of fracture aperture distribution in the natural fracture. This phenomenon can be better appreciated in Fig. 5-42 where the stress component σ_{xx} has higher values over the portions of the natural fracture more distant from the hydraulic fracture, experiencing less stress shadow. It is also important to note that the pressure distribution in the natural fracture is not much different than the previous case as shown in Fig. 5-38.

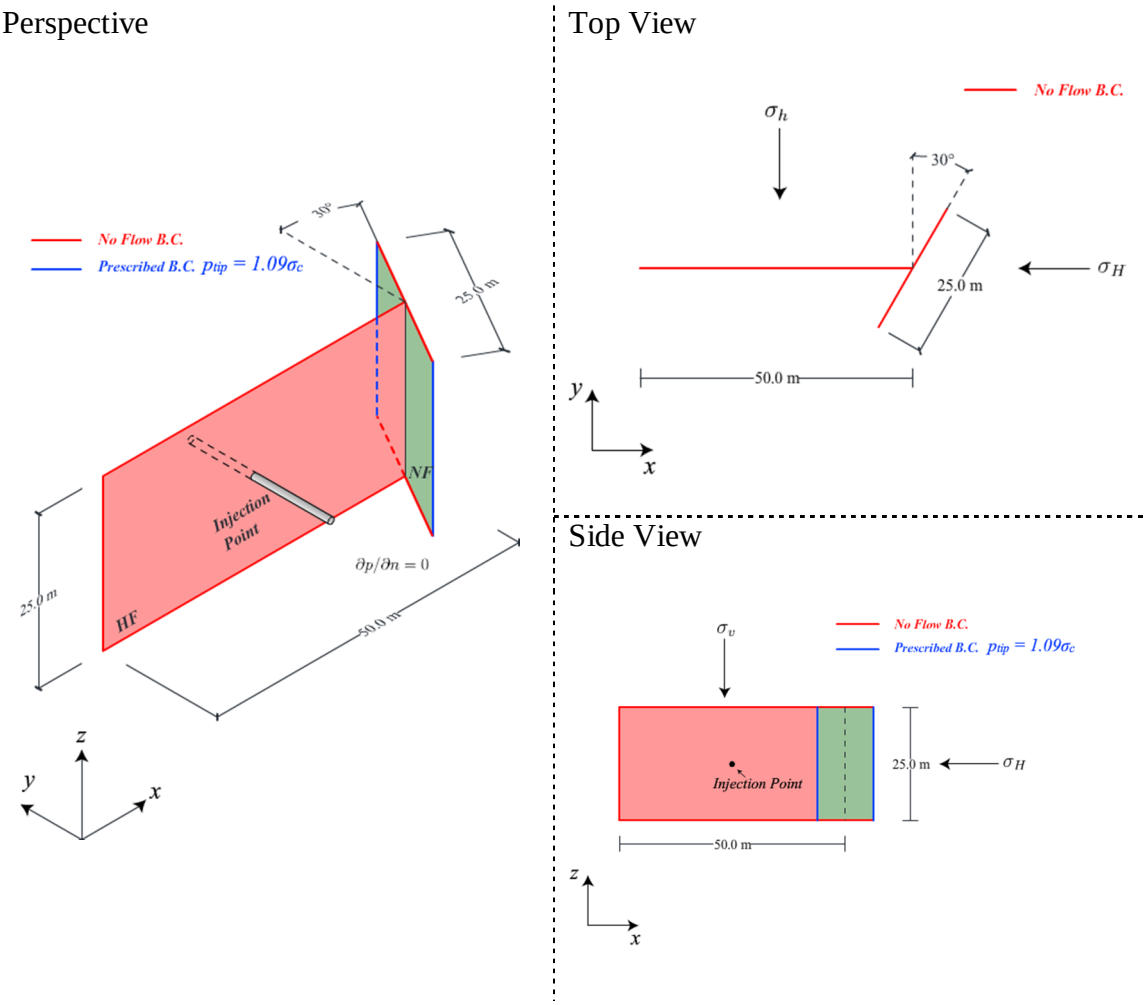

Figure 5-32. Geometry and boundary conditions for a T-shaped fracture network.

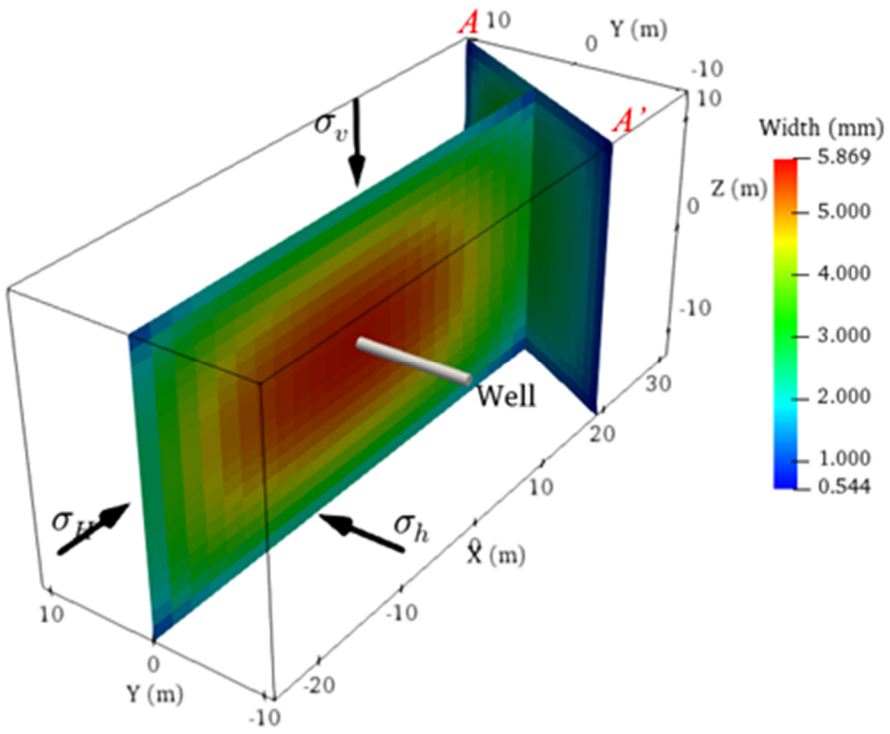

Figure 5-33. Fracture aperture distribution (perspective view) for the case 4 after an injection time of 135 s.

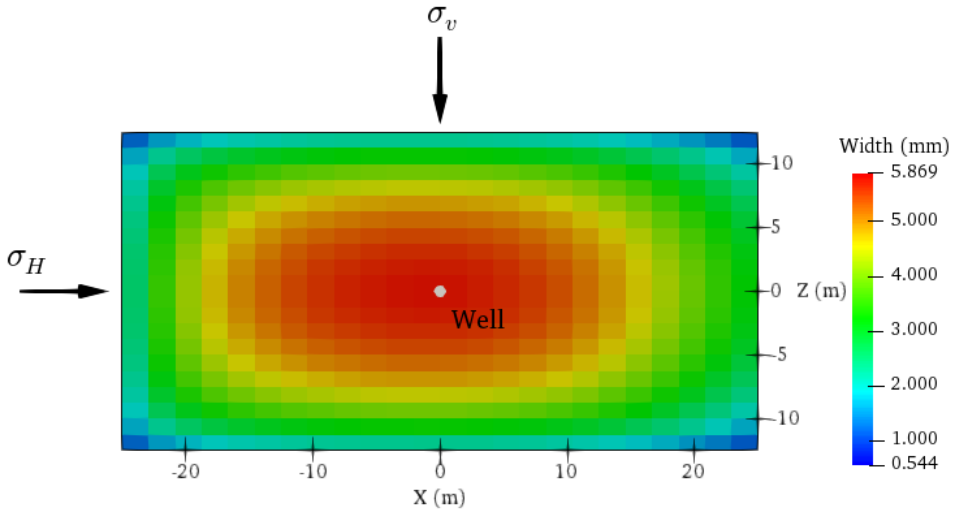

Figure 5-34. Fracture aperture distribution in the hydraulic fracture for the case 4 after an injection time of 135 s.

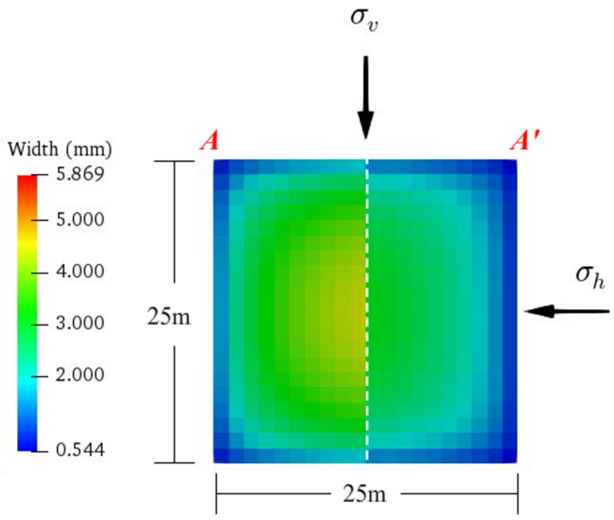

Figure 5-35. Fracture aperture distribution in the natural fracture for the case 4 after an injection time of 135 s. Dotted white line shows intersection of the hydraulic and natural fracture.

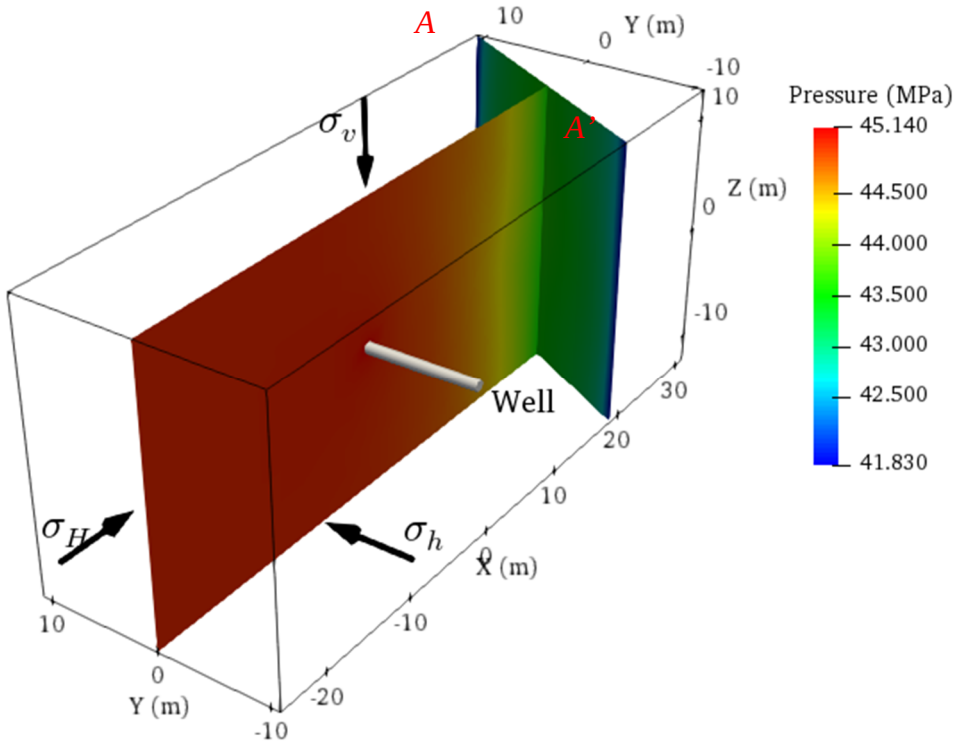

Figure 5-36. Pressure distribution (perspective view) for the case 4 after an injection time of 135 s.

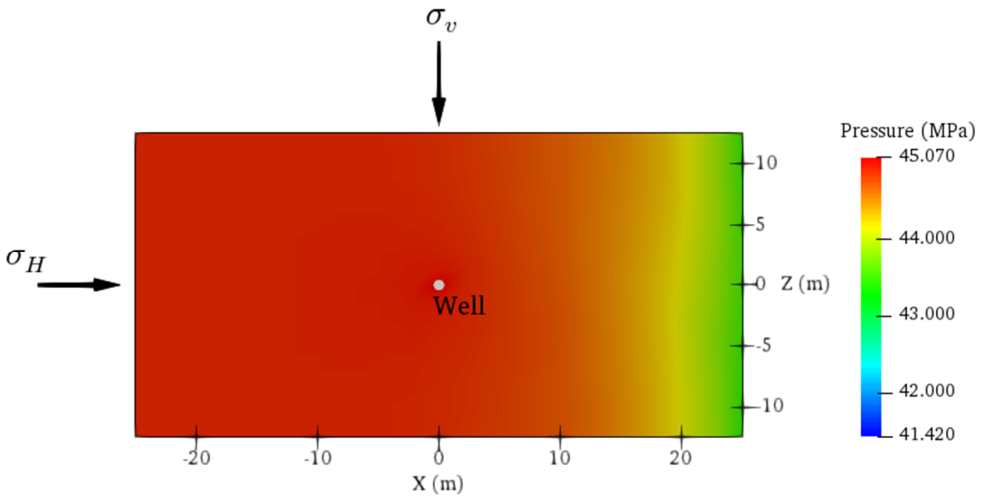

Figure 5-37. Pressure distribution in the hydraulic fracture for the case 4 after an injection time of 135 s.

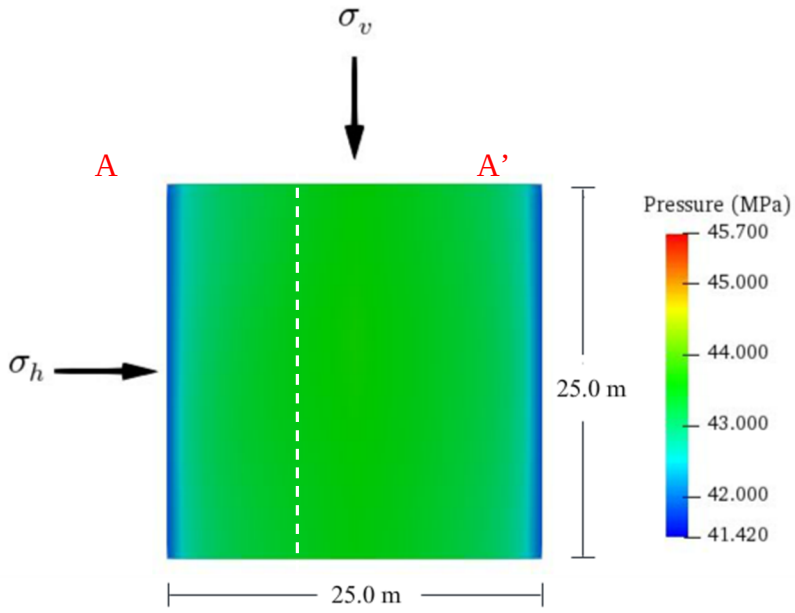

Figure 5-38. Pressure distribution in the natural fracture for the case 4 after an injection time of 135 s. Dotted white line shows intersection of the hydraulic and natural fracture.

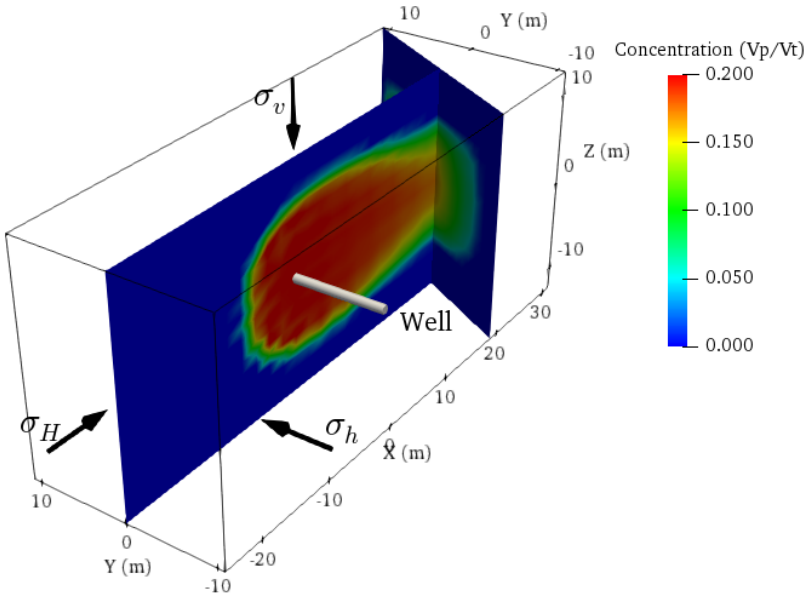

Figure 5-39. Proppant concentration distribution (perspective view) for the case 4 after an injection time of 135 s.

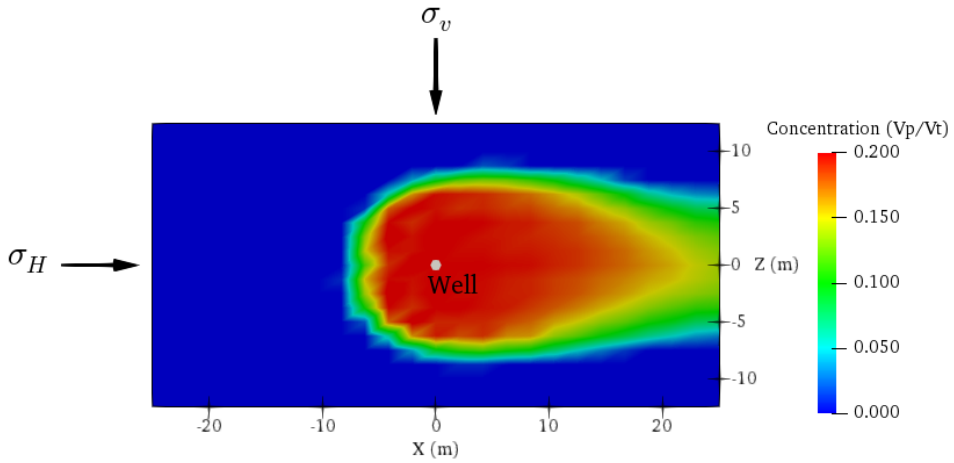

Figure 5-40. Proppant concentration distribution in the hydraulic fracture for the case 4 after an injection time of 135 s.

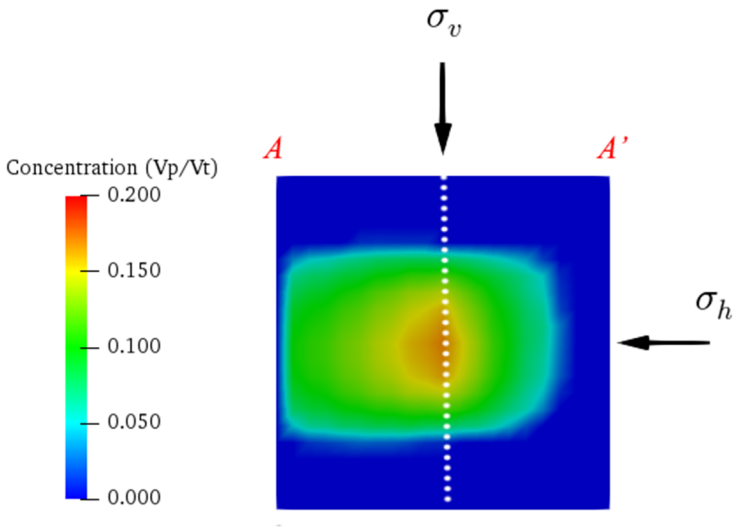

Figure 5-41. Proppant concentration distribution in the natural fracture for the case 4 after an injection time of 135 s. Dotted white line shows intersection of the hydraulic and natural fracture.

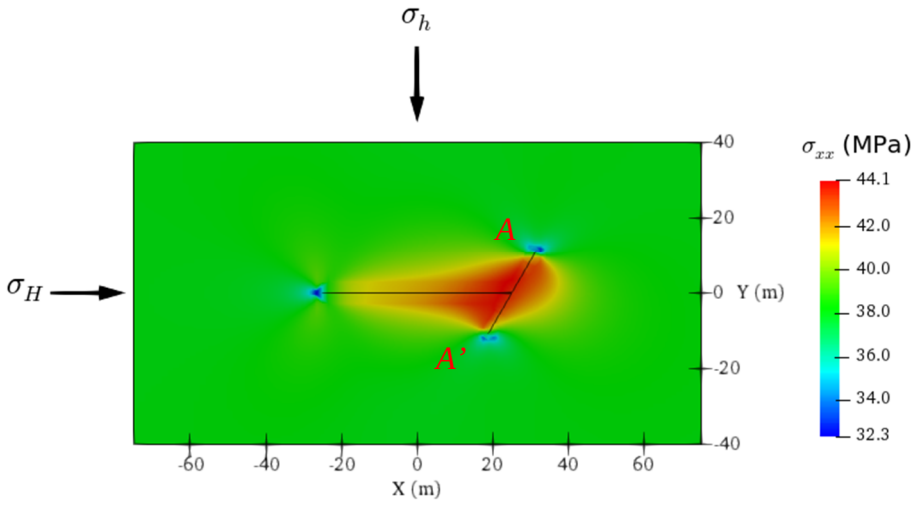

Figure 5-42. Top view showing the horizontal stress (σ_{xx}) distribution along x direction for the case 4 after an injection time of 135 s.

5.1.5. Case 5. Non-orthogonal Intersection of Hydraulic and Natural Fracture with Prescribed Fluid Pressure Boundary Condition in the NF (Intersection Angle = 45°)

In this case a preexisting static fracture network was assumed, the system is initially set to a fracture aperture value of 1e-5 m representing hydraulic aperture, then injection of clean fluid is simulated until the fracture aperture in the hydraulic fracture is enough to ensure proppant transport (greater than 3 times the proppant diameter). The hydraulic fracture is placed in the $x - z$ plane and the natural fracture is not perpendicular but instead it is inclined 45° to the y axis, the injection point is located at the center of the hydraulic fracture as shown in Fig. 5-43. The values of the parameters used in this simulation are listed in Table 5-1 and the total injection time is 135 s. At higher inclination angles, the restriction in aperture at one side of the natural fracture is more evident as shown in Fig. 5-46, as a consequence the proppant front is fully developed in the hydraulic fracture and the proppant is being transported to only one of the sides of the natural fracture as shown in Fig. 5-52. It is also interesting to note that the pressure distribution in the natural fracture is similar to those in Case 3 and Case 4 as shown in Fig. 5-49.

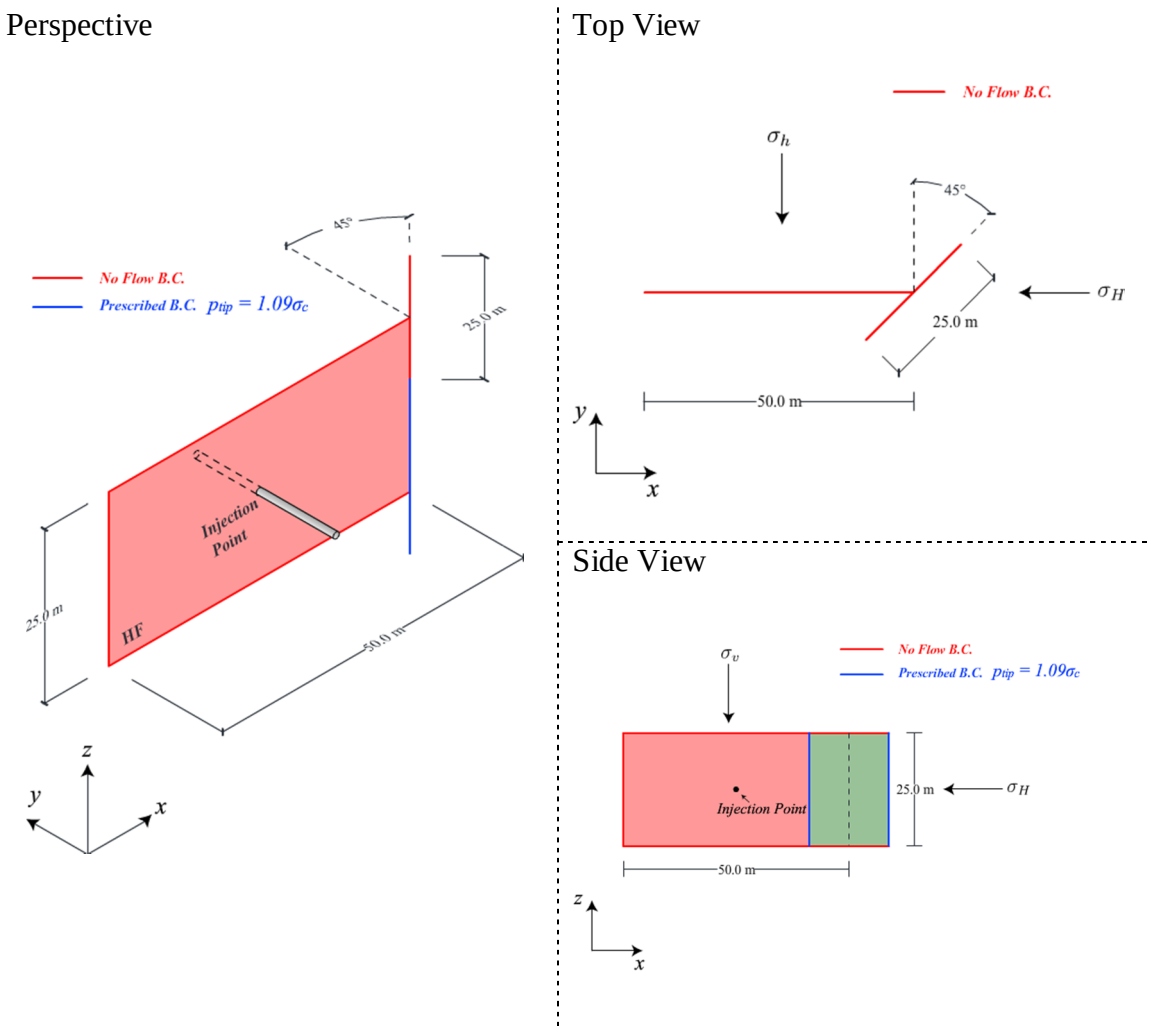

Figure 5-43. Geometry and boundary conditions for a T shaped fracture network.

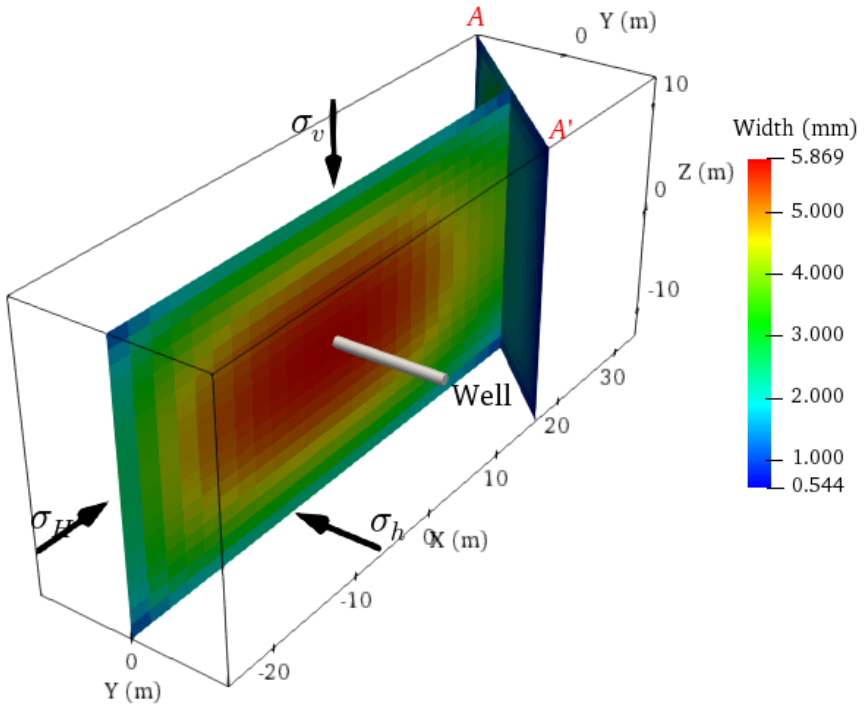

Figure 5-44. Fracture aperture distribution (perspective view) for the case 5 after an injection time of 135 s.

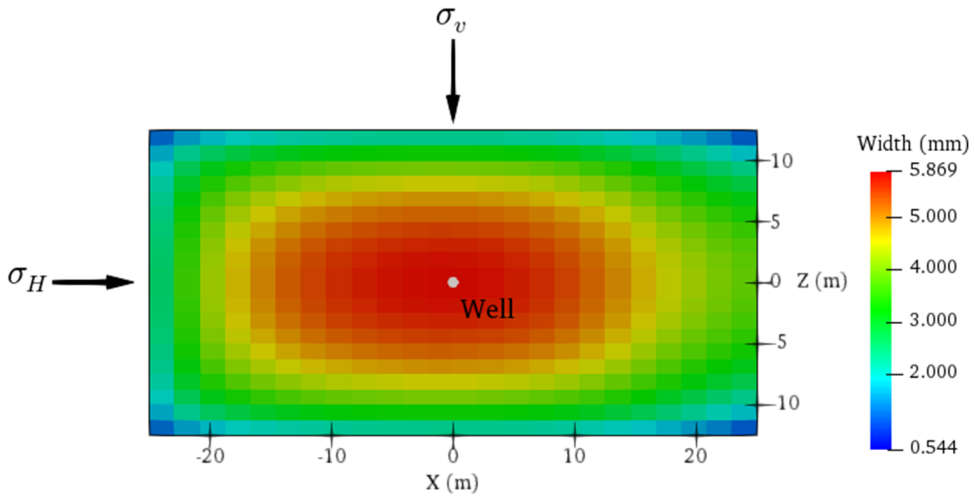

Figure 5-45. Fracture aperture distribution in the hydraulic fracture for the case 5 after an injection time of 135 s.

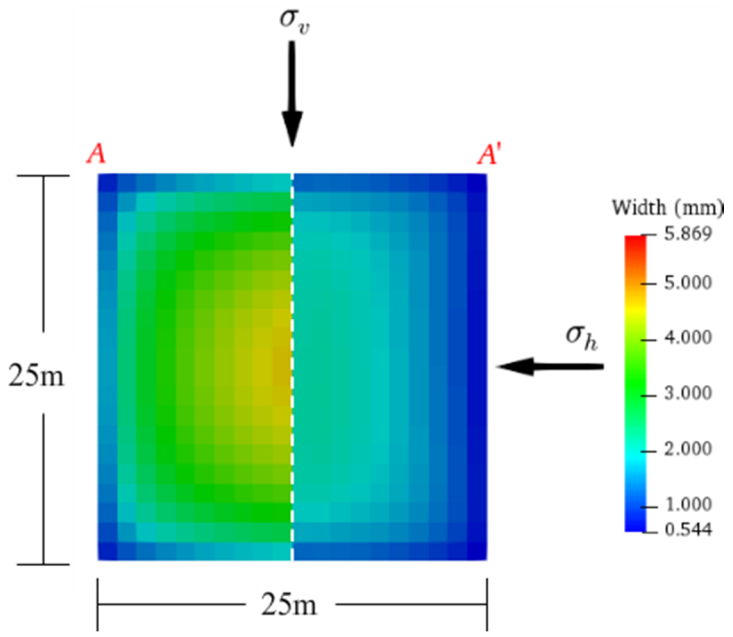

Figure 5-46. Fracture aperture distribution in the natural fracture for the case 5 after an injection time of 135 s. Dotted white line shows intersection of the hydraulic and natural fracture.

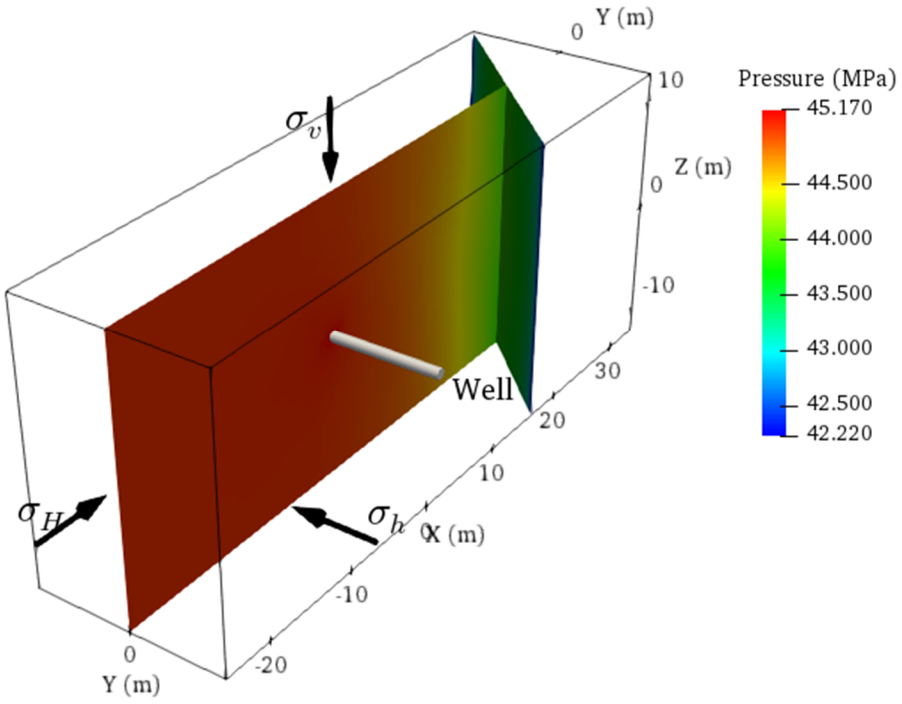

Figure 5-47. Pressure distribution (perspective view) for the case 5 after an injection time of 135 s.

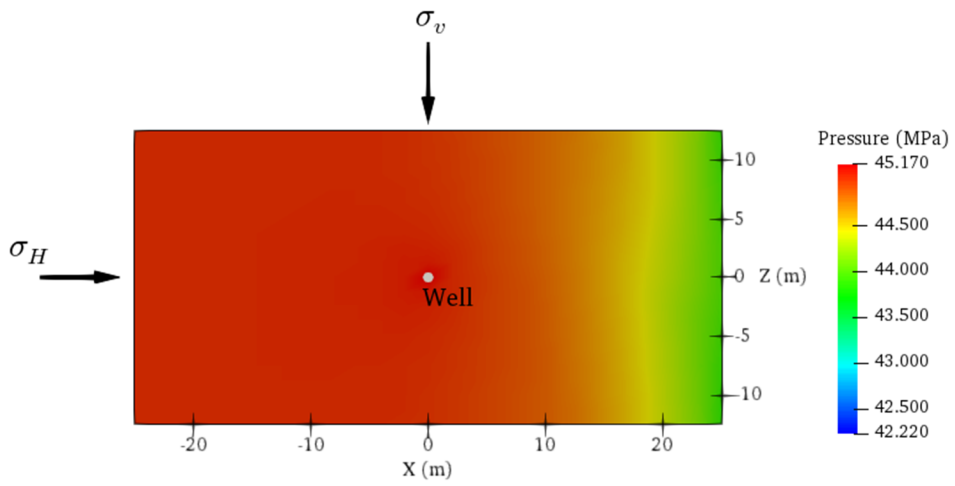

Figure 5-48. Pressure distribution in the hydraulic fracture for the case 5 after an injection time of 135 s.

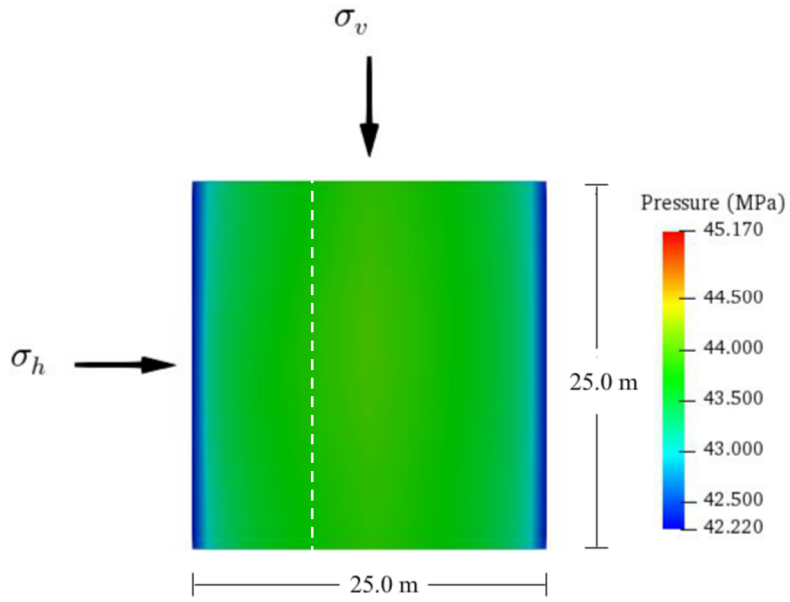

Figure 5-49. Pressure distribution in the natural fracture for the case 5 after an injection time of 135 s. Dotted white line shows intersection of the hydraulic and natural fracture.

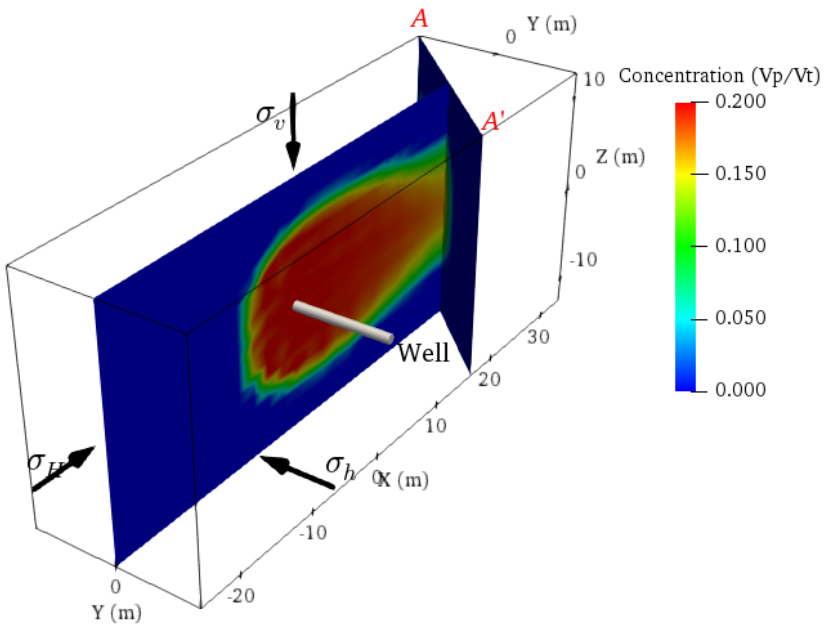

Figure 5-50. Proppant concentration distribution (perspective view) for the case 5 after an injection time of 135 s.

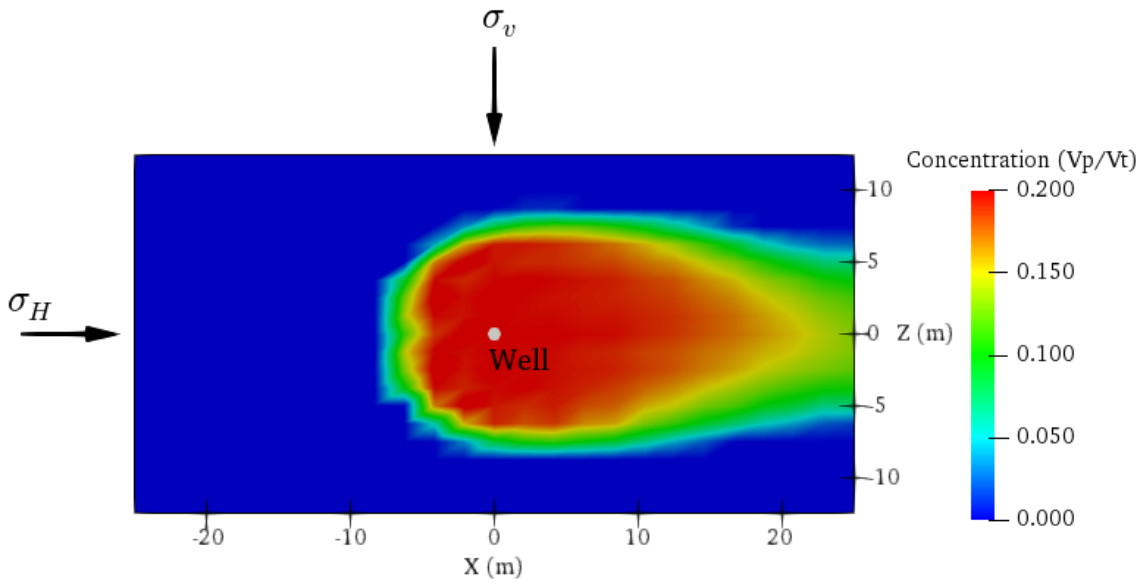

Figure 5-51. Proppant concentration distribution in the hydraulic fracture for the case 5 after an injection time of 135 s.

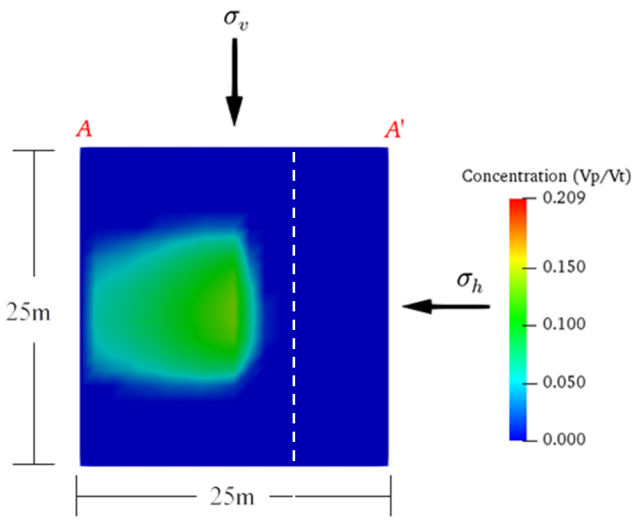

Figure 5-52. Proppant concentration distribution in the natural fracture for the case 5 after an injection time of 135 s. Dotted white line shows intersection of the hydraulic and natural fracture.

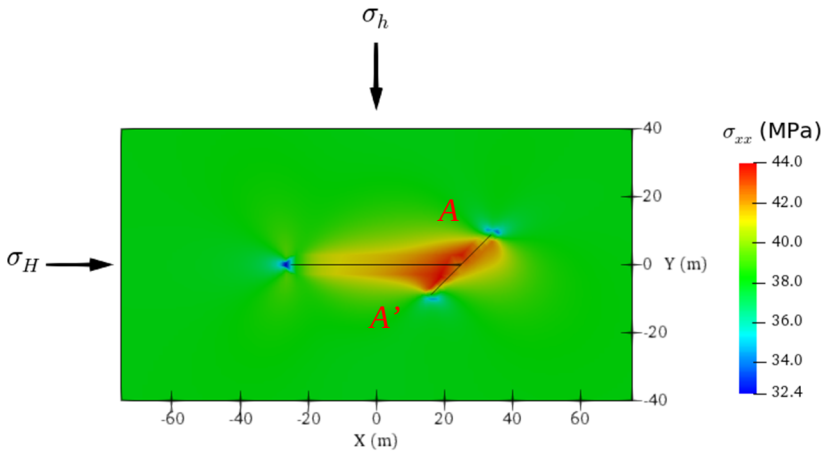

Figure 5-53. Top view showing the horizontal stress (σ_{xx}) distribution along x direction for the case 5 after an injection time of 135 s.

5.1.6. Comparison of Cases 3, 4, and 5

In cases 3, 4 and 5 a hydraulic fracture in the plane (x, z) is intercepting a natural fracture which is rotated to the y axes 0° for case 3, 30° for case 4 and 45° for case 5, the injection point represented by a horizontal wells is located at $(x = 0, y = 0, z = 0)$ in all the cases. To study the effect of the rotation angle to the y axes, fracture width distribution, fluid pressure distribution and proppant concentration distribution are compared. The data are plotted at a simulation time of 150 s, for the point $(x, y, z = 0)$; these coordinates are represented by the red line shown in Fig. 5-54.

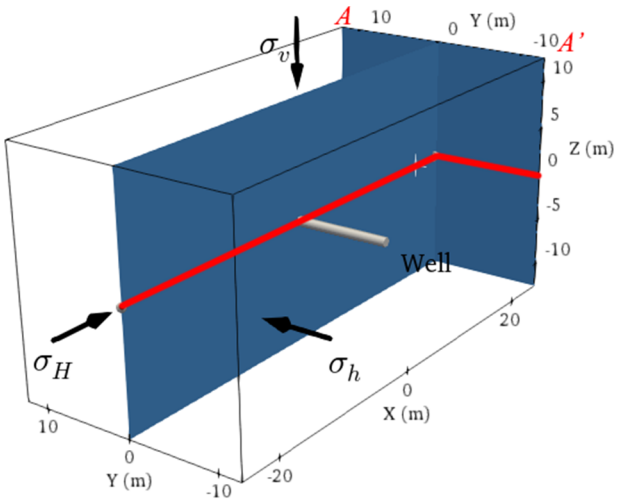

Figure 5-54. Fracture network composed by a hydraulic fracture and a natural fracture, the red line represents z=0 where the data from cases 3, 4 and 4 are compared.

The comparison of the three cases of the fracture width distributions is shown in Fig. 5-56, it can be noted that the aperture increases when the rotation angle of the natural fracture is higher, this behavior can be explained if we consider the fracture width distribution in the natural fractures as shown in Fig 5-56 with higher rotation angle the width of one of the wings of the natural fractures is restricted due to the effect of the stress shadow or the effect of growth of the hydraulic fracture in the natural fracture, then the system will tend to equilibrate with higher values of fractures width

in the hydraulic fracture. Additionally, the pressure tends to be higher in all the system if the rotation angle of the natural fracture is higher as shown in Fig. 5-57 and Fig. 5-58, note that the boundary condition at the tip of the natural fracture imposed in these simulations is $1.09\sigma_c$ (1.09 times closure stress), it was observed that the closure stress increases when the rotation of the natural fracture is higher, since the stress shadow was impeding the opening of one of the wings of the natural fracture, resulting in the increase in pressure in the whole system.

As all the boundaries of the hydraulic fracture are prescribed with the no flow boundary conditions, it can be noted that the pressure is constant from the tip of the hydraulic fracture at $x = -25$ to the injection point at $x = 0$, the absence of pressure differential in this zone of the fracture implies that the proppant would be poorly transported in this area. As mention before the closure pressure p_c increases with higher values of the rotation of the natural fracture, this explains the increase in pressure in all the system as shown in Fig. 5-57. The shape of the curves of pressure are similar in the natural fractures as shown in Fig. 5-58, this can be explained if we consider that both edges of the natural fracture are prescribed with the boundary condition $1.09p_c$, the closure pressure is different among the cases but the length of the fractures is the same allowing this similitude in the behavior.

It can be noted in Fig 5-59 that the difference in the proppant distribution in the hydraulic fracture is almost negligible, this can be explained if we consider the pressure curves shown in Fig. 5-57, although the values of pressure show some difference, the shape of the curves are very similar, implying that the pressure differential would have similar values, leading to values of proppant velocities also similar. The proppant distribution in the natural fractures show big differences

among cases as presented in Fig. 5-60, this is due to the difference in fracture apertures in the natural fractures, in despite the fact that the pressure profiles are similar in this zone.

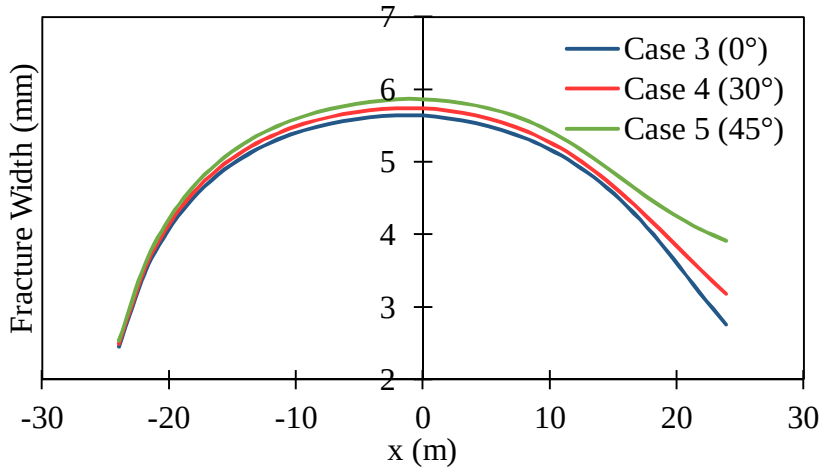

Figure 5-55. Fracture width in the hydraulic fracture traced at z=0.

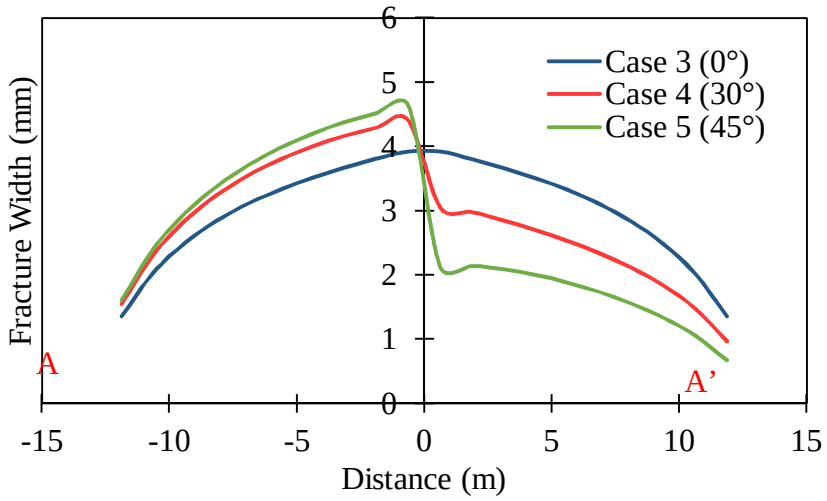

Figure 5-56. Fracture width in the natural fractures traced at z=0.

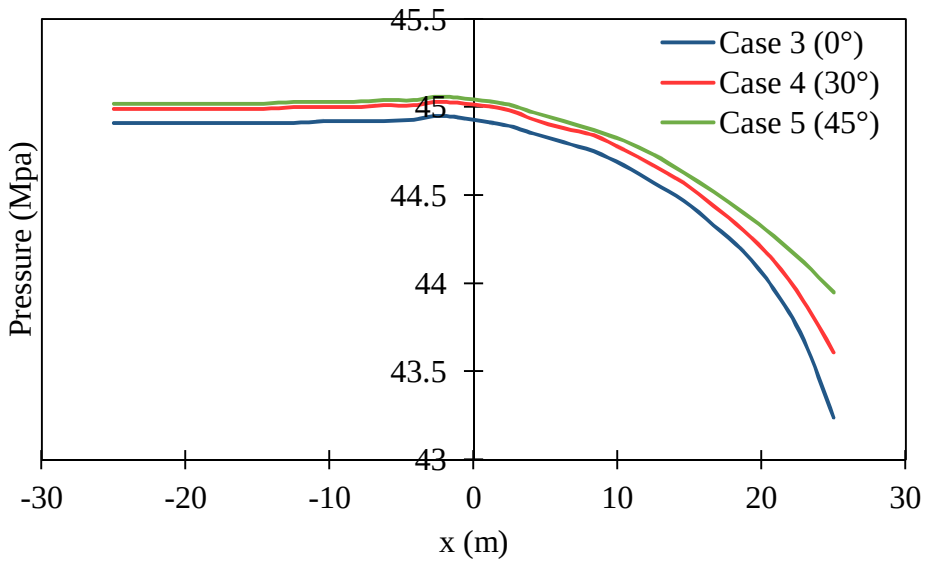

Figure 5-57. Fluid pressure in the hydraulic fracture traced at z=0.

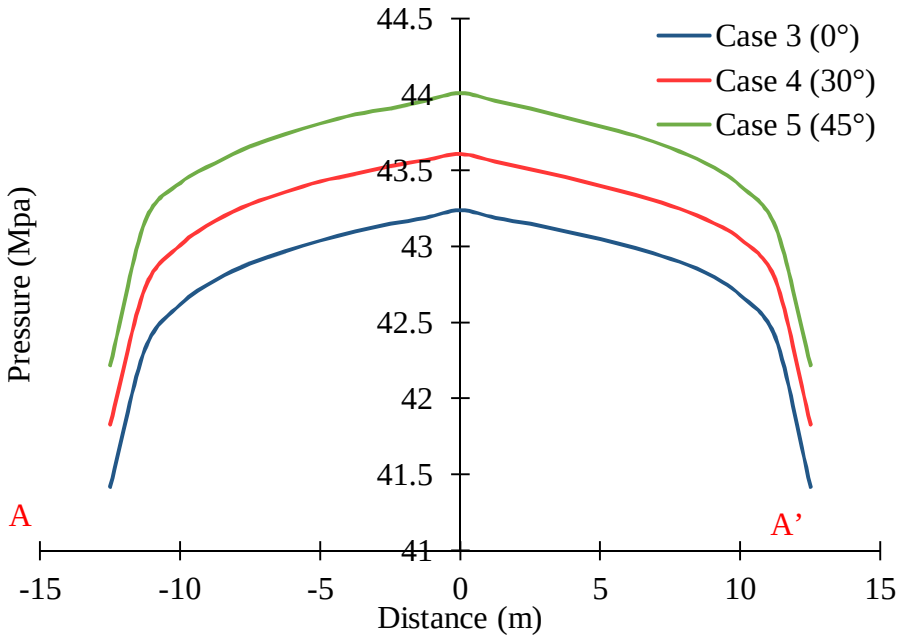

Figure 5-58. Fluid pressure distribution in the natural fractures traced at z=0.

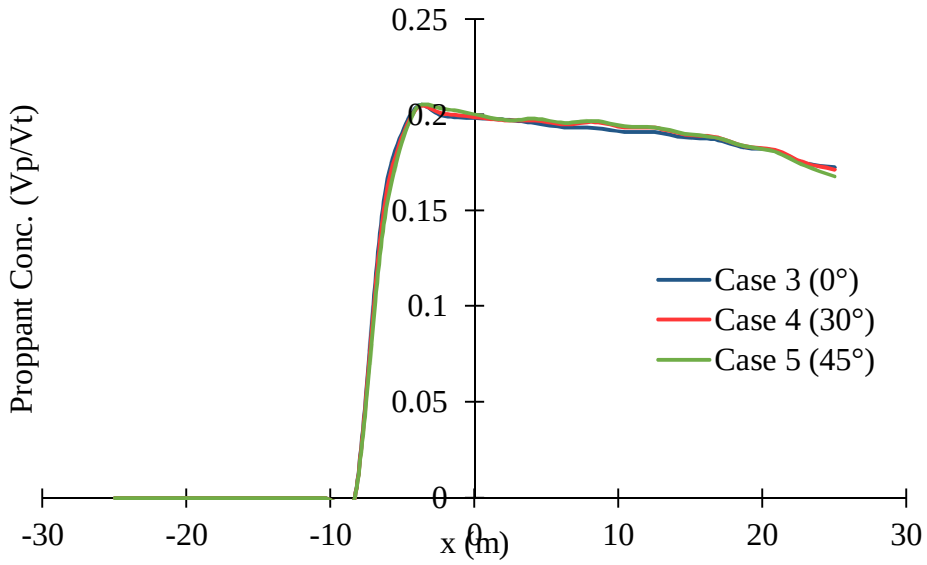

Figure 5-59. Proppant concentration in the hydraulic fracture traced at z=0.

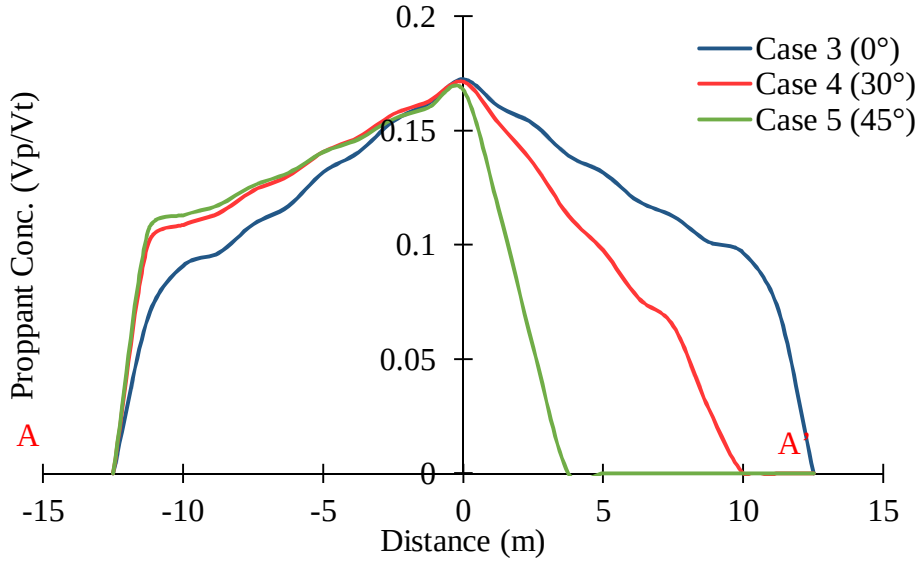

Figure 5-60. Proppant concentration in the natural fractures traced at z=0.

5.2. H-shaped Network, Centered Injection Point and Prescribed Pressure in the NF Boundaries

In this case a preexisting static fracture network was assumed, the system is initially set to a fracture aperture value of 1e-5 m representing hydraulic aperture, then injection of clean fluid is simulated until the fracture aperture in the hydraulic fracture is enough to ensure proppant transport (greater than 3 times the proppant diameter). The network is composed of one hydraulic fracture which is intersecting two natural fractures perpendicularly, forming an H-shape fracture network, and the injection point is located at the center of the hydraulic fracture as shown in Fig. 5-61. The values of the parameters used in this simulation are listed in Table 5-1 and the total injection time is 212s. At the boundaries of the natural fractures the pressure is prescribed to be $1.09p_c$, where p_c is the closure pressure. The proppant front is completely developed in the hydraulic fracture and, as expected for this situation, the proppant transport into the natural fractures is symmetric as shown (see Figs. 5-70, 5-71 and 5-72). The symmetry is also evident in the fracture aperture distribution as shown in Fig. 5-63, Fig. 5-64, Fig. 5-65 and in the pressure distribution as shown in Fig. 5-67, Fig. 5-68 and Fig. 5-69.

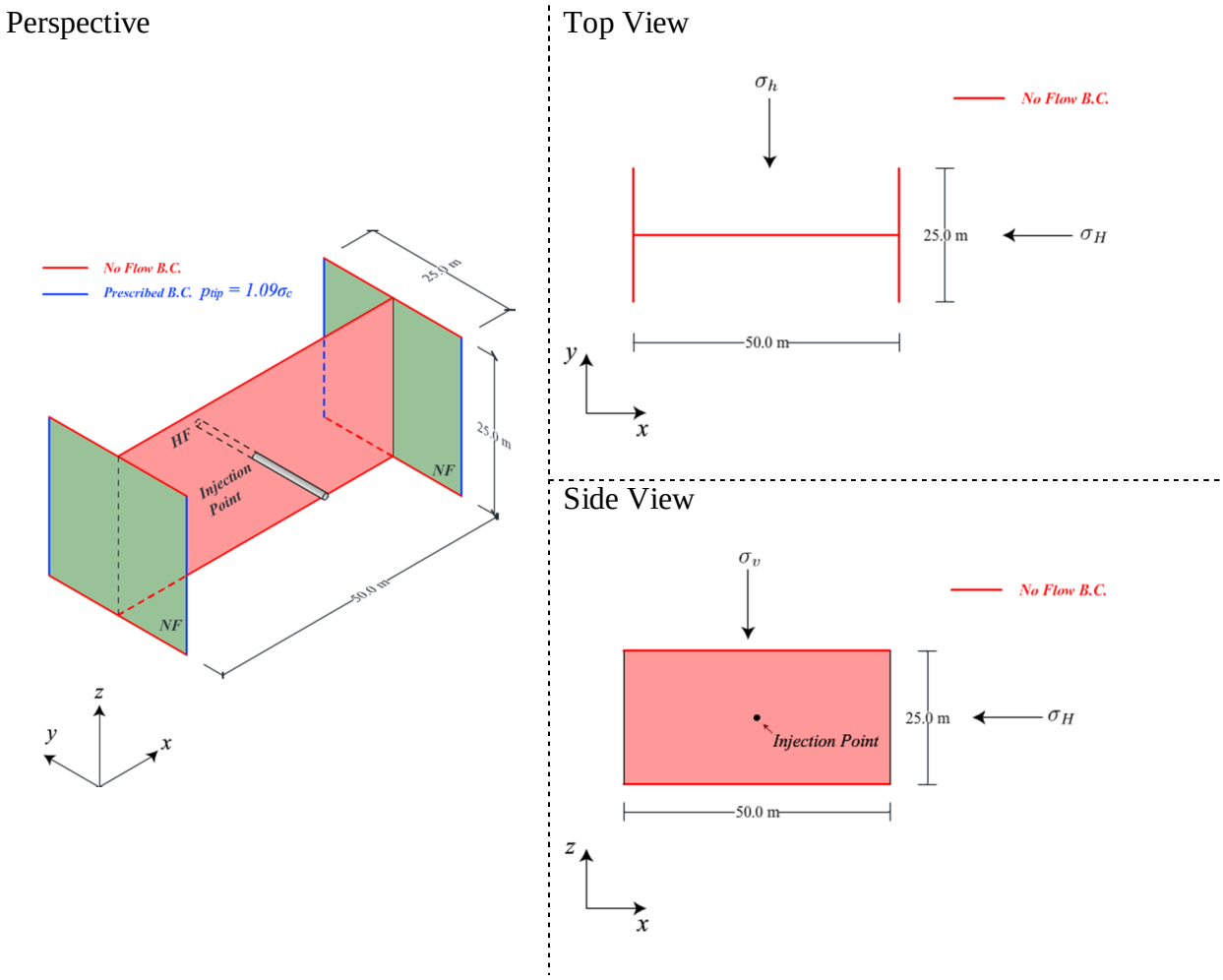

Figure 5-61. Geometry and boundary conditions for an H-shaped fracture network.

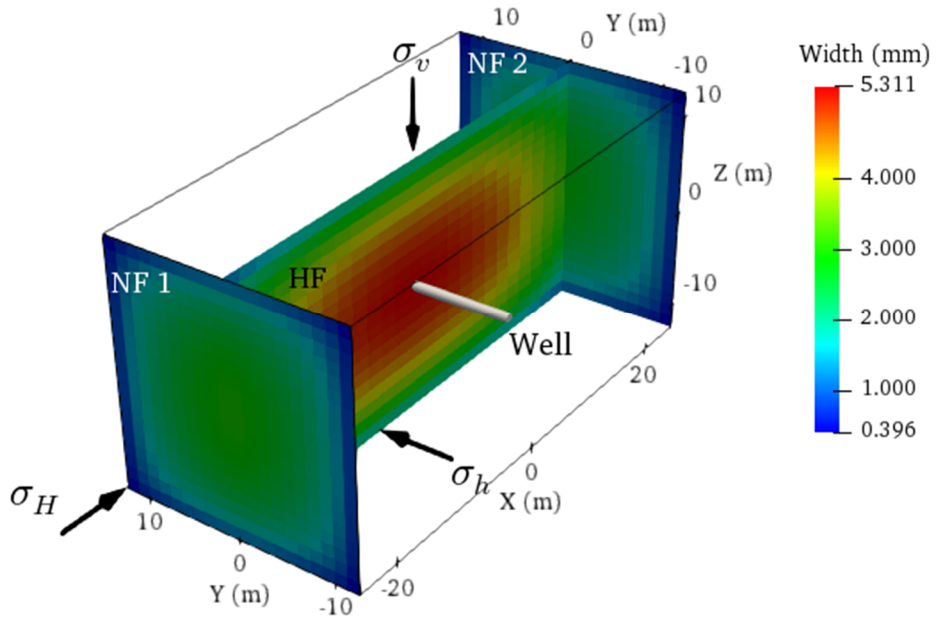

Figure 5-62. Fracture aperture distribution (perspective view) after an injection time of 212 s.

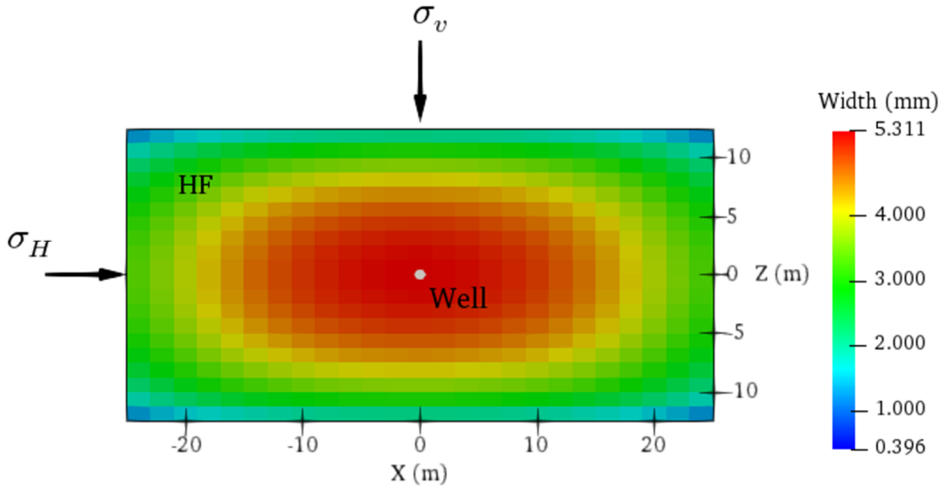

Figure 5-63. Fracture aperture distribution in the hydraulic fracture after an injection time of 212 s.

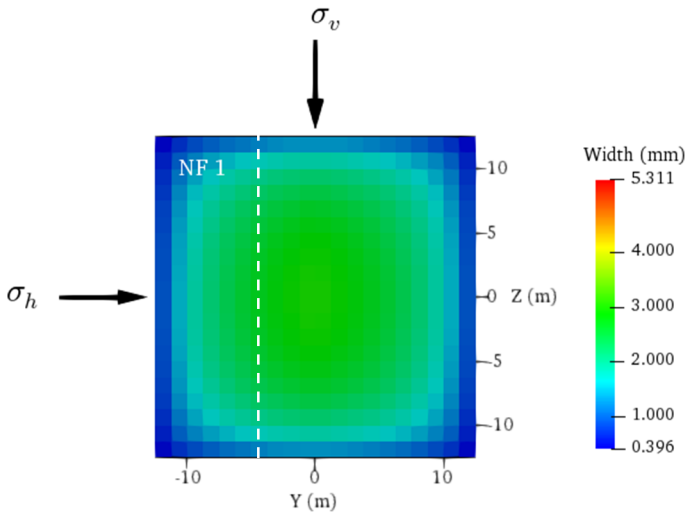

Figure 5-64. Fracture aperture distribution in the first natural fracture after an injection time of 212 s. Dotted white line shows intersection of the hydraulic and natural fracture.

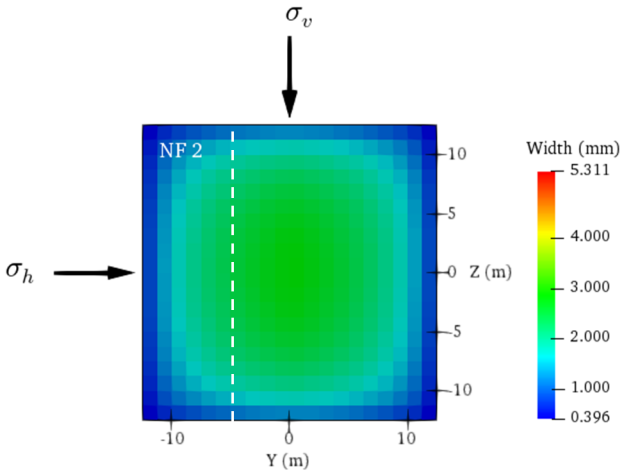

Figure 5-65. Fracture aperture distribution in the second natural fracture after an injection time of 212 s. Dotted white line shows intersection of the hydraulic and natural fracture.

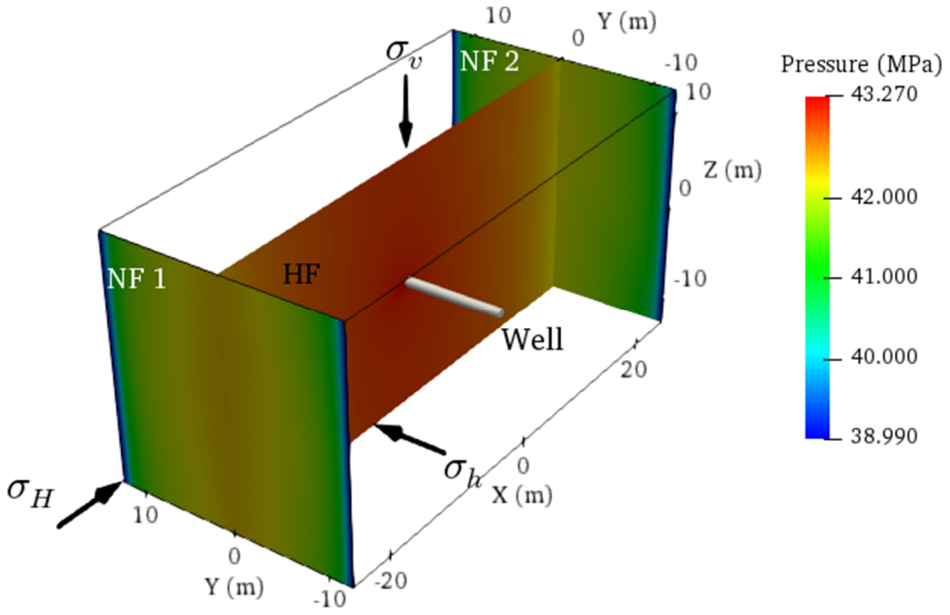

Figure 5-66. Pressure distribution (perspective view) an injection time of 212 s.

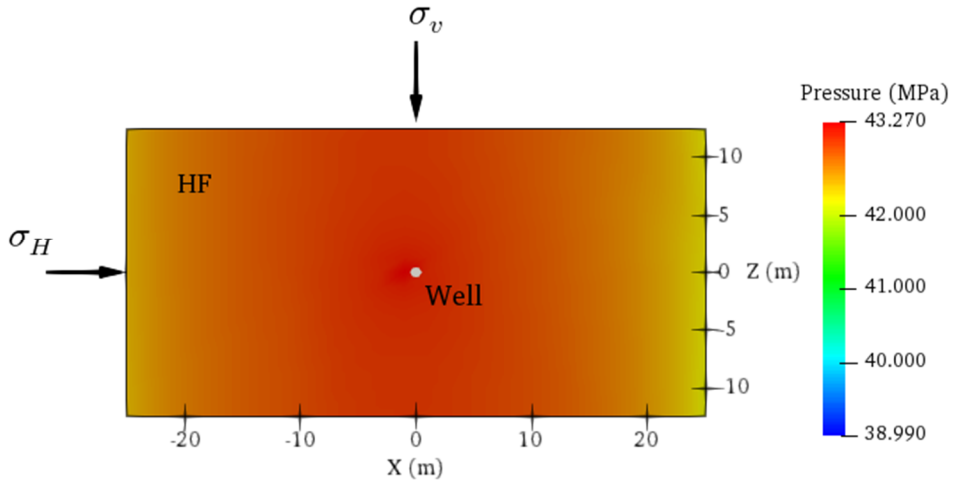

Figure 5-67. Pressure distribution in the hydraulic fracture an injection time of 212 s.

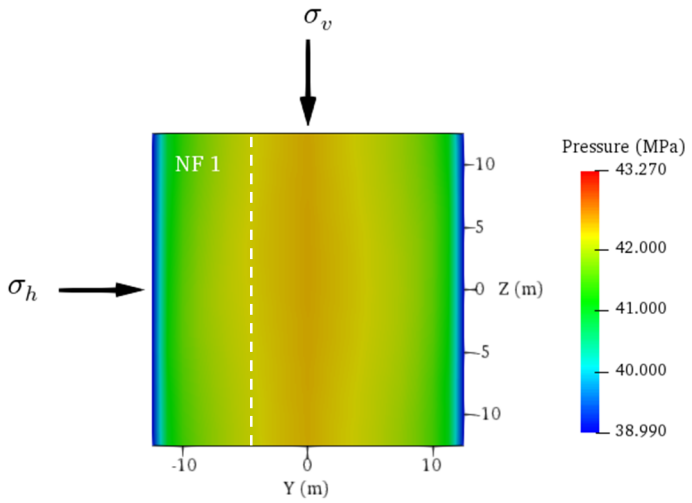

Figure 5-68. Pressure distribution in the first natural fracture an injection time of 212 s. Dotted white line shows intersection of the hydraulic and natural fracture.

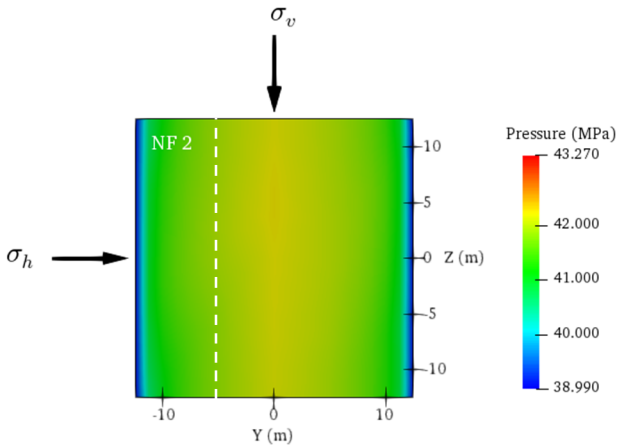

Figure 5-69. Pressure distribution in the second natural fracture an injection time of 212 s. Dotted white line shows intersection of the hydraulic and natural fracture.

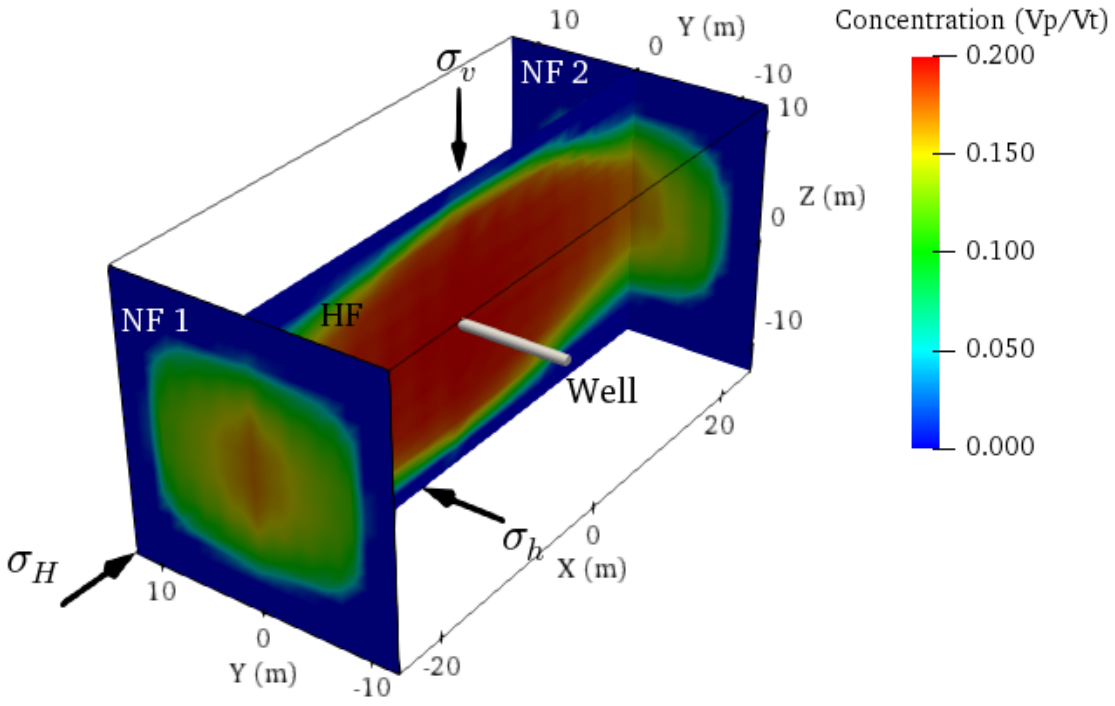

Figure 5-70. Proppant concentration distribution (perspective view) at an injection time of 212 s.

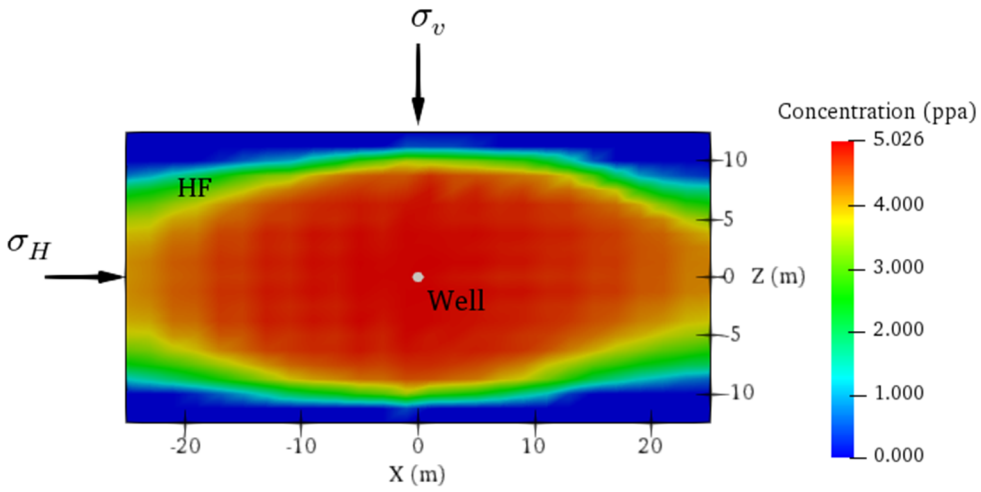

Figure 5-71. Proppant concentration distribution in the hydraulic fracture at an injection time of 212 s.

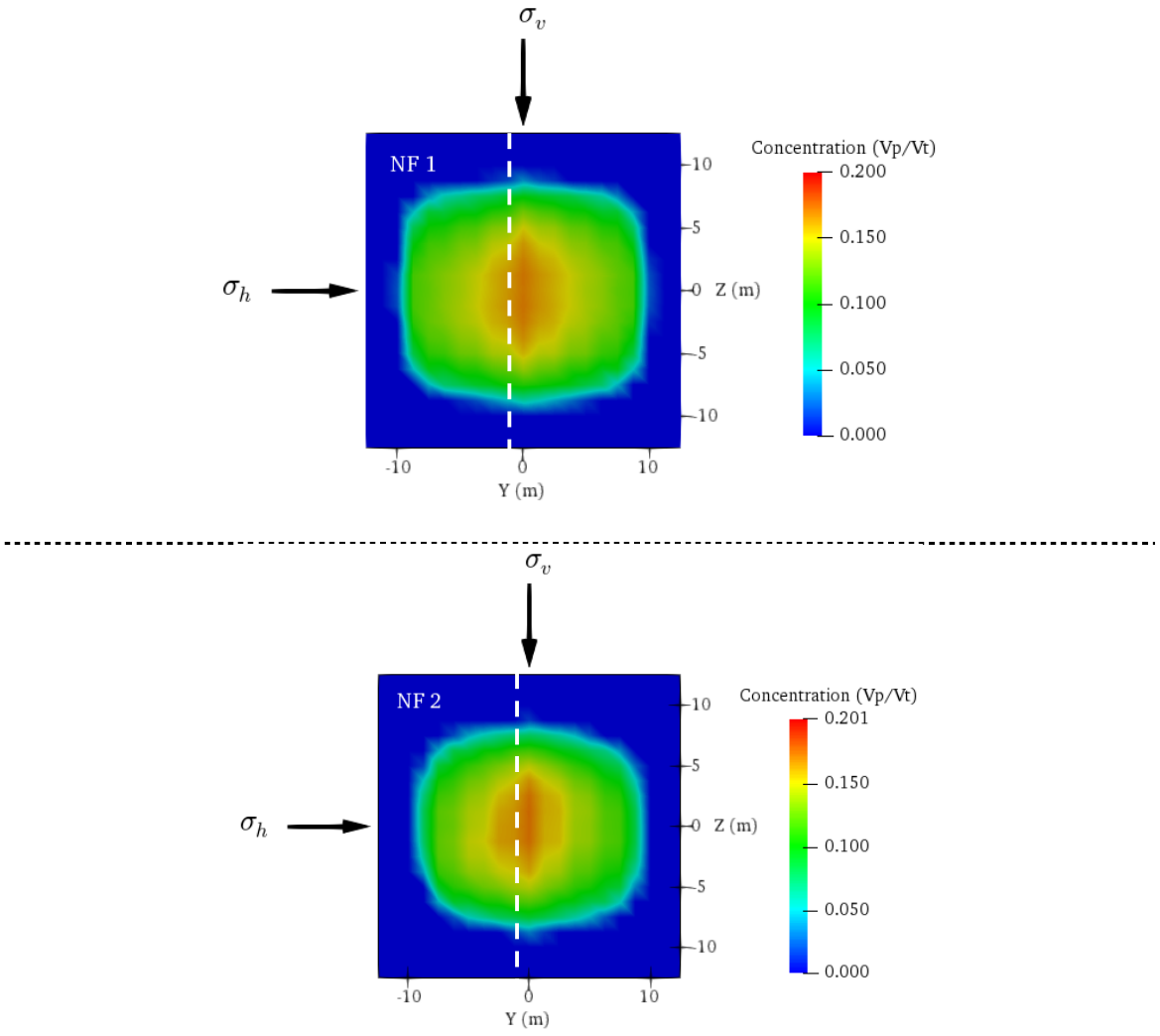

Figure 5-72. Proppant concentration distribution in the natural fractures at an injection time of 212 s. Dotted white line shows intersection of the hydraulic and natural fracture.

5.3. A Fracture Network Consisting of Three Hydraulic Fractures Intersecting Two Natural Fractures with Prescribed Fluid Pressure Boundary Condition in the NFs

In this example a preexisting static fracture network was assumed, the system is initially set to a fracture aperture value of 1e-5 m representing hydraulic aperture, then injection of clean fluid is simulated until the fracture aperture in the hydraulic fracture is enough to ensure proppant transport (greater than 3 times the proppant diameter). The network is composed of three hydraulic fractures simulating a hydraulic fracturing cluster from the same horizontal well which intercept two natural fractures. The spacing between hydraulic fractures is assumed equal to 20 m. The hydraulic fractures HF1 and HF2 are intersecting the natural fracture NF1 and the hydraulic fractures HF2 and HF3 are intersecting the natural fracture NF2 as shown in Fig. 5-74. The fluid injection rate is divided among the fractures in the proportion shown in Fig. 5-73. The pressure at the tips of the natural fractures are prescribed to be $1.09p_c$, where p_c is the closure pressure calculated by the simulator, this boundary condition is set to ensure a steep pressure gradient. The values of the parameter used in this simulation are listed in Table 5-2, and the total injection time is 320 s. In the hydraulic fractures, the proppant front is fully developed but in contrast, in the natural fractures there is a small amount of proppant being transported form the central hydraulic fracture (HF2). Also, the proppant contributed by hydraulic fractures HF1 and HF3 to the natural fractures NF1 and NF2 are flowing preferably away from the center of the system as shown in Figures 5-87 through 5-92, respectively. This can be explained if we consider the pressure distribution in the system. Note that in the natural fracture NF1 in the area between the intersections of the hydraulic fractures HF1 and HF2, the pressure gradient is not very steep, this is represented by the predominant yellow color as shown in Fig. 5-81, Fig. 5-85 and Fig. 5-86. Recall that the velocity

of the fluid and proppant is a function of the pressure gradient so that low velocity values are expected. As a consequence, small amount of proppant are transported to this area. In the area of the natural fracture NF1 between the intersection of the hydraulic fracture HF1 and the end of NF1, the pressure gradient is steeper assuring more efficient transport of proppant to this area. It is also instructive to note that the values of fracture aperture in the natural fractures are large enough to let the proppant flow into these areas as shown if Figures 5-75 through 5-80. In this case the decisive parameter affecting the proppant transport is the pressure distribution.

Table 5-2. Data considered to perform the proppant transport simulations

Property	**Value**	**Unit**
Fluid injection rate (Q)	0.15	m^3/s
Poisson's ratio (v)	0.29	
Young's modulus (E)	27.1	GPa
Fluid density (ρ_f)	1000	Kg/m^3
Fluid viscosity (μ_f)	0.1	Pa.s
Proppant density (ρ_p)	2400	Kg/m^3
Proppant injection volume fraction	0.2	
Carter's leak-off coefficient	1.50E-07	$m/s^{0.5}$
Vertical stress (σ_v)	48	MPa
Minimum horizontal stress (σ_h)	38	MPa
Maximum horizontal stress (σ_H)	39.5	MPa

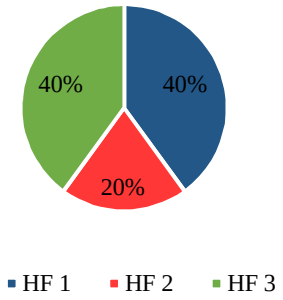

Figure 5-73. Proportions of injection rate assigned to each hydraulic fracture.

Perspective

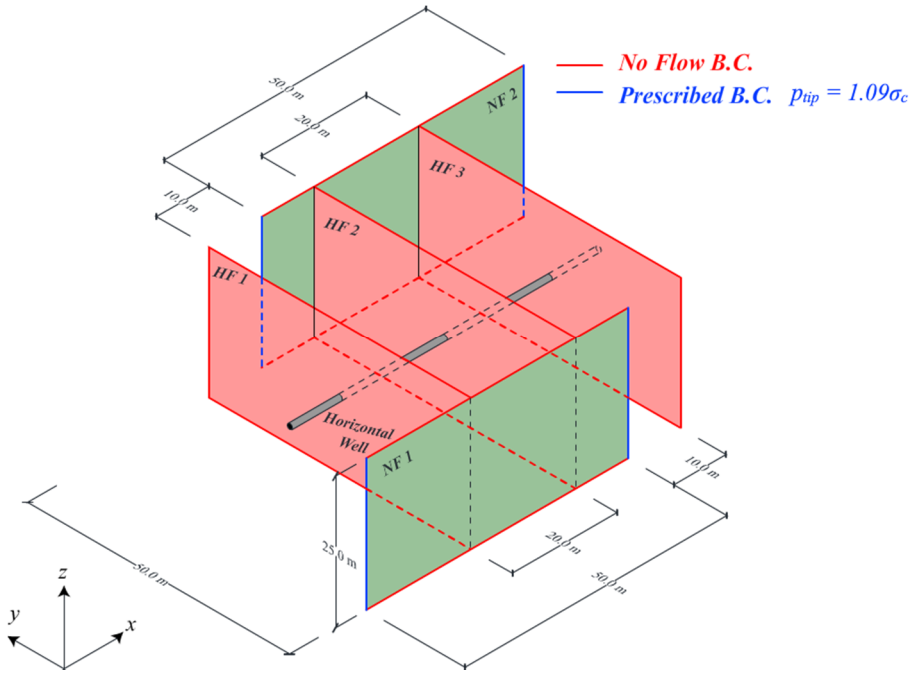

Top View

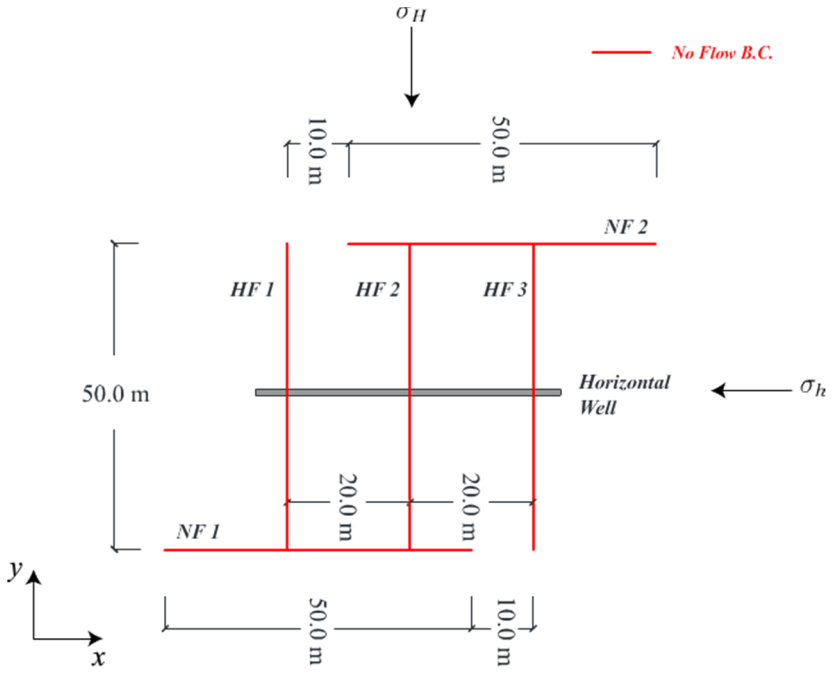

Side View

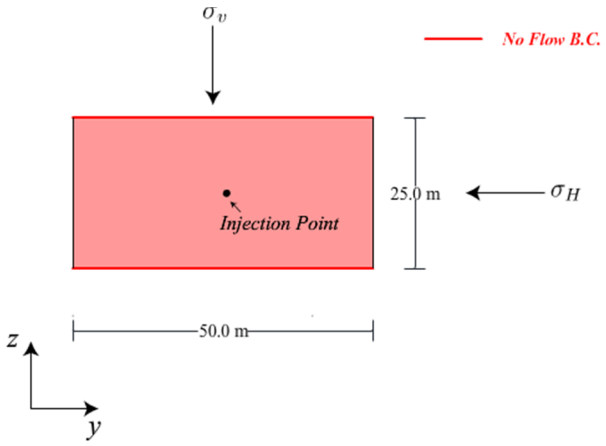

Figure 5-74. Geometry and boundary conditions for a complex fracture network.

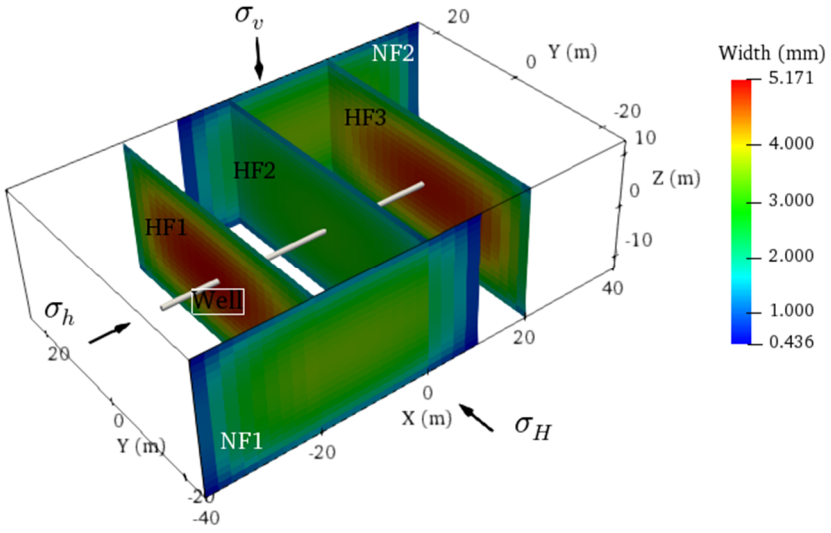

Figure 5-75. Fracture aperture distribution (perspective view) after an injection time of 320 s.

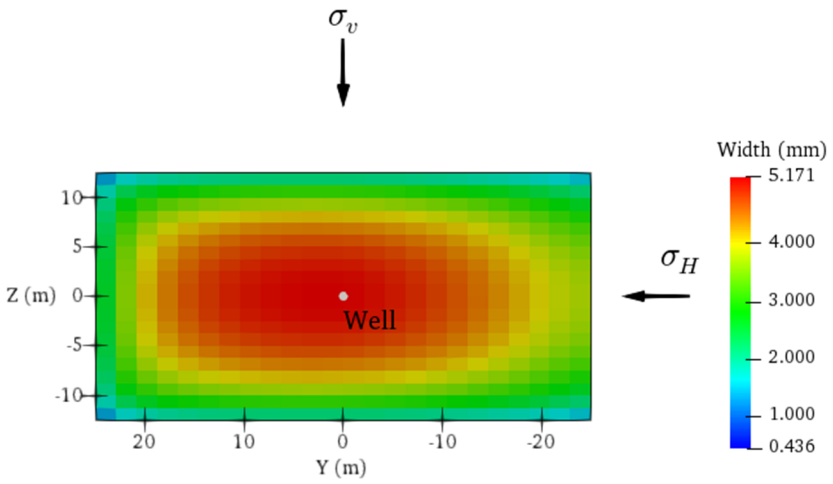

Figure 5-76. Fracture aperture distribution in the first hydraulic fracture after an injection time of 320 s.

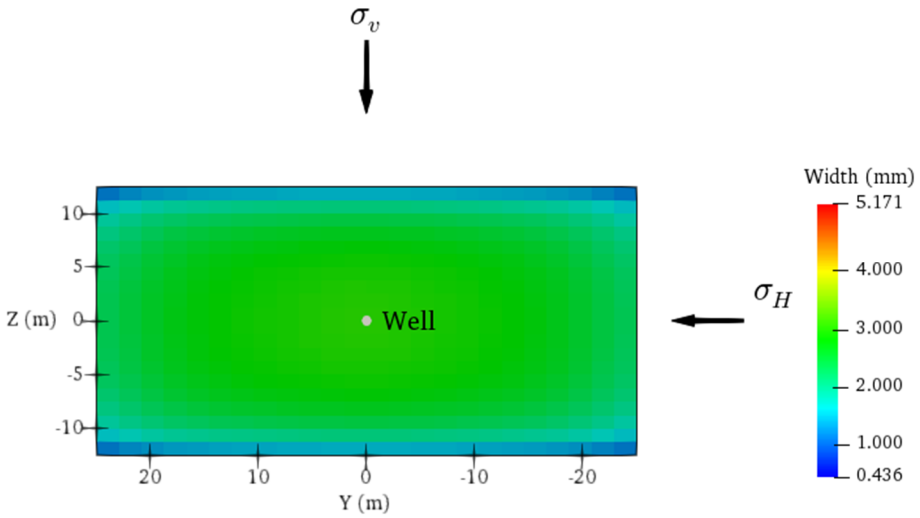

Figure 5-77. Fracture aperture distribution in the second hydraulic fracture after an injection time of 320 s.

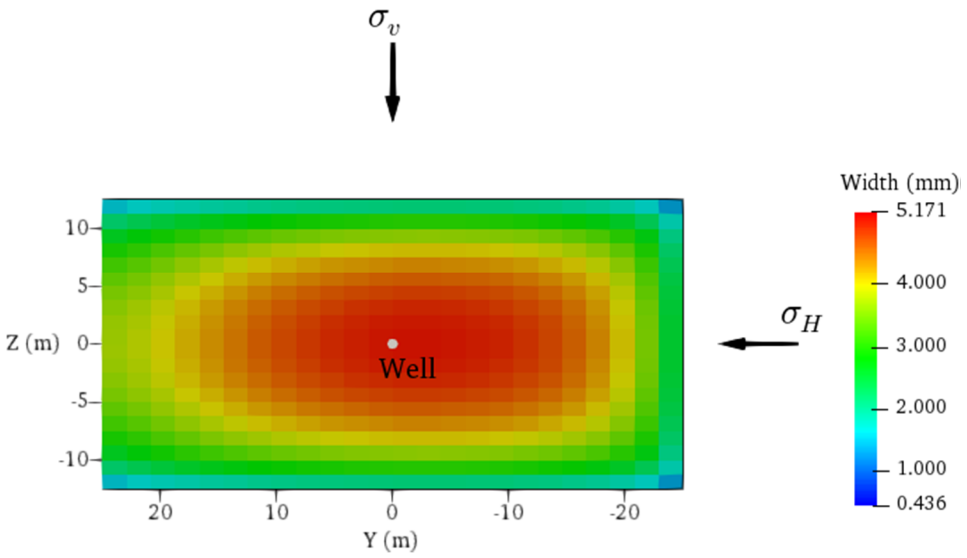

Figure 5-78. Fracture aperture distribution in the third hydraulic fracture after an injection time of 320 s.

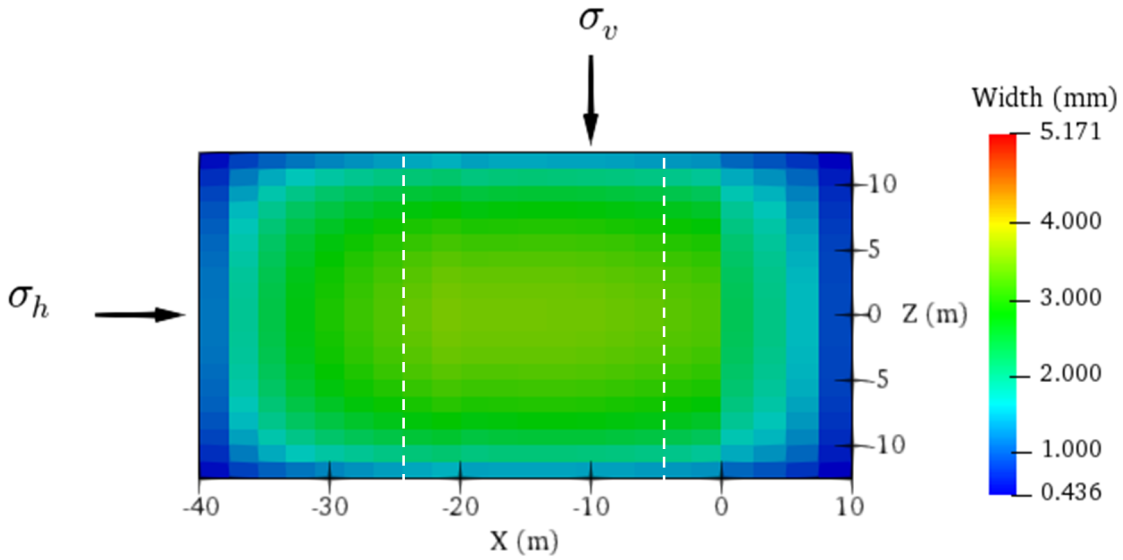

Figure 5-79. Fracture aperture distribution in the first natural fracture after an injection time of 320 s. Dotted white line shows intersection of the hydraulic and natural fracture.

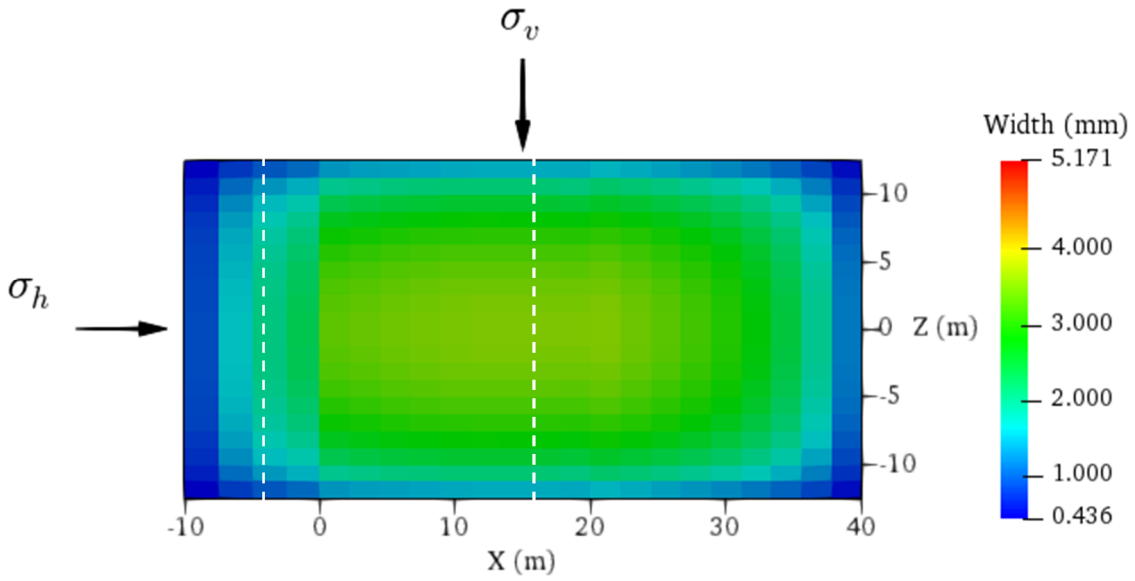

Figure 5-80. Fracture aperture distribution in the second natural fracture after an injection time of 320 s. Dotted white line shows intersection of the hydraulic and natural fracture.

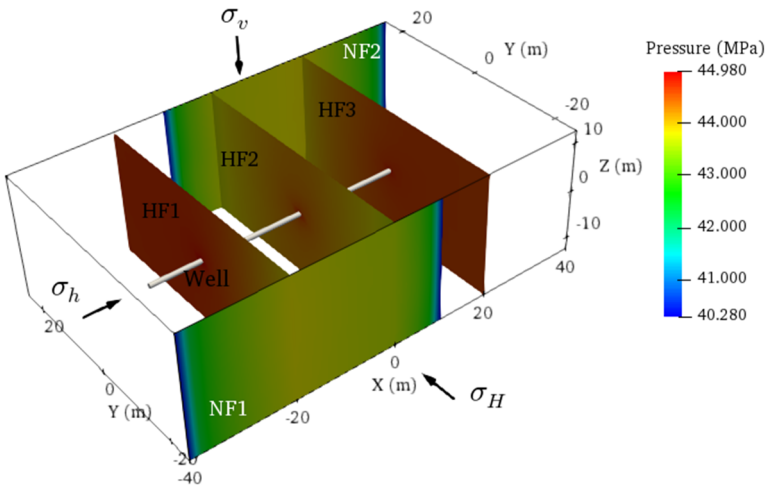

Figure 5-81. Pressure distribution (perspective view) after an injection time of 320 s.

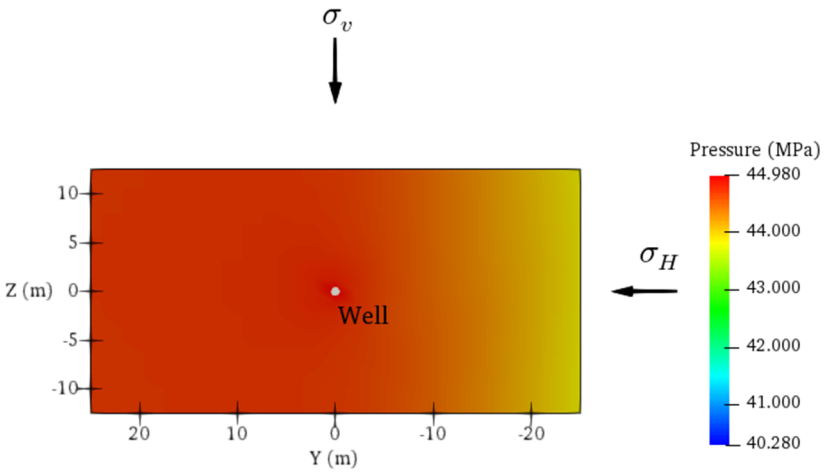

Figure 5-82. Pressure distribution in the first hydraulic fracture after an injection time of 320 s.

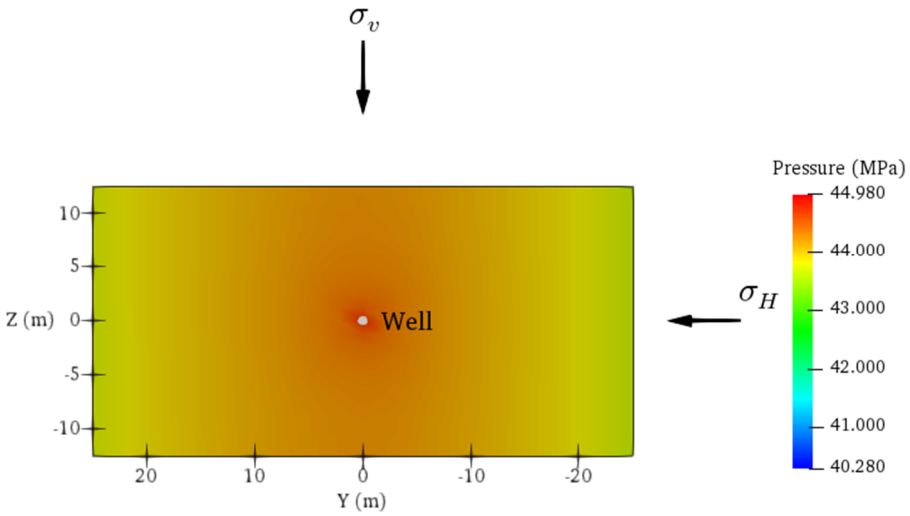

Figure 5-83. Pressure distribution in the second hydraulic fracture after an injection time of 320 s.

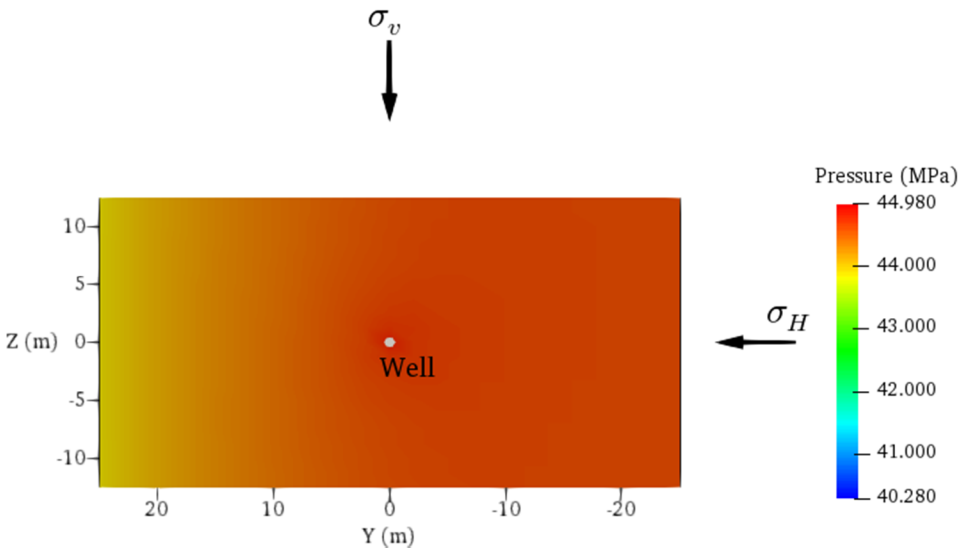

Figure 5-84. Pressure distribution in the in the third hydraulic fracture after an injection time of 320 s.

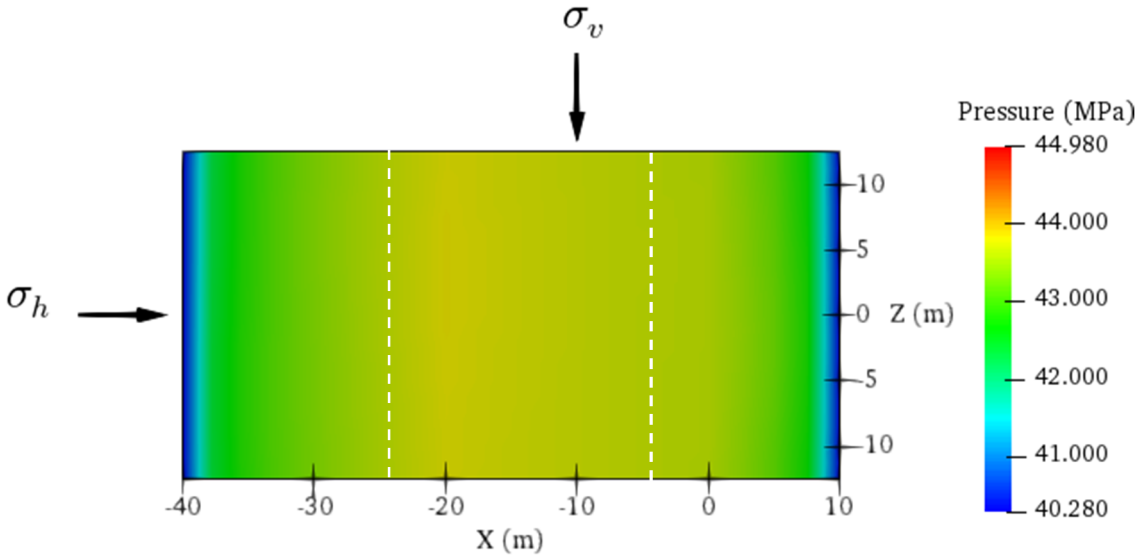

Figure 5-85. Pressure distribution in the first natural fracture after an injection time of 320 s. Dotted white line shows intersection of the hydraulic and natural fracture.

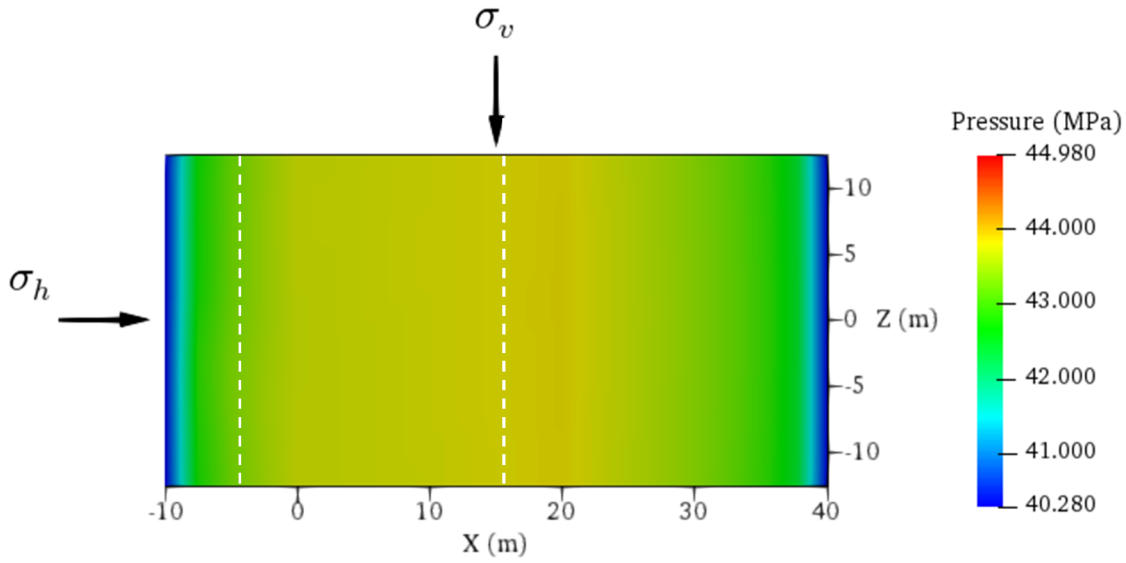

Figure 5-86. Pressure distribution in the in the second natural fracture after an injection time of 320 s. Dotted white line shows intersection of the hydraulic and natural fracture.

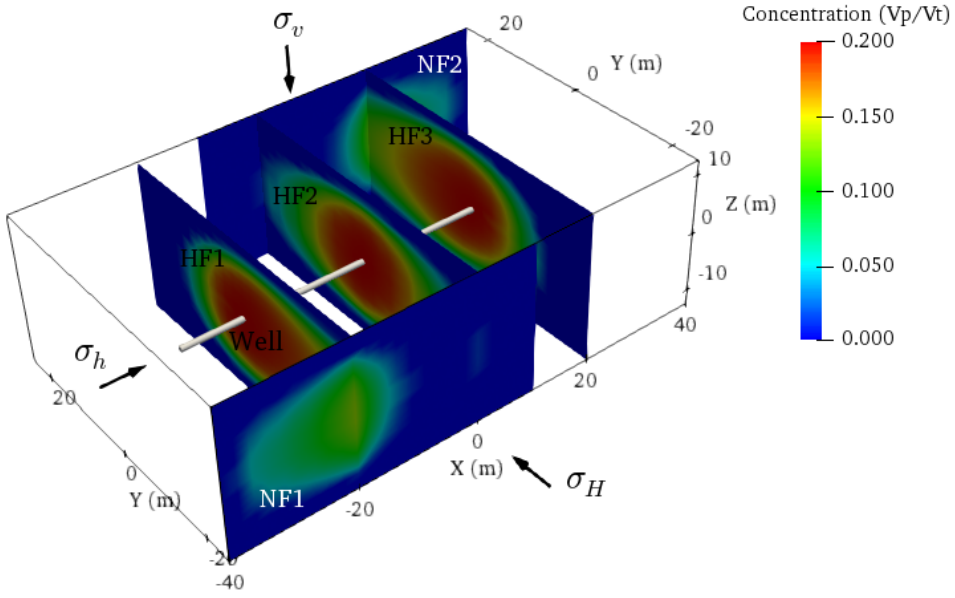

Figure 5-87. Proppant concentration distribution (perspective view) after an injection time of 320 s.

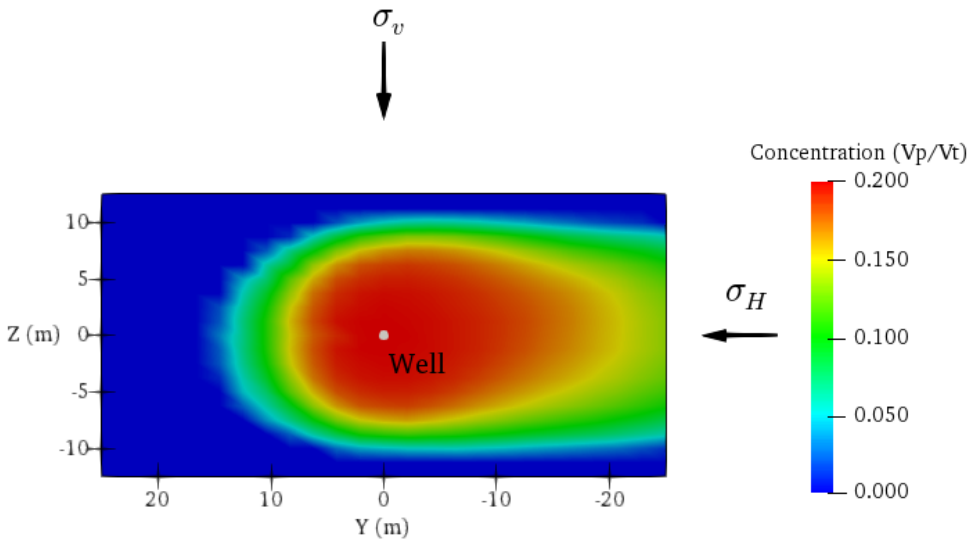

Figure 5-88. Proppant concentration distribution in the first hydraulic fracture after an injection time of 320 s.

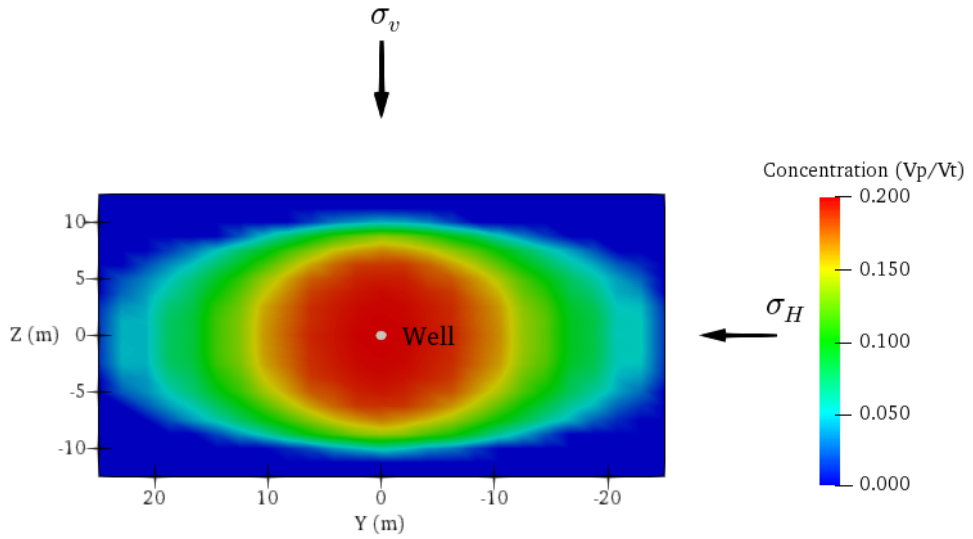

Figure 5-89. Proppant concentration distribution in the second hydraulic fracture after an injection time of 320 s.

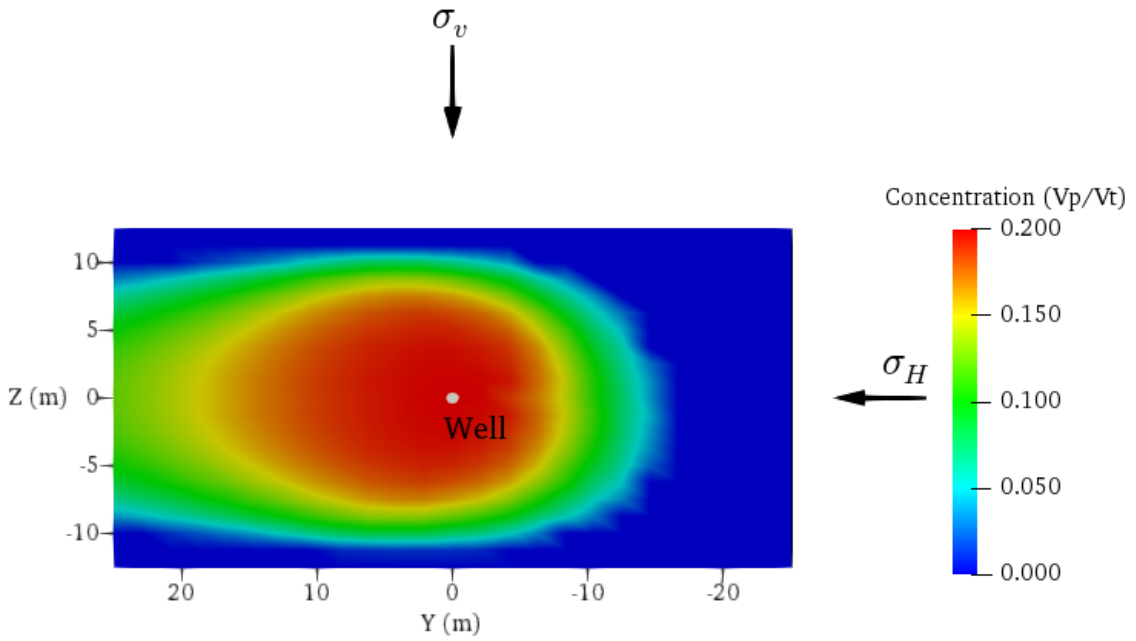

Figure 5-90. Proppant concentration distribution in the third hydraulic fracture after an injection time of 320 s.

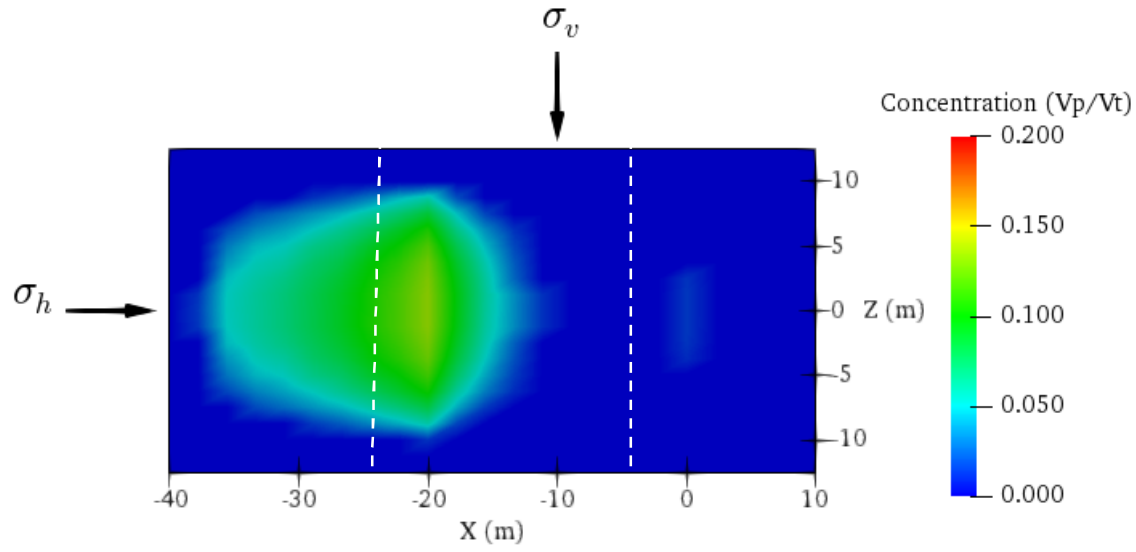

Figure 5-91. Proppant concentration distribution in the first natural fracture after an injection time of 320 s. Dotted white line shows intersection of the hydraulic and natural fracture.

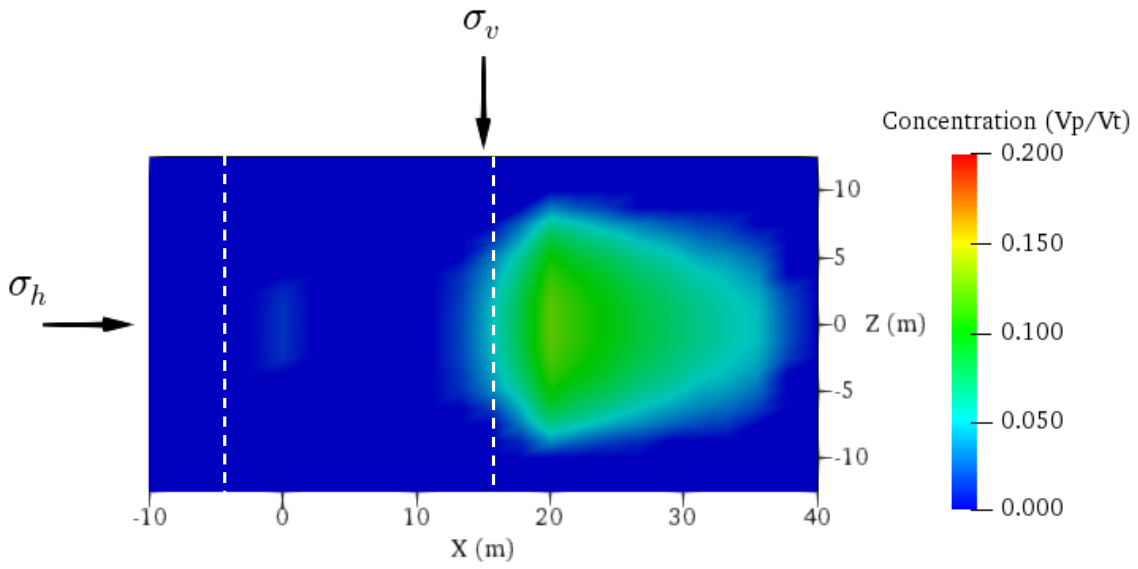

Figure 5-92. Proppant concentration distribution in the second natural fracture after an injection time of 320 s. Dotted white line shows intersection of the hydraulic and natural fracture.

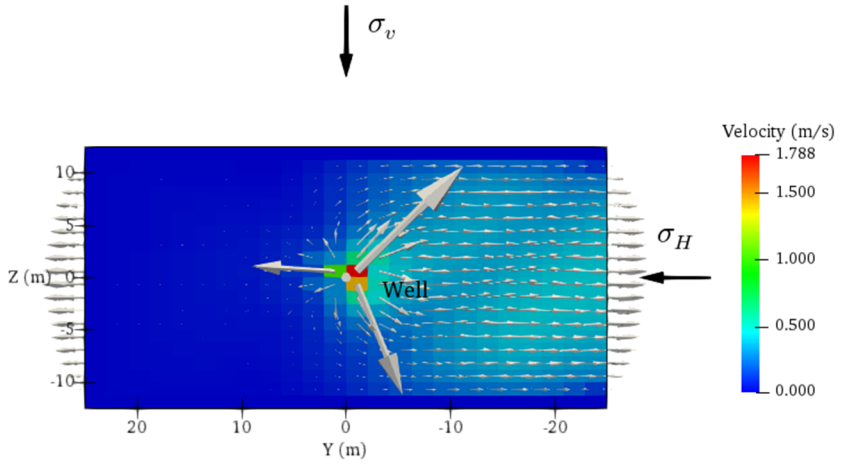

Figure 5-93. Fluid velocity distribution in the first hydraulic fracture after an injection time of 320 s.

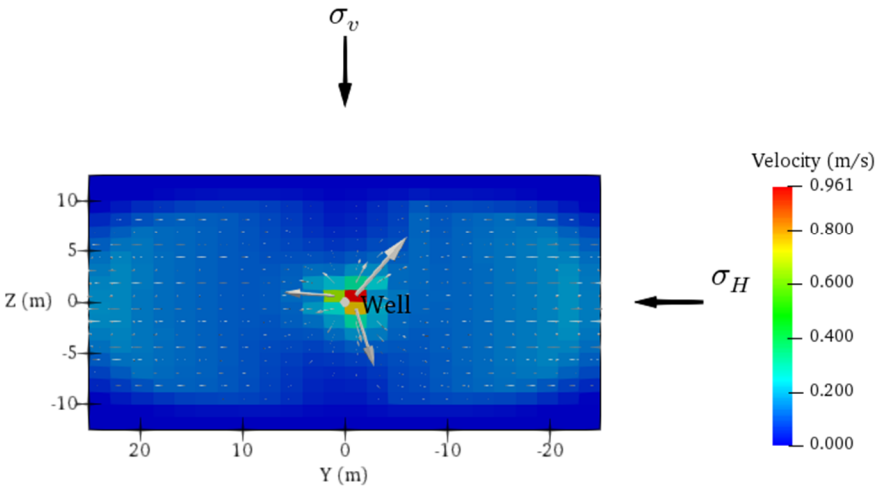

Figure 5-94. Fluid velocity distribution in the second hydraulic fracture after an injection time of 320 s.

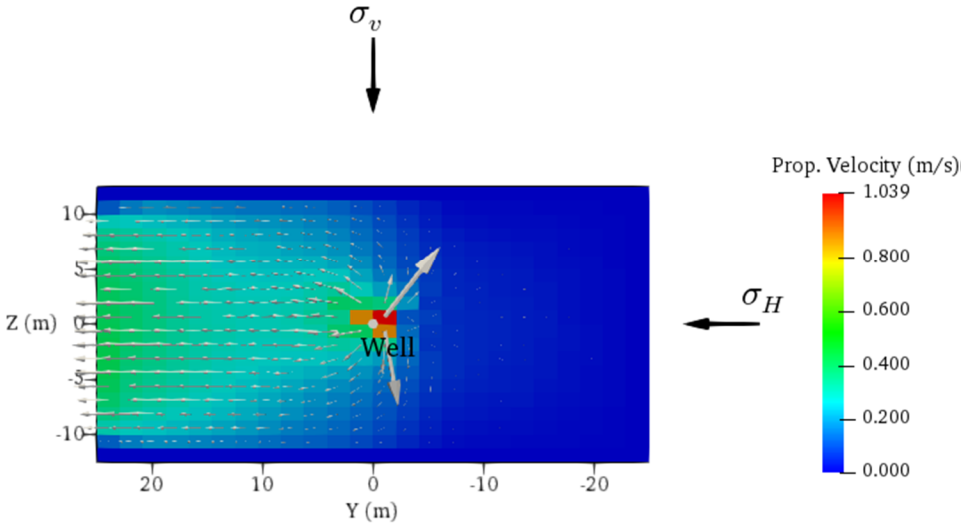

Figure 5-95. Fluid velocity distribution in the in the third hydraulic fracture after an injection time of 320 s.

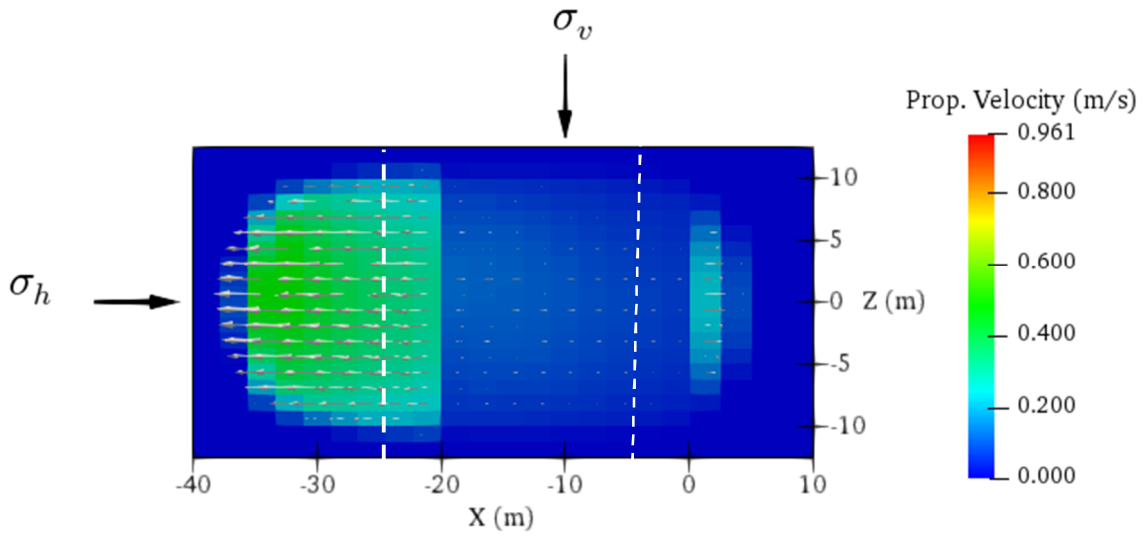

Figure 5-96. Fluid velocity distribution in the first natural fracture after an injection time of 320 s.

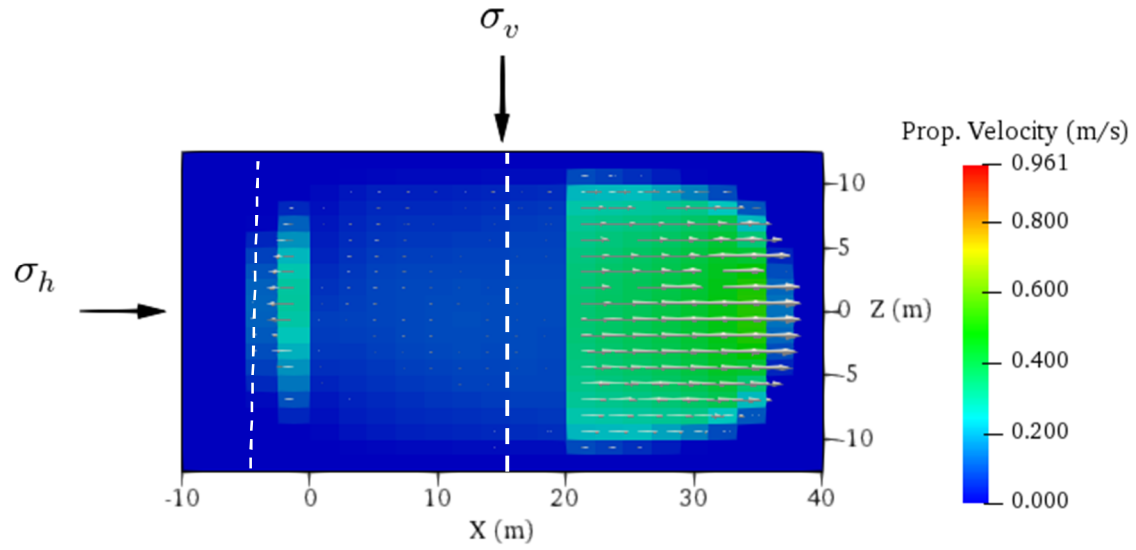

Figure 5-97. Fluid velocity distribution in the in the second natural fracture after an injection time of 320 s.

Summary and Conclusions

A module to estimate the proppant transport and deposition inside a hydraulic fracture has been developed. Instead of solving the flow of fracturing fluid and the flow of proppant separately, the movement of a composed system, the slurry, was analyzed, and then the volume of fracturing fluid and the volume of proppant was estimated with the variable concentration. The governing equation for the proppant transport inside a hydraulic fracture was derived using the principle of mass balance, the domain describing the fractures was discretized geometrically using rectangles, and later the governing equation was spatially semi-discretized with the Finite Element Method (FEM), this governing equation is classified as an advective equation then the Streamline Upwind Petrov Galerkin (SUPG) stabilization was implemented to smooth the numerical instability characteristic of this type of equations, finally for the time discretization and implicit scheme was implemented which is more stable and allows bigger time steps. This study considered the following assumption (1) Static fracture networks with no propagation, (2) All the fractures are completely open before the proppant is injected, (3) Homogeneous and isotropic rock mass, (4) The fracturing fluid is Newtonian, (5) Fluid velocity in laminar regime (lubrication theory holds), (6) Proppant particles and fracturing fluid are incompressible, (7) Proppant particles are spherical with equal sizes and (8) The diameter of proppant particles is much smaller than the width of the fracture. The model was first verified using the method of manufactured solutions and additionally the model was tested varying the elements sizes of the grid used to discretize the fractures to verify convergence and stability. A sensitivity analysis was performed to investigate the limits of the model and the impact in the solutions of fracture width, fluid pressure and proppant distribution of parameters like proppant size, fluid viscosity and simulation grid size. The proppant transport inside a

hydraulic fracture is not an isolated phenomena, to solve it, the parameters fractured width distribution and fracturing fluid pressure are needed as input. For cases of single fractures, a coupled scheme using the Displacement Discontinuity method (DD) and Finite Element Method (FEM) was used to estimate fracture width and fracturing fluid pressure distributions. To study more complex cases where the system is a fracture network composed by hydraulic fractures and natural fractures, the proppant transport algorithm was then implemented in a 3D hydraulic fracture model (GeoFrac-3D) which calculates rock matrix deformation and fluid flow in fractures and can handle the physics involved in a fully 3D hydraulic fracturing problem. The conclusions of this project are:

1. In the cases studied, higher values of fluid viscosity led to better distribution of the proppant. When the simulation was performed with lower values of fluid viscosity, the velocity field was more affected by the settling velocity leading to shorter proppant fronts with higher concentration of proppant towards the bottom of the fracture
2. In the cases studied, larger proppant size such as 20/40 mesh size are more affected by the settling velocity, creating a shorter proppant front with higher values of proppant concentration towards the bottom of the systems of fractures. Smaller sizes of proppant like 40/70 mesh size, showed a longer and more homogeneous proppant front.
3. The proppant is transported in the path traced by the velocity field, the velocity field is affected by the pressure gradient and the width of the fracture. Simulation showed that the velocity field is affected by the settling velocity in a greater measure in zones of low fluid velocity. In high fluid velocity zones, especially close to the injection point, the effect of the settling velocity is limited. In the cases studied the pressure drop caused by the

perforation roughness was not considered, this additional pressure drop might cause proppant settling.

4. In the cases studied, the model captures deposition in zones of low velocities. Low velocities are caused either by small values of fracture aperture or small values in pressure gradient. Small values of fracture aperture can be found in areas closer to the tip of the fracture, inside natural fractures, or in zones greatly affected by the stress shadow produced by adjacent fractures. Small values of pressure gradient can be found in intermediate zones from the injection point inside hydraulic fractures or in zones where the flow from two fractures are meeting and canceling each other.
5. In the cases studied, the stress shadow among fractures greatly affected the final width distribution. This phenomenon was more pronounced in cases were the interception between hydraulic fractures and natural fractures was not perpendicular. Three different rotation angles were studied, 0°, 30° and 45°; comparing the case of 0° and the case of 45°, the volume of proppant entering the natural fracture was cut down almost by half for the case of 45°, as shown in Fig. 5-60.

Recommendations

As stated in Chapter 3, a number of simplifying assumptions have been considered in this study to solve the fracture aperture, fracturing fluid pressure and proppant concentration. The major ones are: static fracture networks with no propagation with all fractures are completely open before proppant injection; the fracturing fluid is Newtonian, incompressible and the flow is laminar with uniform proppant size and incompressible particles and after all the experience gathered in the

analysis of single fractures and fractures networks carried out in this work, the following recommendations are appropriate to enhance the understanding of the proppant transport in deformable networks composed by hydraulic fractures and natural fractures:

1. Proppant distribution calculation inside hydraulic fractures while they propagate
2. Consider non-Newtonian fluid

References

Acharya, A. R. (1984). Particle Transport in Viscous and Viscoelastic Fracturing Fluids. *SPE - Annual Technical Conference and Exhibition*.

Adachi, J., Siebrits, E., Peirce, A., & Desroches, J. (2007). Computer simulation of hydraulic fractures. *International Journal of Rock Mechanics & Mining Sciences, 44*, 739–757. https://doi.org/10.1016/j.ijrmms.2006.11.006

Anderson, J. D. (1995). Computational Fluid Dynamics: The Basics with Applications. *McGrawhill Inc*. https://doi.org/10.1017/CBO9780511780066

Batchelor, G. K. (1967). *An Introduction to Fluid Dynamics. Cambridge University Press*. https://doi.org/https://doi.org/10.1017/CBO9780511800955

Biot, M. A., & Medlin, W. L. (1985). Theory of Sand Transport in Thin Fluids. *SPE 60th Annual Technical Conference and Exhibition of the Society of Petroleum Engineers*.

Boyer, F., Guazzelli, E., & Pouliquen, O. (2011). Unifying Suspension and Granular Rheology. *Physical Review Letters*, 1–5. https://doi.org/10.1103/PhysRevLett.107.188301

Brooks, A. N., & Hughes, T. J. R. (1982). Streamline upwind/Petrov-Galerkin formulations for convection dominated flows with particular emphasis on the incompressible Navier-Stokes equations. *Computer Methods in Applied Mechanics and Engineering*, *32*(1–3), 199–259. https://doi.org/10.1016/0045-7825(82)90071-8

Chakra, R. (2012). *3D Modeling of Coupled Rock Deformation and Thermo-Poro Mechanical Processes in Fractures*. (PhD. Dissertation) Texas A&M University.

Clark, P. (1996). Convective Transport of Proppant Agents During Hydraulic Fracturing. *SPE Eastern Regional Meating*, 229–235.

Clifton, R., Brown, U., & Wang, J.-J. (1988). Multiple Fluids, Proppant Transport, and Thermal Effects in Three-Dimensional Simulation of Hydraulic Fracturing. *63rd Annual Technical Conference and Exhibition*, 175–188.

Crouch, S. L., & Starfield, A. M. (1983). *Boundary Element Methods in Solid Mechanics*. George Allen & Unwin.

Dahl, J., Nguyen, P., Dusterhoft, R., Calvin, J., & Siddiqui, S. (2015). Application of micro-proppant to enhance well production in unconventional reservoirs: Laboratory and field results. *SPE Western Regional Meeting 2015: Old Horizons, New Horizons Through Enabling Technology*, 923–946.

Daneshy, A. A. (1978). Numerical Solution of Sand Transport in Hydraulic Fracturing. *Journal of Petroleum Technology*, 132–140.

Donea, J., & Huerta, A. (2004). *Finite Element Methods for Flow Problems*. Wiley.

Dontsov, E. V., & Peirce, a. P. (2014a). Slurry flow, gravitational settling and a proppant transport model for hydraulic fractures. *Journal of Fluid Mechanics*, *760*, 567–590. https://doi.org/10.1017/jfm.2014.606

Dontsov, E. V., & Peirce, A. P. (2014b). The effect of proppant size on hydraulic fracturing by a slurry. *48th US Rock Mechanics / Geomechanics Symposium*.

Dontsov, E. V., & Peirce, A. P. (2015). Proppant transport in hydraulic fracturing: Crack tip screen-out in KGD and P3D models. *International Journal of Solids and Structures*, *63*, 206–218. https://doi.org/10.1016/j.ijsolstr.2015.02.051

Engelder, T., Lash, G. G., & Uzcátegui, R. S. (2009). Joint sets that enhance production from Middle and Upper Devonian gas shales of the Appalachian Basin. *AAPG Bulletin*, *93*(7), 857–889. https://doi.org/10.1306/03230908032

Evans, M. A. (1994). Joints and decollement zones in Middle Devonian shales: evidence for multiple deformation events in the central Appalachian Plateau. *Geological Society of America Bulletin*, *106*(4), 447–460.

Fisher, M. K., Wright, C. A., Davidson, B. M., Goodwin, A. K., Fielder, E. O., Buckler, W. S., & Steinsberger, N. P. (2002). Integrating Fracture Mapping Technologies to Optimize Stimulations in the Barnett Shale. *SPE Annual Technical Conference and Exhibition*. https://doi.org/10.2118/77441-MS

Fritz, J. (1982). *Partial Differential Equations*. Springer.

Gadde, P. B., & Sharma, M. M. (2005). The Impact of Proppant Retardation on Propped Fracture Lengths. *SPE Annual Technical Conference and Exhibition*.

Gadde, P. B., Yajun, L., Jay, N., Roger, B., & Sharma, M. (2004). Modeling Proppant Settling in Water-Fracs. *Proceedings of SPE Annual Technical Conference and Exhibition*. https://doi.org/10.2523/89875-MS

Gale, J. F. W., Reed, R. M., & Holder, J. (2007). Natural fractures in the Barnett Shale and their importance for hydraulic fracture treatments. *AAPG Bulletin*, *91*(4), 603–622. https://doi.org/10.1306/11010606061

Ghassemi, A. (2003). A Thermoelastic Hydraulic Fracture Design Tool for Geothermal Reservoir Development.

Goodman, R. (1989). *Introduction to Rock Mechanics*. Wiley.

Gu, H. (1987). *A study of propagation of hydraulically induced fractures*. (PhD Dissertation) The University of Texas at Austin.

Howard, G. C., & Fast, C. R. (1970). *Hydraulic fracturing. SPE monographVol. 2, Henry L. Doherty series.*

Irwin, G. R. (1957). Analyses of stresses and strains near the end of a crack transversing a plate. *J. Appl. Mech*, 361–364.

Kern, L. R., Perkins, T. K., & Wyant, R. E. (1959). The Mechanics of Sand Movement In Fracturing. *AIME Thecnical Note 2037*, 55–57.

Kullman, J. (2011). The complicated world of proppant selection.

Kumar, D., Gonzalez, R.A., and Ghassemi, A. (2018). The Role of Mirco-proppants in Conductive Fracture Network Development. *SPE Hydraulic Fracturing Technology Conference and Exhibition, Woodlands, Texas, USA*, 1–20.

Kumar, D., & Ghassemi, A. (2015). 3D Simulation of Mixed-Mode Poroelastic Fracture Propagation for Reservoir Stimulation. *GRC Transactions*, *39*, 937–946.

Kumar, D., & Ghassemi, A. (2016). A three-dimensional analysis of simultaneous and sequential fracturing of horizontal wells. *Journal of Petroleum Science and Engineering*, *146*, 1006–1025. https://doi.org/10.1016/j.petrol.2016.07.001

Kumar, D., & Ghassemi, A. (2018). Three-Dimensional Poroelastic Modeling of Multiple Hydraulic Fracture Propagation from Horizontal Wells. *International Journal of Rock Mechanics and Mining Sciences*, *105*(December 2017), 192–209. https://doi.org/10.1016/j.ijrmms.2018.01.010

Lavrov, A. (2011). Models for proppant transport and deposition in hydraulic fracture simulation: A review of the state of the art. *SINTEF Petroleum Research Report*.

Novotny, E. J. (1977). Proppant Transport. *52nd Annual Fall Technical Conference and Exhibition of the Society of Petroleum Engineers of AIME*.

Osiptsov, A. A. (2017). Fluid Mechanics of Hydraulic Fracturing : a Review. *Journal of Petroleum Science and Engineering*, *156*(May), 513–535. https://doi.org/10.1016/j.petrol.2017.05.019

Ouyang, S. (1994). *Propagation of hydraulically induced fractures with proppant transport*. (PhD Dissertation) The University of Texas at Austin. https://doi.org/10.16953/deusbed.74839

Ouyang, S., Carey, G. F., & Yew, C. H. (1997). An adaptive finite element scheme for hydraulic fracturing with proppant transport. *International Journal for Numerical Methods in Fluids*, *24*(7), 645–670. https://doi.org/10.1002/(sici)1097-0363(19970415)24:7<645::aid-fld458>3.0.co;2-z

Pearson, J. R. A. (1994). On suspension transport in a fracture : framework for a global model. *Journal of Non-Newtonian Fluid Mechanics*, *54*, 503–513.

Roache, P. J. (1998). *Verification and Validation in Computational Science and Engineering*. Hermosa Pub.

Roache, P. J. (2002). Code Verification by the Method of Manufactured Solutions. *Journal of*

Fluids Engineering, 4–10. https://doi.org/10.1115/1.1436090

Safari, R. (2013). *Thermo-Hydro-Mechanical Analysis of Fractures and Wellbores in Petroleum / Geothermal Reservoirs*. (PhD Dissertation) Texas A&M University.

Sahai, R., Miskimins, J. L., & Olson, K. E. (2014). Laboratory Results of Proppant Transport in Complex Fracture Systems. *Hydraulic Fracturing Technology Conference*. https://doi.org/10.2118/168579-MS

Salari, K., & Knupp, P. (2000). Sandia Report: Code Verification by the Method of Manufactured Solutions.

Sesetty, V., & Ghassemi, A. (2017). COMPLEX FRACTURE NETWORK MODEL FOR STIMULATION OF UNCONVENTIONAL RESERVOIRS. *ARMA17 - 51st US Rock Mechanics / Geomechanics Symposium*.

Sesetty, V., & Ghassemi, A. (2018). Hydraulic Fracture Propagation in Naturally Fractured Anisotropic Shale. *ARMA18 - 52nd US Rock Mechanics / Geomechanics Symposium*.

Shook, C. A., & Roco, M. C. (1991). *Slurry Flow: Principles and Practice*. Elsevier Inc.

Sneddon, I. N. (1945). The Distribution of Stress in the Neighbourhood of a Crack in an Elastic Solid. *Proceedings of the Royal Society of London. Series A, Mathematical and Physical*, 229–260.

Stokes, G. G. (1905). On the Effect of the Internal Friction of Fluids on the Motion of Pendulums. *Mathematical and Physical Papers*, 1–10. https://doi.org/10.1017/CBO9780511702266.002

Strack, O. D. L. (1989). *Groundwater Mechanics*. Prentice Hall.

Tang, H., Winterfeld, P. H., Wu, Y., Huang, Z., Di, Y., Pan, Z., & Zhang, J. (2016). Integrated simulation of multi-stage hydraulic fracturing in unconventional reservoirs. *Journal of Natural Gas Science and Engineering*, *36*, 875–892. https://doi.org/10.1016/j.jngse.2016.11.018

Timoshenko, S. P., & Goodier, J. N. (1970). *Theory of Elasticity* (3rd ed.). McGraw Hill.

Tong, S., & Mohanty, K. K. (2016). Proppant transport study in fractures with intersections. *Fuel*, *181*, 463–477. https://doi.org/10.1016/j.fuel.2016.04.144

Vandamme, L., & Curran, J. H. (1989). A three-dimensional hydraulic fracturing simulator. *International Journal for Numerical Methods in Engineering*, *28*(4), 909–927. https://doi.org/10.1002/nme.1620280413

Wahl, H. A., & Campbell, J. M. (1963). Sand Movement in Horizontal Fractures. *Journal of Petroleum Technology*, 1239–1246.

Wiles, T., & Curran, J. H. (1982). A general 3-D displacement discontinuity method. *Proceedings*

of the Fourth International Conference on Numerical Methods in Geomechanics, 103–111.

Zienkiewicz, O. C., & Taylor, R. L. (2000). *The Finite Element Method, Volume 3, Fluid Dynamics*. Butterworth - Heinemann.

Appendix A. Parallel Plates Flow Model

The dimensional variables to describe a hydraulic fracture are: height, length and width, and pressure. The width is significantly smaller compared to height and length so that flow is at most two-dimensional. If a low rate of fluid injection and high fluid viscosity are assumed, then the flow regime in the fracture is laminar. These considerations allow to apply the lubrication approximation to solve for pressure and flow rates calculating the local uniform flow between parallel plates separated by the local fracture width (Pearson, 1994). The parallel plates flow model is widely accepted to estimate the relationship between the velocity and the pressure of the fracturing fluid in a hydraulic fracture (Lavrov, 2011; Osiptsov, 2017). This relationship is fundamental to describe the movement of fracturing fluid or proppant.

Assuming, a Newtonian, incompressible, and single phase fluid, the mass conservation for the flow of slurry leads to the governing equation as (Irwin, 1957):

$$\frac{\rho D\boldsymbol{V}}{Dt} = \rho\boldsymbol{F} - \nabla p + \mu\nabla^2\boldsymbol{V} + (\mu + \lambda)\nabla(\nabla \cdot \boldsymbol{V}) \qquad \text{(A.1)}$$

where $D()/Dt$ is the material derivative, ∇ is de divergence operator, ∇^2 is the Laplacian operator, $\boldsymbol{V} = (v_x, v_y, v_z)$ is the velocity vector, $\boldsymbol{F} = (f_x, f_y, f_z)$ is the body force vector, ρ is fluid density, p is the fluid pressure, μ is the fluid viscosity and λ is the second viscosity coefficient. If the body forces are neglected and considering the assumption of incompressible fluid where the rate of fluid volume dilation $\nabla \cdot \boldsymbol{V}$ vanishes the equation (A.1) reduces to:

$$\frac{\rho D\boldsymbol{V}}{Dt} = -\nabla p + \mu\nabla^2\boldsymbol{V} \qquad \text{(A.2)}$$

Expanding the material derivative $D()/Dt$, the divergence operator ∇, and the ∇^2 Laplacian operator equation (A.2) takes the form:

$$\rho\left(\frac{\partial v_x}{\partial t}+v_x\frac{\partial v_x}{\partial x}+v_y\frac{\partial v_x}{\partial y}+v_z\frac{\partial v_x}{\partial z}\right)=-\frac{\partial p}{\partial x}+\mu\left(\frac{\partial^2 v_x}{\partial x^2}+\frac{\partial^2 v_x}{\partial y^2}+\frac{\partial^2 v_x}{\partial z^2}\right) \quad \text{(A.3)}$$

$$\rho\left(\frac{\partial v_y}{\partial t}+v_x\frac{\partial v_y}{\partial x}+v_y\frac{\partial v_y}{\partial y}+v_z\frac{\partial v_y}{\partial z}\right)=-\frac{\partial p}{\partial y}+\mu\left(\frac{\partial^2 v_y}{\partial x^2}+\frac{\partial^2 v_y}{\partial y^2}+\frac{\partial^2 v_y}{\partial z^2}\right) \quad \text{(A.4)}$$

$$\rho\left(\frac{\partial v_z}{\partial t}+v_x\frac{\partial v_z}{\partial x}+v_y\frac{\partial v_z}{\partial y}+v_z\frac{\partial v_z}{\partial z}\right)=-\frac{\partial p}{\partial z}+\mu\left(\frac{\partial^2 v_z}{\partial x^2}+\frac{\partial^2 v_z}{\partial y^2}+\frac{\partial^2 v_z}{\partial z^2}\right) \quad \text{(A.5)}$$

The dimensions, height and length of the fracture, are in the order of meters, while the fracture width is only in the order of millimeters as can be seen in Fig. A-1, then v_y can be neglected as it is much smaller than v_x and v_z

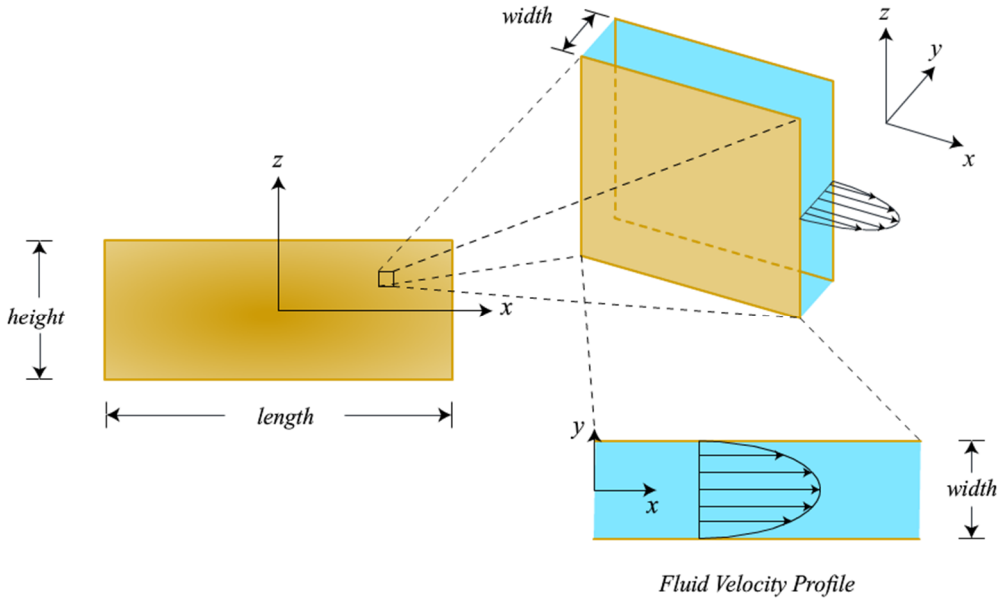

Figure A-1. Rectangular fracture schematic showing the principal geometrical dimensions and the fluid velocity profile.

Substitution of $v_y = 0$, equations (A.3), (A.4) and (A.5) reduce to:

$$\rho\left(\frac{\partial v_x}{\partial t} + v_x\frac{\partial v_x}{\partial x} + v_z\frac{\partial v_x}{\partial z}\right) = -\frac{\partial p}{\partial x} + \mu\left(\frac{\partial^2 v_x}{\partial x^2} + \frac{\partial^2 v_x}{\partial y^2} + \frac{\partial^2 v_x}{\partial z^2}\right) \tag{A.6}$$

$$\frac{\partial p}{\partial y} = 0 \tag{A.7}$$

$$\rho\left(\frac{\partial v_z}{\partial t} + v_x\frac{\partial v_z}{\partial x} + v_z\frac{\partial v_z}{\partial z}\right) = -\frac{\partial p}{\partial z} + \mu\left(\frac{\partial^2 v_z}{\partial x^2} + \frac{\partial^2 v_z}{\partial y^2} + \frac{\partial^2 v_z}{\partial z^2}\right) \tag{A.8}$$

Considering the no slip condition, which means zero fluid velocity at the fracture walls and a maximum fluid velocity at the center of the fracture, as shown in the velocity profile in the Fig. A-1. The changes of the velocity in the directions z and x which are the directions along the fracture can be neglected, then $\frac{\partial v_x}{\partial x} = \frac{\partial v_z}{\partial x} = \frac{\partial v_x}{\partial z} = \frac{\partial v_z}{\partial z} = 0$. Additionally, if a fully developed flow steady-state flow (it does not change with time), is considered then $\frac{\partial v_x}{\partial t} = \frac{\partial v_z}{\partial t} = 0$. Equations (A.6), (A.7) and (A.8) are further simplified as:

$$\frac{\partial p}{\partial x} = \mu\frac{\partial^2 v_x}{\partial y^2} \tag{A.9}$$

$$\frac{\partial p}{\partial y} = 0 \tag{A.10}$$

$$\frac{\partial p}{\partial z} = \mu\frac{\partial^2 v_z}{\partial y^2} \tag{A.11}$$

Integrating twice equations (A.9) and (A.11) and with respect to y yields:

$$v_x = \frac{y^2}{2\mu}\frac{\partial p}{\partial x} + c_1 y + c_2 \tag{A.12}$$

$$v_z = \frac{y^2}{2\mu}\frac{\partial p}{\partial z} + c_3 y + c_4 \tag{A.13}$$

Considering $y = 0$ at the center of the fracture due to the symmetry of the fluid flow velocity profile, letting w be the fracture width, and considering the slip condition $v_x = v_z = 0$ at the fracture walls or $y = \frac{w}{2}$ and $y = -\frac{w}{2}$, substituting these boundary conditions into equation (A.12):

$$0 = \frac{\left(\frac{w}{2}\right)^2}{2\mu}\frac{\partial p}{\partial x} + c_1\frac{w}{2} + c_2 \tag{A.14}$$

$$0 = \frac{\left(-\frac{w}{2}\right)^2}{2\mu}\frac{\partial p}{\partial x} - c_1\frac{w}{2} + c_2 \tag{A.15}$$

Adding equations (A.14) and (A.15) results:

$$2c_2 = -\frac{w^2}{4\mu}\frac{\partial p}{\partial x} \tag{A.16}$$

$$c_2 = -\frac{w^2}{8\mu}\frac{\partial p}{\partial x} \tag{A.17}$$

Following the same procedure, c_4 is calculated:

$$c_4 = -\frac{w^2}{8\mu}\frac{\partial p}{\partial z} \tag{A.18}$$

To find c_1, equation (A.17) is replaced into equation (A.14):

$$0 = \frac{w^2}{8\mu}\frac{\partial p}{\partial z} + c_1\frac{w}{2} - \frac{w^2}{8\mu}\frac{\partial p}{\partial z} \tag{A.19}$$

Solving for c_1

$$c_1 = 0 \tag{A.20}$$

Similarly

$$c_3 = 0 \tag{A.21}$$

Replacing c_1, c_2, c_3 and c_4 into equations (A.12) and (A.13) v_x and v_z are:

$$v_x = \frac{y^2}{2\mu}\frac{\partial p}{\partial x} - \frac{w^2}{8\mu}\frac{\partial p}{\partial x} \tag{A.22}$$

$$v_z = \frac{y^2}{2\mu}\frac{\partial p}{\partial z} - \frac{w^2}{8\mu}\frac{\partial p}{\partial z} \tag{A.23}$$

The average velocities over the distance w are calculated by integrating v_x and v_z from $-\frac{w}{2}$ to $\frac{w}{2}$ and divide by w:

$$\bar{v}_x = \frac{1}{w}\int_{-w/2}^{w/2}\left(\frac{y^2}{2\mu}\frac{\partial p}{\partial x} - \frac{w^2}{8\mu}\frac{\partial p}{\partial x}\right)dy = \frac{1}{2\mu w}\frac{\partial p}{\partial x}\left(\frac{y^3}{3} - \frac{w^2 y}{4}\right)\Bigg|_{-w/2}^{w/2} \tag{A.24}$$

$$\overline{v_x} = \frac{1}{2\mu w}\frac{\partial p}{\partial x}\left(\frac{w^3}{24} - \frac{w^3}{8} + \frac{w^3}{24} - \frac{w^3}{8}\right) \tag{A.25}$$

$$\overline{v_x} = \frac{1}{2\mu w}\frac{\partial p}{\partial x}\left(\frac{w^3}{12} - \frac{w^3}{4}\right) \tag{A.26}$$

$$\overline{v_x} = -\frac{w^2}{12\mu}\frac{\partial p}{\partial x} \tag{A.27}$$

Following the same procedure v_z is:

$$\overline{v_z} = -\frac{w^2}{12\mu}\frac{\partial p}{\partial z} \tag{A.28}$$

The cross-sectional area open to flow for a hydraulic fracture is the product of the fracture width w and the height of the fracture h, the flow rate is then defined as:

$$q_x = -\frac{w^3 h}{12\mu}\frac{\partial p}{\partial x} \tag{A.29}$$

$$q_z = -\frac{w^3 h}{12\mu}\frac{\partial p}{\partial z} \tag{A.30}$$

Then the flow rate per unit height is:

$$q_x = -\frac{w^3}{12\mu}\frac{\partial p}{\partial x} \tag{A.31}$$

$$q_z = -\frac{w^3}{12\mu}\frac{\partial p}{\partial z} \tag{A.32}$$

Appendix B. Numerical Solution of the Rock Deformation Governing Equation

For the sake of completeness the calculation of rock deformation using the displacement discontinuity method (DD) is listed here. The DD method is based on the fundamental solution of the stress-strain relation of an infinite elastic medium. It is assumed that a discrete approximation of a continuous distribution of DD can be made along a fracture surface. The concept of the DD was first proposed by Crouch and Starfield (1983) based on the constant line DD formulation for an infinite elastic medium for 2D or 3D problems. The DD formalization was later generalized the point load DD solutions based on the Kelvin's fundamental solution for elasticity by several authors developed (Vandamme & Curran, 1989; Wiles & Curran, 1982). In this work, the generalized DD model is used to simulate multiple fracture and fracture network problems in Chapter 5. The DD method is a computationally efficient numerical technique for the rock deformation modeling; since; it reduces the problem dimensionality by one and only the fracture surfaces discretization is required. Additionally, since the DD method is indirect boundary element method, it allows to represent the fracture with a single surface instead of two separated surfaces. The surface. A schematic representing the fracture surface is geometrically discretized with squares of sides 2a as shown in Fig. B-1.

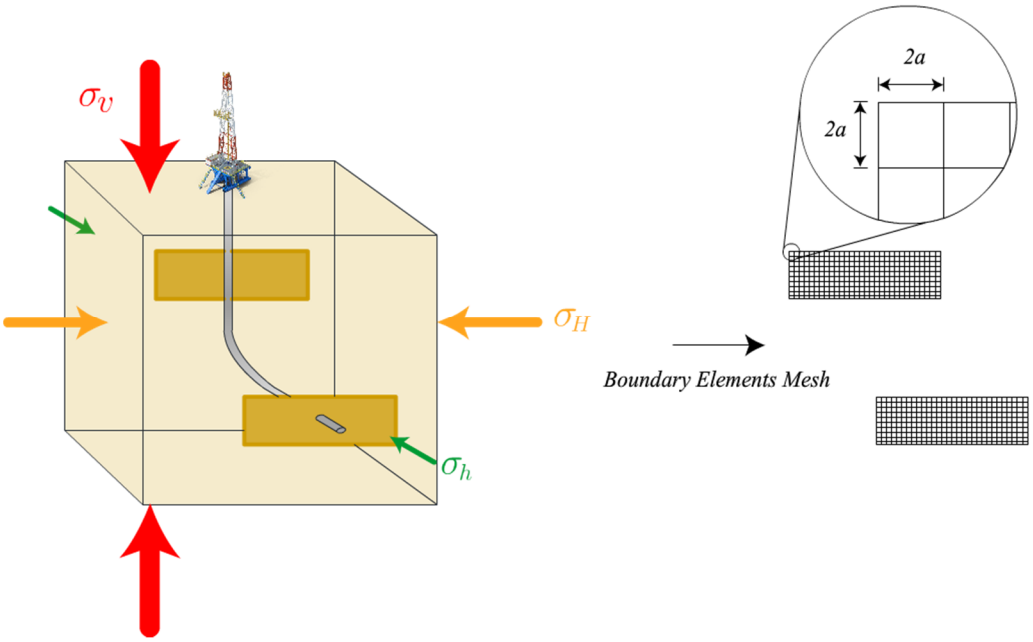

Figure B-1. Schematic of hydraulic fractures geometrical discretization using DD method, instead of the entire domain only the fracture discretization is required.

The constant DD components over a square element, which are defined as the difference of displacement of each face relatively to the local axis $\bar{z} = 0$ mathematically expressed as (Crouch & Starfield, 1983):

$$\bar{D}_{\bar{x}} = \bar{u}_{\bar{x}}(\bar{x}, \bar{y}, 0_-) - \bar{u}_{\bar{x}}(\bar{x}, \bar{y}, 0_+) \quad \text{(B.1)}$$

$$\bar{D}_{\bar{y}} = \bar{u}_{\bar{y}}(\bar{x}, \bar{y}, 0_-) - \bar{u}_{\bar{y}}(\bar{x}, \bar{y}, 0_+) \quad \text{(B.2)}$$

$$\bar{D}_{\bar{z}} = \bar{u}_{\bar{z}}(\bar{x}, \bar{y}, 0_-) - \bar{u}_{\bar{z}}(\bar{x}, \bar{y}, 0_+) \quad \text{(B.3)}$$

where $\bar{u}_{\bar{x}}, \bar{u}_{\bar{y}}, \bar{u}_{\bar{z}}$ are the displacements in the $\bar{x}, \bar{y}, \bar{z}$ local coordinate plane respectively, $\bar{D}_{\bar{x}}, \bar{D}_{\bar{y}}, \bar{D}_{\bar{z}}$ represents the three components of the DD in the local plane. The three components of the DD, the normal opening $\bar{D}_{\bar{z}}$, in-plane shear ride $\bar{D}_{\bar{y}}$ and out-off plane shear ride $\bar{D}_{\bar{x}}$ are shown in Fig. B-2.

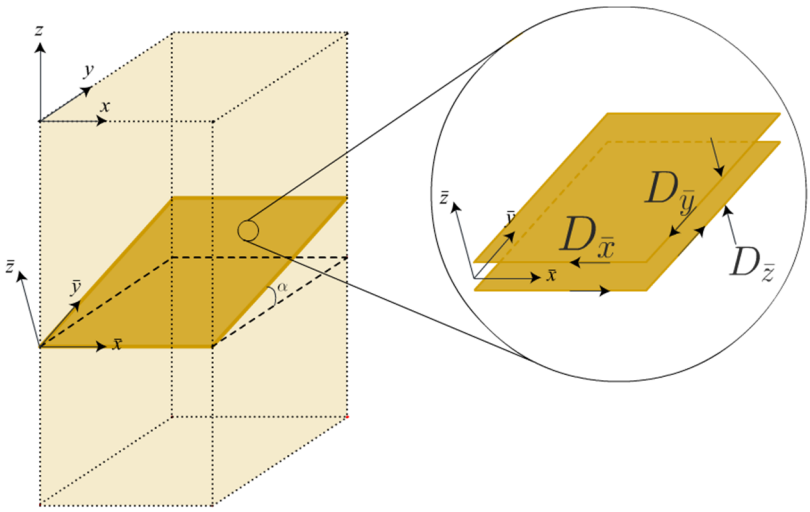

Figure B-2. Fracture in elastic solid arbitrarily oriented with magnification of constant DD components.

The tractions acting on the plane of fracture as shown in Fig. B-2, are related to the DD as follows (Crouch & Starfield, 1983):

$$\sigma_{\bar{x}\bar{z}} = \frac{G}{4\pi(1-v)}\left[\left(\frac{\partial^2 I}{\partial \bar{z}^2} + v\frac{\partial^2 I}{\partial \bar{y}^2}\right)D_{\bar{x}} - v\frac{\partial^2 I}{\partial \bar{x}\partial \bar{y}}D_{\bar{y}}\right] \tag{B.4}$$

$$\sigma_{\bar{y}\bar{z}} = \frac{G}{4\pi(1-v)}\left[-v\frac{\partial^2 I}{\partial \bar{x}\partial \bar{y}}D_{\bar{x}} + \left(\frac{\partial^2 I}{\partial \bar{z}^2} + v\frac{\partial^2 I}{\partial \bar{x}^2}\right)D_{\bar{y}}\right] \tag{B.5}$$

$$\sigma_{\bar{z}\bar{z}} = \frac{G}{4\pi(1-v)}\left[\frac{\partial^2 I}{\partial \bar{z}^2}D_{\bar{z}}\right] \tag{B.6}$$

where G is the shear modulus, v is the Poisson's ratio.

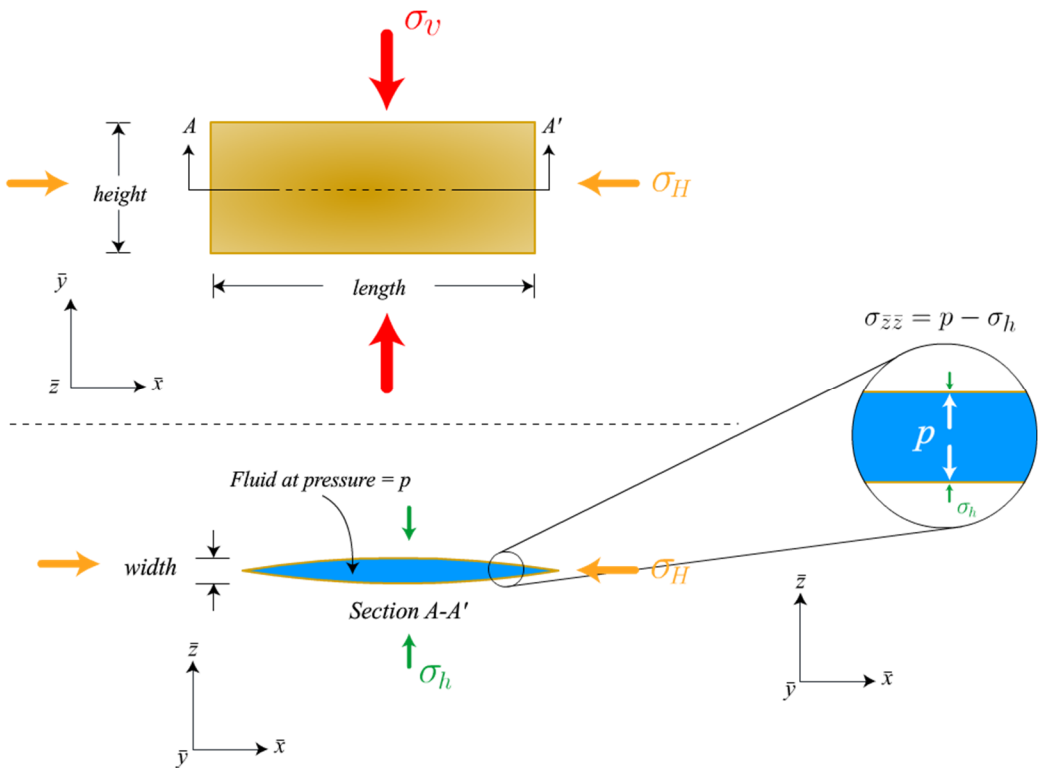

Figure 5-1. Hydraulic fracture and tractions acting on the plane of fracture, a local coordinate system is imposed for the analysis.

The derivatives of the function $I(\bar{x}, \bar{y}, \bar{z})$ are evaluated at $\bar{z} = 0$, the results are given as:

$$\left(\frac{\partial^2 I}{\partial \bar{x}^2}\right)_{\bar{z}=0} = \frac{1}{\bar{\rho}_1} - \frac{1}{\bar{\rho}_2} + \frac{1}{\bar{\rho}_3} - \frac{1}{\bar{\rho}_4} \tag{B.7}$$

$$\left(\frac{\partial^2 I}{\partial \bar{x}^2}\right)_{\bar{z}=0} = -\frac{\bar{y}-a}{\bar{x}-a}\frac{1}{\bar{\rho}_1} + \frac{\bar{y}-a}{\bar{x}+a}\frac{1}{\bar{\rho}_2} - \frac{\bar{y}+a}{\bar{x}+a}\frac{1}{\bar{\rho}_3} + \frac{\bar{y}+a}{\bar{x}-a}\frac{1}{\bar{\rho}_4} \tag{B.8}$$

$$\left(\frac{\partial^2 I}{\partial \bar{y}^2}\right)_{\bar{z}=0} = -\frac{\bar{x}-a}{\bar{y}-a}\frac{1}{\bar{\rho}_1} + \frac{\bar{x}+a}{\bar{y}-a}\frac{1}{\bar{\rho}_2} - \frac{\bar{x}+a}{\bar{y}+a}\frac{1}{\bar{\rho}_3} + \frac{\bar{x}-a}{\bar{y}+a}\frac{1}{\bar{\rho}_4} \tag{B.9}$$

$$\left(\frac{\partial^2 I}{\partial \bar{z}^2}\right)_{\bar{z}=0} = \frac{\bar{\rho}_1}{(\bar{x}-a)(\bar{y}-a)} - \frac{\bar{\rho}_2}{(\bar{x}+a)(\bar{y}-a)} + \frac{\bar{\rho}_3}{(\bar{x}+a)(\bar{y}+a)} - \frac{\bar{\rho}_4}{(\bar{x}-a)(\bar{y}+a)} \tag{B.10}$$

where $\bar{x}$ and $\bar{y}$ are the local coordinates of the element (i,j) where the tractions are been induced. The coefficients $\bar{\rho}_1,\ \bar{\rho}_2,\ \bar{\rho}_3,\ \bar{\rho}_4$ in the above equations are defined as:

$$\bar{\rho}_{1i,j} = \sqrt{\left(\bar{x}_{i,j} - a_i\right)^2 + \left(\bar{y}_{i,j} - a_i\right)^2} \tag{B.11}$$

$$\bar{\rho}_{2i,j} = \sqrt{\left(\bar{x}_{i,j} + a_i\right)^2 + \left(\bar{y}_{i,j} - a_i\right)^2} \tag{B.12}$$

$$\bar{\rho}_{3i,j} = \sqrt{\left(\bar{x}_{i,j} + a_i\right)^2 + \left(\bar{y}_{i,j} + a_i\right)^2} \tag{B.13}$$

$$\bar{\rho}_{4i,j} = \sqrt{\left(\bar{x}_{i,j} - a_i\right)^2 + \left(\bar{y}_{i,j} + a_i\right)^2} \tag{B.14}$$

The relationship between the induced tractions at the midpoint of element (i,j) and the DD components at all elements (k,l) is given as:

$$\overset{i,j}{\sigma'_{\bar{x}\bar{z}}} = \sum_{k=1}^{M}\sum_{l=1}^{N}\left(\overset{i,j;k,l}{A}_{\bar{x}\bar{x}}\overset{k,l}{D'_{\bar{x}}} + \overset{i,j;k,l}{A}_{\bar{x}\bar{y}}\overset{k,l}{D'_{\bar{y}}}\right) \tag{B.15}$$

$$\overset{i,j}{\sigma'_{\bar{y}\bar{z}}} = \sum_{k=1}^{M}\sum_{l=1}^{N}\left(\overset{i,j;k,l}{A}_{\bar{y}\bar{x}}\overset{k,l}{D'_{\bar{x}}} + \overset{i,j;k,l}{A}_{\bar{y}\bar{y}}\overset{k,l}{D'_{\bar{y}}}\right) \tag{B.16}$$

$$\overset{i,j}{\sigma'_{\bar{z}\bar{z}}} = \sum_{k=1}^{M}\sum_{l=1}^{N}\overset{i,j;k,l}{A}_{\bar{z}\bar{z}}\overset{k,l}{D}_{\bar{z}} \tag{B.17}$$

where ${}^{i,j;k,l}A_{\bar{j}\bar{k}}$, $(\bar{j},\bar{k}) = (\bar{x},\bar{y},\bar{z})$ are defined as the influence coefficients. The resultant system of equations size is $(M+N)\times(M+N)$.